UNIVERSIDADE FEDERAL DO RIO GRANDE DO SUL
ESCOLA DE ENGENHARIA
DEPARTAMENTO DE ENGENHARIA QUÍMICA
PROGRAMA DE PÓS-GRADUAÇÃO EM ENGENHARIA QUÍMICA

EXPLORING THE EFFECTS OF EMERGING TECHNOLOGIES ON FOOD PROCESSING THROUGH MOLECULAR DYNAMICS SIMULATIONS

TESE DE DOUTORADO

WAGNER AUGUSTO MÜLLER

PORTO ALEGRE, RS
2023

Universidade Federal do Rio Grande do Sul
Escola de Engenharia
Departamento de Engenharia Química
Programa de pós-graduação em engenharia química

Exploring the Effects of Emerging Technologies on Food Processing through Molecular Dynamics Simulations

Wagner Augusto Müller

Tese de doutorado apresentada ao Programa de Pós-Graduação como requisito parcial para obtenção do título de Doutor em Engenharia.

Orientador:
Prof. André Rodrigues Muniz, Dr.

Prof.ª Ligia Damasceno Ferreira Marczak, Dr.ª

Coorientador:
Prof.ª Júlia Ribeiro Sarkis, Dr.ª

Porto Alegre, RS
2023

Müller, W. A.
Exploring the Effects of Emerging Technologies on Food Processing through Molecular Dynamics Simulations / Wagner Augusto Müller. -- 2023.
234 f.

Orientador: André Rodrigues Muniz, Dr.
Ligia Damasceno Ferreira Marczak, Dr.ª
Coorientador: Júlia Ribeiro Sarkis, Dr.ª

Tese (doutorado) - Universidade Federal do Rio Grande do Sul, Escola de Engenharia, Departamento de Engenharia Química, Porto Alegre, BR-RS, 2023.

Campos Elétricos, Altas Pressões, Ultrassom, Biomembranas. I. Muniz, A. R., orient. II. Marczak, L. D. F., orient. III. Sarkis, J. R., coorient. IV. Título.

Acknowledgments

(in Portuguese)

A todos que colaboraram para a execução dessa tese. Em especial, à educação pública, que me permitiu concretizar toda minha formação escolar e acadêmica.

Aos meus orientadores, professores André, Ligia e Júlia, cuja orientação e apoio foram fundamentais em todas etapas do meu doutoramento. Seus conhecimentos, paciência e dedicação foram fundamentais para o desenvolvimento desse trabalho.

Aos meus pais, Ilar e Isolde, pelo amor incondicional e apoio constante. Desde o início, vocês foram fonte de inspiração e encorajamento, sempre me incentivando a perseguir meus sonhos. Ao meu irmão Vinicius, por toda amizade e por estar sempre ao meu lado.

A minha namorada, Jaqueline, por seu amor, apoio, paciência e pelo privilégio de dividir seus dias comigo. Sua presença constante tornou essa jornada mais leve e o seu encorajamento foi fundamental para superar os desafios que surgiram ao longo do caminho.

Aos colegas do Nanomaterials and Process Simulation Group (NAPSIG) e Laboratório de Tecnologia e Processamento de Alimentos (LATEPA), por todo auxílio e intercâmbio de ideias.

Aos supercomputadores Cesup (UFRGS) e SDumont (LNCC), pelos recursos computacionais necessários para elaboração desse trabalho.

O presente trabalho foi realizado com apoio da Coordenação de Aperfeiçoamento de Pessoal de Nível Superior - Brasil (CAPES) - Código de Financiamento 001 (Número dos processos: 88887.470200/2019-00 e 88887.696995/2022-00)

(in English)

To Professor Lars Jeuken, for sharing his knowledge and allowing me to work with his research group during my time in The Netherlands. To my friends of the Jeuken group, which made my stay abroad more enjoyable.

Resumo

Simulações de dinâmica molecular têm se revelado uma ferramenta de grande utilidade na análise mecanística de diversos fenômenos em biomoléculas. Essa técnica é particularmente promissora no estudo dos efeitos de tecnologias emergentes no processamento de alimentos, embora sua aplicação nesse campo seja ainda recente. O propósito dessa tese foi empregar tais simulações para a análise de diferentes sistemas relevantes à ciência de alimentos. No primeiro estudo, adotou-se uma abordagem atomística para analisar as alterações estruturais na ovalbumina em resposta a campos elétricos. Verificou-se uma notável estabilização da estrutura secundária, além de um aumento no tamanho médio, momento de dipolo e área superficial da proteína induzidos pelos campos. Esses resultados contribuíram para a compreensão dos mecanismos que alteram as propriedades tecnológicas desta proteína quando submetidas a esses processos. No segundo estudo, investigou-se a influência da temperatura e da pressão no fenômeno da eletroporação, empregando uma abordagem de modelagem em mesoescala. Observou-se que a formação e recuperação de poros em bicamadas lipídicas foi catalisada em temperaturas elevadas e pressões baixas. Esse comportamento cinético influenciou a migração de íons na bicamada, e combinações de baixas temperaturas e com pressões de 1000 atm demonstraram o melhor desempenho para a extração iônica. No terceiro estudo, foram analisados os efeitos sinérgicos da aplicação combinada de eletroporação e sonoporação em bicamadas lipídicas. Observou-se que a redução na espessura da bicamada durante a passagem da onda ultrassônica pode catalisar a formação de poros, embora esse efeito se manifeste principalmente em situações em que o campo elétrico, por si só, não seria capaz de criar poros. A sinergia entre o processo de cavitação e a eletroporação resultou no efeito de combinação mais significativo, onde o nanojato gerado contribuiu para guiar o processo de formação do poro induzido pelo campo elétrico. Por fim, foi conduzida a análise de vesículas híbridas compostas por polímeros e fosfolipídeos. As simulações revelaram diversas possíveis conformações de membrana dependendo da relação lipídeo-polímero, bem como um aumento na estabilidade da membrana em frações poliméricas elevadas. Adicionalmente, a análise de um peptídeo WALP inserido na bicamada demonstrou que apenas membranas com até 50% de conteúdo de polímero favoreceram aplicações biotecnológicas. Em síntese, os estudos demonstram o potencial das simulações de dinâmica molecular em desvendar os mecanismos subjacentes a processos bioquímicos complexos em tecnologias emergentes no processamento de alimentos.

Palavras-chave: Campos Elétricos, Altas Pressões, Ultrassom, Biomembranas.

Abstract

Molecular dynamics simulations have proven to be an useful tool in the mechanistic analysis of various phenomena in biomolecules. This technique is particularly promising in the study of the effects of emerging technologies in food processing, although their application in this field is still recent. The purpose of this thesis was to employ these simulations for the analysis of different systems relevant to food science. In the first study, an atomistic approach was adopted to analyze the structural changes in ovalbumin in response to electric fields. A notable stabilization of the secondary structure was observed, along with an increase in the average size, dipole moment, and surface area of the protein induced by the fields. These results contributed to the understanding of the mechanisms that alter the technological properties of this protein when subjected to these processes. In the second study, the influence of temperature and pressure on the electroporation phenomenon was investigated, employing a mesoscale modeling approach. It was observed that the formation and recovery of pores was catalyzed at high temperatures and low pressures. This kinetic behavior influenced the ion migration in the bilayer, and combinations of low temperatures with pressure of 1000 atm demonstrated the best performance for ionic extraction. In the third study, the synergistic effects of the combined application of electroporation and sonoporation on lipid bilayers were analyzed. It was observed that the reduction in bilayer thickness during the passage of an ultrasonic wave could catalyze pore formation, although this effect mainly manifested in situations where the electric field alone would not be able to create pores. The synergy between the cavitation process and electroporation resulted in the most significant combined effect, where the generated nanojet contributed to guiding the process of field-induced pore formation. Moreover, a comprehensive analysis of hybrid vesicles formed by polymers and phospholipids was conducted. The simulations revealed various possible membrane conformations depending on the lipid-to-polymer ratio, and an increased bilayer stability at higher polymeric fractions. Additionally, the analysis of a WALP peptide inserted in the bilayer demonstrated that only membranes with up to 50% polymer content favored biotechnological applications. In summary, the studies demonstrate the potential of molecular dynamics simulations in elucidating the underlying mechanisms of complex biochemical processes in emerging technologies.

Palavras-chave: Electric Fields, High Hydrostatic Pressure, Ultrasound, Biomembranes.

Contents

List of Figures

List of Tables

List of Symbols

$\vec{E}$	Electric field vector	
$\vec{v}$	Velocity	
A	Lateral area	
a	Theoretical response at zero concentration	
b	Slope factor	
C	Coulomb's constant	$8{,}99 \times 10^{9}\,\mathrm{N\,m^{2}\,C^{-2}}$
c	Inflection point	
C_1, C_2	Generic constants of the Arrhenius model	
D	Mass diffusivity	
d	Theoretical response at infinite concentration	
E	Energy	
$F_{i,j}$	Force exerted by particle i on particle j	
F_{max}	Maximum electric force per voltage squared	
HP	High pressure gel phase	
k	Energy gain constant	
K_A	Area compressibility modulus	
k_b	Boltzmann's constant	$1{,}38 \times 10^{-23}\,\mathrm{m^{2}\,kg\,s^{-2}\,K^{-1}}$
k_c	Bending modulus	
L_α	Liquid-crystalline phase	
$L_{\beta'}$	Gel II phase	
L_i	Length of an arc of size i	

m	Mass
N	Total number of atoms or particles
n	number of potential minima generated in a 360° rotation
P	Pressure
P_m	Transmembrane potential
$P_{\beta'}$	Gel I phase
q	Charge
R	van der Waals radius
r	Distance
r_*	Minimum radius of pores
R_g	Radius of gyration
r_h and r_t	Constants of advection velocity
R_{MAX}	Pore maximum radius
S_{cd}	Order parameter
T	Temperature
t	Time
t_m	Time to achieve the maximum radius
t_r	Pore resealing time
t_s	Stabilization time
t_{eq}	Time for ionic migration to cease
T_m	Temperature of phase transition
U	Force field potential
V	Volume
V_n	Energy barriers for rotation around the central bond
Z_i	Perpendicular distance of section i from the center of the sphere

Greek letters

β	Steric repulsion energy

χ	Improper dihedral angle between 4 atoms	
ϵ_0	Permittivity in a vacuum	$8{,}854 \times 10^{-12}\,\mathrm{C\,V^{-1}\,m^{-2}}$
γ	Edge energy	
κ_G	Gaussian curvature modulus	
λ	Tension on a compressed bilayer	
λ_{eff}	Effective tension of the membrane	
μ	Chemical potential	
ν	Kinematic viscosity	
ω	Frequency	
ϕ	Dihedral angle between 4 atoms	
ψ	Angle between the Cα/C atoms of the peptide chain	
ρ	Charge density	
σ	Theoretical distance of zero force	
τ	Pressure profile	
θ	Angle between 3 atoms	
θ_{order}	Angle between the bilayer normal plane and the acyl group particles	
ε	Potential well depth	
φ	Angle between the Cα/N atoms of the peptide chain	
h	Bilayer thickness	
I_ρ	Fraction of overlap between a bilayer leaflets	

Subscript

α	Liquid phase
β'	Gel phase
χ	Improper dihedral angle
ϕ	Dihedral angle
i	Atom i
0	Equilibrium

b	Bond
C	Coulomb
kin	Kinetic
L	Lateral
LJ	Lennard-Jones
N	Normal
ub	Urey-Bredley Equilibrium

Acronyms

AA	All-atom
AC	Alternating Current
CG	Coarse-graining
CHP	Conventional Heating Process
DC	Direct Current
DLS	Dynamic Ligth Scattering
DPPC	Dipalmitoylphosphatidylcholine
EDP	Electron Density Profile
EF	Electric Field
FF	Force Field
Gromacs	Groningen Machine for Chemical Simulations
HHP	High Hydrostatic Pressure
HV	Hybrid vesicles
Lammps	Large Atomic/Molecular Massively Parallel Simulator
MD	Molecular Dynamics
NMR	Nuclear Magnetic Resonance
OVA	Ovalbumin
PBD	Polybutadiene
PDB	Protein Data Bank

PEF	Pulsed Electric Fields
PEO	Polyethylene glycol
PMF	Potential of Mean Force
POPC	1-palmitoyl-2-oleoyl-sn-glycero-3-phosphocholine
PPPM	Particle–Particle Particle–Mesh
RAR	Ramachandran Allowed Regions
RFR	Ramachandran Favored Regions
RMSD	Root Mean Square Displacement
SASA	Solvent Available Surface Area
SAXS	Small-Angle X-ray Scattering
SMALP	Styrene-Maleic-Acid Lipid Particle
STRIDE	Structural Identification algorithm
US	Ultrasonic
VMD	Visual Molecular Dynamics
WHAM	Weighted Histogram Analysis Method

Chapter 1

Introduction

The production of safe and high-quality products is of utmost importance in the food industry, and a key aspect to achieve this goal involves managing the growth of harmful microorganisms in these matrices. Conventional processing for microbial inactivation uses heat transfer by convective or conductive mechanisms, which denatures proteins and enzymes required for the cell metabolism. However, this method has some drawbacks, including the loss of thermosensitive compounds by volatilization, long processing times for foods with non-ideal thermophysical properties, and low energy efficiency. As a result, scientists and engineers have been exploring alternative processes, which created a new research field known as *emerging technologies*. Initially, these technologies were intended to replace or supplement conventional heating methods. Nevertheless, their unique physical mechanisms have enabled the achievement of a wide range of objectives beyond just microbial inactivation (e.g., improving mass transfer and enhancing sensory attributes). Some of these unit operations have already been commercially introduced, while others are still in research/development phase.

As the food industry continues to develop, it is important to explore how these new and innovative methods impact different products. Although the application of emerging technologies is a relatively new research field, significant effects on various macro and micronutrients have already been reported after their application. The structural changes include protein denaturation, the formation of pores in lipid bilayers, phase separation, change in the degradation rates of vitamins/minerals, among others. These phenomena are typically evaluated using experimental techniques like X-ray crystallography, nuclear magnetic resonance (NMR), high-performance liquid

chromatography and fluorescence spectroscopy. However, these procedures have some limitations, such as high equipment costs, low resolution, and the difficulty in evaluating mechanisms, as structural parameters are obtained only at the beginning and at the end of the process.

In recent decades, atomistic computational simulations have become an indispensable tool for analyzing molecular systems, enabling advances in various fields such as chemistry, physics, biology, and materials science. These simulations allow the acquisition of macroscopic information using numerical techniques and statistical mechanics concepts, while not presenting the limitations of experimental methods. The earlier reports of molecular simulations date back to the 1950s, when the first computers capable of solving complex calculations were developed. Their application was limited to the analysis of simple systems such as noble gases, diatomic molecules, and crystalline solids. In the following years, the field expanded considerably with the development of more sophisticated techniques, allowing the investigation of increasingly complex molecules like polymers, proteins and lipids. Since then, molecular simulations have constantly evolved due to the creation of more efficient algorithms and increased processing capacity of modern computers. These advances helped to mitigate the major limitation of these techniques related to the temporal and spatial scales that can be accessed by such simulations.

The term *molecular simulation* covers a wide range of methods with distinct applications and theoretical backgrounds. The selection of a technique for a given problem should take into account the phenomenon being analyzed and its characteristic temporal and spatial scales. Although widely used in several fields, these methods have only recently been employed in food science. Applications include elucidating the structures and functions of carbohydrates, proteins, and lipids relevant to the food industry. Molecular simulations also enable the understanding of the interactions between different biomolecules and the investigation of atomic properties dependence on process variables such as temperature and pressure. Recently, these methods have also been applied to analyze the molecular effects of emerging technologies in nutrients.

1.1 Objectives

The objective of this thesis is to employ molecular dynamics simulations to study the effects of emerging technologies on different molecules and systems. As the application of computational methods in food science is a developing area and has become increasingly valuable for evaluating and explaining relevant phenomena, this thesis aims to contribute to this field by providing insights into the molecular effects related to the application of some emerging technologies. The specific objectives are divided in four topics:

- analyze changes caused by the application of continuous and alternating electric fields on the structural, solubility, and electrical properties of ovalbumin;
- investigate the influence of pressure and temperature on the electroporation of a lipid bilayer;
- examine the relation between electric fields and ultrasonic waves when concurrently applied to lipid bilayers, focusing on understanding the synergy between these two processes;
- evaluate physicochemical, mechanical, and biochemical properties of lipid-polymer hybrid vesicles to optimize these membranes for their biotechnological applications.

The present work is structured as follows: Chapter 2 provides a literature review of the theoretical aspects relevant to the subsequent studies. It covers concepts related to emerging technologies, their processing effects, the biochemistry of the molecules under investigation, and the principles of molecular dynamics simulations. In Chapter 3, titled "Molecular dynamics study of the effects of static and oscillating electric fields in ovalbumin", the impact of continuous and alternating electric fields on ovalbumin is examined using classical molecular dynamics simulations. Chapter 4, titled "Molecular dynamics insights on temperature and pressure effects on electroporation", explores the effects of temperature and pressure on the electroporation phenomenon.

In Chapter 5, titled "Computational analysis of the simultaneous application of ultrasonic waves and electric fields in a lipid bilayer", the synergy between ultrasonic waves and electric fields is analyzed along with their effects on lipid bilayers. Chapter 6, entitled "Unraveling the Phase Behavior, Mechanical Stability, and Protein Reconstitution Properties of Polymer-Lipid Hybrid Vesicles", investigates the structural and biochemical behavior of hybrid polymer-lipid vesicles. Finally, the concluding chapter presents the key findings from these studies and outlines future prospects for research in this field.

Chapter 2

Literature review

The purpose of this chapter is to present the fundamental concepts that provide the theoretical foundation of this thesis. Specific sections will address the analyzed emerging technologies and their processing effects, the simulation techniques employed in the studies, and the biochemistry of relevant molecules.

2.1 Emerging technologies

Preservation processes are one of the most critical stages in the manufacture of foods, as they are responsible for delaying or preventing the proliferation of pathogenic and spoilage microorganisms. The two predominant preservation processes are pasteurization and sterilization, which are thermal operations distinguished by the applied temperature range. Generally, pasteurization involves lower temperatures (typically between 60 to 85°C), while sterilization involves temperatures above 100°C. As a result, pasteurization does not completely inactivate all microorganisms in the food matrix, and an additional preservation technique, such as cold storage, is also necessary. On the other hand, sterilization is employed when long-term shelf stability is required without the need for refrigeration.

These two thermal processes are commonly known as conventional methods due to their widespread application. In both, the product undergoes heating through conductive and/or convective heat transfer. The processing time is therefore influenced by the thermo-physical characteristics of the food. Consequently, products with less favorable properties (e.g., low thermal conductivity) experience higher tempera-

ture gradients, resulting in longer processing times (SINGH; DENNIS, 2014). This undesired characteristic leads to potential disadvantages, such as low energy efficiency and loss of sensory and nutritional components by volatilization or thermal degradation (ATUONWU et al., 2019).

Given the growing level of consumer expectations, who are increasingly aware of sensory and environmental aspects of products (CARACCIOLO et al., 2020; BOWEN; GRYGORCZYK, 2021), alternative processing methods have been studied in recent decades. The term *emerging technologies* refers to these unit operations, which include the application of ultrasound (CHEMAT et al., 2011), ultraviolet and infrared radiation (DELORME et al., 2020), application of cold plasma (THIRUMDAS et al., 2014), application of electric fields (E.A.; EISS, 2012), high pressure processing (ATUONWU et al., 2019), and membrane separation processes (DHINESHKUMAR, 2017). These technologies are at different development stages, depending on how long they have been researched and the safety of their application. Some, such as ultrasound and ultraviolet radiation, are well-established and already used in commercial food processing. Others, such as cold plasma and ultra shear technologies, are still under development (GAVAHIAN et al., 2021). This section will focus on the emerging technologies that were studied in the present thesis, which include the application of electric and electromagnetic fields, high hydrostatic pressure, ultrasound, and microencapsulation processes.

2.1.1 Electric and electromagnetic fields

The use of electric and electromagnetic fields in food processing has gained great interest in recent years. Technologies based on electric fields apply a potential difference to the product through electrodes connected to a direct or alternating current generator. In the case of alternating current, the process is dependent on the frequency of the device. Technologies using alternating electric fields are generally considered thermal because the field oscillation causes charged molecules to continuously change direction in response to the field re-orientation. This behavior leads to atomic collisions and heat generation. Alternating current technologies typically apply electric fields below 1,000 V cm^{-1}, with examples including ohmic heating and moderate electric field

processing (SASTRY, 2008). According to Alkanan et al. (2021), the main applications of these processes are in microbial inactivation and in the improvement of mass transfer processes, such as fermentation, drying, and extraction.

The pulsed electric field (PEF) technology is a non-thermal method that applies direct current. In PEF, pulses of high voltage (> 1,000 V cm^{-1}) are used; as the duration of the electric pulses is short (milliseconds to microseconds), heat generation by Joule effect is minimized (E.A.; EISS, 2012). On the other hand, electrical effects are amplified due to the high voltages employed, favoring mass transfer phenomena based on cell electroporation (PUÉRTOLAS et al., 2012), which will be discussed in Section 2.2. It can be emphasized that further research is needed to fully understand the effects of PEF on microorganisms. While satisfactory inactivation rates have been reported for Gram-negative bacteria, Gram-positive bacteria, viruses, and yeasts (GARNER, 2019), the inactivation of thermoresistant fungi and bacterial spores remains relatively unexplored.

Technologies based on electromagnetic fields differ by the properties of the incident radiation. Figure 2.1 shows a representation of the classical electromagnetic spectrum, where it is possible to identify the types of radiation used by different technologies spread across a wide range of frequencies/wavelengths.

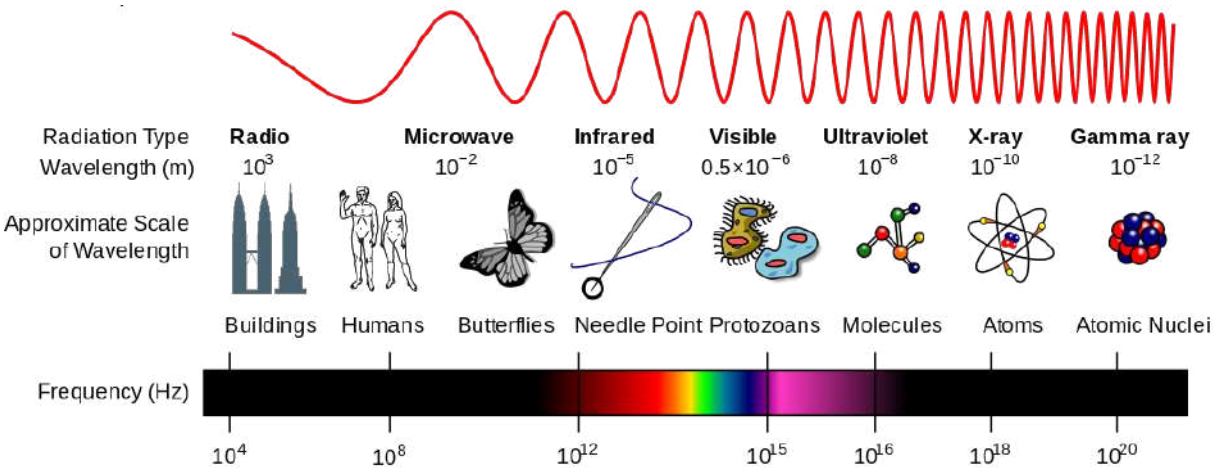

FIGURE 2.1. Electromagnetic spectrum.

Source: Inductiveload (2007)

According to Lima et al. (2018), processes using electromagnetic fields can be

classified as ionizing or non-ionizing. Ionizing technologies, positioned on the right side of the electromagnetic spectrum, have sufficient energy to break chemical bonds. Examples of ionizing technologies include gamma and ultraviolet radiation. This category is outside the scope of analysis of this thesis and will not be addressed hereafter; a comprehensive review about such operations can be found in Andrews et al. (1998). Non-ionizing electromagnetic technologies are positioned toward the left side of the spectrum and are characterized by longer wavelengths and lower frequencies. The energy of photons in this category is below 0.0016 eV, significantly lower than the energy of atomic bonds ($\approx$ 1 eV). As a result, these processes are not able to break atomic bonds, although they can alter the structure of several molecules (KIDDLE, 2006). Examples of such technologies include radiofrequency, microwave, and infrared heating.

The microwave radiation heats the product through the generation of an electric field by the electromagnetic waves. This field induces the rotation of water dipoles and the displacement of ions, resulting in temperature increases caused by intermolecular friction (MULLIN, 1995). The main applications of this technology are the pasteurization, tempering, dehydration, baking, bleaching and frying of products (SWAMY; MUTHUKUMARAPPAN, 2021). Radiofrequency operates on similar principles, although with lower frequencies and energies, resulting in a decreased heating rate. At the same time, this radiation is characterized by a longer wavelength (λ), enhancing its penetration in products, as radiations with low λ are rapidly absorbed, restricting their ability to reach deeper layers (RAMASWAMY; TANG, 2008). All the applications mentioned for the microwave technology can also be cited for radiofrequency, although with lower intensity due to the decreased energy of this radiation. Radiofrequency is commonly applied as a pretreatment to conventional thermal processing, helping to mitigate its associated drawbacks. In addition, the radiofrequency application has been effective in processes such as thawing, tempering, and pest infestation control (LI et al., 2017; XU et al., 2019). On the other hand, infrared is characterized by higher energies but shorter wavelengths, and is mostly used for heating the surface of products (KRISHNAMURTHY et al., 2008).

2.1.2 High hydrostatic pressure

The high hydrostatic pressure (HHP) treatment is an emerging technology which subjects the product to high mechanical forces. The pressure transmitting medium (usually water) is pumped into a sealed vessel until the desired compression is achieved, at which point filling is stopped (YAMAMOTO, 2017). Figure 2.2 shows a schematic representation of this process. A considerable advantage of HHPs compared to thermal processing is that, in ideal cases, no additional energy or mass is required once the process starts. In contrast, the temperature gradients in thermal processing imposes the continuous need for energy supply (KNORR et al., 2011).

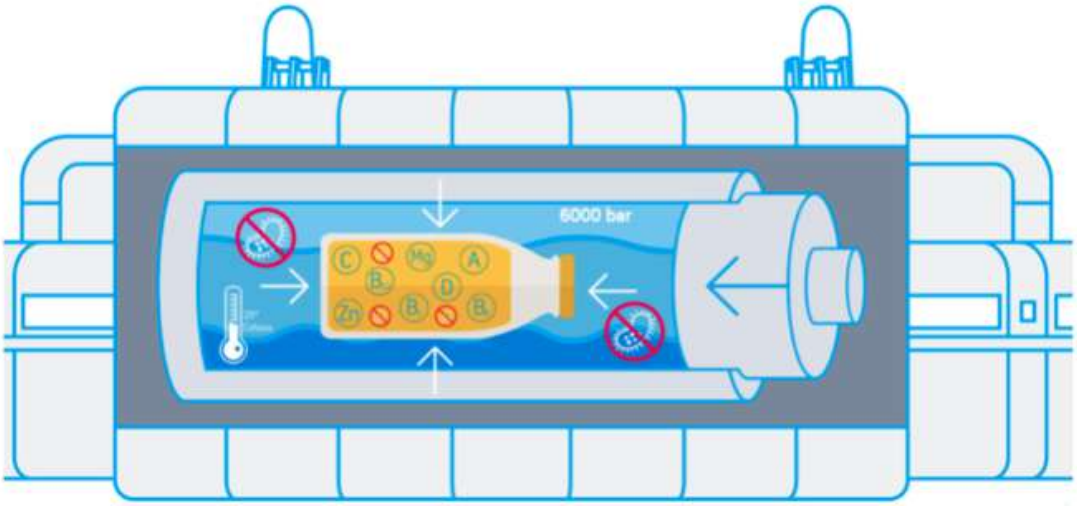

FIGURE 2.2. Representation of the HHP process.
Source: Thyssenkrupp (2021)

While high-pressure processing is generally regarded as non-thermal, temperature and pressure are thermodynamic properties closely interconnected. Therefore, a slight heating of the product during compression/expansion cycles is often observed. This deviation from the isothermal case depends on the thermo-physical properties of the product, although an increase of 3-9°C is typically visualized for every 100 MPa added in relation to the atmospheric condition. Due to the isostatic principle, all molecules are compressed by a similar force, resulting in a highly homogeneous processing. The main molecular effect of HHPs is the disruption of non-covalent bonds (e.g., hydrophobic interactions and hydrogen bonds). Consequently, the loss of volatile

components is reduced in comparison with conventional heating process (MASSOUD et al., 2016). This is because thermosensitive compounds typically have low molecular weight and covalent bonds, making them unaffected by HHP.

The major application of HHPs in the food industry is the inactivation of pathogenic microorganisms using pressures in the range of 300-800 MPa (MUSSA; RAMASWAMY, 1997; HUANG et al., 2015; ALLISON; FOULADKHAH, 2018). High pressures affect vegetative microorganisms by the unfolding of metabolic proteins and the mechanical damage to the cytoplasmic membrane. However, HHP alone is not effective for the inactivation of spores, and the combined application with heat or another emerging technology is necessary when such microorganisms are considered (SOKOŁOWSKA et al., 2012; DARYAEI et al., 2016). The advantages of HHP processing include high energy efficiency, reduced need for chemical preservatives, treatment homogeneity, and reduced environmental impact, since the process only requires water (which can be reused). The major disadvantages include the operating regime (either batch or semicontinuous), low efficacy for spore inactivation, and potential undesired effects on the structure of certain products (e.g.,starch granules) (AGANOVIC et al., 2021).

2.1.3 Ultrasound

In ultrasound processing, sound waves with a frequency higher than the human hearing limit (20 kHz) are used to modify the properties of foods. These waves are created by transducers that convert electrical into ultrasonic energy. This technology offers versatility and finds various applications in altering the physicochemical (MULLAKAEV et al., 2015), mechanical (SHARMA et al., 2017) and biochemical (HUANG et al., 2017) properties of products. By adjusting parameters of the applied wave, such as frequency and amplitude, a broad spectrum of outcomes are obtained.

Ultrasound can be characterized in terms of its energy in two classes: high intensity, with frequencies between 20 and 100 kHz and intensity greater than 1 W cm^{-2}, and low intensity, with frequencies above 100 kHz and intensity below 1 W cm^{-2}. This classification is important as the application of waves with different intensities leads to distinct outcomes. Low-intensity ultrasound (US) waves are generally used in chem-

ical analyses and monitoring of food quality, and examples of application include the determination of composition, structure, and physical state of products (CHÁVEZ-MARTÍNEZ et al., 2020). On the other hand, high-intensity US waves can modify the structure of different molecules, and can be used to improve mass transfer and alter the texture of products (KHAN et al., 2020). The difference between high and low intensity US is evident in their effect on microorganisms: while low-intensity increases microbial proliferation and the yield of synthesized compounds (PITT; ROSS, 2003), high-intensity causes their inactivation (PIYASENA et al., 2003).

Considering the differences between high- and low-intensity ultrasound, it is important to understand how the US process operates on a molecular level to explain this distinct phenomena. In general, the passage of an acoustic wave creates areas of compression and rarefaction in the medium, generating zones of high and low pressure, respectively. These pressure variations create forces capable of moving small molecules and ions, a process known as acoustic transmission. This is the main physical effect that occurs during the application of low-intensity US (WU, 2018), resulting in the low shear forces of this category.

Above a certain frequency/energy threshold, empty spaces (cavities) are created in the regions of low pressure. This occurs because liquids are not very compressible and can not support large pressure variations. As a result, vapor bubbles are formed, as illustrated in Figure 2.3. These bubbles can increase in size by absorbing volatile gases, a process known as rectified diffusion (CRUM, 1984). As they grow, the bubbles become unstable and collapse violently, creating zones of high temperature and pressure (BUI et al., 2018) and intense shear forces. This phenomenon, known as cavitation, is responsible for the more pronounced effects of high-intensity ultrasound.

2.1.4 Microencapsulation

The microencapsulation process aims to coat an active compound within an encapsulating agent, resulting in the formation of small spheres (1-500 μm) containing the target molecules. These spheres protect the core material from adverse changes and sensory alterations that are undesirable for consumers (MOHAMMADALINEJHAD; KUREK, 2021). These spheres can be intentionally disrupted through specific stimuli

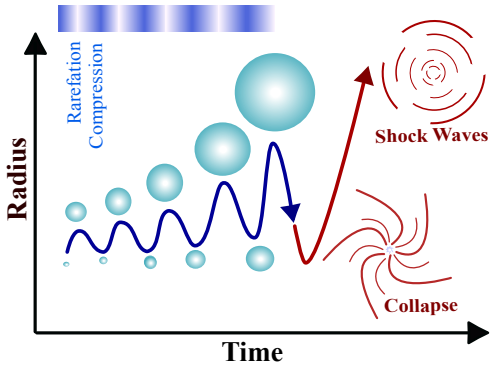

FIGURE 2.3. Cavitation due to the application of ultrasonic waves.

(e.g., heat or pH changes), promoting the controlled release of the active compound under specific conditions. This technique has applications in several fields such as medicine, biochemistry, cosmetics and textile industry. In the food and pharmaceutical industry, this process is also widely used, although with some additional specifications. The encapsulating material must exhibit compatibility and non-reactivity with the encapsulated substance, and pose desirable mechanical attributes such as flexibility, robustness, and stability (AMARAL et al., 2019).

Microencapsulation can be performed by various techniques, selected according to the active compound and the desired properties of the final product. Common techniques include spray drying, extrusion, and in situ polymerization. One of the most prevalent approaches involves the use of liposomes, globular structures formed by amphipathic phospholipids (further information on these molecules is provided in Section 2.4.2). The biggest advantage of liposomes is their ability to encapsulate both hydrophilic (internally) and hydrophobic (within the hydrophobic portion of the acyl chain) materials, sometimes simultaneously (MIRAFZALI et al., 2014). Some applications of these structures are:

- **Protection of the target molecule against degradation, hydrolysis, or chemical reactions:** an example is the preservation of β-galactosidase, which is added to milk for consumption by lactose-intolerant individuals. Direct supplementation of this enzyme in the beverage alters the flavor of the product, which can be resolved through encapsulation (RAO et al., 1994).

- **Microbial inactivation:** encapsulation of antimicrobial agents can enhance their effectiveness. For example, nisin, a peptide composed of 34 amino acids, exhibits inhibitory effects against Gram-positive bacteria. However, its efficacy is compromised due to inhibitors and unwanted interactions. The use of liposomes to encapsulate nisin has proven to be a viable strategy to preserve its antimicrobial activity(BOUALEM et al., 2013).

- **Acceleration of cheese maturation:** exogenous enzymes can be added to cheese to accelerate the maturation process, but they negatively impact the sensory attributes, and encapsulation of these enzymes helps to mitigate these effects (ALKHALAF et al., 1988).

- **Control of the Maillard reaction:** the occurrence of the Maillard reaction pose challenges in microwave processing (WANG et al., 2023), and to address this, liposomes have been used to encapsulate the basic amino acids. The reaction is triggered thermally in the desired condition, releasing the amino acids and resulting in the desired color and aroma products (HAYNES et al., US5089278A, 1989).

Although liposomes are widely used for microencapsulation, they have some drawbacks, like the high cost and low physicochemical stability. As an alternative, polymeric vesicles have gained recent attention due to their excellent encapsulation performance and high mechanical robustness (LU et al., 2021). The main limitation of polymeric membranes is their low biocompatibility, which affects the encapsulation of certain compounds like proteins and peptides. To overcome this, hybrid vesicles composed of lipids and polymers have been proposed in recent years, combining the advantages of both constituents (WANG et al., 2018; MUKHERJEE et al., 2019). Further details on these structures are discussed in Section 2.4.3.

2.2 Non-thermal effects

As discussed in the previous section, emerging technologies are viable alternatives to complement or substitute conventional processing methods. However, since

the physical principles of these technologies are fundamentally different from those of conventional heating, different phenomena may occur during their application. These phenomena are known as non-thermal effects and, in the context of this thesis, are defined as the differences between a process guided by an emerging technology compared to a process by conventional heating under similar conditions. In the sequence, some relevant non-thermal phenomena will be addressed, with special emphasis on those analyzed in this thesis.

Microbial inactivation is one of the most important applications of emerging technologies, representing the initial impetus for their adoption in the food industry. Considering the application of electric fields, it was initially believed that the benefits of these processes came from the uniform temperature profile and the faster heating, which are characteristics of the Joule effect. However, pioneering research conducted in the 1990s (KIM et al., 1996; CHO et al., 1999) reported additional microbiological inactivation rates during the application of electric fields compared to conventional thermal processing. This phenomenon was initially attributed to the distinct heating ramps between processes, affecting the adaptability of microorganisms and altering their inactivation kinetics. However, subsequent studies reported higher inactivation rates even when the heating profiles were similar. Nowadays, such effects have been observed in several microorganisms, such as Gram-positive and Gram-negative bacteria (HASHEMI et al., 2019), spores (MURASHITA et al., 2016), fungi (MÜLLER et al., 2021) and yeasts (YILDIZ; BAYSAL, 2006).

In most of these studies, the acceleration of the inactivation rate is attributed to the electroporation (or electropermeabilization) of the cells. This phenomenon occurs due to the generation of a transmembrane potential by the electric field, which creates a potential difference between the ions within the cell and those in the surrounding medium. When this potential exceeds the bilayer critical rupture threshold, pores are formed in the cytoplasmic membrane. Consequently, cellular content is released and external components ingress into the interior of the cell (CARTER; SHIEH, 2015). Some applications of electroporation include extraction processes, microbial inactivation, electrofusion, and even cancer treatment (related to the death of cancerous cells). A schematic representation of this phenomenon is provided in Figure 2.4.

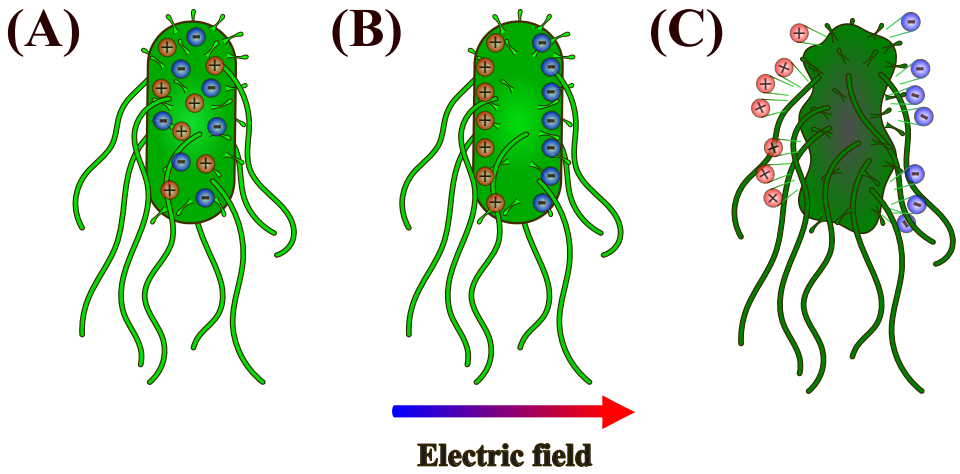

FIGURE 2.4. Electroporation of an *Escherichia coli* cell, where (A) shows the cell before field application, (B) the influence of the electric field (ion gradient according to the external field), and (C) cell death resulting from exudation of cellular material.

According to Barba et al. (2020), electroporation can be classified as reversible or irreversible, depending on process parameters (intensity and frequency of the applied field) and cell characteristics (size, shape, and orientation relative to the applied field). If electroporation is reversible, the cell membrane undergoes temporary rupture but returns to its original state once the external electric field is removed. Reversible electroporation is employed to enhance mass transfer processes, such as dye extraction or the insertion of desired compounds into the cells (MARTÍNEZ et al., 2020; VAESSEN et al., 2018). To inactivate microrganisms during reversible electroporation, additional chemical or physical inactivation methods are required, such as introducing antimicrobial agents while the membrane pores are open. When electroporation causes permanent damage to the cell membrane, the process is considered irreversible. This method is mainly applied when the objective is to induce cell death (BARBA et al., 2020).

Non-thermal inactivation phenomena are also observed during the application of high hydrostatic pressures. These are not yet completely understood as they exhibit a lack of uniformity across the cells, resulting in sub-populations of the same species displaying different degrees of resistance to the treatment (KNORR et al., 2011). The effects of applying high pressures on microorganisms are closely linked to phase changes in the membrane, and a detailed description of the lipids phase behavior is provided in Section 2.4.2. Additionally, the high mechanical stresses caused by the application of high-pressures have several practical implications in microbial cells, notably:

- Unfolding of globular proteins, leading to alterations in enzymatic

metabolic pathways;

- Damage to the cytoplasmic membrane;
- Disintegration of ribosomes into their subunits;
- Changes of intracellular pH.

Ultrasound can also induce the formation of pores on biomembranes, leading to microbial inactivation. In this case, the pores result from the violent collapse of the cavitation bubbles, which exerts a shock wave on the lipid bilayer. Ultrasound is often enhanced by combining it with other technologies, such as high temperatures (thermo-sonification) and high pressures (mano-sonification). Sound waves have also been combined with electric fields, revealing a synergistic effect (i.e., the combined effects of these two technologies exceeds the sum of their individual impacts) (LARKIN et al., 2005; HSIEH et al., 2018; MANZOOR et al., 2019; GOMEZ-GOMEZ et al., 2021; NORTON, 2003; BEHRUZIAN et al., 2017; WIKTOR et al., 2018; KUMARI et al., 2017; VANGA et al., 2021; GALVÁN-D'ALESSANDRO; CARCIOCHI, 2018). It is theorized that pore formation processes in both methods may somehow interact, with electroporation and cavitation collectively contributing to these effects. However, this hypothesis is based on experimental analysis, and further comprehensive studies are needed to unveil its underlying mechanisms. This is the topic of the study presented in Chapter 5 of this thesis.

Another relevant non-thermal effect observed during the application of almost all emerging thecnologies is the structural alteration of compounds. The current literature suggests that non-ionizing technologies have the capacity to modify the secondary and tertiary structures of proteins without affecting the primary structure (i.e., without breaking chemical bonds). This behavior leads to changes in solubility, emulsibility, foaming capacity, and gel formation of various foods (HAN et al., 2018). A review conducted by Han et al. (2018) on changes in the functional properties of molecules subjected to electric fields found that these phenomena may be associated with the quantity of hydrophobic amino acids present in proteins. However, the specific mechanisms underlying these modifications remain poorly explored, requiring further experimental and simulation studies for their comprehensive evaluation and understanding.

2.3 Molecular Dynamics Simulations

Molecular simulation is a term that refers to a series of computational techniques used to understand and predict the properties, structures, and functions of molecular systems, using deterministic or stochastic rules. In this context, one of the most widespread techniques is the molecular dynamics (MD) method, which enables the calculation of condensed matter properties, enhances the comprehension of macroscopic phenomena and facilitates the discovery of new molecules/materials/processes. The main references for this section are Rapaport (2004) and Braun et al. (2019), unless another study is referenced.

MD considers a system composed of N interacting atoms/particles that follow the laws of classical mechanics, where the dynamics are described by the second law of Newton:

$$\sum_{\substack{j=1 \\ j \neq i}}^{N} \vec{F}_{i,j} = m_i \frac{d\vec{v}_i}{dt} \tag{2.1}$$

where $\vec{F}_{i,j}$ is the force exerted by particle j on particle i, m_i is the mass of particle i, $\vec{v}_i$ is the velocity vector ($\frac{d\vec{r}_i}{dt}$) and t is the time. To apply Equation 2.1 to atomic systems, it is necessary to model the intra- and intermolecular interactions with a force field/interatomic potential, denoted as $U(r)$. The force can then be obtained from the gradient of the potential, as indicated in Equation 2.2:

$$\vec{F} = -\vec{\nabla} U \tag{2.2}$$

Therefore, a total of N second-order ordinary differential equations are numerically integrated. The results of this integration are the atomic trajectories, i.e., the position and velocity vectors of each particle as a function of time. This information enable monitoring molecular-level changes and the calculation of macroscopic properties of the system using concepts of statistical mechanics. For example, the kinetic energy can be determined from the atomic velocities by Equation 2.3. Then, the temperature can be inferred using the kinetic energy and the number of degrees of freedom of the system by application of the equipartition theorem, as shown in Equation 2.4. To obtain the macrostate temperature, the temporal average of the kinetic energy must

be obtained for a sufficiently long time interval. This is due to Boltzmann's ergodic hypothesis, which suggests that over a sufficiently long time period, the temporal average of a property becomes identical to the phase space average, i.e., the temporal average is equal to the ensemble average.

$$E_{kin} = \sum_{i=1}^{N} \frac{m_i \vec{v_i}^2}{2} \tag{2.3}$$

$$T = \frac{2}{N_{DOF} k_B} E_{kin} \tag{2.4}$$

In the equations above, E_{kin} is the total kinetic energy, T is the temperature, N_{DOF} is the number of degrees of freedom, and k_B is the Boltzmann constant (1.38x10^{-23} m^2 kg s^{-2} K^{-1}). N_{DOF} is calculated by the relation $N_{DOF} = Nn_{dim} - n_{dim} - N_{constraints}$, where n_{dim} is the number of dimensions (2 for 2D and 3 for 3D) and $N_{constraints}$ is the number of degrees of freedom of algorithms that constrain molecular motion.

To perform MD simulations, it is necessary to fix state variables (which can be extensive or intensive) to characterize the dynamics of the system. Examples include the total energy E, temperature T, pressure P, volume V, number of atoms N and chemical potential μ. These variables can be interpreted as experimental controlled parameters that specify the conditions under which an experiment it executed (TUCKERMAN; MARTYNA, 1999). The set of possible microstates, considering the constraints imposed by the constant variables, is called the ensemble. Some commonly used ensembles are the microcanonical (which maintains the number of atoms, volume, and energy of the system constant - NVE), canonical (constant number of atoms, volume, and temperature - NVT), grand-canonical (constant chemical potential,volume and temperature - μVT) and isobaric-isothermal (constant number of atoms, pressure and temperature - NPT).

The direct integration of Newton's second law leads to microstates of the microcanonical ensemble, representing isochoric and isolated systems. Additional algorithms are required to control thermodynamic variables for simulations in other ensembles. In the case of temperature and pressure, these algorithms are called thermostats and barostats, respectively. Thermostats regulate temperature by manipulating the atomic velocities through various approaches, including velocity rescaling,

stochastic collisions with a particle bath, or introducing additional degrees of freedom to the Lagrangian of the system. On the other hand, barostats change the simulation box dimensions to control pressure. The Nosé-Hoover thermostat and barostat are briefly discussed in the sequence, but other methods area avaiable (e.g., thermostats of Berendsen, Langevin and Andersen; barostats of Berendsen, Parrinello-Rahman and Martyna-Tuckerman-Klein), which differ in how they change the system's velocities/energy and volume/dimensions to control the variables of interest.

The Nosé-Hoover thermostat is based on the premise that temperature, being proportional to the mean square velocity, can be controlled by manipulating the rate at which time progresses in the system. To achieve this, a new degree of freedom s is introduced to simulate an artificial interaction with an external thermal bath. This interaction affects the time scale of the problem, as expressed in Equation 2.5. As a result, this thermostat operates with two distinct time variables: the physical or real time (t') and the virtual or scaled time (t). Additionally, this thermostat introduces a parameter Q, which is linked to the mass or inertia of the bath. Additional terms associated with the variables s and Q are incorporated into the Lagrangian of the system, as shown in Equation 2.6:

$$dt' = sdt \tag{2.5}$$

$$\mathcal{L} = \sum_{\substack{i=1 \\ i \neq j}}^{N} \frac{m_i s^2 \vec{v_i}^2}{2} - U(r) + \frac{1}{2} Q \frac{\partial s}{\partial t} - N k_B T_0 ln(s) \tag{2.6}$$

In Equation 2.6, the first two terms represent the kinetic and potential energies of the system, while the additional terms represent the kinetic and potential energies associated with the variable s. The Nosé-Hoover barostat extends this approach by introducing an auxiliary variable responsible for adjusting the dimensions of the system, similar to how the Nosé-Hoover thermostat changes velocities.

In physical systems, the number of atoms in 1 mole of matter is 6.02x10^{23}. Traditional MD simulations are limited to considerably smaller systems (between 10^1 – 10^6 atoms). Consequently, the proportion of atoms interacting with the boundaries in a real system is lower compared to an MD simulation box. To avoid the overestimation of the boundary effects and emulate a bulk system, periodic boundary conditions are typically employed, where the simulation box is considered to be infinitely replicated

in all directions. On this approach, when an atom moves within the original box, its periodic image simultaneously moves in all other replicated boxes. Therefore, if a particle leaves the simulation box at one of its boundaries, its periodic image enters with the same velocity on the opposite face of the same box. The use of periodic boundary conditions artificially creates an infinite system, allowing a more accurate estimation of macroscopic properties of bulk systems from simulation boxes containing considerably fewer atoms.

The limitations of MD are mainly related to the spatial and temporal scales involved in the simulations. The number of atoms in a system can be increased, but the computational cost increases along with it, limiting the size and duration of the simulation. As previously discussed, the number of atoms analyzed in a typical MD simulation is much lower than the number of atoms present in real systems, although the use of periodic boundary conditions helps to mitigate this. Similarly, the time scale is limited by the atom with the lowest vibrational frequency (usually hydrogen). This results in time steps on the order of femtoseconds (10^{-15} s) and simulations that reach a maximum of hundreds of nanoseconds. In addition, the dependence on empirical interatomic potentials and the lack of explicit description of electronic effects can also be considered limitations of this technique.

In the following sections, aspects related to interatomic potentials will be discussed. The division of these forces into non-bonded and bonded (used to model the attraction/repulsion interactions between atoms and their chemical bonds, respectively) will be considered. This categorization is an approximation for practical purposes, as the Schrödinger equation, which governs atomic-scale phenomena, does not make such distinctions. Lastly, mesoscale models and force fields frequently used in MD simulations will be addressed, with emphasis on those used in the present thesis.

2.3.1 Non-bonded forces

Intermolecular (or non-bonded) forces act between atoms and molecules that are not directly linked by a chemical bond. These forces can be electrostatic, van der Waals attractions, or short-range repulsions. Each of these forces, along with their typical representation in MD simulations, will be discussed below.

Van der Waals forces (also called London dispersion forces) are attractive interactions that occur due to the correlations between the instantaneous electron densities around two atoms. According to quantum calculations of charge density in neutral atoms, this force has the form $u = cte \times \vec{r}^{-6}$, where $\vec{r}$ is the atomic distance. As the particles approach each other, a repulsive energy begins due to the overlap of the electron clouds. There is no analytic function with a defined physical meaning to describe this repulsive interaction, but generally, this force can be modeled by $u = cte \times \vec{r}^{\,-m}$, where m is a number greater than 6. A common way to simulate attractive and repulsive forces in MD is the Lennard-Jones potential, shown in Equation 2.7, which illustrates the potential energy as a function of the distance between atoms for attraction and repulsion forces, as well as for the resulting potential. The Lennard-Jones potential considers the dependence $u = cte \times \vec{r}^{\,-12}$ for repulsion.

$$E_{LJ} = 4\varepsilon \left[\left(\frac{\sigma}{r}\right)^{12} - \left(\frac{\sigma}{r}\right)^{6} \right] \tag{2.7}$$

where ε is the potential well depth, and σ is the distance at which the potential energy is zero (van der Waals radius). These parameters can be estimated using ab initio simulations based on first-principles quantum calculations or by fitting experimental data, such as the PvT equilibrium data, enthalpy of vaporization, and molecular volumes (YIN; MACKERELL, 1998). The direct application of the Lennard-Jones potential is restricted to nonpolar molecules or noble gases. For charged systems, the description of electrostatic forces must also be considered.

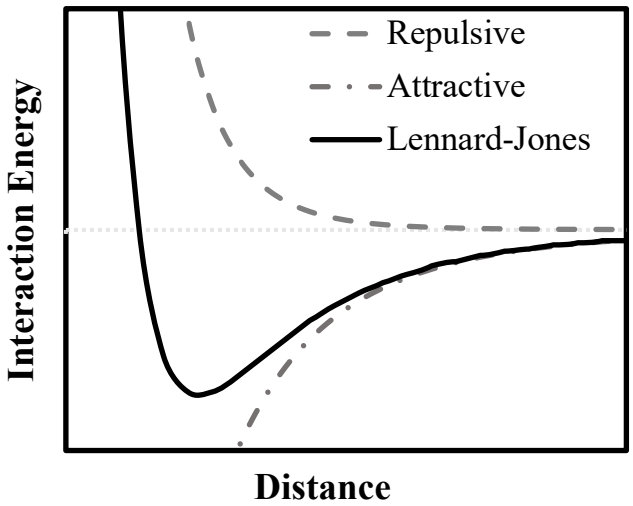

FIGURE 2.5. Representation of the attractive, repulsive and Lennard-Jones potentials.

If the system can be modeled using classical electromagnetism, it is assumed that the atoms possess either partial charges (due to polarization between atoms with different electronegativities) or integral charges multiples of the fundamental electron charge. Electrostatic forces decrease with the square of the distance, more slowly than repulsive and attractive forces. This means that even distant molecules still have significant electromagnetic interactions. Electrostatic interactions are usually modeled by Coulomb's law, presented in Equation 2.8:

$$E_C = \frac{Cq_iq_j}{r} \tag{2.8}$$

where q_i and q_j are the electric charges of atoms i and j, and C is Coulomb's constant ($8{,}988 \times 10^9$ J.m.C^{-2}).

2.3.2 Bonded forces

Bonded (or intramolecular) forces are related to chemical bonding and are responsible for creating and maintaining the structures of different molecules and solids. In the context of MD, these forces capture the geometry and vibrational rigidity of particles and are mainly modeled by the bonding of two atoms, the resulting angle of three bonded atoms, or by dihedrals, which are spatial arrangements of four sequential atoms. These forces are illustrated in 2.6.

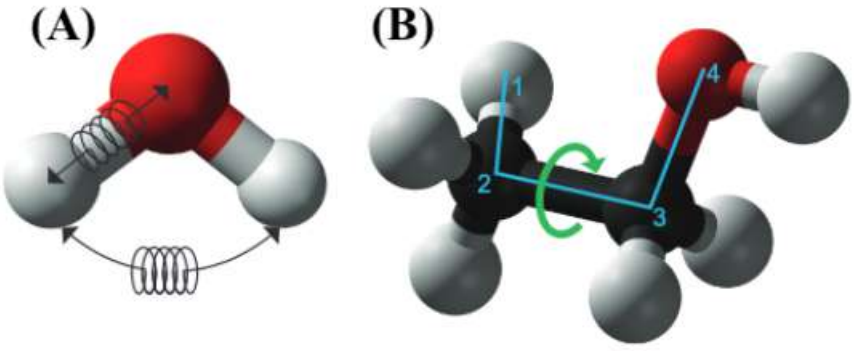

FIGURE 2.6. Representation of (a) covalent bonding and bond angles and (b) proper dihedrals.

Source: Braun et al. (2019)

Bond forces, also known as 1-2 forces, occur between adjacent atoms and are associated with the force needed to stretch a chemical bond. These interactions are com-

monly represented by a Taylor expansion around an equilibrium bond length, denoted as r_0. When the expansion is truncated at its second-order term, it yields a harmonic potential, as depicted in Equation 2.9:

$$E_B = k_b(r - r_0)^2 \tag{2.9}$$

where E_B is the bonding energy, r is the instantaneous distance between atoms, respectively, and k_b is a constant that represents the energy variation (per squared distance) of the system for distances different from r_0. The harmonic potential is a relatively simple and effective model used to describe small deformations. For more complex cases (anharmonic interactions), other descriptive models are necessary, such as the Morse or quartic potential.

Angle forces, often referred to as 1-3 forces, manifest between three atoms that are separated by two bonds. These forces are related to the energy necessary to bend the angle created by the three atoms. One of the most common angular potentials is the harmonic potential with the addition of a Urey-Bradley term (which restricts the motion of the bonds involved in the angle), as shown in Equation 2.10:

$$E_\theta = k_\theta(\theta - \theta_0)^2 + k_{ub}(r - r_{ub})^2 \tag{2.10}$$

where E_θ is the angular energy, θ and θ_0 are the actual and equilibrium angles, respectively, r_{ub} is the Urey-Bradley equilibrium distance, and k_θ and k_{ub} are the constants that represent the energy variation with the change in angle and distance, respectively. If the angular interactions can be described only by the harmonic potential, the Urey-Bradley term can be omitted.

Dihedral terms (also called 1-4 or torsional forces) represent the torsional rotations of 4 atoms around a central chemical bond. Unlike the bonded energies discussed above, the torsional energy exhibit a periodic behavior with respect to the dihedral angle (ϕ), meaning that if the bond undergoes a 360° rotation, the energy should return to its original value. In addition, dihedral angles introduce a significant level of complexity due to the energy landscape associated with their rotations, which displays multiple local minima and maxima. This results in a non-linear relation between the dihedral angle and the corresponding energy. Employing a Taylor expansion would assume linearity between the dihedral deformation and its energy, disregarding potential energy

barriers and the presence of multiple landscapes. Consequently, this approach would fail to capture the correct dynamics of the molecule. To accurately calculate the energy of dihedrals, a periodic potential is employed, typically derived from a Fourier series expansion, as shown in Equation 2.11:

$$E_\phi = \sum_{n=1} V_n cos(n\phi) \tag{2.11}$$

where E_ϕ is the energy of the dihedral and ϕ is the dihedral angle. The variable n represents the number of potential minima generated in a 360° rotation, with n = 1 describing a rotation that is periodic by 360°, n = 2 by 180°, n = 3 by 120°, and so on. In general, three terms are enough to model the most common torsional potentials. The V_n constants determine the energy barrier for rotation around the central bond and, depending on the situation, some of these constants may be zero.

If one of the central atoms in a dihedral is sp^2-hybridized, there is a significant energy penalty associated with forcing it into a pyramidal configuration, as the four atoms prefer to lie in a plane. Improper dihedrals are utilized to preserve this flat arrangement between the four atoms. This term is commonly applied to maintain the correct structure of aromatic rings and represents the force required to deviate the atoms from their equilibrium conformation (χ_0). Similar to the previous cases, a simple harmonic potential can be utilized to describe this interactions, as depicted in Equation 2.12:

$$E_\chi = k_\chi(\chi - \chi_0)^2 \tag{2.12}$$

where E_χ and χ are the energy and angle of the improper dihedral, respectively.

2.3.3 Force fields

A force field is a collection of functions (including parameters) and specific implementation details that describe the interactions between particles, enabling the calculation of the forces that act on the constituents of the system. These fields typically include the terms discussed in Sections 2.3.1 and 2.3.2, as well as other mathematical expressions for specific purposes, such as stabilizing hydrogen bonds. An example of additional term is the CMAP correction in proteins, which models the dependence of

the internal angles ψ and φ of amino acids and results in improvements in the spatial description of crystalline protein residues or in solutions. The empirical parameters of force fields can be estimated from experimental data or first-principles calculations. The total energy is calculated by summing the intermolecular and intramolecular terms, as shown in Equation 2.13:

$$E_{total} = E_{intermolecular} + E_{intramolecular} \tag{2.13}$$

It is impossible to describe all the physical and chemical phenomena in natural processes by a single potential (i.e., force fields have limited transferability). To expand the applicability of the force field, additional terms must be incorporated to account for distinct phenomena. Thus, force field developers usually have to balance the generality and computational cost of the proposed model for a given application. Understanding the limitations of the force field is vital for simulations, and the choice of the potential for a particular application depends on the physical phenomenon analyzed and on the available computational resources. In the sequence, the CHARMM and Martini force fields, used in the simulations of this thesis, will be discussed in more details.

One of the most widely used force fields is CHARMM (Chemistry at Harvard Macromolecular Mechanics), which was also used in the all-atom simulations of this thesis. In the context of molecular dynamics, the term CHARMM can refer to either the empirical force field or to a molecular dynamics software, both initially proposed by Brooks et al. (1983). The formulation of this force field takes into account the energies previously discussed in sections 2.3.1 and 2.3.2, and the total energy is calculated as shown in Equation 2.14:

$$E = \sum_{i=1}^{N} \sum_{j=i+1}^{N} (E_{LJ} + E_C) + \sum_{bonds} E_B + \sum_{angles} E_\theta + \sum_{dihedrals} E_\phi + \sum_{impropers} E_\chi \tag{2.14}$$

where E_{LJ} is the energy of Lennard-Jones interactions (Eq. 2.7), E_C is the energy of electrostatic interactions (Eq. 2.8), E_B is the bond energy (Eq. 2.9), E_θ is the angular energy (Eq. 2.10), E_ϕ is the dihedral energy (Eq. 2.11), and E_χ is the improper dihedral energy (Eq. 2.12).

The CHARMM force field has undergone reparameterizations over the years to increase its scope and improve the description of specific systems, as listed below.

Reiher (1985) developed the CHARMM 19, which used the united-atom approach to reduce the need for computational resources. In this context, light atoms such as hydrogen are joined with a neighboring atom of greater molecular mass. In its later version (CHARMM 22, proposed by MacKerell et al. (1998)) the united-atom approach was abandoned, and the force field started to model water molecules explicitly using the TIP3P model. In addition, the binding and interaction parameters were optimized using gas phase geometry, vibrational spectra, and energy surfaces of torsion, supplemented by ab initio simulations.

Later, this force field was extended to simulate lipids and nucleic acids (CHARMM 27) by MacKerell et al. (2000). For proteins, the CHARMM 27 version is considered to be the CHARMM 22 version with the addition of CMAP corrections (CHARMM 22/CMAP), as proposed by MacKerell et al. (2004). The most recent version of this force field is CHARMM 36, developed by Klauda et al. (2010). For proteins, this version improves the description of helical structure equilibrium and secondary structure unfolding. Improvements have also been implemented for the description of nucleic acids, lipids, and carbohydrates. As this was the most recent version during the development of this thesis, the CHARMM 36 force field was used in the simulations.

2.3.4 Mesoscale models

Due to the spatial and temporal limitations of all-atom classical molecular dynamics, a variety of phenomena that require a large number of atoms, or that occur on timescales larger than microseconds, are inaccessible from a practical point of view. Moreover, the disparity in the diffusion rates between solvent molecules and the dispersed compounds complicates the determination of an optimal time step. This occurs since the solvent tends to move more quickly than the solutes, often leading to unnecessarily small time steps that do not align with the characteristic scales of the solute.

One strategy to address these limitations involves the use of mesoscale models, where individual atoms are grouped into effective particles, as illustrated in Figure 2.7. This technique, known as *coarse-graining*, uses effective potentials to describe interactions among these particles, simplifying the sampling of the phase space and enabling simulations in larger temporal and spatial scales. Within this framework, structural

properties remain reliable even when employing time steps on the order of tens of femtoseconds, in contrast to the $\mathcal{O}$(fs) steps in all-atoms simulations (WINGER et al., 2009). At the same time, the adoption of a mesoescale model results in a reduction in the degrees of freedom associated with atomic motion.

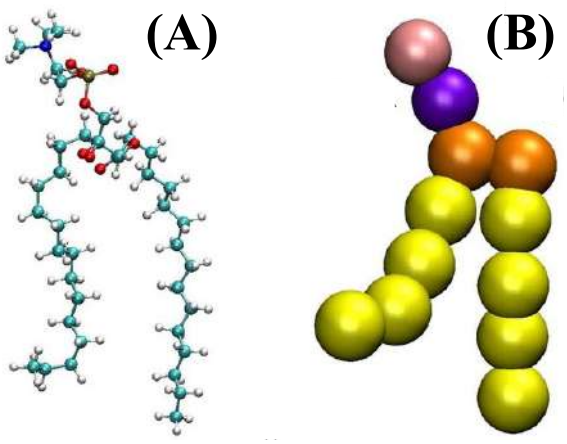

FIGURE 2.7. (A) All-atom and (B) united-atom representation of a DPPC molecule. Source: Adapted from Gkeka (2010)

Currently, there are several methods and force fields for mesoscale analysis. The Brownian method, for example, treats solvent particles as a continuous medium and includes their interactions in the dynamics of the system through stochastic forces (HUBER; MCCAMMON, 2019). This is especially useful to describe the kinetic behavior of gases, but can also be used for macromolecules. Dissipative particle dynamics (DPD) follows a similar approach, also considering stochastic forces between solvent and solute particles. However, DPD also includes terms related to the dissipation of particle energy (ESPAÑOL; WARREN, 2017). It should be noted that these methods (Brownian and DPD) have modifications in their formulation compared to the classical MD method discussed in the last two subsections (mainly related to the way solute/solvent interactions are computed and the inclusion of stochastic and dissipative terms).

Martini is one of the most applied force fields in coarse-grained simulations, and employs potentials similar to those used in all-atom classical MD. Developed by Marrink et al. (2007), this model was initially proposed for the analysis of lipids and DNA, and later extended to proteins (Martini 2.0) by Monticelli et al. (2008). Currently, its pa-

rameterization covers a series of biomolecules, including lipids, amino acids, sugars, DNA, fullerenes, collagen, among others (SOUZA et al., 2021). The intermolecular interaction potential was determined from the experimental partition coefficient between the polar and apolar phases of a large number of compounds, while the intramolecular potential was derived from all-atom simulations.

In general, the model uses a 4-1 strategy, approximating four heavy atoms (and their associated hydrogen atoms) by one particle. For more complex cases, 3-1 and 2-1 strategies can also be applied. The force field employs four different types of particles (polar, apolar, neutral, and charged), each with subtypes that generate an accurate representation of distinct atomic structures. These subtypes can be associated with the hydrogen interactions (whether donor, acceptor, both, or none) or with the degree of polarity (between 1 and 5, with 1 being low polarity and 5 high polarity) of the particles (MARRINK et al., 2007). The potential associated with this force field is similar to the expressed in Equation 2.14, although the improper dihedral term is normally used only to describe some amino acids. The value of ϵ varies between 5.6 kJ mol^{-1} for highly polar particles and 2.0 kJ mol^{-1} for interactions between apolar and polar groups, resulting in an adequate description of hydrophobic effects. The σ parameter depends solely on the strategy used (whether 4-1, 3-1, or 2-1).

The classical Martini water model does not have charges and therefore can not describe polarization effects. Although this approximation is suitable for several applications, some problems occur when modeling interfaces between water and other phases or when charged particles are considered. To overcome such limitations, the polarized water model was proposed by Yesylevskyy et al. (2010), which includes a dipole formed by two particles with opposite charges attached to the main water particle. This model meets basic description criteria, such as the reproduction of the dielectric constant and density of water, and is also capable to describe phenomena dependent on polarization effects, such as electroporation.

As previously discussed, mesoscale models have some limitations. In the specific case of the Martini potential, this force field was developed to describe fluid phases and therefore can not describe the properties of crystalline solids. Additionally, mesoscale models generally predict lower entropies when compared to real systems.

In the Martini force field, this is compensated by enthalpy decreases, as the model was parameterized using free energies. Therefore, the enthalpy/entropy balance is compromised. Finally, the need to fix the secondary structure of proteins *a priori* and the difficulty in correctly representing polar compounds in apolar solvents are additional limitations of this potential (ALESSANDRI et al., 2019).

2.4 Biochemistry of the relevant molecules

The objective of this section is to introduce the fundamental biochemical concepts concerning the molecules analyzed in the context of this thesis. The base references of this section are Belitz et al. (2009) and Damodaran e Parkin (2017), unless another study is referenced.

2.4.1 Proteins

Proteins are complex polymers and one of the most important and diverse classes of organic macromolecules. They are essential for several biological processes such as catalyzing biochemical reactions, transporting nutrients, converting chemical energy into work, producing antibodies, and maintaining the structure of skin, hair, and nails. All proteins, with their wide range of applications and sizes, are generated by the combination of 21 different essential amino acids, which have a generic structure shown in Figure 2.8. This generic amino acid is formed by a central carbon covalently bonded to an amine group (basic), a carboxyl group (acid), a hydrogen atom and a **R** radical (side chain). The **R** group distinguishes the 21 amino acids from one another, providing them with unique characteristics like size, molecular weight, polarity, and solubility. Table 2.1 presents the list of amino acids along with their molar mass, solubility in water (g L^{-1}), polarity, and electric charge. The resulting electric charge of basic and acidic polar amino acids is pH-dependent. At low pHs, basic residues tend to accept a H^+ ion, becoming positively charged, whereas acidic residues tend to remain neutral. Conversely, at high pHs, basic residues tend to be uncharged, while acidic residues tend to exhibit a negative charge.

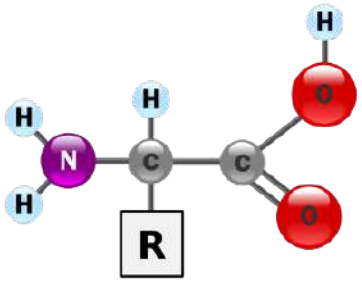

FIGURE 2.8. Generic structure of an amino acid.

TABLE 2.1. Characterization of amino acids regarding some physicochemical properties.

Aminoacid	Molecular mass	Solubility	Polarity	Charge
Alanine (Ala)	89,1	167,2	Nonpolar	Neutral
Arginine (Arg)	174,2	855,2	Polar	Neutral/Positive
Asparagine (Asn)	132,1	28,5	Polar	Neutral
Aspartic acid (Asp)	133,1	5,0	Polar	Neutral/Negative
Cysteine (Cys)	121,1	280	Polar	Neutral
Glutamine (Gln)	146,1	41.5	Polar	Neutral
Glutamic acid (Glu)	147,1	8,5	Polar	Neutral/Negative
Glycine (Gly)	75,1	249,9	Nonpolar	Neutral
Histidine (His)	155,2	42.9	Polar	Neutral/Positive
Isoleucine (Ile)	131,2	34,5	Nonpolar	Neutral
Leucine (Leu)	131,2	21,7	Nonpolar	Neutral
Lysine (Lys)	146,2	739,0	Polar	Neutral/Positive
Methionine (Met)	149,2	56,2	Nonpolar	Neutral
Phenylalanine (Phe)	165,2	27,6	Nonpolar	Neutral
Proline (Pro)	115,1	365,0	Nonpolar	Neutral
Selenocysteine (SeCys)	167,1	400,0	Nonpolar	Neutral
Serine (Ser)	105,1	422,0	Polar	Neutral
Threonine (Thr)	119,1	96,2	Polar	Neutral
Tryptophan (Trp)	204,2	13,6	Apolar	Neutral
Tyrosine (Tyr)	181,2	0,4	Polar	Neutral
Valine (Val)	117,1	58,1	Apolar	Neutral

Proteins have four levels of structural organization, known as primary, secondary, tertiary, and quaternary structures. The primary structure is formed by the linear sequence of amino acids linked by peptide bonds. These bonds occur between the carboxyl radical of a generic residue i and the amino radical of the residue $i + 1$,

with the release of a water molecule. The peptide bond between two amino acids is simple (CO−NH), but has a partial double bond character due to resonance effects between the electrons of the oxygen and nitrogen atoms. This can be experimentally observed by the length of this bond, which is an intermediate between a single and a double bond.

The presence of partial double bond character in protein structures leads to several consequences. These include the formation of hydrogen bonds between adjacent amino acids and the potential for cis and trans configurations, although the trans is more prevalent due to its higher thermodynamic stability. The partial double bond character also restricts the rotation of the carboxyl and amino groups, causing each segment of 6 atoms (C_α−CO−NH−C_α) to be aligned in a planar form. This behavior limits the number of three-dimensional conformations that can be adopted, since only N−C_α and C_α−C bonds have rotational degrees of freedom. The angles formed by such bonds are known as φ and ψ, which also have restrictions due to steric effects between the amino acids side chains. The Ramachandran plot, discussed in Chapter 3, considers this limited number of possible conformations to propose a systematic validation of protein structures obtained from both experiments and simulations.

The secondary structure refers to the spatial arrangement of a peptide chain filament, where some consecutive residues have similar values for the φ and ψ angles. These highly ordered conformations occur due to short-range non-covalent interactions, resulting in a reduction in local free energy. When the φ and ψ angles of two amino acids differ and there is no ordered arrangement, the structure is called aperiodic or randomic. Helical and sheet-like structures are the two most frequent secondary structures, presented in Figure 2.9 and briefly discussed below.

Helical structures in proteins emerge when the torsion angles of two consecutive amino acids adopt similar values. The most prevalent and well-known helical structure is the α-helix, characterized by approximately 3.6 amino acids per turn and an axial extension of approximately 1.5 Å. In an α-helix, hydrogen bonds form between the carbonyl oxygen atom of one amino acid residue and the amide hydrogen atom of the fourth amino acid residue ahead in the sequence. While the α-helix is the most common, there are also other possible helical arrangements. Two examples are the π-

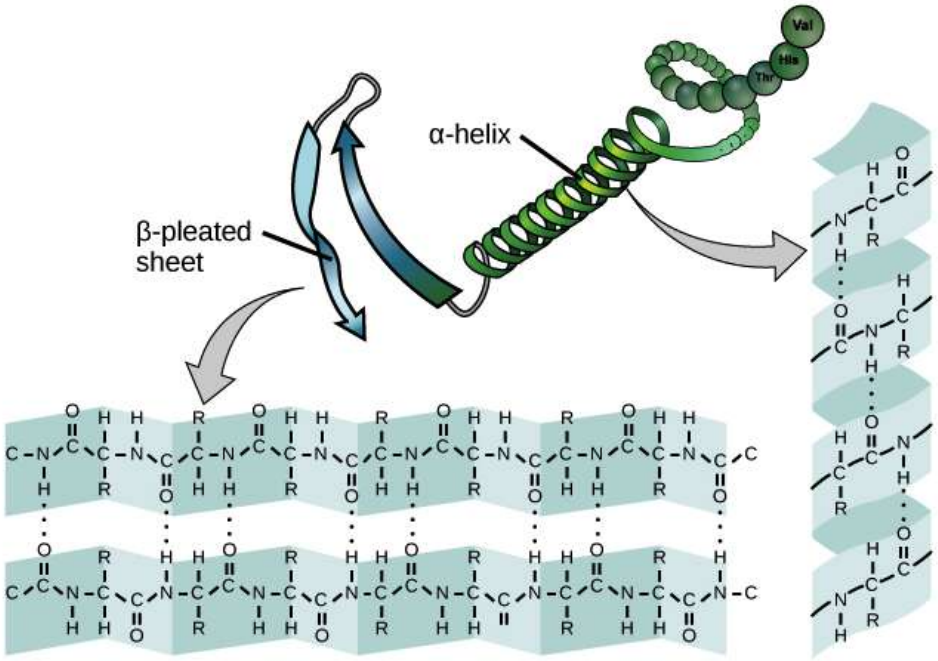

FIGURE 2.9. α-helical and β-sheet secondary structures.
Source: OpenStax (2015)

helix and the 3_{10}-helix, which exhibit different axial distances and numbers of residues per turn.

The most common sheet-like structures are the β sheets, caused by adjacent linear β strands forming hydrogen bonds. Therefore, unlike helical structures, where hydrogen bonds form within the segment, in β sheets, hydrogen bonds occur between segments, as shown in Figure 2.9. Depending on the orientation of the N$-$C bond, parallel or anti-parallel sheets can be observed, with the latter being more thermodynamically stable. Proteins featuring β-type structures exhibit high stability, and those with a substantial proportion of residues organized in this manner tend to have higher denaturation temperatures compared to proteins rich in other secondary structures.

The tertiary structure defines the equilibrium spatial configuration when the primary chain, with its secondary local conformations, folds into a three-dimensional arrangement. From a thermodynamic point of view, the folding of a protein into a tertiary structure is the result of the optimization of several non-covalent interactions, such as van der Waals and electrostatic forces and hydrogen bonds. These interactions overcome the entropic effects that destabilize the protein, leading to a ordered structure

and a reduction in the surface area of the molecule. On the other hand, the quaternary structure occurs when more than one protein are involved in a peptide chain. These complexes (also called oligomers) are extremely important in various biochemical processes, and many biologically important proteins are dimers or trimers.

One of the most relevant protein examples in the field of food science is ovalbumin (OVA), the subject of the molecular dynamics simulations presented in Chapter 3 of this thesis. This protein is the main macronutrient of albumin, constituting between 45 to 55% of its total protein content. Thus, understanding the physicochemical properties of this compound is essential to the field of egg-based product processing (TAKAHASHI et al., 2010). In addition, this biomolecule constitutes the largest protein fraction of the egg and is widely used industrially as an emulsifier and foam/gel former(GUO et al., 2008). Ovalbumin is composed of 385 amino acids, where approximately 49% are in α-helix conformations, 27% in β-type conformations, and 24% in irregular conformations. Figure 2.10 shows a representation of this protein colored according to its different secondary structures.

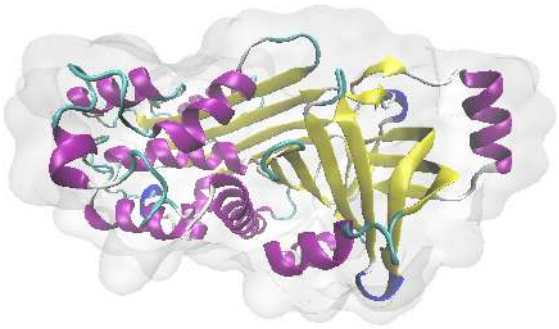

FIGURE 2.10. Ovalbumin colored according to its secondary structure, where pink/yellow/blue/light blue domains correspond to α-helices/β-sheet/3_{10}-helices/ disordered conformations, respectively.

Ovalbumin is a globular protein (i.e., has an elliptical shape resulting from the folding of the peptide chain), with an average diameter of 5.5 nm. This molecule is also a phosphoglycoprotein (i.e., has a phosphate group attached to a serine residue) and presents glycidic groups attached to other residues in the chain. Its molecular weight is approximately 45.2 kDa and its isoelectric point is 4.9. About half of its amino acids are

hydrophobic, while 30% are negatively charged acidic (PHILLIPS; WILLIAMS, 2011). Therefore, ovalbumin may be particularly sensitive to the application of electric fields. Finally, this protein is not stable at high temperatures, and such conditions result in the denaturation of its secondary and tertiary structures. This process begins at approximately 66°C, although previous changes such as the denaturation of α-helices may occur even at lower temperatures (LLAVE et al., 2018).

As discussed in section 2.2, the application of emerging technologies can cause significant structural modifications in proteins. Typically, these alterations are evaluated by experimental techniques such as X-ray crystallography, NMR, and fluorescence spectroscopy. However, these methods often necessitate sophisticated equipment, and the structural parameters obtained are typically limited to the initial and final stages of experiments, hindering a comprehensive understanding of mechanisms. In this context, MD is a useful tool for analyzing conformational changes without the limitations of experimental methods. Astrakas et al. (2011) analyzed the effects of the application of direct current electric fields on a small peptide using MD simulations. The authors simulated the system for 10 ns at a temperature of 300 K and observed a decrease in the number of hydrogen bonds after electrical treatment at high fields (upon 0.5 V nm^{-1}). This resulted in the unfolding of the protein and the loss of beta conformations. In a subsequent study, Astrakas et al. (2012) analyzed the same peptide under the effects of an alternating electric field. At high frequencies, the peptide remained in its native conformation, whereas low frequencies induced the destabilization of the secondary structure. These results suggest that the effects of electric fields on biological molecules depend on both the intensity and frequency of the applied field.

Singh et al. (2013a) investigated the effect of direct current electric fields on gliadin, which is the water-soluble fraction of gluten protein, using the CHARMM 27 force field. The authors observed non-thermal effects only in the secondary structure. Singh et al. (2013b) analyzed three different electric fields (0.002, 0.004, and 3 V nm^{-1}) to evaluate conformational changes in soy protein at 300 K. The authors did not observe any effects when the two smaller electric fields were applied. However, the largest electric field resulted in changes in the solubility parameters and in the secondary structure of the protein.

Wang et al. (2014) examined the effects of continuous electric fields on bovine insulin. The results showed that the structure remained intact for fields smaller than 0.15 V nm^{-1}, but changes in the secondary structure were observed for fields equal to or greater than 0.25 V nm^{-1}. Furthermore, the authors demonstrated a cumulative effect of stress on the protein due to long exposure to the field. Meanwhile, Vagadia et al. (2016) investigated the influence of alternating electric fields (0.5 V nm^{-1} and 2.45 GHz) on the stability of the trypsin inhibitor soy protein at four different temperatures (300, 343, 373, and 394 K). The frequency used was chosen as it is typical for microwave applications in food. The authors found that the protein structure remained stable for most of the time, with just occasional rearrangements. Additionally, the study showed that residues with aromatic rings are particularly important in stabilizing the tertiary structure of the analyzed protein.

2.4.2 Lipids

Lipids are a group of macromolecules with diverse functions and structures, all of which are soluble in organic solvents. They can be classified based on their physical state at room temperature (fats if they are solids or oils if they are liquids) and their polarity. The main constituents of lipids are fatty acids, i.e., aliphatic chains linked to a carboxylic acid group, usually with 12 or 24 carbon atoms. Fatty acids can be classified as saturated (only single bonds) or unsaturated (containing double bonds). Generally, unsaturated fatty acids have non-linear structures that hinder their ability to form a compact structure. Due to weaker van der Waals interactions, they also have a lower melting point in comparison with saturated fatty acids.

One of the most relevant classes of lipids are phospholipids. These molecules are amphipathic, i.e., they consist of a hydrophilic portion (usually a phosphate group linked to another polar group or an alcohol derivative(LONDON, 2013)) and a hydrophobic portion (fatty acid chains). This unique structure enables phospholipids to self-assemble in contact with polar solvents, keeping the hydrophilic portion in contact with the solvent, and the hydrophobic portion aggregated to minimize contact with the surrounding medium. Depending on the characteristics of the lipids (e.g., length of the hydrophobic chain), different structures can arise from this self-assembly process,

such as micelles, monolayers, or tubular shapes. Among the possible conformations, the most common is the formation of lipid bilayers, which are biological membranes formed by two layers of phospholipids arranged in the same plane but in opposite direction. These structures have great relevance in biological processes, as they are responsible for the formation of cell walls. There is a variety of lipids that form bilayers (e.g., DPPC, DOPC, DMPC), and Figure 2.11 shows a scheme of this conformation, along with the resulting cell wall.

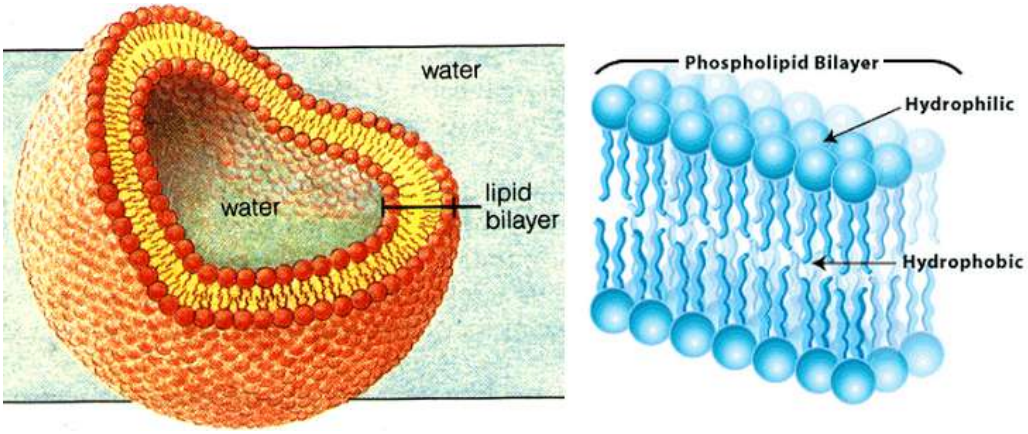

FIGURE 2.11. Representation of the cell wall/lipid bilayer.
Source: Adapted from Allott e Mindorff (2014)

Membranes are formed by a mixture of different phospholipids, which play a crucial role in determining the permeability characteristics of the cell. The composition of this mixture is relevant for several biochemical processes, including the inactivation of microorganisms (CASTRO et al., 1993), extraction of cellular compounds (POSTMA et al., 2016), and genetic modification of cells (LANGTON, 2020). One of the most extensively studied phospholipids is dipalmitoylphosphatidylcholine (DPPC), which consists of two groups of palmitic acid C_{16} linked to a phosphatidylcholine group, as shown in Figure 2.7. Several studies have shown that the bilayers formed by DPPC exhibit a rich and complex phase behavior, and Figure 2.12 shows the pressure-temperature diagram for this molecule.

According to Wong et al. (1988), DPPC molecules are in a liquid phase at high temperatures and low pressures, also known as the L_α phase, where the acyl chains are highly disordered. At lower temperatures or higher pressures, different gel phases

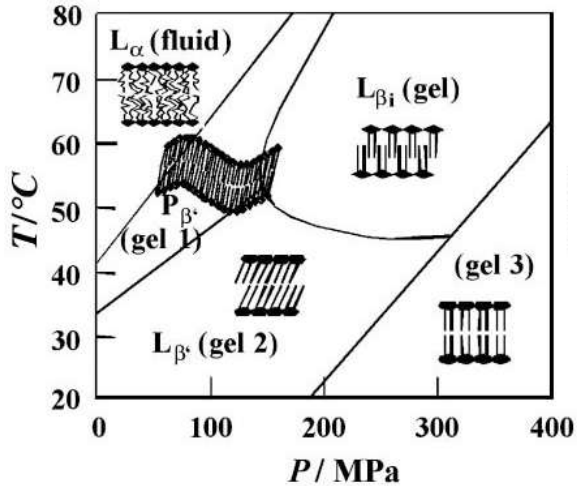

FIGURE 2.12. Pressure-Temperature diagram for a DPPC bilayer.

Source: Adapted from Daniel et al. (2006)

are observed. At ambient pressure, the first gel phase is the $P_{\beta'}$ phase (or gel 1). In this phase, the fluctuations in acyl groups decrease considerably and the chains adopt a hexagonal arrangement. In the gel 2 phase (or $L_{\beta'}$), the acyl groups are completely extended, and the bilayer is unidimensionally oriented. At pressures above 2000 bar, new states are observed, characterized by decreases in membrane thickness due to the interdigitation caused by pressure forces.

Lipid bilayers have a regular organization, with a well-defined distribution of lipids along their extension. Therefore, coarse-graining force fields have been widely used to model these structures. Among these techniques, the Martini model stands out, which has been widely used to study the dynamics of lipid bilayers under different conditions. In Chapter 4, this model was used to evaluate the dependence of the electroporation process on pressure and temperature. Thus, studies that analyzed the dynamics of bilayers under high pressures or the effect of electroporation using coarse-graining techniques will be reviewed next.

In a study conducted by Lai et al. (2012), several physical parameters of DPPC membranes were investigated as a function of temperature and pressure, such as phase transition temperature, bilayer thickness, lateral diffusion coefficient, and order parameter. The results showed that high pressures caused fewer structural changes compared to high temperatures, suggesting that the effects of pressure on the membrane are less significant. Furthermore, it was observed that the relationship between the

peak of the lateral pressure profile and the degree of acyl chain interdigitation was not influenced by pressure, oppositely to what occurred with temperature. This indicates that the effects of high pressures cannot simply be reproduced by decreasing the temperature, suggesting that these processes can be used together to obtain bilayers with distinct properties.

Zhou e Liu (2019) analyzed the phenomenon of electroporation using the Martini force field and showed that although the process is well-known, the involved mechanisms still need more detailed analysis. The study employed the ionic imbalance method in two bilayers separated by solvent layers: in one solvent region, 178 sodium ions were positioned, while in the other, 356 chlorine ions and 178 sodium ions were inserted. Thus, the resulting system was electrically neutral, although with a transmembrane potential due to the difference in charges between both sides of the bilayer. The electroporation process occurred naturally for 100 ns, starting with the formation of pores on the surface of the bilayer. These pores increased in size and, after a characteristic time scale, remained stable. As the transmembrane potential tended to zero, the pores were closed due to the spontaneous resealing process of the structure. The study highlights the importance of simulations for electroporation analysis and shows that an appropriate description of this phenomenon can be obtained using the Martini force field.

MD simulations of lipid bilayers can also offer valuable insights into the synergistic effects that arise when two emerging technologies are combined. Such phenomenon was studied in Chapter 5 of this thesis, where the simultaneous use of ultrasound waves and electric fields was investigated. These technologies were specifically selected due to their previously reported synergistic effects. For instance, (GOMEZ-GOMEZ et al., 2021) demonstrated a -1.3 log inactivation when PEF was applied to inactivate *Aspergillus niger* in a water-oil emulsion, while a -4.3 log reduction was observed with the application of high power ultrasound alone. However, when these two technologies were applied sequentially, a reduction of -6.6 log on the microbial count was achieved. This shows that the processes are interacting to amplify their individual effects, as the combined result surpasses the sum of the individual processes. Similar results were also obtained in other studies on microbial inactivation or compounds extraction featuring these two technologies (NORTON, 2003; BEHRUZIAN et al., 2017;

WIKTOR et al., 2018; HSIEH et al., 2018; MANZOOR et al., 2019; VANGA et al., 2021).

To simulate ultrasound in MD simulations, two distinct methods can be employed: the momentum mirror approach or the modification of the simulation barostat (MAN et al., 2021). In this thesis, the momentum mirror approach was used due to its established ability to accurately reproduce the effects of ultrasound, both in the presence (CHOUBEY et al., 2011) and absence (KOSHIYAMA et al., 2006; VEDADI et al., 2010) of cavitation. Numerous studies have examined the ultrasound phenomenon using this technique, exploring variations in factors such as the bilayer composition (WEI et al., 2021), acoustic wave velocity (VEDADI et al., 2010), cavitation bubble radius (SANTO; BERKOWITZ, 2014b), and position (SANTO; BERKOWITZ, 2014a). Within this thesis, the US process was analyzed alongside the application of electric fields, aiming to unravel the underlying mechanisms driving the reported synergistic effects.

2.4.3 Hybrid membranes

The rapid deterioration of purely lipid membranes (liposomes, represented in Figure 2.13.A), is an undesirable factor in many practical applications. This degradation occurs due to the oxidation of unsaturated acyl chains of tge lipids and the formation of transient pores on the surface of the membrane, which increase the permeability of the vesicle and lead to loss of mechanical stability (GRIT; CROMMELIN, 1993; CHEMIN et al., 2012). This behavior is undesirable in biochemical applications, where durability and robustness are critical aspects. To solve this issue, alternative vesicles composed of polymers with amphipathic character (polymersomes, represented in Figure 2.13.B), have been analyzed since the early 2000s. The vesicles formed by the copolymers exhibit enhanced robustness and versatility, due to the various types of polymers that can be used in their formulation (ZHAO, 2017; LIU et al., 2020). However, with some notable exceptions (e.g., (STOENESCU et al., 2004; KUMAR et al., 2012; HABEL et al., 2015)), the reconstitution of proteins in these membranes is not efficient. Lipids that are biocompatible with proteins have been selected over many years of evolution, which has not occurred with polymers. Therefore, protein modifications by genetic engineering or in the environment of the polymer vesicle are necessary to achieve the desired function.

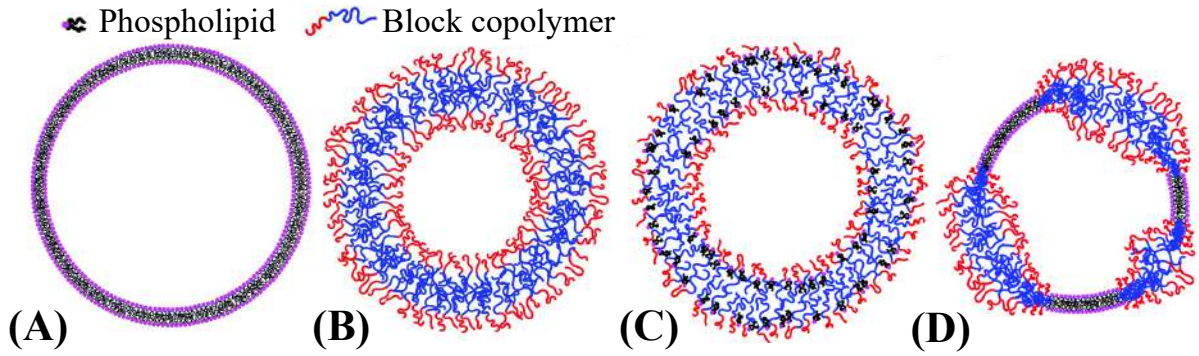

FIGURE 2.13. Structure of pure and hybrid membranes: (A) lipidic; (B) polymeric; (C) homogeneous hybrid; (D) heterogeneous hybrid.

Source: Rideau et al. (2018).

In the last decade, the use of hybrid membranes (which combine polymers and phospholipids) has been considered an effective approach that allows the combination of the desired characteristics of both constituents: the chemical versatility and robustness of polymers, along with the biocompatibility and biofunctionality of lipids. Depending on the distribution of the constituents, the resulting membrane can be organized heterogeneously, with areas of high concentration of lipids/polymers, or homogeneously, with uniform distribution of the constituents, as illustrated in Figures 2.13.C and .D, respectively. The properties of such membranes will be analyzed through molecular dynamics simulations in Chapter 6 of this thesis to clarify some phenomena recently reported in these nanostructures. In this context, the remaining of this section will present a more detailed discussion on the phenomena that will be analyzed.

In a recent study, Seneviratne et al. (2023) analyzed the resulting structures formed by the combination of poly(1,2-butadiene)-*b*-polyethylene glycol (PBD-*b*-PEO) and palmitoyl-2-oleoyl-sn-glycero-3-phosphocholine (POPC) using cryoelectron tomography and small-angle X-ray scattering. While the electron density profiles for liposomes were previously known, resulting in a bilayer thickness of 36 Å, this study marked the first measurement of polymer vesicles (polymersomes) profiles, indicating a thickness of 108 Å. This suggests that polymeric membranes tend to be approximately three times thicker than lipid membranes. The analysis of hybrid vesicles revealed an interesting behavior: electron profiles for all hybrid compositions resembled

either pure liposomes (thin structure) or polymersomes (thick structure). This observation is particularly intriguing given that fluorescence experiments demonstrated the formation of well-mixed, homogeneous vesicles for all analyzed compositions. The authors concluded that the analysis of electron density profiles alone is insufficient to determine how and why polymers and lipids organize themselves to form such structures.

In the study by Khan et al. (2016), the reconstitution of the cytochrome bo_3 was investigated in the same system described in the previous paragraph (POPC/PBD_{22}-*b*-PEO_{14}). The results indicated that the protein exhibited higher initial activity when reconstituted in pure liposomes. Vesicles with a composition of 75% lipids and 25% polymers showed 95% of this maximum activity, while vesicles with 50:50, 25:75, and 0:100 presented, respectively, 82, 35, and 5 %. Notably, the decrease in activity was more pronounced for vesicles with 50:50 and 75:25 compositions. Additionally, the authors assessed how this activity was preserved over time. After 21 days, almost all of the protein activity was lost in the pure liposome, while membranes with a higher polymer content retained some of their activity even after 500 days. Considering both the initial activity and long-term durability, hybrid membranes with equal proportions of both molecules (50:50) yielded the most promising results. Similar findings were also reported by Catania et al. (2022) and Otrin et al. (2017).

Regarding mechanical properties, the study by Seneviratne et al. (2020) showed that hybrid vesicles are more resistant to rupture than pure phospholipid vesicles. Moreover, some recent studies indicated that these membranes may have regions with lower surface tension, making them more favorable for the reconstitution of proteins. For example, Catania et al. (2022) showed that nanodiscs formed by hybrid vesicles offer a favorable environment for the reconstitution of cytochrome bo_3, without the need for detergent addition to insert the protein into the membrane. On the other hand, lipid membranes required the addition of a surfactant. Similar results were also reported by Jacobs et al. (2019). Although these studies have pointed to superior mechanical properties in hybrid vesicles, a better understanding of the mechanisms leading to these results is still necessary.

Given the disparity between the properties of copolymers and lipids, it is sur-

prising that their combination results in mixed vesicles with superior performance when compared to pure biological or polymeric membranes. As a result, the study of the behavior of the mixture between lipids and polymers in hybrid vesicles has been at the forefront of the characterization of these materials. However, these studies are still in the early stages of development, and there are still a series of questions to be answered to understand the interactions in these structures (BEALES et al., 2017). In particular, there is a need to optimize the environment of the hybrid vesicle for its various applications, which can be achieved through a detailed understanding of the coupling between membrane composition and its properties. MD can serve as a valuable tool to the analysis of this phenomena. Recently, all-atom MD simulations were performed to investigate HVs composed of DOPC and PBD-*b*-PEO, with polymer fractions of 10 and 20 mol% (STEINKÜHLER et al., 2022). These simulations offered valuable insights into the molecular structure of these vesicles. However, atomistic simulations face limitations in their ability to analyze systems with more than hundreds of thousands of atoms over long time scales as required for these membranes. With this in mind, chapter 6 analyzed the same system but proposing a parameterization to perform simulations in the mesoscale.

Chapter 3

Molecular dynamics study of the effects of static and oscillating electric fields in ovalbumin

The findings from the *Molecular dynamics study of the effects of static and oscillating electric fields in ovalbumin* are presented in this chapter. It examined the structural changes caused by continuous and alternating electric fields in the ovalbumin molecule using classical molecular dynamics. The assessed metrics were correlated with phenomena previously reported in this protein regarding the application of electric fields. This study has been published in the journal *Innovative Food Science & Emerging Technologies* (DOI: <https://doi.org/10.1016/j.ifset.2021.102911>).

Abstract: Understand the conformational changes caused by emerging technologies in nutrients is important to assess the total impact of these processes in foodstuff. In this study, molecular dynamics simulations were used to analyze the effects of static and oscillating electric fields in ovalbumin at different temperatures. The results indicate that the protein secondary structure is more thermally stable under electric processing. While molecular size, dipole moment and surface area increased, number of hydrogen bonds decreased with field application. The results agree with experimental observations and were used to discuss the mechanisms of some already reported non-thermal effects of ovalbumin. This paper helps to shed some light on the influence of electric fields in proteins structures and may contribute to the creation of peptides with improved technological properties by alternative processing.

Industrial relevance text: Molecular dynamics simulations were used to study the conformational changes caused by continuous and oscillating electric fields in ovalbumin at four temperatures (300, 320, 340 and 360 K), representative of different food processing scenarios. The present results can be used to understand the consequences of electric field treatments in a large protein and may help to improve functional properties of this molecule. The analyzed variables at molecular level can be correlated to experimental observations, helping to explain some of the mechanisms responsible for non-thermal effects in ovalbumin.

Keywords: Molecular simulations; Proteins; Non-thermal effects; Eggs processing.

3.1 Introduction

Electromagnetic and electric field treatments are promising alternatives to conventional heating process of foodstuff, reducing losses of desirable compounds and decreasing processing time, while improving energy efficacy (PEREIRA; VICENTE, 2010; RODRIGUEZ-GONZALEZ et al., 2015; HAN et al., 2018). Several technologies can be categorized in this group, which differ on the strength of the applied field, wavelength and frequency (e.g., gamma rays, pulsed electric fields (PEF), microwaves and radio frequency assisted processing). Conventional heating process (CHP) is capable of altering the structure of biomolecules by heat driven mechanisms; however, the application of electric fields (EF) may cause additional structural changes, which are usually referred in the literature as non-thermal effects (RODRIGUES et al., 2020; VANGA et al., 2021; BALDI et al., 2021).

Proteins are one of the most complex and important macronutrients and special attention must be given to these molecules once they play diverse roles in food systems. They are highly affected by EF application: Qian et al. (2016) revealed a decrease in the α-helix conversion to random coils under application of PEF in egg white protein; Qin et al. (2016) observed an increased denaturation of the secondary structure of soybean protein isolate under the application of microwaves; Guo et al. (2017) showed that the β-sheet content in soy protein isolate increased under the applica-

tion of radio frequency processing. Recently, a review of the EF-induced non-thermal effects in proteins was presented by Han et al. (2018). Ovalbumin (OVA) is an important food protein since its peptide chain has an ideal amino acid balance, representing more than 50% of the total proteic content of egg albumen and, therefore, being of crucial importance in eggs processing (TAKAHASHI et al., 2010). In addition, this protein is industrially used to form foams, gels and emulsions upon heating (GUO et al., 2008). Concerning its chemical characterization, OVA is a phosphorylated globular glycoprotein and a member of the serpin superfamily, with an average diameter of 5.5 nm, a molecular weight of 45 kDa and an isoelectric point of 4.5 (TING et al., 2013; GUHA et al., 2019). Around 50% of its total amino acids are hydrophobic, and 30% are acidic and negatively charged (PHILLIPS; WILLIAMS, 2011). Therefore, this protein can be especially sensible to the application of EF. In fact, several studies have already shown non-thermal effects in OVA under the presence of EF, such as increments in foaming and emulsifying capacity; these effects, however, are not fully understood yet (ALLEONI, 2006; ZHAO; YANG, 2010; MONFORT et al., 2012; YOGESH, 2015; HU et al., 2019).

A variety of experimental techniques has been typically employed to analyze the influence of EF in the atomic structure of proteins. According to Ravi et al. (2005), they can be categorized as high resolution techniques (e.g., X-ray crystallography and NMR) or low resolution techniques (circular dichroism, Raman and fluorescence spectroscopy, Raman optical activity and Fourier transform infrared spectroscopy). In general, these procedures are expensive and time-demanding, and the molecular structures are only analyzed at the beginning and at the end of the experiment, limiting the proper investigation of non-thermal mechanisms (VAGADIA et al., 2016). Molecular dynamics (MD) simulation is a computational technique which can be used to obtain detailed information of several interesting phenomena at molecular level, in particular those not easily accessible by conventional experimental techniques (RAPAPORT, 2004). A drawback of MD is the limited time and length scales achieved in the simulations (up to millions of atoms and nanoseconds), due to its computational cost (CHEN et al., 2018). Despite of its limitations, MD has been successfully used to study the dynamics of proteins and other macromolecules of biological interest. Studies analyzing the effects of emerging technologies in macronutrients by MD are still scarce in literature (CHEN et al., 2018). A series of studies (ASTRAKAS et al., 2011; SINGH et al.,

2013a; VANGA et al., 2015; VAGADIA et al., 2016; PRŮŠA; CIFRA, 2019; MARRACINO et al., 2019; TODOROVA et al., 2020) have investigated the EF-induced effects in proteins by MD. However, these studies are usually restricted to small peptides, while the study of larger biomolecules of practical interest still needs to be properly addressed.

The objective of this study was to analyze the effects of electric driven technologies on the structure of ovalbumin using MD simulations, aiming to improve the knowledge on the effects of EF on biomolecules relevant to food science. More specifically, independent MD simulations of the protein under direct or alternating current fields and in the absence of a field were carried out. A comparative analysis of the secondary structure and structural rearrangements observed in each scenario is made, leading to a better understanding of the EF effects at the molecular level. The results were correlated with experimental observations from previous studies related to the application of EF in ovalbumin, aiming to shed some light on the mechanisms involved in the reported phenomena.

3.2 Computational Methodology

3.2.1 System setup

The analyzed system consists of an ovalbumin molecule positioned at the center of a simulation box filled with water, as illustrated in Figure 3.1. The protein initial structure was obtained from the Protein Data Bank (PDB) with entry code 1OVA. The structure, determined by Stein et al. (1991) using X-ray diffraction, exhibits 12 α-helices, 15 β-sheet structures, and some smaller or irregular structures. To ensure consistency with the atomic nomenclature used in the current version of the CHARMM force field, a pre-processing step was performed using the CHARMM-GUI software, developed by Jo et al. (2008). This software is continuously updated and can be accessed at <https://www.charmm-gui.org>.

The system was created using the FORTRAN90 code *ch2lmp*, which is available alongside LAMMPS. This code generated the necessary input files for the sim-

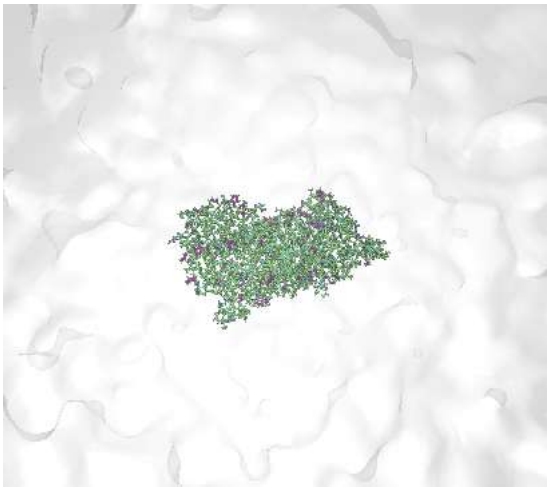

FIGURE 3.1. Simulation box containing ovalbumin in water.

ulations. In addition to the protein coordinates, the program required a structural *.psf* file containing the molecule topological information, which was generated using the Visual Molecular Dynamics (VMD) software. Furthermore, a separate file containing the force field parameters, obtained from the official CHARMM website <https://www.charmm.org>, was also necessary.

The protein was inserted into a simulation box measuring 11.5 $\times$ 11.5 $\times$ 11.5 nm^3 and was solvated with 46901 TIP3P water molecules. Interatomic interactions were described by the CHARMM 36 force field. This potential represents the latest version of the generic CHARMM force field and accurately describes dihedrals and hydrogen interactions in proteins (BEST et al., 2012). As OVA has a resultant negative charge, 12 sodium ions were introduced in the system to make it neutral, as described in previous works (ASTRAKAS et al., 2011; SINGH et al., 2013a; WANG et al., 2014).

3.2.2 MD simulations

The SHAKE constraint algorithm, developed by Ryckaert et al. (1977) to describe the Newtonian dynamics in rigid bodies, was employed to restrict the bonds and angles of TIP3P water molecules, as well as the bonds involving heavy atoms and hydrogen. To determine an appropriate simulation time step, the component with the smallest vibrational frequency in the system must be considered, which typically corresponds to the smallest atom (i.e., hydrogen). The SHAKE algorithm allows the use of

larger time steps, specifically 2 fs, by restricting the motion of hydrogen atoms. Without the algorithm, it would be necessary to use time steps below 1 fs. Long-range electrostatic interactions were evaluated using the particle-particle particle-mesh (PPPM) method. Cut-off radii of 1.2 nm were used for both Lennard-Jones and long-range electrostatic interactions.

The open-source Large-scale Atomic/Molecular Massively Parallel Simulator (LAMMPS), originally proposed by Plimpton (1995) and freely distributed at <http://lammps.sandia.gov>, was used in all simulations. Initially, the whole system was relaxed by running a simulation at 0.1 K for 40 ps. This initial relaxation aimed to reduce the risk of numerical divergence in early time steps when the system is far from its minimum energy state. The protein was then maintained constrained, while velocities were randomly assigned to the remaining system according to the Boltzmann distribution at temperatures of 300, 320, 340 and 360 K. These conditions were chosen to represent different food processing scenarios: while 340 and 360 K are representative of conventional pasteurization processes, lower temperatures (300 and 320 K) can be used for non-thermal pasteurization in electrically powered technologies. Two subsequent equilibration runs (300 ps each) were performed under the canonical (NVT) and isobaric-isothermal (NPT, P = 1 atm) ensembles. The Nosé-Hoover method was used for temperature and pressure control in all simulations, with barostat and thermostat damping parameters of 500 and 100 fs, respectively.

After the initial equilibration, the protein molecule was released and runs for data collection were performed. Three scenarios (under electric field absence (CHP), and under direct current (DC) and alternating current (AC) electric fields) were analyzed at each temperature for 5 ns. To avoid false conclusions in MD simulations of proteins, Knapp et al. (2018) suggests the use of replicated simulations to compute the equilibrium properties. Therefore, three independent simulations were performed, and the measured metrics were averaged throughout the trajectories. Extended simulations spanning up to 10 ns were also conducted to assess stability of the results over longer time periods. The results, presented in Figure 3.2, demonstrate that the trends in the measured properties remain consistent over this extended time scale.

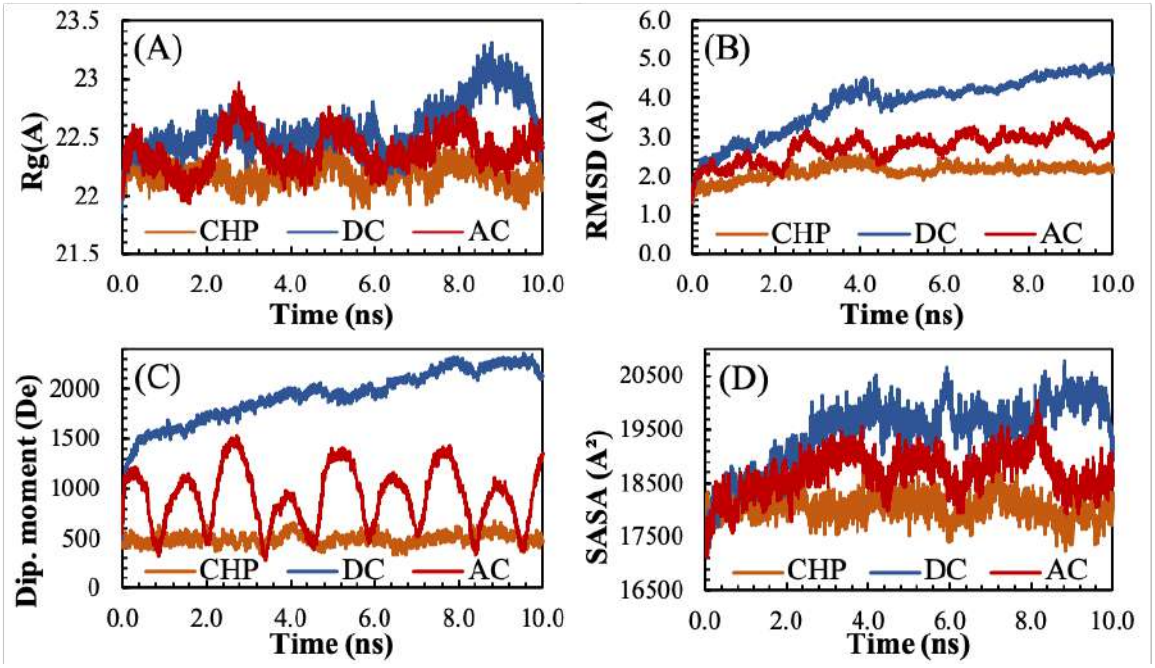

FIGURE 3.2. OVA (A) radius of gyration, (B) RMSD, (C) dipole moment and (D) SASA for 10 ns simulations at 360 K.

The simulations conducted here included the application of both direct current and alternating electric fields, along with a control simulation without an electric field for reference. Due to the MD limited time scale, the fields applied in the simulations are larger than the ones used in experiments (SAM et al., 2019). Therefore, a field strength of 0.5 V/nm was applied for all cases. The application of electric fields at the atomic scale introduces an additional force on each atom with an electric charge, as described by Equation 3.1:

$$\vec{F}_{EF} = q\vec{E} \tag{3.1}$$

where $\vec{F}_{EF}$ and $\vec{E}$ are the electric force and field vectors, respectively. In the alternating field simulations, a frequency of 2.5 GHz was used to replicate microwave processing conditions, as suggested by Vagadia et al. (2016). In this scenario, an instantaneous electric field is employed, defined by the maximum field and frequency, as shown in 3.2:

$$\vec{E}(t) = \vec{E}_0 \cos(\omega t) \tag{3.2}$$

where $\vec{E}_0$ is the maximum field (0.5 V nm^{-1}) and ω the frequency (2.5 GHz). The electric field was applied along the x-axis of the simulation box, although preliminary tests

indicated that the qualitative trends remained consistent when the field was applied along the y and z axes, as shown in Figure 3.3.

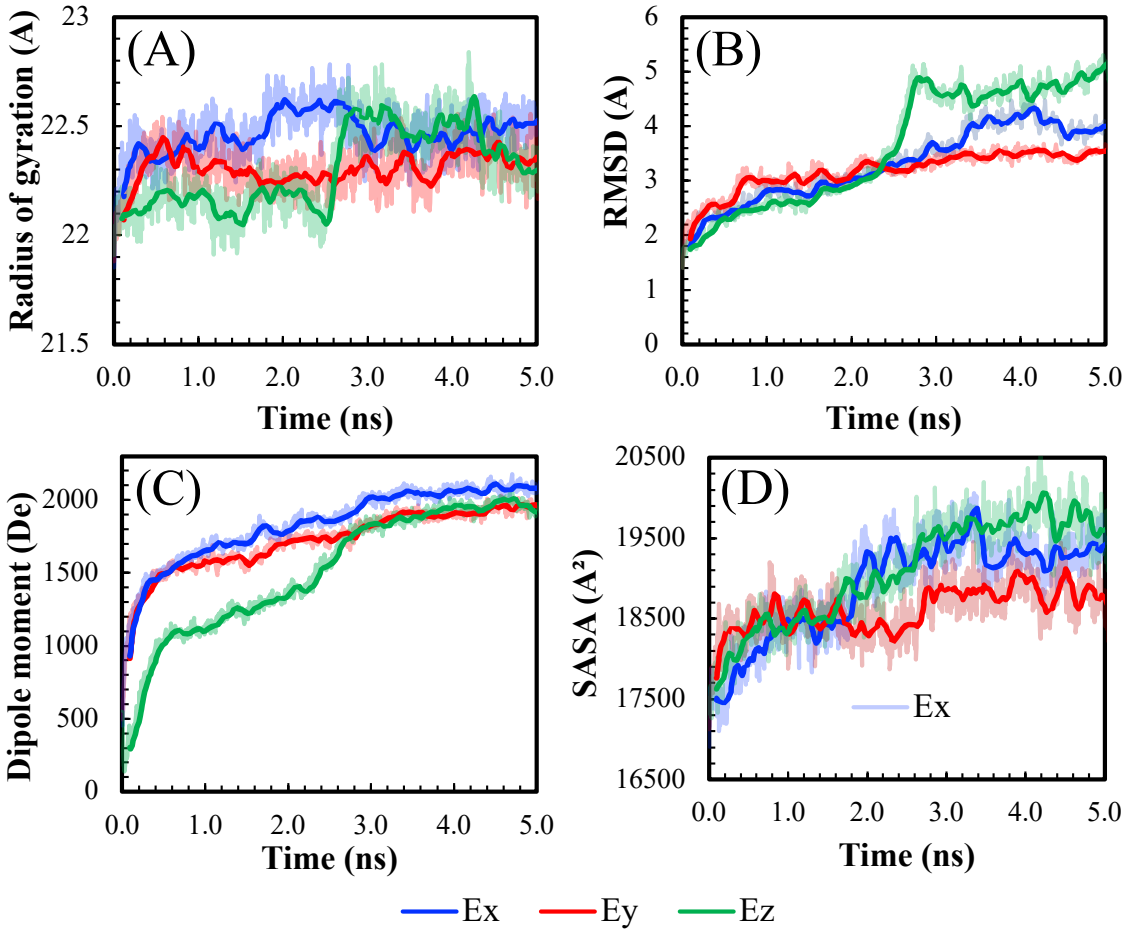

FIGURE 3.3. OVA (A) radius of gyration, (B) RMSD, (C) dipole moment and (D) SASA for different field directions at 360 K.

3.2.3 Structure validation

As discussed in Section 2.4.1, peptide chains exhibit a partial double bond character, resulting in local planar arrangements for each six-atom segment. Consequently, only the N$-$C$_\alpha$ and C$_\alpha-$C bonds possess angular degrees of freedom, known as φ and ψ angles, respectively. Ramachandran et al. (1963) demonstrated that some combinations of these angles can lead to steric clashes (collisions between the side chains of consecutive amino acids), making such conformations highly improbable. By exam-

ining the φ-ψ plot for each residue in a given protein, it becomes possible to identify which amino acids display such unfavorable conformations. The φ-ψ plot, called Ramachandran plot, can therefore serve as a validation tool for the simulated structures.

When this analysis was first suggested, the resolution level of experimental apparatus did not allow for the determination of protein structures at atomic resolution. Four decades later, hundreds of thousands of structures are stored in the PDB, and Hovmöller et al. (2002) observed deviations from the original allowed angles for some amino acids. More specifically, proline, glycine, valine, and isoleucine residues began to be analyzed separately due to their unique conformational characteristics. To evaluate the predicted structure of the ovalbumin and verify the favorable positioning of amino acids, the Ramachandran plots of the molecules obtained after each simulation were analyzed using the MolProbity software (WILLIAMS et al., 2017).

3.2.4 Structural analysis

A series of analyses were performed to assess changes in the protein structure. Similar metrics can be measured experimentally using techniques such as NMR and X-ray crystallography. The trajectory files were saved every 4 ps, resulting in 1250 frames. The main analyses performed and their objectives are outlined below. ANOVA and Tukey tests ($p < 0{,}05$) were used to assess the statistical dependence of the measured variables on temperature and treatment.

The radius of gyration R_g measures the distance from the center of mass of the molecule to a point with the same inertia as the actual mass distribution of the molecule, assuming uniform mass distribution. This metric provides insights into protein compactness and unfolding, making it useful for studying molecular stretching or compression. Mathematically, R_g is calculated by the square root of the sum of the distances between each atom and the center of mass of the molecule, as shown in Equation 3.3:

$$R_g = \sqrt{\frac{1}{N}\sum_{i=1}^{N} |\vec{r}(i) - \vec{r}_{com}|^2} \tag{3.3}$$

where $\vec{r}(i)$ and $\vec{r}_{com}$ are the coordinates of atom i and its center of mass, respectively, and N is the number of atoms.

The root mean square deviation (*RMSD*) quantifies the average distance between atoms of two superimposed molecules. In proteins, it is common to consider only the overlap of heavy constituents of the peptide chain, as hydrogen atoms are usually restricted by algorithms like SHAKE or RATTLE. *RMSD* is calculated using Equation 3.4:

$$RMSD = \sqrt{\frac{1}{N}\sum_{i=1}^{N} |\vec{r}(i) - \vec{r}_{REF}|^2} \tag{3.4}$$

where $\vec{r}_{REF}$ are the atomic coordinates in the reference molecule. Translation and rotation algorithms are commonly employed to minimize the RMSD value, aiming to quantify only the structural changes not related to the movement of the molecule in the simulation box.. In this study, the Kabsch algorithm was employed using internal functions of the VMD software.

The dipole moment measures molecular polarity, with higher values indicating greater polarity and null values indicating nonpolar compounds. This metric is useful to quantify the electrostatic aspects of proteins and influences several properties of the molecule, such as solubility (CARDOSO et al., 2020), melting and boiling points and its reactivity (SIEBLER et al., 2015). The dipole moment vector for a discrete charge distribution is calculated by multiplying each atomic charge by its position vector, as shown in Equation 3.5

$$\vec{d} = \sum_{i=1}^{N} q(i)\vec{r}(i) \tag{3.5}$$

where $\vec{d}$ is the dipole moment and $q(i)$ is the charge of atom i. The scalar dipole moment is obtained by employing the relation $d^2 = \vec{d_x}^2 + \vec{d_y}^2 + \vec{d_z}^2$. The vector components were calculated using the function *compute dipole* of LAMMPS.

Determining the secondary structure of a protein is vital for understanding its technological properties. The Define Secondary Structure of Proteins (DSSP) program is the most widely used approach to delineate these conformations, which relies on hydrogen bond patterns to identify the most probable secondary structure for each amino acid. In this study, the STRIDE algorithm was used, which not only considers hydrogen bonds patterns, but also evaluates angles and dihedrals of residues, thus providing an enhanced assessment of the secondary structure. In cases where the two

algorithms diverged, STRIDE exhibited superior predictive accuracy in 70% of cases (MARTIN et al., 2005).

The solvent-accessible surface area (SASA) quantifies the molecular surface available for interactions with the solvent and other molecules, influencing properties such as gel formation, foaming, and emulsification. The SASA, also known as the Lee-Richards area in honor of the pioneering work that defined it (LEE; RICHARDS, 1971), is calculated using Equation 3.6:

$$SASA = \sum_{i=1}^{N} \frac{R}{\sqrt{(R^2 - Z_i^2)}} L_i \left(\frac{\Delta Z}{2} + \Delta' Z \right) \tag{3.6}$$

where R represents the van der Waals radius, L_i represents the length of an arc of size i, Z_i represents the perpendicular distance of section i from the center of the sphere, ΔZ represents the space between sections, and $\Delta' Z$ is either $\Delta Z/2$ or $R - Z_j$ (whichever is smaller). According to similar studies, the solvent radius was considered to be 1.4 Å (VANGA et al., 2015).

Hydrogen bonds (H-bonds) are very important in protein dynamics since they play a central role in stabilizing the secondary structure. In addition, H-bonds losses are related to protein unfolding and destabilization. A H-bond forms when a hydrogen atom (donor) interacts with a highly electronegative atom (acceptor), such as fluorine, oxygen, or nitrogen. In this study, a disruptive distance of 3.5 Å and an angular cutoff of 30° between donor and acceptor atoms were adopted, as suggested in previous studies (ASTRAKAS et al., 2011; SINGH et al., 2013a; WANG et al., 2014). The evaluation of hydrogen bonds was performed using internal functions of the VMD software.

3.3 Results and Discussion

3.3.1 Validation

The final structures were validated using the Ramachandran plot, as suggested by Vagadia et al. (2016). The Ramachandran plot typically divides conformations into three distinct regions: energy favored (with recurrent structures like α-helix, β-strands and turns), energy allowed, and outliers (energy disfavored conformations with steric

interference). Notably, nearly three-quarters of possible φ-ψ angle conformations are disfavored, as two atoms cannot occupy the same position simultaneously (ROBINSON et al., 2014). Figure 3.4 displays the Ramachandran analysis of the native OVA structure obtained from the PDB. The light blue boundaries delimit the Ramachandran favored regions (RFR), while the dark blue limits delimit the Ramachandran allowed regions (RAR); any residues falling outside these zones are considered outliers. It can be seen that one amino acid (Arginine (68)) appears as an outlier. Table 3.1 summarizes this analysis for each combination of process and temperature. The total proportion of outliers remained below 2.5% in all scenarios, falling within the acceptable range observed in MD and experimental studies (VAGADIA et al., 2016; PRIAMBODO et al., 2019; SOBOLEV et al., 2020). This suggests that the obtained structures had proper spatial arrangements considering both φ and ψ angles.

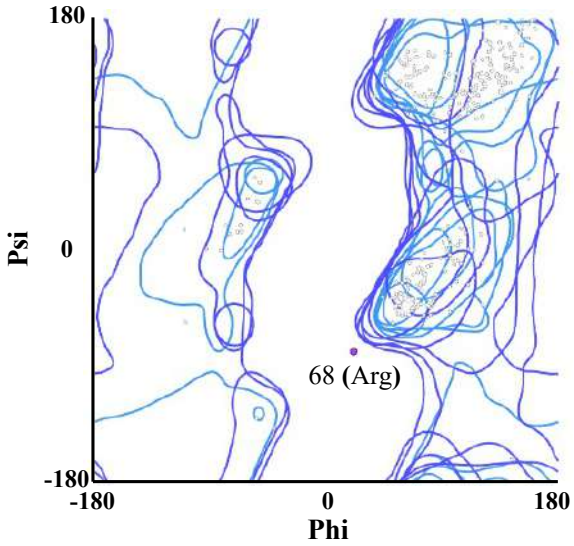

FIGURE 3.4. Ramachandran plot of the initial configuration obtained from the PDB (1OVA).

In general, proteins subjected to EF treatments presented higher outliers counts due to possible side-chain reorientation, leading to additional steric interference. The number of outliers is also influenced by interactions between the amino acids and the solvent (TIMASHEFF, 1970). Increased solvent-accessible surface areas of hydrophobic residues in the presence of the EF (as addressed further) may also collaborate to increase the outliers counting in such conditions. Moreover, results show that Serine

TABLE 3.1. Ramachandran analysis of the final structures obtained in the simulations.

Process	Residues in RFR (%)	Residues in RAR (%)	Outliers (%)	Outliers residues
300K/CHP	95.88	4.12	0	-
320K/CHP	93.08	6.12	0.80	Val(79); Asn(159); Ser(313)
340K/CHP	94.94	4.79	0.27	Gly(128)
360K/CHP	91.21	7.97	0.82	Arg(58); Arg(126); Ser(320)
300K/DC	86.29	11.79	1.92	Ser(164); Ser(165); Trp(184); Asp(190); Ser(250); Leu(252);Ser(309)
320K/DC	88.46	9.89	1.65	Arg(58); Asn (154); Asn(159); Ser(309); Ser(320); Ser(384)
340K/DC	86.96	10.84	2.20	Cys(73); Asp(190); Gln(191); Phe(217); Pro(246); Lys(277); Ser(308); Glu(319)
360K/DC	89.56	7.97	2.47	Lys(16); Tyr(125); Lys(206); Val(249); Ser(250); Ser(316); Ala(345); Asn(374); Ser(384)
300K/AC	88.29	10.34	1.37	Asp(47); Glu(70); Asn(159); Ser(307); Ser(309)
320K/AC	91.21	7.14	1.65	Ser(2); Pro(93); Ser(236); Ile(259); Ser(308); Ser(384)
340K/AC	85.28	13.9	0.82	Thr(136); Thr(193); Leu(321)
360K/AC	86.96	11.39	1.65	Pro(93); Glu(109); Ile(113); Val(249); Ser(309); Ala(384)

was the most frequent residue in the outliers section. Prior studies have noted that specific amino acids are more commonly associated with steric interference: Vagadia et al. (2016) reported that phenylalanine was highly associated with this phenomenon, possibly due to its aromatic ring, while Chen e He (2020), in an experimental study, observed that serine, phenylalanine, and leucine were the most frequent amino acids in outlier zones.

3.3.2 Stride analysis

The STRIDE analysis of OVA under the studied conditions is presented in Figure 3.5. The analysis shows that, in the absence of an EF, a partial conversion of α-helices into turns and 3_{10}-helices is observed at 320 K; at 340 and 360 K, all α-helices were converted, indicating the onset of the denaturation process. 3_{10}-helices are commonly con-

sidered as intermediate conformations, and are frequently present in the early stages of the denaturation process (DAGGETT; LEVITT, 1992). Moreover, these predictions align with the results of Llave et al. (2018); the authors found an experimental value for OVA minimum denaturation temperature of 339.8 K using differential scanning calorimetry.

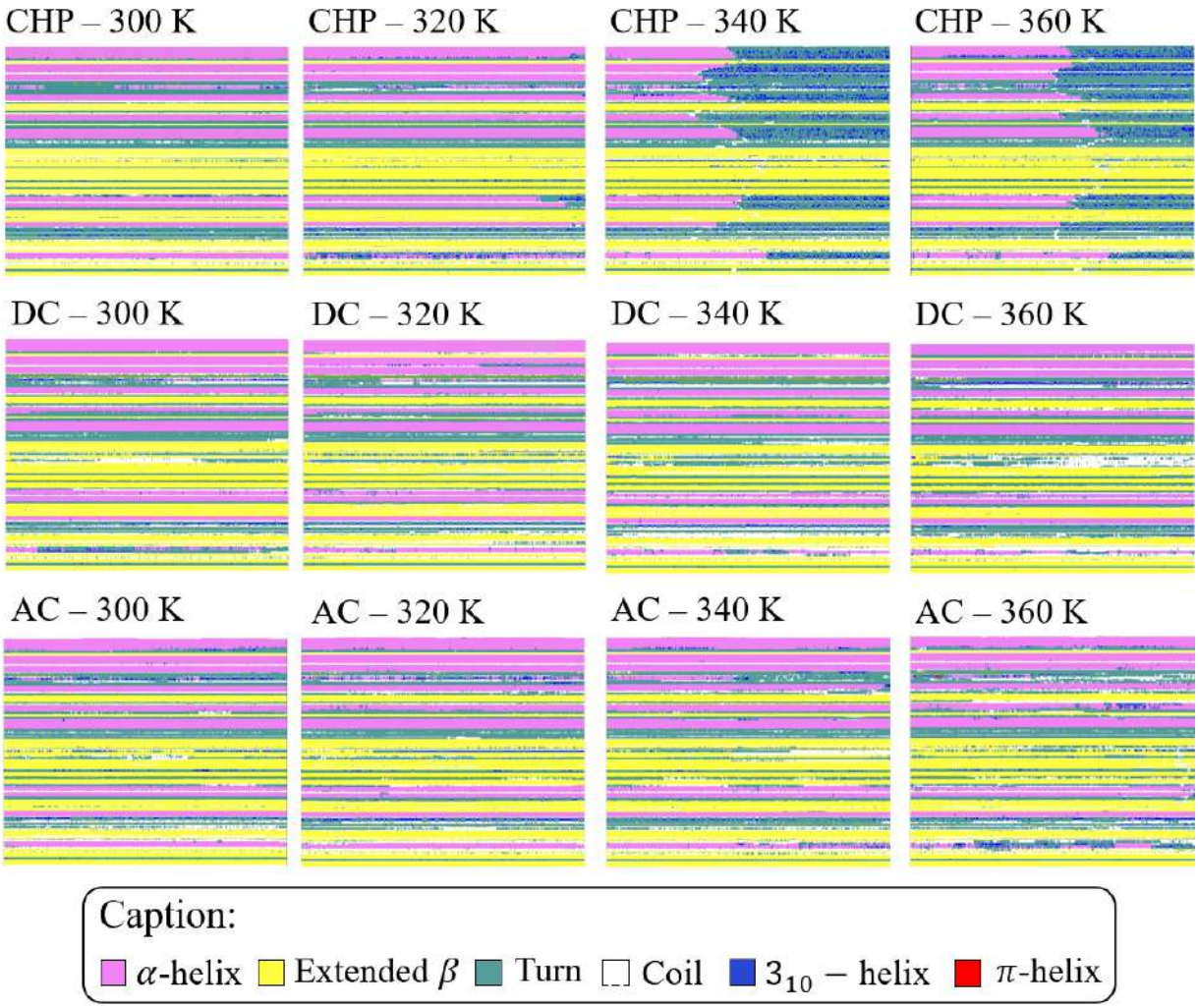

FIGURE 3.5. Stride analysis of OVA. The x axis represents the simulation time and the y axis represents the amino acid residues present in the molecule, sequentially; the colors correspond to the most probable secondary structure of the residue in a given time according to the caption shown at the bottom.

Liu et al. (2018) analyzed the interaction of OVA and curcumin by MD and also observed a decrease in α-helices followed by an increase in coil configurations; negligible or no modification was observed in the β structures. Similarly to the present

results, the α-helix content had a smaller decrease at lower temperatures, and more significant changes were observed at 343 K. However, the α-helix content reported by these authors was higher than those observed in the present simulations, which may be attributed either to differences in the number of solvent molecules or to the algorithm used to access the secondary structures (some analysis may consider 3_{10}-helices as α-helices due to the similarity of these two secondary structures, as reported by Zhang e Sagui (2015)).

Under lower temperatures, the STRIDE analysis of OVA under CHP was similar to those obtained with the application of DC and AC. Interestingly, the denaturation of α-helices tended to occur more slowly under the presence of an EF at higher temperatures. The only residues that showed a relevant α to 3_{10}-helix conversion were the amino acids sequences 67-71 and 344-373 at 360 K. This conversion was more significant under the application of AC when compared to DC, mostly when the instantaneous EF approached to zero. Additionally, a small conversion of the extended β structure of amino acids 190-205 into random coils was observed in the DC treatment at 360 K.

These results may indicate that the secondary structure of OVA is more stable under the application of heat combined with an EF in comparison to CHP. Qian et al. (2016) analyzed experimentally the effects of PEF in ovalbumin secondary structure using infra-red spectroscopy under several conditions (voltage varying from 0 to 35 kV, frequency varying from 50 to 1000 Hz and pulse width varying from 3 to 15 μs), and also reported stabler α-helices under the EF influence. In addition, the number of random coils was higher in the control treatment (CHP). These results corroborate the present findings, although the relative differences observed in the experimental study were not as high as the ones presented here. These discrepancies might be expected considering that the experiment was performed under lower temperatures and fields strengths, and with multiple proteins (in this case, it can be hypothesized that protein-protein interactions can play a role in the secondary arrangements, as addressed by Taechalertpaisarn et al. (2019)).

The limited time scale of the MD simulations may hide partial transformations of α-helix over longer time periods. Samaranayake e Sastry (2021) studied the

pectin methylesterase dynamics under a 50 kV cm^{-1} field in longer time-scales (up to 1 μs) and reported an interesting phenomenon: initially, the secondary structure was more stable under field application, probably due to the higher diffusion rates of water molecules compared to the protein, which allowed the formation of more intra-molecular bonds and stabilization of the structure. For longer periods, this pattern changed once the enzyme started to unfold and the intermolecular bonds between protein and water decreased, destabilizing the secondary structure. In fact, Yang et al. (2017) analyzed the secondary structure of OVA using far-UV circular dichroism and found that the helix content increased when a 35 kV cm^{-1} EF was applied for 60 μs; an opposite trend was seen for longer pulse times (120 μs and 180 μs). This suggests that the phenomenon described by Samaranayake e Sastry (2021) may occur with longer treatments, although stabilization may occur with shorter electrical pulses.

Salt bridge interactions were also investigated to analyze changes in the secondary structure. Salt bridges are non-covalent bonds between two ionized residues resulting from the combination of hydrogen bonding and electrostatic interactions, and they play a crucial role in structural stability (HENDSCH; TIDOR, 1994). As suggested by Thomas e Elcock (2004), a cut-off distance of 4 Å was employed and the results at 360 K are showed in Figure 3.6. No significant differences were observed in the total number of bridges (17.4$\pm$2.7, 17.5$\pm$1.9 and 17.9$\pm$2.1 for CHP, DC and AC simulations, respectively). In addition, the frequency spectrum (Fig 3.6.B) showed that the bridges were almost identically distributed regardless of the treatment. Ghosh et al. (2003) noted that the glutamic/acid-lysine interactions are particularly relevant for the stabilization of the α-helices, and therefore they are plotted separately in Fig. 3.6.C. A slight decrease in the number of Glu-Lys bridges in CHP was observed (6.1$\pm$1.7, compared to 7.6$\pm$1.3 and 7.8$\pm$1.3 for DC and AC, respectively). There are two concentration peaks located at 2.8 and 3.7 Å in the corresponding frequency spectrum (Figure 3.6.D). The first peak is relatively smaller in the CHP simulation, related to the aforementioned decrease in Glu-Lys bridges, which could be responsible for the stronger destabilization of the helices in this scenario.

In conclusion, the application of an EF enhances the stability of the secondary structure of OVA under pasteurization conditions ($T > 333$ K). These results agree with previous experimental studies and computational simulations, and are of great

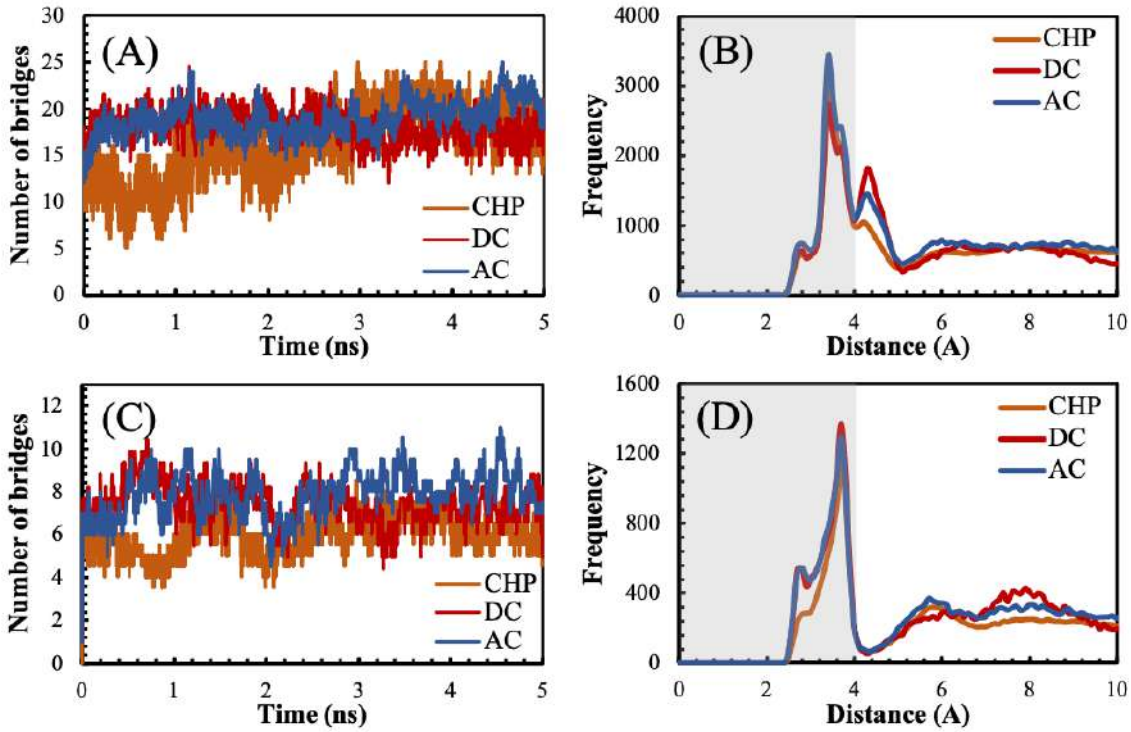

FIGURE 3.6. OVA (A) total salt bridges at 360 K, (B) histogram of distances between bridge atoms, (C) Glu-Lys bridges at 360 K and (D) histogram of distances between Glu-Lys bridges. The shaded areas in (B) and (D) correspond to the bridge formation zones.

relevance for the understanding of egg processing. Given the strong correlation between secondary structure and protein functionality, thermal denaturation by CHP (as reported by Oliveira et al. (2020), for example) may be minimized or even avoided with the application of electrically driven treatments.

3.3.3 Radius of Gyration

3.7 shows the OVA R_g as a function of temperature and applied treatment, and Table 3.2 shows the average values and results of the statistical analysis. It can be seen that the results were temperature independent for the same treatment, suggesting either that the protein is stable under these conditions or that the analyzed time scale is not long enough to access other states. In CHP, thermal unfolding is expected after 339.8 K, resulting in higher R_g values. This phenomenon was not visualized probably due to the limited time scale of simulations, although the STRIDE analysis showed a

decrease in α-helices content, related to the early stages of denaturation.

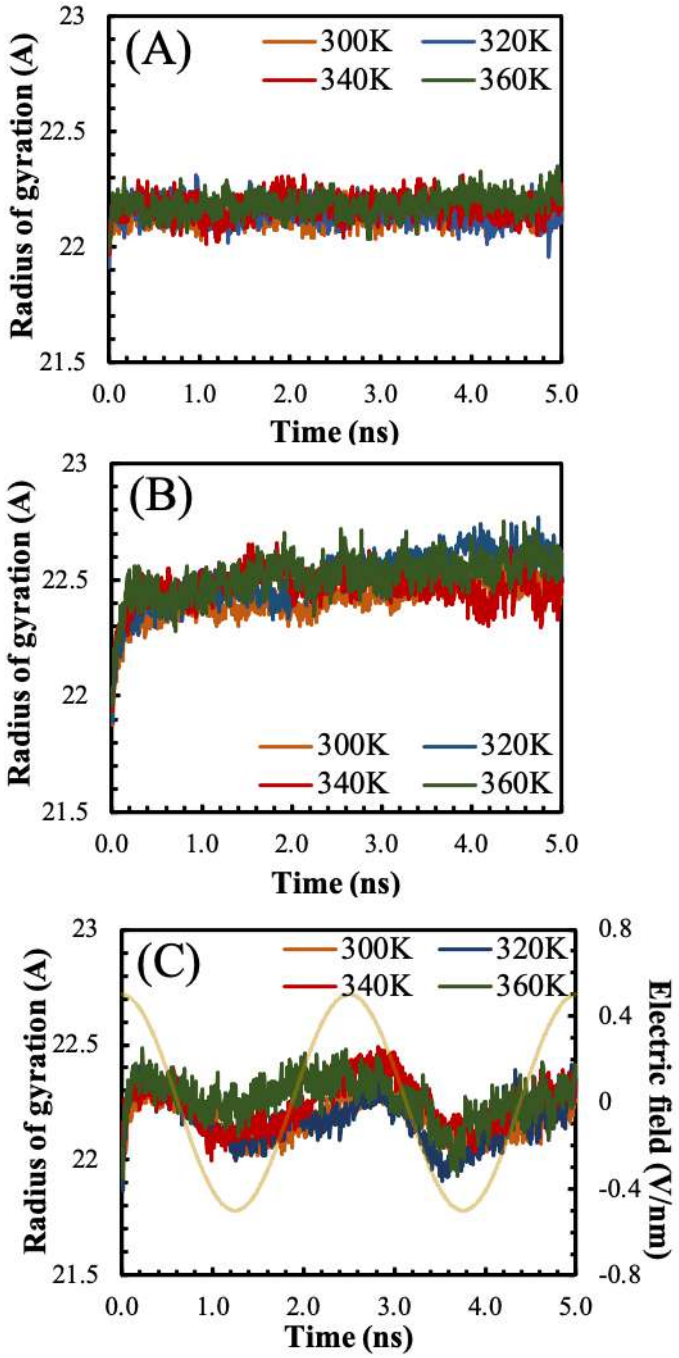

FIGURE 3.7. OVA radius of gyration under (A) CHP, (B) DC and (C) AC processing. For the sake of clarity, a continuous yellow line was added in (C) to represent the instantaneous applied EF, according to the secondary y axis.

The R_g increased from about 22.2 to 22.5 Å when a DC was applied, indicating

TABLE 3.2. OVA radius of gyration (Å) as function of the applied process and temperature. Results with the same superscript are not significantly different from each other ($p > 0{,}05$).

Temperature	CHP	DC	AC
300 K	22.13±0.02^{a}	22.45±0.02 ^{d}	22.18±0.05 ^{a,b,c}
320 K	22.15±0.01^{a,b}	22.49±0.02 ^{d}	22.18±0.05 ^{a,b,c}
340 K	22.17±0.02^{a,b}	22.47±0.06 ^{d}	22.24±0.06 ^{b,c}
360 K	22.18±0.01^{a,b,c}	22.52±0.05 ^{d}	22.27±0.05 ^{c}

a increase in the molecule size under EF application. As OVA has a resultant negative charge, the molecule is expected to stretch along the direction of the applied field (FERNANDEZ-DIAZ et al., 2000; WU et al., 2014), which was confirmed in the simulations (as discussed latter in Section 3.3.6). In fact, several experimental and MD studies showed that folding/unfolding processes differ between thermal and electrically treated proteins (ASTRAKAS et al., 2011; SINGH et al., 2013a; VANGA et al., 2015; HAN et al., 2018); depending on the charge distribution of the molecule, this may lead to an increase or a decrease in the denaturation rate. Therefore, while the secondary structure remains more stable in the presence of an EF, the tertiary structure tends to undergo faster modifications in such conditions. The increased unfolding rate of OVA under the presence of electric fields has been already reported and it is important in many technological applications, mostly in gelling properties. Yang et al. (2017) found by UV absorption spectroscopy that the application of 35 kV cm^{-1} for 60 μs or 25 kV cm^{-1} for 180 μs leaded to partial unfolding of OVA, similarly to what was observed in the present study under higher fields and shorter time periods.

Concerning the application of AC, an interesting phenomenon was observed. At the initial stages of the simulation, the radius of gyration tended to ascend similarly to the DC condition; when the field reached approximately 0.3 V/nm, the protein returned to its original state, until the cycle achieved 0.3 V/nm again and the protein restarted to unfold. This behavior was repeated in both simulated cycles, suggesting that the unfolding process might be reversible or slower under AC compared to DC. In fact, the average R_g in the AC case was similar to that of the CHP at all temperatures. Barsotti et al. (2001) indicated that the application of exponentially decaying electric pulses of 31.5 kV cm^{-1} and 1 Hz lead to partial OVA unfolding. However, these alterations were temporary and the protein folded back to its original configuration after 30

TABLE 3.3. OVA root mean square displacement (Å) as function of the applied process and temperature. Results with the same superscript are not significantly different from each other ($p > 0{,}05$).

Temperature	CHP	DC	AC
300 K	1.73±0.02^{a}	2.55±0.17 ^{e}	2.16±0.22 ^{c,d}
320 K	1.82±0.06 ^{a,b}	2.80±0.03 ^{e,f}	2.18±0.05 ^{d}
340 K	1.88±0.04 ^{a,b,c}	2.96±0.11 ^{f}	2.51±0.13 ^{e}
360 K	2.05±0.14 ^{b,c,d}	3.55±0.11 ^{g}	2.93±0.03 ^{f}

min, indicating reversible processing damage. The obtained results corroborate these observations, considering that the protein returned to its original R_g when the AC electric field approached zero. The use of DC or higher electric fields and lower frequencies could lead to irreversible damage, as already showed by spectroscopic analysis in Yang et al. (2017) and Fernandez-Diaz et al. (2000).

3.3.4 Root mean square displacement

Figure 3.8 shows the *RMSD* plots of OVA as a function of temperature for the studied processes, and Table 3.3 shows the average values and results of the statistical analysis. *RMSD* was temperature independent at 300, 320 and 340 K under CHP, while small increases were observed for the DC and AC treatments within this temperature range. A larger increase in *RMSD* was observed at 360 K, especially in the DC simulations. As previously discussed, thermal unfolding is capable of altering the molecular structure and it is expected to occur under higher temperatures. Even though a temperature dependence of the radius of gyration was not observed, which would indicate denaturation at 360 K, the increase in the $RMSD$ may be related to the early stages of the unfolding process.

Small discrepancies with respect to PDB original structure were observed in all scenarios (below 4.2 Å). More significant differences were visualized when the molecule was subjected to electric fields (both AC and DC), and therefore is possible to observe that the results are dependent on the applied treatment, with higher $RMSD$ values associated to EF processes. This behavior is in agreement with previous simulations and indicates internal rearrangements under field presence (ASTRAKAS et al., 2011; VANGA et al., 2015; VAGADIA et al., 2016). The results obtained upon

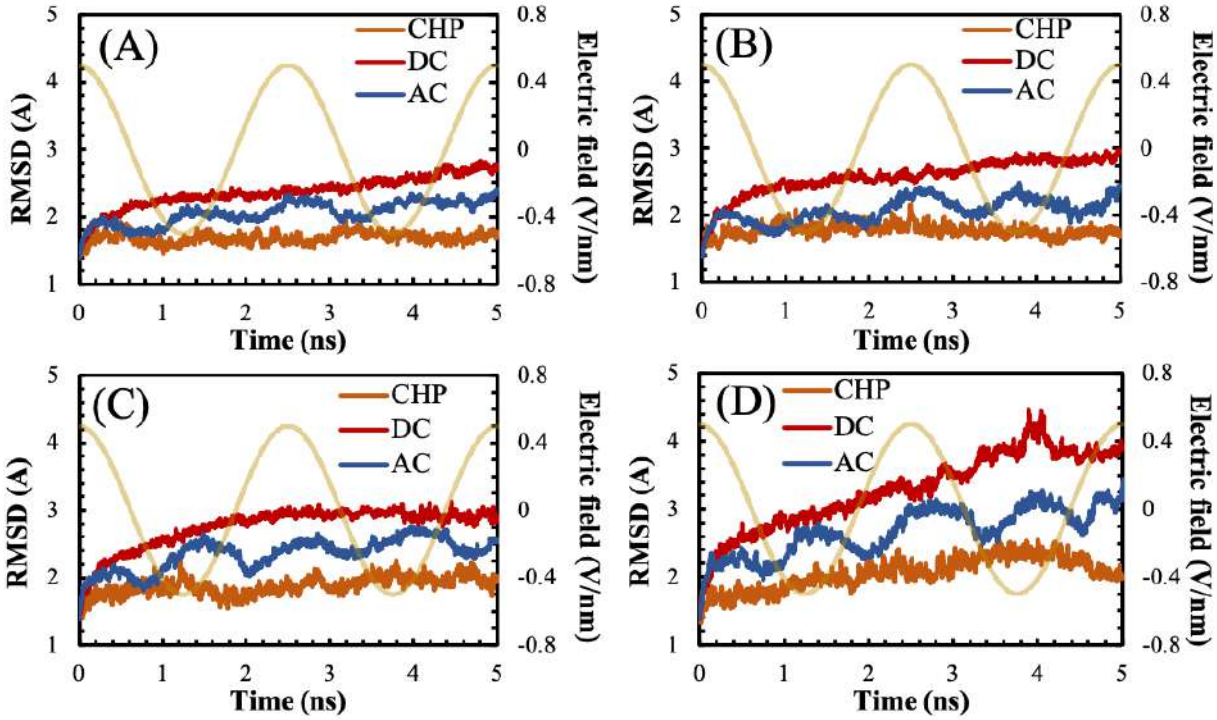

FIGURE 3.8. OVA root mean square displacement at (A) 300, (B) 320, (C) 340 and (D) 360 K. For the sake of clarity, a continuous yellow line was added to represent the instantaneous applied EF, according to the secondary y axis.

application of DC field agree with the R_g analysis of Section 3.3.3, considering that the stretching process naturally leads to structural deviations in relation to the native molecule. For the AC simulation, the increases in *RMSD* at 360 K in comparison with 340 K was not followed by increments in the radius of gyration, probably because the spatial rearrangements occurred within the inner parts of the molecule, not affecting its average size. A slight tendency of decreasing *RMSD* was observed when the field approached zero, but its value started to increase again when the field was closer to its maximum and minimum peaks.

3.3.5 Hydrogen bonds

Hydrogen bonds (H-bonds) are very important in protein dynamics since they play a central role in stabilizing the secondary structure. In addition, H-bonds losses are strongly related to protein unfolding and destabilization. Figure 3.9 shows the average number of the protein intramolecular H-bonds and the standard deviation for each simulation. The results were process independent at lower temperatures, while

a decrease in the number of bonds was observed for electric driven treatments at 340 and 360 K. As discussed previously, the proteins R_g and $RMSD$ increased under EF application and high temperatures, which may be related to the decrease on H-bonds. In addition, higher temperatures increase the molecules kinetic energy, enhancing vibrational and rotational movements that cause bonds disruption (OHTAKI, 2003).

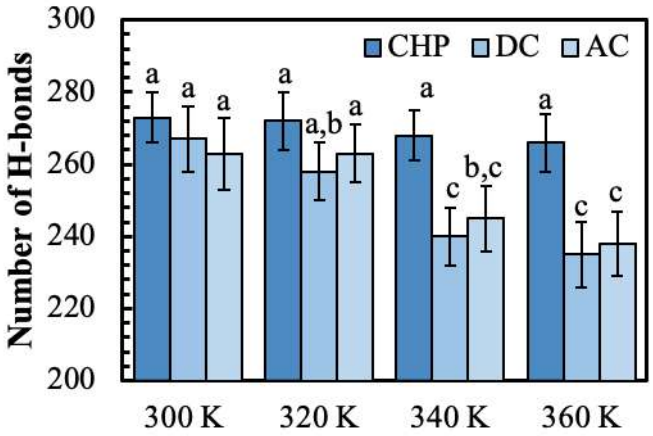

FIGURE 3.9. Average number of intramolecular hydrogen bonds of OVA in each analyzed scenario. Results with the same letter are not significantly different from each other ($p > 0{,}05$).

Suresh et al. (2006) stated that an increase in H-bonds with EF application may be expected as a result of electrostatic interactions that approximate potential donor and acceptor atoms. For OVA, a reverse effect was observed. Higher applied electric fields resulted in a further reduction in the number of bonds, as illustrated in Figure 3.10. This behavior agrees with other studies regarding EF effects in proteins (ASTRAKAS et al., 2011; SINGH et al., 2013a; WANG et al., 2014). Despite the decrease in H-bonds under EF treatments, the α-helix content was more stable in this process. A similar behavior was also reported for egg white protein using UV spectroscopy by Qian et al. (2016). Moreover, the number of intermolecular H-bonds is similar between the different processes (see Figure 3.11). This suggests that, in the case of ovalbumin, the impact of the EF on H-bonds is intramolecular.

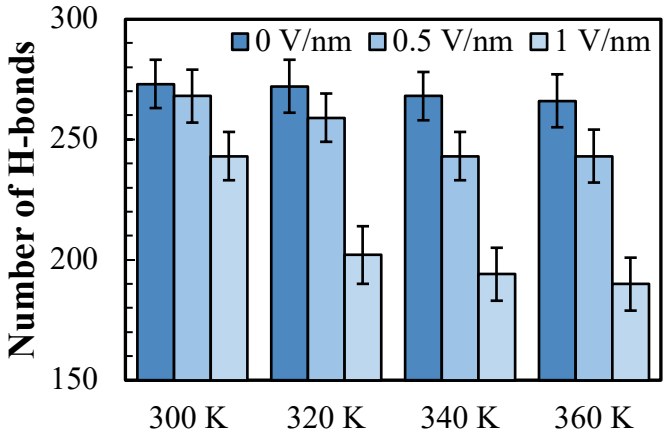

FIGURE 3.10. Average number of intramolecular hydrogen bonds of OVA under different DC electric fields.

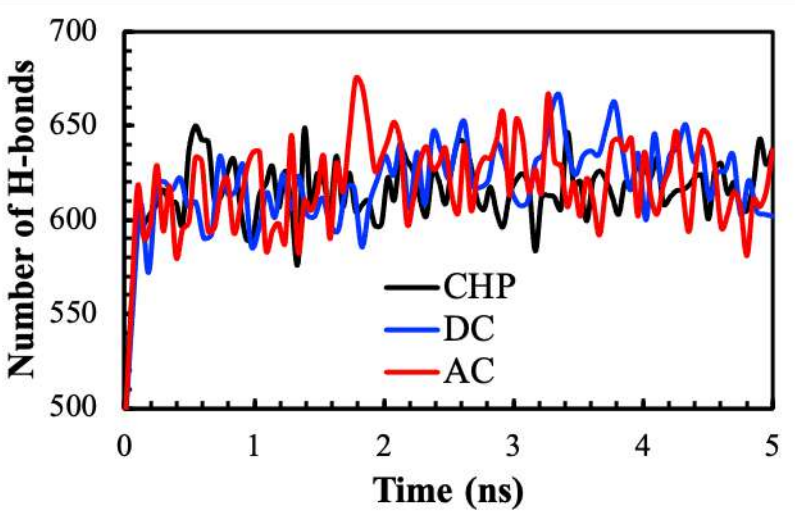

FIGURE 3.11. Average number of intermolecular hydrogen bonds of OVA at 360 K.

3.3.6 Dipole moment

The dipole moment of the protein structure is useful to quantify its electrostatic aspects, influencing several properties of the system, such as solubility (CARDOSO et al., 2020), melting and boiling points and its reactivity (SIEBLER et al., 2015). Figure 3.12 shows the scalar total dipole moment of OVA as a function of temperature and applied EF. Higher dipole moments were observed within electric driven treatments at 360 K, probably caused by the increase in the molecular vibration amplitudes in such

conditions (DAVYDOV, 1996).

The dipole moment is considerably higher under DC treatment in comparison with CHP. Figure 3.13 shows a charged colored representation of OVA at 360 K in the absence of EF and under DC application. The protein stretching in the direction of the applied field (previously discussed in Section 3.3.3) can be visualized, and the maximum distance between the residues at the edges increased from 72.90 to 78.42 Å in CHP and DC, respectively. This contributes to the increase in the dipole moment as expressed in Eq. 3.5. In addition, electrically charged amino acids are more affected by the presence of external fields and the figure shows a tendency of these residues to concentrate in the molecule extremities. This side-chains re-alignment in the field direction is expected and confirmed in the simulations. The experimental results of Qian et al. (2016) using far-UV circular dichroism spectroscopy also indicated molecular dipole moment changes when EF was applied. In addition, similar MD studies also reported increases in the total dipole moment of proteins (SINGH et al., 2013a; JIANG et al., 2019).

Concerning the AC simulation, a re-orientation of the dipole moment depending on the EF intensity was observed: when the field modulus was high (in ridges or valleys of the sinusoidal function), a higher dipole moment was observed; as the modulus of the field approached zero, the dipole moment dropped closer to its original value (CHP condition). This behavior may be related to process reversibility, as previously discussed. These results also agree with the findings of the prior sections. As the overall molecule size increases (as suggested by the radius of gyration), the charges distances in relation to the molecule center of mass also tend to increase, enhancing the dipole moment as expressed in Eq. 3.5. Moreover, similarly to the $RMSD$, a dependence of the dipole moment with the momentary EF was observed in the AC case, which is related to the stretching and folding of the molecule under this scenario.

Additionally, the interaction between the ovalbumin and the EF led to a displacement of the molecule, as can be seen in Figure 3.14. Under field absence, the center of mass of the protein remained almost stationary. Under DC conditions, a linear movement towards the $-x$ direction of the simulation box was observed, consistent with the net negative charge of the protein. In contrast, under AC conditions, the dis-

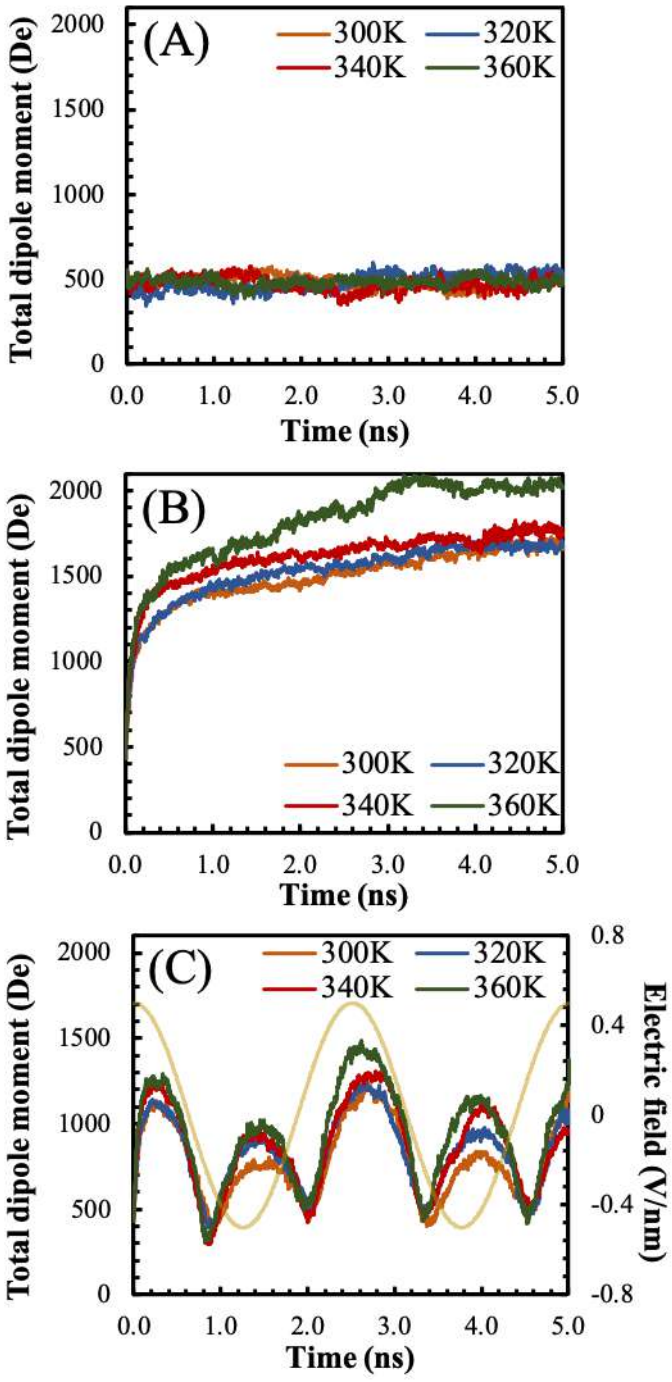

FIGURE 3.12. OVA total dipole moment under (A) CHP, (B) DC and (C) AC processing. For the sake of clarity, a continuous yellow line was added in (C) to represent the instantaneous applied EF, according to the secondary y axis.

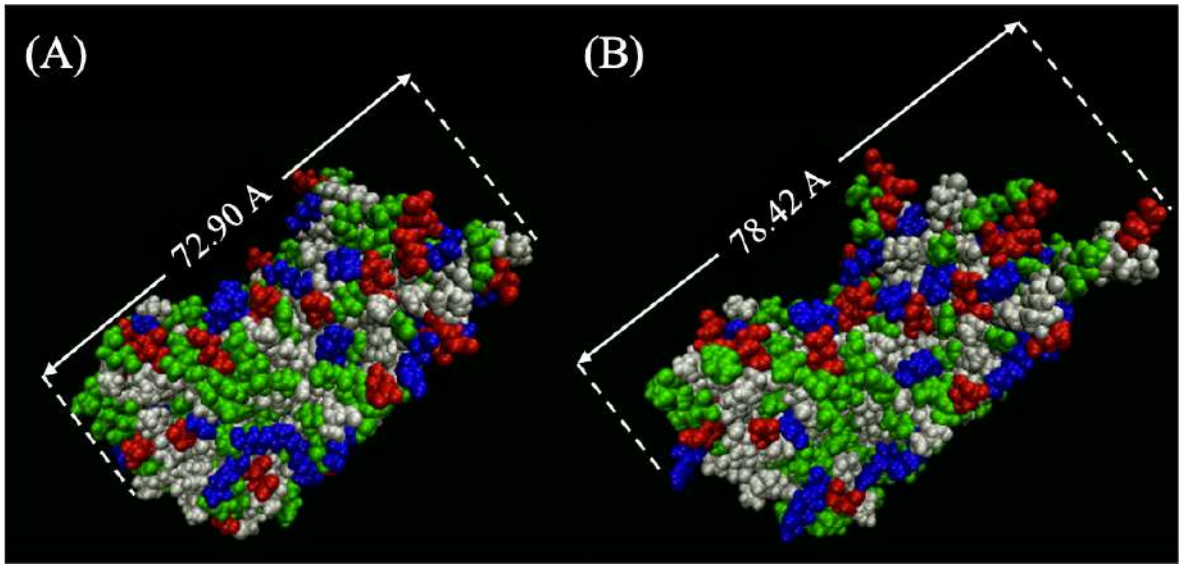

FIGURE 3.13. Snapshot of OVA at 360 K and (A) 0 V nm^{-1} and (B) 0.5 V nm^{-1} DC. The white, green, blue and red colors correspond to non-polar, polar, basic and acidic residues, respectively.

placement was dependent on the instantaneous EF.

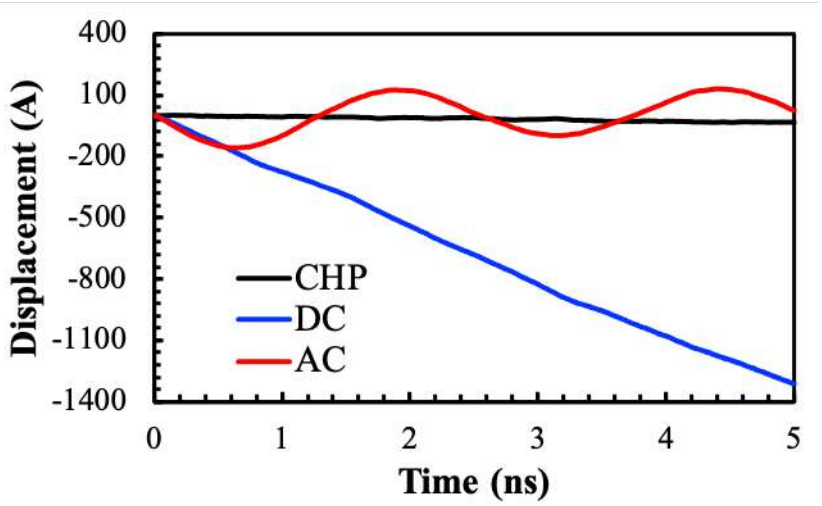

FIGURE 3.14. OVA center of mass displacement at 360 K for all applied processes.

3.3.7 Solvent accessible surface area

SASA is the protein surface area available to establish contact with solvents and/or other molecules, and it is related to several functional properties (e.g. emulsifying and gelling capacity). Figure 3.15 shows the SASA evolution of OVA in all analyzed

TABLE 3.4. OVA solvent accessible surface area (Å^2) as function of the applied process and temperature. Results with the same superscript are not significantly different from each other ($p > 0{,}05$).

Temperature	**CHP**	**DC**	**AC**
300 K	17969±210 ^{a,b}	17851± 145^{a,b}	17916±172 ^{a,b}
320 K	17780±116 ^{a}	18116±125 ^{b,c}	17947±154 ^{a,b,c}
340 K	17922±106 ^{a,b}	18104±318 ^{b,c}	18430±309 ^{c,d}
360 K	17965±121 ^{a,b}	18928±354 ^{d}	18617±13 ^{c,d}

scenarios, and Table 3.4 shows the averages and statistical analysis of the data. The results were temperature independent within the analyzed time scale under CHP, and an average value of 17909 Å^2 was found. An increase in SASA was observed as temperature increases in the DC and AC simulations. Overall, its possible to conclude that EF application in OVA increases the surface area and that this effect is more pronounced at higher temperatures. Vanga et al. (2015) stated that, due to its specifics spatial arrangements and to the presence of H-bonds, α-helices are probably the secondary structure that affect SASA the most. This statement is in agreement with Vagadia et al. (2016), who showed that the soybean trypsin inhibitor protein, which does not have α-helices in its structure, is highly stable under EF application. For OVA, when an EF was applied, the helices residues tended to orientate themselves in the direction of the field, causing a resulting stress in the whole protein and an increasing its surface area.

Additional information of the SASA considering hydrophilic and hydrophobic residues is shown in Figure 3.16 at 360 K. In common situations, hydrophobic residues tend to conform internally in the protein, as interactions with water are mostly of repulsive nature. In the absence of EF, an average area of 13700 Å^2 is observed for polar residues, whereas for apolar residues, smaller areas ($\approx$ 4400 Å^2) were found. A significant increase in the apolar SASA is found when an EF is applied. However, the application of an EF significantly increased the SASA of apolar residues, as the protein structure stretched, exposing non-polar residues to the surrounding medium. This alteration in solute-solvent interactions could lead to distinct functional properties (which will be addressed in Section 3.3.8). Increases in the surface hydrophobic area of OVA under the influence of PEF were observed experimentally by Yang et al. (2017) using fluorescence spectroscopy after 180 μs - 25kV cm^{-1} or 60 μs - 35 kV cm^{-1} treatments. These results may also explain the reduction in egg white protein solubility

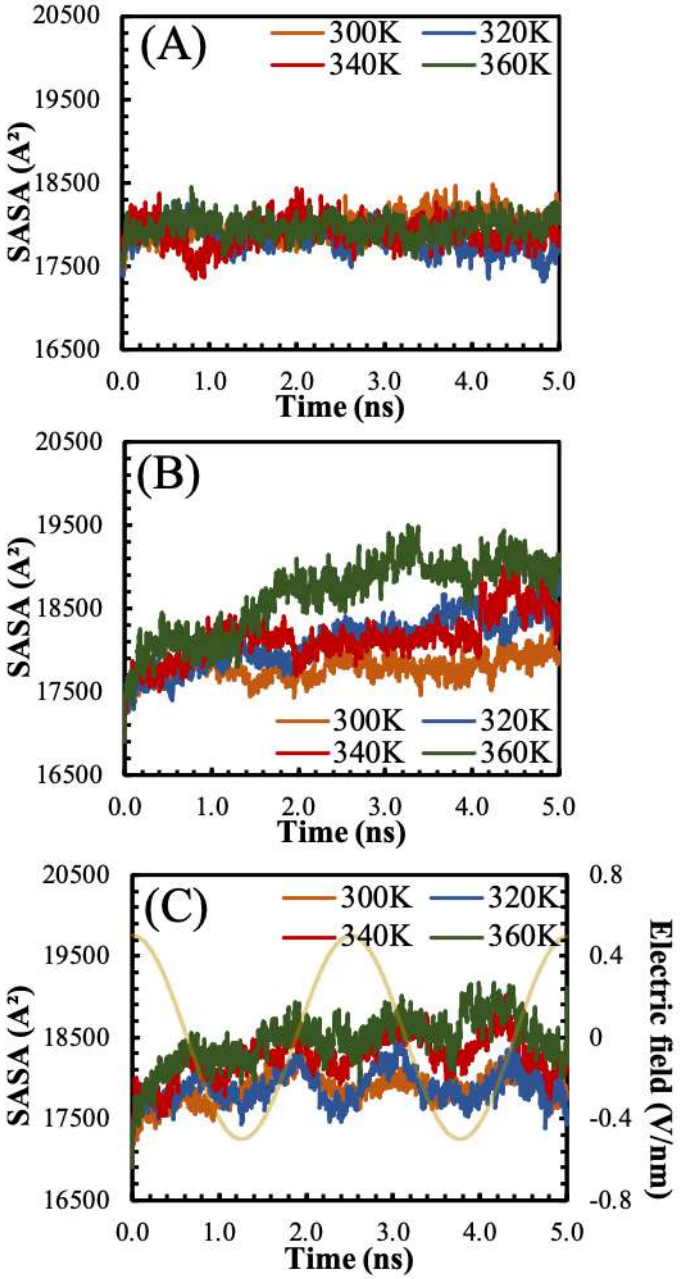

FIGURE 3.15. OVA solvent accessible surface area under (A) CHP, (B) DC and (C) AC processing. For the sake of clarity, a continuous yellow line was added in (C) to represent the instantaneous applied EF, according to the secondary y axis.

in water after PEF, as reported by Wu et al. (2015).

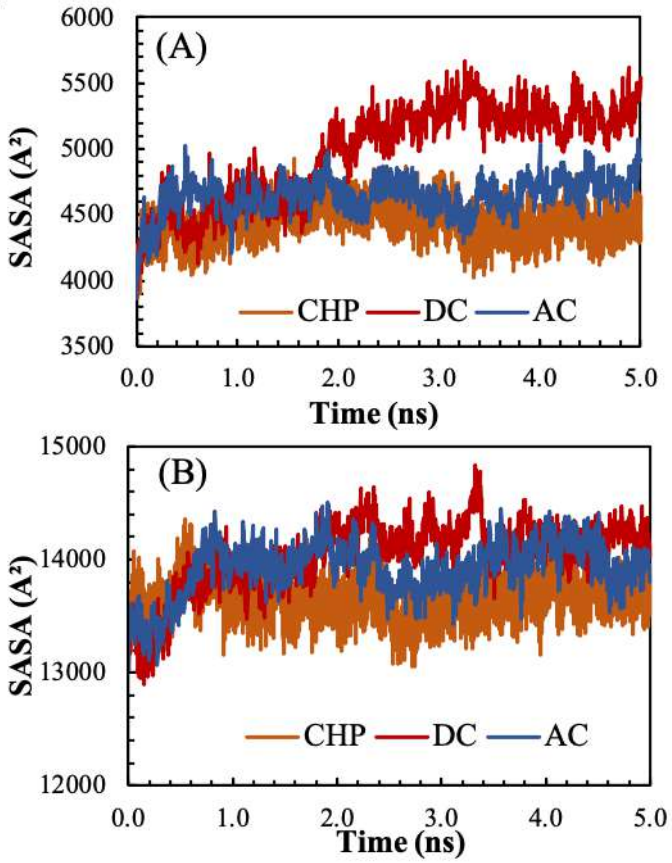

FIGURE 3.16. OVA solvent accessible surface area for apolar and polar residues.

3.3.8 Relationship of the results with experimental studies

As shown in the previous sections, several structural properties of OVA are affected by EF application, indicating that this molecule is highly susceptible to non-thermal effects. A review of EF-induced non-thermal effects in egg-based products was performed by Yogesh (2015). The present simulations can help to shed some light in the mechanisms involved in these modifications. According to the simulations, the main effects of applying EF in ovalbumin are:

- stabilization of the secondary structure;
- increase in R_g, $RMSD$ and total dipole moment;
- decrease in the number of H-bonds at high temperatures;

- increase in the SASA of apolar residues.

Egg viscosity is a transport property modified by EF application: Monfort et al. (2012) showed an increase in average viscosity when a 25 kV/cm PEF treatment was applied, and Bozkurt e Icier (2011) reported a difference in the temperature dependence of this variable using a 20 V/cm ohmic heating process. Molecules with larger number of H-bonds usually lead to more viscous fluids, as the intermolecular forces are stronger under such conditions, causing more resistance to fluid flow (FANG et al., 2019). In the simulations, a small decrease in the number of H-bonds was visualized under EF treatments, which contradicts the expected behavior. However, this transport property can also be affected by the relation between intermolecular friction and molecule shape; larger molecules are associated with more viscous solutions (NGUYEN et al., 2007) due to increases in intermolecular forces. Zidar et al. (2020) experimentally studied how to control the viscosity of proteins formulations and found that the major contributions are caused by London dispersion forces and electrostatic interactions. The authors proposed a mechanism to electrostatically enhance viscosity, based on the orientation of proteins under shearing conditions; the most negative pole of a given protein would tend to face the most positive pole of the neighboring molecule, resulting in molecular assembling and increased viscosity. As observed in the present simulations, the OVA dipole moment is higher under EF application, which is related to increases in electrostatic interactions, corroborating the aforementioned mechanism. In addition, increases in SASA and R_g for electric driven treatments indicate that the overall molecular size is larger under such conditions, which enhances intermocular friction and, consequently, the viscosity.

The mechanism proposed by Zidar et al. (2020) (that aggregation may happen due to electrostatic interactions among proteins) is corroborated by the experiments of Zhao e Yang (2010), who also reported higher OVA aggregation under EF treatments using high-performance chromatography. The present results agree with this mechanism, since: (i) the molecule tended to unfold under the influence of an external field, and increases in the dipole moment showed that the most affected areas are the charged amino acids; (ii) as these residues are more concentrated in the extremities due to EF induced re-orientation, the dipole-dipole forces among adjacent proteins may lead to higher aggregation. In addition, it may be hypothesized a second mechanism

considering the solvent repulsive forces: as hydrophobic SASA increases, a rise in the van der Waals interactions among apolar residues of two proteins is favored, which is followed by a solvent-solute repulsion. Roth et al. (1996) indicated that London forces can highly contribute to the dynamics of protein aggregation. Therefore, it is possible to state that the higher aggregation degree of OVA is probably primarily caused by the electrostatic forces, but may also be influenced by the increases in apolar SASA. It is important to point out that this is a hypothesis, and further research is needed for its validation.

Concerning proteins technological properties, increases in foaming and emulsifying capacity and stability were correlated with the application of PEF in liquid whole eggs (MONFORT et al., 2012). According to Zayas (1997b), the foaming process can be summarized in three stages: (i) proteins diffuse to the air/water interface, concentrate and reduce surface tension; (ii) proteins unfold at the interface, orientating the hydrophilic and hydrophobic residues at the aqueous and non-aqueous phases, respectively; (iii) proteins interact to form a stable film around the bubbles, with partial denaturation. The function of polypeptides in foams is to decrease the superficial tension, to increase viscous and elastic properties of the liquid phase and to form strong films. In this context, OVA denaturation observed in the present simulations may increase liquid whole egg viscosity under EF application, which can improve foam formation (ALLEONI, 2006). In addition, the partial unfolding observed can also accelerate and improve the second stage of foam formation. Moreover, the increase in apolar interactions is strongly related to the foaming capacity of the product, due to decreases in the surface activity, which are also enhanced under applied EF.

Similarly, increases in the emulsyfing capacity and stability of egg white or whole eggs under EF treatments were also reported by several authors (TU et al., 2013; HU et al., 2019; MONFORT et al., 2012). Proteins with higher apolar area are better surface active agents and more efficient emulsifiers. The simulations showed partial unfolding of OVA under small time scales and at low temperatures when an EF is applied, which could improve emulsifier capacity even at mild heat treatments. This behavior was observed experimentally by Zayas (1997a) under the application of heat in time scales higher than those studied in the present work. In addition, Mine et al. (1991) stated that a higher emulsifier ability is observed under low pHs, which was

explained by increases in the hidrophobic surface area caused by acidic environments. This enhancement in surface area can also be caused by the molecule stretch under the application of EF.

3.4 Conclusion

The purpose of the present study was to analyze the conformational changes of ovalbumin under the influence of electric fields by molecular dynamics simulations, improving the current understanding of the protein dynamics during EF processing of foodstuff. The results showed that electrically driven treatments at high temperatures led to a higher stabilization of the secondary structure compared to conventional temperature driven processing. Application of an EF leads to an increase in the molecule overall size, dipole moment and solvent accessible surface area, and a decrease in hydrogen bonds. These results agree with several experimental studies performed in similar systems, and help explain some observed phenomena in EF processing of foodstuff containing OVA, such as the enhancement of the protein stability, and changes on viscosity and emulsifying capacity. This study makes a contribution towards a better understanding of non-thermal effects in proteins and may motivate further theoretical and experimental studies on the field.

Chapter 4

Molecular dynamics insights on temperature and pressure effects on electroporation

The findings from the study titled *Molecular Dynamics Insights on Temperature and Pressure Effects on Electroporation* are presented and discussed in this chapter. In this study, the electroporation phenomenon of a lipid bilayer was examined at various temperatures and pressures, aiming to analyze the influence of these variables on kinetic parameters and the migration flow of chemical species across the bilayer. The results contribute to a deeper comprehension of electroporation in diverse thermodynamic scenarios and may aid in selecting processing conditions for a wide range of applications of this technique. This study has been published in the journal *Biochimica et Biophysica Acta (BBA) - Biomembranes* (DOI: <https://doi.org/10.1016/j.bbamem.2022.184049>).

Abstract: Electroporation is a cell-level phenomenon caused by an ionic imbalance in the membrane, being of great relevance in various fields of knowledge. A dependence of the pore formation kinetics on the environmental conditions (temperature and pressure) of the cell membrane has already been reported, but further clarification regarding how these variables affect the pore formation/resealing dynamics and the transport of molecules through the membrane is still lacking. The objective of the present study was to investigate the temperature (288-348 K) and pressure (1-5000 atm) effects on the electroporation kinetics using coarse-grained molecular dynamics simulations.

Results shown that the time for pore formation and resealing increased with pressure and decreased with temperature, whereas the maximum pore radius increased with temperature and decreased with pressure. This behavior influenced the ion migration through the bilayer, and the higher ionic mobility was obtained in the 288 K/1000 atm simulations, i.e., a combination of low temperature and (not excessively) high pressure. These results were used to discuss some experimental observations regarding the extraction of intracellular compounds applying this technique. This study contributes to a better understanding of electroporation under different thermodynamic conditions and to an optimal selection of processing parameters in practical applications which exploit this phenomenon.

Keywords: DPPC; Lipid Bilayer; Electric Field; High Pressure.

4.1 Introduction

Lipid bilayers are biological structures formed by amphiphilic lipids (i.e., composed by a hydrophilic phosphate head and a hydrophobic side-chain) that exhibit diverse phases influenced by external factors like temperature and pressure (TADA et al., 2009), pH (PETELSKA; FIGASZEWSKI, 2000) and degree of hydration (ULRICH et al., 1994). At low temperatures, the Gel II or $L_{\beta'}$ phase is found, characterized by palmitic acid groups mostly elongated and highly ordered. As temperature increases, the side-chains become more disordered, and gauche conformations start to form (WONG et al., 1988). This leads to an intermediate phase known as Gel I, rippled gel phase or $P_{\beta'}$. The $L_{\beta'} \rightarrow P_{\beta'}$ conversion is called pre-transition. When the bilayer reaches the main transition temperature (T_m), a liquid crystalline phase (L_α) is formed, which is characterized by an increased number of gauche conformations and high entropy in the hydrophobic fatty acid chains. The $P_{\beta'} \rightarrow L_\alpha$ conversion is known as the main transition. Bilayers formed by saturated lipids (e.g. DPPC, DPCO, DPPG) exhibit additional gel phases at pressures above 3,000 atm (MACDONALD, 1984; WONG et al., 1988; DRISCOLL et al., 1991; CZESLIK et al., 1998).

The main function of lipid bilayers is to regulate the passage of compounds into and out of the cells. Permeability control is desirable in many industrial and biological applications, and mass transfer can be enhanced in these systems by electroporation (GOLBERG; RUBINSKY, 2013). For this purpose , a transmembrane electrical gradient is used to form pores on the bilayer surface, provided that the electric field energy is higher than the critical free energy required for structural rearrangements (JOSHI; SCHOENBACH, 2000). Electroporation is used in various fields of knowledge, such as the transfer of drugs and genes into living cells (SHI et al., 2018; JACOBS et al., 2020), microbial inactivation in foods (BARBA et al., 2020), and cell electrofusion processes (USAJ; KANDUSER, 2012). Recently, this technology has also been used in cancer research and showed promising results related to the death of carcinogenic cells (HANSON et al., 2021; BURBACH et al., 2021; WEI et al., 2021). Furthermore, according to Aycock e Davalos (2019), this phenomenon can be divided into two classes, distinguished by the extent of the damage imposed to the bilayer: (i) reversible electroporation (pores revert to their original conformation after the electric potential ceases), and (ii) irreversible electroporation (the damage imposed to the cell is permanent).

Electroporation is a pressure and temperature dependent process (HEINZ; KNORR, 2000; ZÁRATE-RODRÍGUEZ et al., 2000; ÁLVAREZ; HEINZ, 2007; CARULLO et al., 2018; BENSALEM et al., 2020). This dependence is probably related to phase transitions in the bilayer, although the mechanisms are still unclear. Molecular dynamics (MD) simulations are useful tools for analyzing conformational changes in biomolecules and have been widely applied to elucidate alterations at the molecular level that are not readily accessible in experiments. Previous MD studies investigating the behavior of lipid bilayers under high pressure have shown that their properties and structures are correctly reproduced (JIANG et al., 2004; CHEN et al., 2011; LAI et al., 2012; DING et al., 2017). The electroporation phenomenon in these biological structures has also been replicated successfully at atmospheric pressure using both all-atom and coarse-grained models (TAREK, 2005; ZHOU; LIU, 2019).

The present study aims to analyze the influence of pressure (P) and temperature (T) in the electroporation of a dipalmitoylphosphatidylcholine (DPPC) bilayer using coarse-grained MD simulations with the Martini force field. A comprehensive analysis of this process is provided, discussing the pore formation and resealing kinetics

under varied T and P conditions, and its effect on the ion migration rates throughout the bilayer. The results contribute to a better understanding of this phenomenon under different thermodynamic scenarios and can help to elucidate which are the optimal temperature and pressure conditions to be used when applying this technique for practical purposes.

4.2 Computational Methodology

4.2.1 System creation and equilibration

In this chapter simulations were conducted using the open-source software GROningen MAchine for Chemical Simulations 5.1 (Gromacs 5.1). Initially, 512 DPPC molecules were randomly placed within a simulation box with dimensions of $13 \times 13 \times 13$ nm^3, as shown in Figure 4.1.A. The initial DPPC structure was obtained directly from the Martini website (<http://cgmartini.nl/index.php>). Since the phenomenon analyzed in the present study is the electroporation, the electrostatic interactions must be described as accurately as possible. Therefore, the polarizable water model was employed (YESYLEVSKYY et al., 2010). Figure 4.2 provides a comparison of the DPPC bilayer lateral area using the polarizable water and the original water models of Martini 2 and Martini 3. This comparison demonstrates the accurate representation of experimental data when employing the polarizable water model.

Initially, 512 DPPC phospholipids and 10,477 coarse-grained polarizable water beads were randomly placed inside a $13 \times 13 \times 13$ nm^3 simulation cell, resulting in 82 real water molecules per lipid (fully hydrated conditions). The system was then energy-minimized using a steepest descent algorithm, followed directly by 100 ns equilibration runs at different temperatures (T) and pressures (P) in the isobaric-isothermal ensemble (NPT, T = 288, 308, 328 and 348 K; P = 1, 500, 1000 and 5000 atm) with isotropic pressure coupling. The Berendsen thermostat and Parinello-Rahman barostat were utilized with coupling constants of 1 and 12 ps, respectively. Electrostatic interactions were computed using the PPPM method, and cutoff radii of 1.2 nm were employed for long-range and van der Waals interactions, consistent with the original Martini specifications (MARRINK et al., 2007). The 16 combinations of temperature

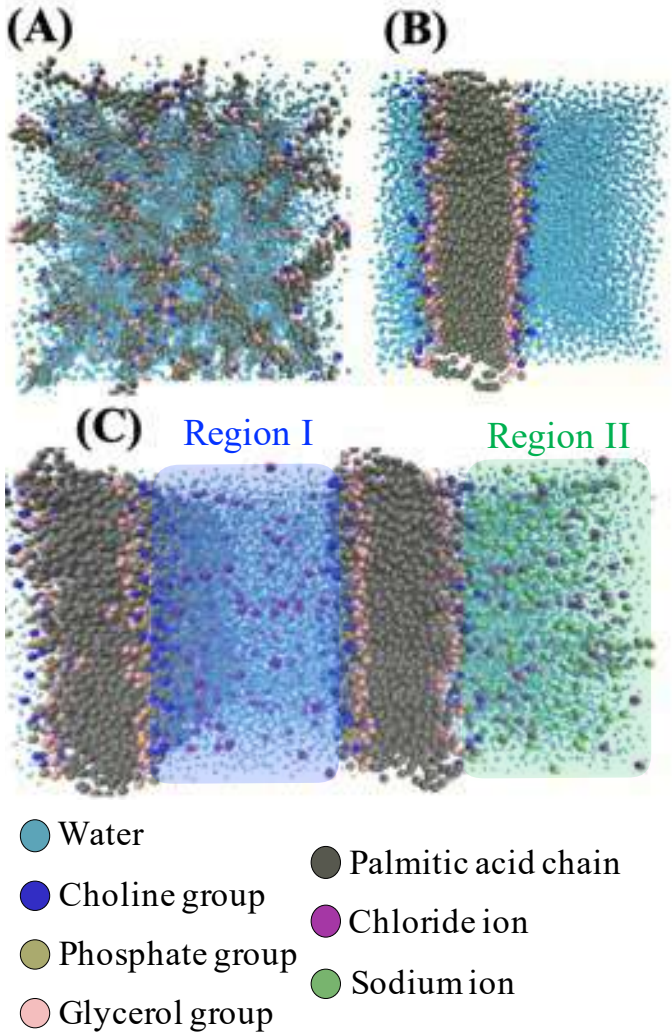

FIGURE 4.1. Molecular representation of (A) the initial randomized system, (B) the formed bilayer and (C) the system created to study the electroporation phenomenon.

and pressure were analyzed, and lipid bilayers spontaneously formed under all conditions, as depicted in Figure 4.1.B. The organized structures obtained after the initial equilibration were under stress due to the isotropic coupling scheme. Therefore, independent pressure coupling along the plane of the bilayer and its perpendicular direction (semi-isotropic scheme) was applied in the subsequent simulations.

As the bilayers were spontaneously formed, a slightly different number of DPPC molecules could be observed in each leaflet. To assure that the same number of lipids are present in each side, after 100 ns they were redistributed using a Matlab code to place (as 512 phospholipids were considered, this procedure resulted in 256 molecules in each side). Thereafter, at least 5 μs runs were performed in each $T - P$ combina-

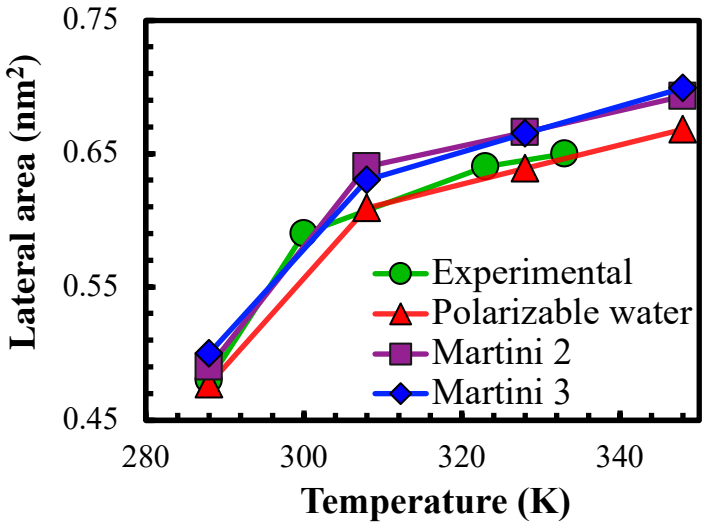

FIGURE 4.2. Influence of the water model (Martini 2, Martini 3, and polarizable water) on the lateral area of a DPPC lipid bilayer.

tion; since longer time scales are required to bring the system to equilibrium at lower temperatures and higher pressures, 20 μs were used in such cases (WANG et al., 2016). The absence of changes in structural properties for at least 2 μs was considered as a convergence criterion and as an indication of the absence of metastable states.

4.2.2 Bilayer analysis

To validate the behavior of the simulated bilayers, the structures were characterized by their lateral area, thickness, lateral diffusion coefficient, deuterium order parameter, specific mass profile, and pressure distribution profile. The lateral area of the lipid bilayer is a parameter which indicates the lipid packing density. It can be determined experimentally through techniques like X-ray scattering and neutron diffraction. In MD simulations, the lateral area is obtained using Equation 4.1:

$$A(T,P) = \frac{L_x L_y}{N_{DPPC}/2} \tag{4.1}$$

where A is the lateral area, L_x and L_y are the equilibrated simulation box dimensions in the x and y directions, respectively, and N_{DPPC} is the total number of DPPC molecules. The factor of two accounts for the equal number of molecules at both leaflets of the bilayer. The lateral diffusion coefficient was determined from the Mean Square Displacement (MSD) of DPPC molecules according to the Einstein's relation. While this

method is limited to homogeneous media, numerous studies have reported good results when applied to lipid membranes (GUO et al., 2017; AGHAZADEH et al., 2020; HADRIOUI et al., 2020)

Density profiles provide valuable insights into the interaction, distribution and concentration of the components. Additionally, these profiles can be compared with experimental data obtained by different techniques (e.g., Nagle e Tristram-Nagle (2000), Kučerka et al. (2011) and Moradi et al. (2019)). In this study, density profiles were obtained by discretizing the simulation box into 200 equally sized slices oriented to the normal of the bilayer plane. The density was computed in each section based on the spatial distribution of each component of interest. Additionally, the thickness of the membrane was determined by the distance between the phosphate groups density peaks, as shown in Figure 4.3.

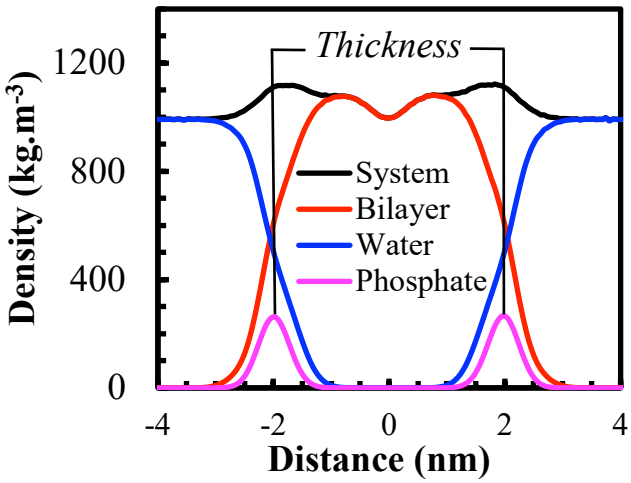

FIGURE 4.3. Density profiles and its relation with the bilayer thickness.

The aforementioned discretization procedure was also used to analyze the pressure profile, which represents the stress distribution along the lipid bilayer. Biological membranes emerge due to the interplay of several forces, including repulsive lipid-lipid and cohesive hydrophobic interactions (MARSH, 2013). Thus, the stress tensor is distributed non-uniformly along the membrane. The pressure profile (τ) is calculated by the difference between the normal and lateral components of the stress tensor, as shown in Equations 4.2 to 4.4:

$$\tau(T, P) = \tau_L - \tau_N \tag{4.2}$$

$$\tau_L = \frac{1}{2}(\tau_{xx} + \tau_{yy}) \tag{4.3}$$

$$\tau_N = \tau_{zz} \tag{4.4}$$

Phase transitions in the system can be analyzed using metrics like radial distribution functions or order parameters, the latter being more commonly applied in membranes. The deuterium order parameter (S_{cd}) of lipids indicates the orientation of the acyl acid chain to the normal plane of the bilayer. In the liquid phase, lipids undergo a range of random movements, including rotations around chemical bonds and gauche conformations (time magnitude of ps), axial diffusion and oscillations (ns) and lateral diffusion (μs) (VERMEER et al., 2007). The majority of these movements primarily impact the lateral carbon chains, and therefore, this parameter has been computed specifically for these groups. The calculation of S_{cd} is performed by Eq 4.5:

$$S_{cd}(T, P) = \frac{1}{2}\langle 3\cos^2\theta_{order} - 1\rangle \tag{4.5}$$

The parameter θ_{order} is the angle between the direction in which the molecules are aligned (given by the solution of the tensor order parameter) and the distance vector of acyl group particles. As this study employed a coarse-grained approach, it was assumed that the molecules where aligned according to the normal plane of the bilayer (z axis). The value of S_{cd} varies between 1 (indicating perfect ordering relative to the normal) and -1/2 (indicating perfect ordering relative to the perpendicular direction).

4.2.3 Electroporation simulations

After the preparation and equilibration of the systems, electroporation simulations were conducted for all combinations of pressure and temperature discussed in Section 4.2.1. The equilibrated systems were duplicated along the z-axis, resulting in supercells featuring two bilayers separated by solvent zones (labeled as regions I and II), as shown in Figure 4.1.C. This approach can be considered as an approximation of the the internal and external environment of a cell, as depicted in Figure 4.4. Electroporation can be induced to the system in two ways: (i) by applying a generic electric field, similar to that described by Equation 3.1, or (ii) by inducing an ionic imbalance in

the bilayer. In the present study, the second approach was chosen due to its closer resemblance to the phenomenon occurring in real cells (LIN; ALEXANDER-KATZ, 2016; IKEDA et al., 2021).

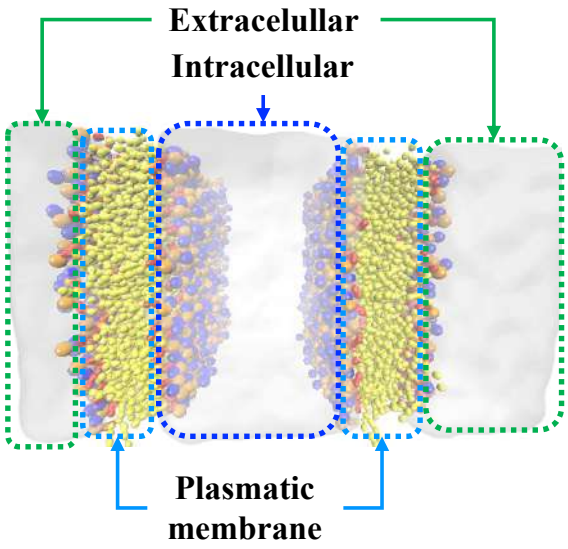

FIGURE 4.4. Simulation box containing two lipid bilayers in water.

In this setup, 178 sodium ions were distributed in both aqueous regions, while 356 chloride ions were placed only in region II, resulting in an ionic concentration of 0.15 M (ZHOU; LIU, 2019). Although the system was electrically neutral, the ionic imbalance causes a transmembrane potential, spontaneously generating an electric field across the simulation box. The resulting initial field had an average magnitude of 25 V/nm, although some variations were observed depending on the applied temperature and pressure. Due to the applied model (featuring two bilayers) and the use of periodic boundary conditions, two independent analyzes were performed in each run (one for each bilayer), and the results are averaged out. An initial 10 ns run was conducted to bring the system to equilibrium under ionized conditions, taking into account just short-range electrostatic interactions, therefore not allowing the formation of pores. After, long-range interactions were introduced, and the electroporation simulations were carried out for at least 100 ns. In the cases where the pore did not close, additional 10 μs runs were performed to check whether the pore was stable for longer time periods. The simulations were performed at least in triplicate, and the computed metrics (described below) were averaged out throughout the trajectory, as suggested

before (KNAPP et al., 2018).

The double bilayer approach is based on a phenomenon that occurs in the cell after the application of an external electric field (E_{ext}). At equilibrium, there is no ion concentration gradient, but after the application of an E_{ext}, the ions become unevenly distributed and attracted towards their opposite electric charge. This ultimately leads to a local electric field caused by ionic imbalance (namely E_{ion}), which would persist until a new equilibrium state is reached (regardless whether E_{ext} is removed or not). Atomic force microscopy measurements showed that E_{ion} is much higher than E_{ext}, therefore the influence of the external potential can be neglected after the ionic imbalance is established (BI et al., 2018). Moreover, some authors (ZHOU; LIU, 2019; KIRSCH; BÖCKMANN, 2019) pointed out that this approach is more consistent with the behavior of cell electroporation and emulates real physiological conditions more closely than the direct application of an external field E_{ext}.

4.2.4 Electroporation analysis

The electroporation simulations were analyzed by measuring kinetic, electrostatic, and mass transfer aspects. Teissie et al. (2005) identified the presence of five stages during the pore formation:

1. induction of the transmembrane potential;
2. pore formation and enlargement;
3. stabilization at maximum radius;
4. pore resealing;
5. memory effects (structural alterations occurring hours after closure).

Stages 1 and 5 were not captured in the simulations. The first stage was not observed because the applied approach assumes that the ionic imbalance was already established in the medium. The fifth stage is not visualized due to temporal restrictions in MD simulations. To analyze the electroporation kinetics, the time of pore formation,

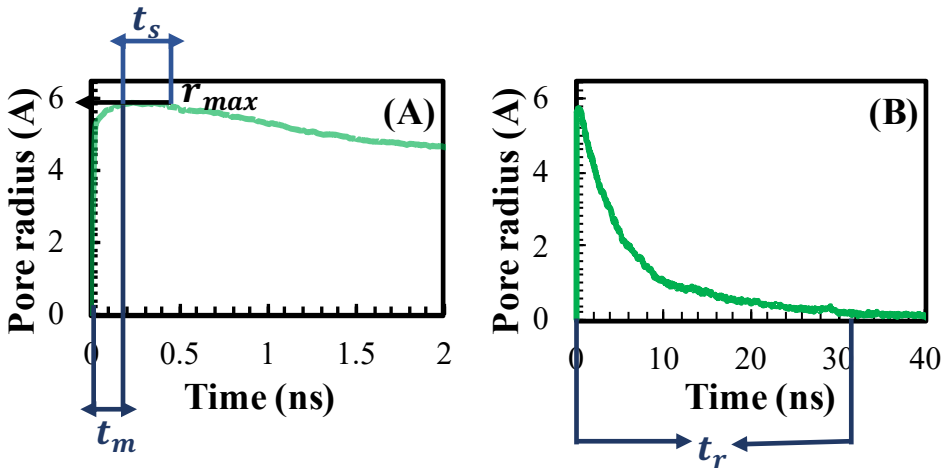

FIGURE 4.5. Graphical representation of the pore radius as a function of time for the analysis of (A) r_{MAX}, t_m, and t_s, and (B) t_r.

stabilization, and closure, as well as the maximum radius achieved (r_{MAX}), were analyzed. The formation time (t_m) was defined as the time required for the defect to reach r_{MAX}. This was evaluated by analyzing the time derivatives of the pore size (dr/dt): when the pore was forming, the derivatives were positive (> 0). The stabilization time (t_s) was considered as the period where the pore remained stable at r_{MAX} ($dr/dt \approx 0$). The resealing time (t_r) was defined as the time required for the pore size to reach a constant value after initiating the resealing process. During the resealing phase, the time derivatives had negative values (< 0), but when the reseal was completed, $dr/dt \approx 0$. At the end of the simulations, the membranes have either a pore size $= 0$ (complete recovery) or $\neq 0$ (incomplete recovery). An illustration of the analyzed variables in the pore radius x time plot is shown in Figure 4.5.

Ionic migration was evaluated using 3 metrics: the number of chlorine and sodium ions in Region I (see Figure 4.1.C), and the time required for the concentration gradient to decrease and cease the ion flow. To analyze these variables, post-processing of the trajectories was performed using a Matlab 2012b code. Kinetic and ionic flow analyses were subjected to ANOVA and Tukey tests ($p < 0{,}05$) to verify if the obtained parameters were dependent on temperature and pressure.

The electrostatic aspects were evaluated by solving the Gauss equation of electromagnetism (Eq. 4.6), yielding electric field profiles at various time intervals:

$$\vec{\nabla} \cdot \vec{E} = \frac{\rho}{\epsilon_0} \tag{4.6}$$

where ρ represents the charge density and ϵ_0 is the permittivity of vacuum. Since an analytical solution for Eq. 4.6 is unavailable, the system was discretized into 200 compartments along the z direction. The total charges were then integrated within each compartment to obtain ρ. One-dimensional profiles were generated for times $t = 0{,}00; 0{,}05; 0{,}10; 0{,}25; 0{,}50; 1{,}00; 5{,}00; 10{,}00$ ns using the function *gmx potential* of Gromacs. Two-dimensional profiles were calculated by partitioning the box into 200 segments in the z direction and in 100 segments in the y direction. The charge density of each element was calculated using the *PMEPot* tool of the VMD software, and its integration was carried out using a custom Matlab code.

4.2.5 Comparison with all-atom simulations

All-atom (AA) simulations were conducted on a bilayer comprising 128 DPPC molecules, employing the same hydration and ion concentration as in the original system (82 water molecules/lipid and 0.15 M, respectively). These simulations aimed to validate the observed behavior at the coarse-grained (CG) scale. The Slipids force field, which has previously demonstrated accurate descriptions of membrane properties, was employed (GROTE; LYUBARTSEV, 2020). The AA simulations were conducted at 348 K due to the faster pore resealing at higher temperatures. Coarse-grained simulations for this reduced system were also conducted, and the results were compared. All four pressures were examined.

4.3 Results and Discussion

4.3.1 DPPC bilayer characterization

Figure 4.6 shows the lateral area per lipid, membrane thickness, order parameter and lateral diffusion coefficient of the formed bilayers as a function of temperature for each applied pressure. The membranes are found in different phases according to T and P, which are characterized according to the similarity of their properties; these are distinguished in Figure 4.6 using symbols with different colors. At low temperatures, the gel II $L_{\beta'}$ phase is observed, characterized by low lateral area, large thickness and

high order parameter. The main transition occurs as temperature increases, and the bilayer becomes less ordered and thinner (liquid crystalline (L_α) phase). At 5000 atm, all simulations showed a similar behavior, which is different from the aforementioned phases, indicating the existence of a particular state at this pressure. The rippled gel phase ($P_{\beta'}$) is not visualized using the Martini CG force field, as shown before (WANG et al., 2016). However, the temperature range in which this phase occurs is quite narrow (MACDONALD, 1984; WONG et al., 1988; DRISCOLL et al., 1991; CZESLIK et al., 1998) and, therefore, a good description of the thermodynamic behavior of the DPPC bilayer is reproduced despite of this limitation.

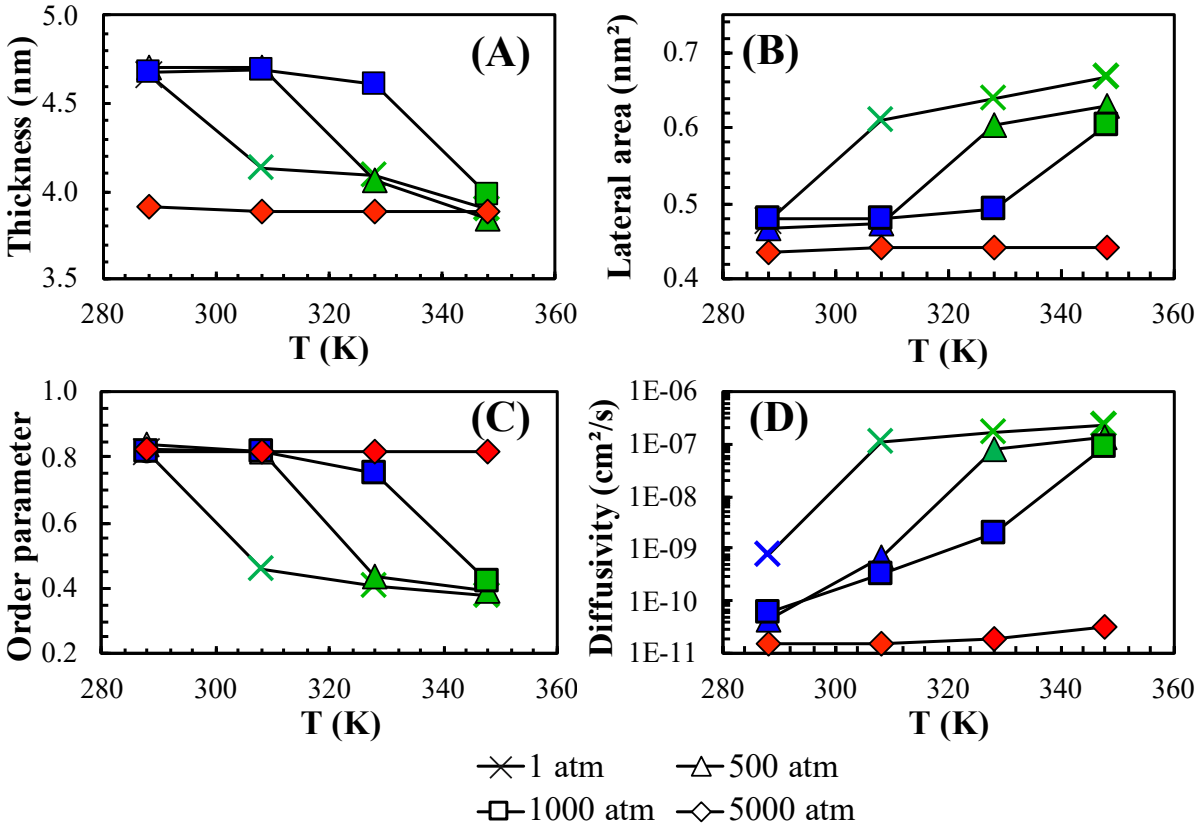

FIGURE 4.6. (A) Thickness, (B) lateral area, (C) deuterium order parameter, and (D) lateral diffusion coefficient of the DPPC bilayer as a function of temperature for each applied pressure. For clarity, the symbols were colored according to the proposed corresponding phase, where blue represents the $L_{\beta'}$, green the L_α and red the high pressure (HP) phases.

Particular attention can be given to the deuterium order parameter (Figure 4.6.C), which is the best metric to characterize the different phases. Since the liquid

crystalline and the Gel II states are characterized by a low and a high degree of order, respectively, the $L_{\beta'}$ and L_{α} phases are visualized in the upper ($\approx 0{,}8$) and lower ($\approx 0{,}4$) parts of the plot. At 5000 atm, the order parameters are practically constant ($\approx 0{,}82$) and similar to those observed for the $L_{\beta'}$ phase, indicating that the structures are organized in a high-pressure gel phase. Complete S_{cd} profiles are provided in Figure A.1 of the Appendix A.

At 1 atm, the main transition occurs at 314 K. According to Lai et al. (2012), the relationship between the transition temperature T_m with pressure can be calculated using Eq. 4.7:

$$\frac{dT_m}{dP} = \left(\frac{\partial T}{\partial P}\right)_A = -\frac{\left(\frac{\partial A}{\partial P}\right)_T}{\left(\frac{\partial A}{\partial T}\right)_P} = 0{,}022 K atm^{-1} \tag{4.7}$$

where A is the lipid area. This equation predicts phase transitions at 325 K, 336 K, and 424 K for 500 atm, 1000 atm, and 5000 atm, respectively. These estimations are in good agreement with the aforementioned S_{cd} characterization, which suggests that the transitions occurred between 298 K and 308 K at 1 atm, between 308 K and 328 K at 500 atm, and between 328 K and 348 K at 1000 atm. The transition temperature at 5000 atm is outside the limits of the simulations, corroborating that the structure is in a HP gel phase, as suggested in previous studies (MACDONALD, 1984; WONG et al., 1988; DRISCOLL et al., 1991; CZESLIK et al., 1998).

Nagle e Tristram-Nagle (2000) compiled data from several high resolution techniques (e.g., X-ray and neutron diffraction) to provide the best estimates for structural parameters of DPPC bilayers. According to these authors, bilayer thicknesses of 3.83 and 4.42 nm are expected for the L_{α} and $L_{\beta'}$ phases, respectively. The simulations slightly overestimate these experimental values by 0.1 to 6 %, as seen in Figure 4.6.A, which is adequate considering similar studies (WANG et al., 2016; CHEN et al., 2011; LAI et al., 2012). In the gel state, the palmitic acid chains are mainly stretched, while in the L_{α} phase they are disordered and tangled, resulting in a decreased length. At 5000 atm, a thickness of 3.9 nm is observed, which is expected since higher pressures tend to increase the degree of interdigitation of the membrane. The length of the acyl chains is smaller in HP phases in comparison to the $L_{\beta'}$ phase (CHEN et al., 2011), which is also consistent with the present simulations.

Results for the bilayer area per lipid are presented in Figure 4.6.B. Experimental

values of 47.9 Å^2 (at 288 K) and 64.0 Å^2 (at 323 K) at ambient pressure were reported in Nagle e Tristram-Nagle (2000). In addition, an area of 64.8 Å^2 was measured at 333 K using small-angle neutron scattering (BALGAVÝ et al., 2001). These results are in good agreement with the simulations – 47.7 Å^2 at 288 K, 63.9 Å^2 at 328 K and 66.8 Å^2 at 348 K. The lateral area within the $L_{\beta'}$ phase is pressure and temperature independent ($\approx$ 47 Å^2). In contrast, this property increases with temperature and decreases with pressure when the bilayer is in liquid crystalline state, as already reported in previous studies (KUČERKA et al., 2011; WANG et al., 2016). After the main transition, the DPPC bilayers decrease in thickness while increasing in lateral area, as a consequence of the volume incompressibility of these structures (KIRSCH; BÖCKMANN, 2019). At 5000 atm, a lateral area of 44.0 Å^2 was found for all temperatures, which is similar to the values in the $L_{\beta'}$ phase.

The calculation of the lateral diffusion coefficient was performed to verify if the correct mass transfer behavior is reproduced. Overall, this coefficient is expected to increase with temperature and decrease with pressure; this trend was properly reproduced in the simulations as shown in Figure 4.6.D. The main transition is followed by a significant increase in the diffusion rate, which has already been reported before (HARB et al., 2013; LEE et al., 1995). This behavior is expected since liquids have higher molecular mobility compared to gels or solids. Moreover, the results at ambient pressure agree well with the experimental curve obtained by Harb et al. (2013) using the fluorescence after photobleaching technique. In addition, a value of $2{,}0 \times 10^{-7}$ cm^2 s^{-1} has been reported at 330 K (KARAKATSANIS; BAYERL, 1996), which is similar to that obtained in the simulations at 328 K ($1{,}78 \times 10^{-7}$ cm^2 s^{-1}).

The density and pressure profiles along the normal direction of the DPPC bilayer are depicted in Figure 4.7. The symmetry with respect to the center of the structure indicates an even distribution of lipids across both sides. Similar density profiles were obtained at 288 K for 1, 500 and 1000 atm, which correspond to the pattern of the Gel II phase, as shown by Kučerka et al. (2011) using X-ray scattering data. Peaks in the profiles are primarily attributed to the concentration of phosphatidylcholine heads and glycerol groups. Complete density profiles for each group under all temperature-pressure combinations are presented in Figure 4.8. The decrease in density towards the center is attributed to the soft repulsive forces of two palmitic acid side chains oriented

in the same plane but in opposite directions. Notably, at 5000 atm, the profile displays higher density due to bilayer compression and interdigitation under this condition. This behavior was observed at all temperatures, aligning with earlier discussions regarding the existence of a distinctive phase at this pressure. In addition, the profile is qualitatively similar to the one obtained by MD simulations to analyze the effects of high surface tension (58 mN.m^{-1}) in DPPC bilayers (LAI et al., 2012). At 308 K, the bilayers equilibrated at 500 and 1000 atm showed similar density profiles (as also seen at 288 K); at 1 atm, a decrease in density and a smoother distribution was observed, which is related to the phase change under these conditions. At 328 K and 1000 atm, the density remained high, although the concentration peaks were less-defined. At 348 K, a similar behavior was found at 1, 500, and 1000 atm, suggesting that all bilayers are in the L_α phase. The liquid crystalline density distribution obtained using all-atom simulations in Notman et al. (2007) is qualitatively and quantitatively similar to the one observed in the present work.

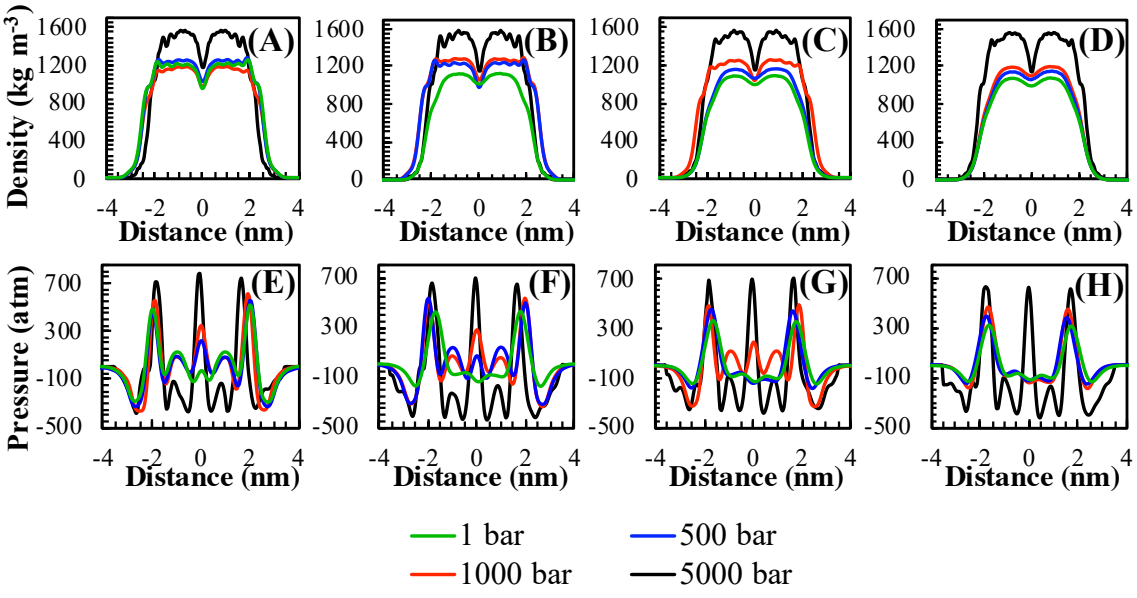

FIGURE 4.7. DPPC density profiles along the main axis at (A) 288 K, (B) 308 K, (C) 328 K and (D) 348 K. Pressure profiles at (E) 288 K, (F) 308 K, (G) 328 K and (H) 348 K.

The pressure profiles are also showed in Figure 4.7. All curves tend to zero at the edges of the simulation box, indicating that the system is fully hydrated (PATRA, 2005). Similar qualitative behavior was observed in all simulations, i.e., the existence of negative and positive peaks located in equivalent regions of each bilayer. The first

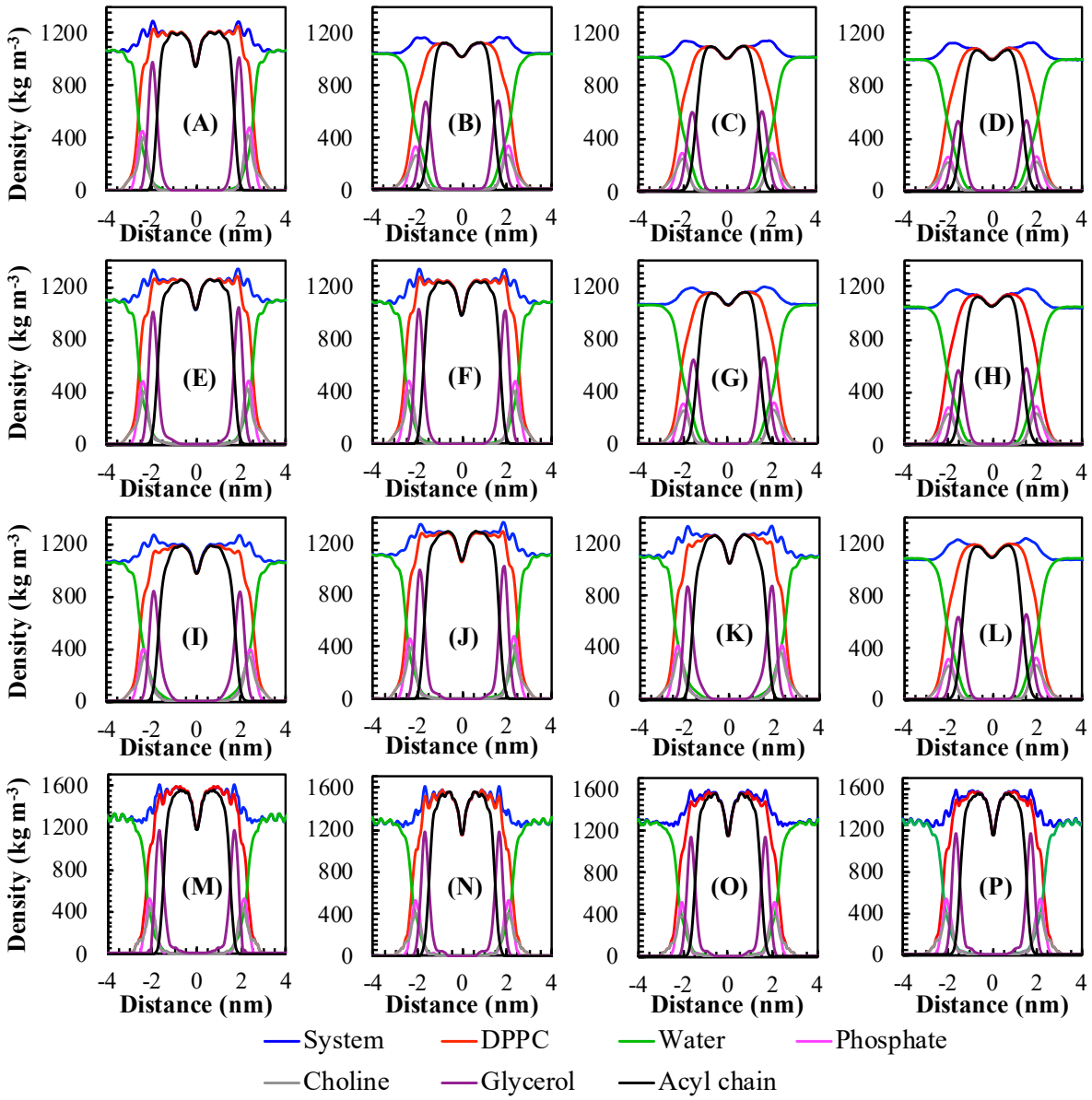

FIGURE 4.8. Complete density profiles at (A) 288 K/1 atm, (B) 308 K/1 atm, (C) 328 K/1 atm, (D) 348 K/1 atm, (E) 288 K/500 atm, (F) 308 K/500 atm, (G) 328 K/500 atm, (H) 348 K/500 atm,(I) 288 K/1000 atm, (J) 308 K/1000 atm, (K) 328 K/1000 atm, (L) 348 K/1000 atm, (M) 288 K/5000 atm, (N) 308 K/5000 atm, (O) 328 K/5000 atm, (P) 348 K/5000 atm

negative peak is related to the hydrophilic core of the membrane, and its value indicates that these groups are contracting the system. The first positive peak corresponds to the glycerol groups, and the peaks in the center of the bilayer are due to the side-chains. These positive peaks indicate that the glycerol and carbon chains are expanding the system, in agreement with other results (LINDAHL; EDHOLM, 2000). As liquids present a higher compressibility compared to gels, a significant smoothing in the pres-

sure profile can be observed after the main transition (CHEN et al., 2011). The profiles at 5000 atm are qualitatively similar, although both positive and negative peaks are higher, indicating that the compression/expansion forces are stronger in this situation. The obtained profiles are in good agreement with previous studies (PENG et al., 1995; HARB et al., 2013; LINDAHL; EDHOLM, 2000; PATRA, 2005; CHEN et al., 2011).

4.3.2 Electroporation simulations

Once the simulated systems properly described the structure and properties of real lipid bilayers, they were used to perform the electroporation analysis as described in Sec. 4.2.3. The results are presented below in three subsections, addressing the pore formation kinetics, the transport of ions through the bilayer and electrostatic aspects.

4.3.2.1 Pore formation kinetics

Figure 4.9 shows the computed pore radius as a function of time under different conditions (the time range is different in each plot due to the faster pore recovery at higher temperatures). Although electroporation is generally considered a non-thermal phenomenon (FESMIRE et al., 2020), a dependence of this process on temperature and pressure has been reported in previous researches (PYATKOVSKYY et al., 2018; FESMIRE et al., 2020; LEBAR et al., 2021; MURALIDHARAN et al., 2021), indicating that the kinetics is indeed affected by T and P. An illustration of the dynamics of pore formation is shown in Figure 4.10. At the beginning of the process, pores were formed and the thickness of the membrane decreased (Fig. 4.10.B). During this phase, several minor defects were observed in the bilayer, which eventually coalesced into larger channels, allowing the migration of solvent and ions. Thereafter, the pore radius remained constant at a maximum value (r_{MAX}) for a few picoseconds, indicating a stabilization phase (Fig. 4.10.C).

After a significant decrease in the gradient of ion concentration, the pores started to close, leading to the healing of the bilayer structure (Fig. 4.10.D). The healing of the membranes can led to two different situations: the stabilization - reaching a permanent characteristic pore size (Fig. 4.10.E) - or the complete restoration of the membrane

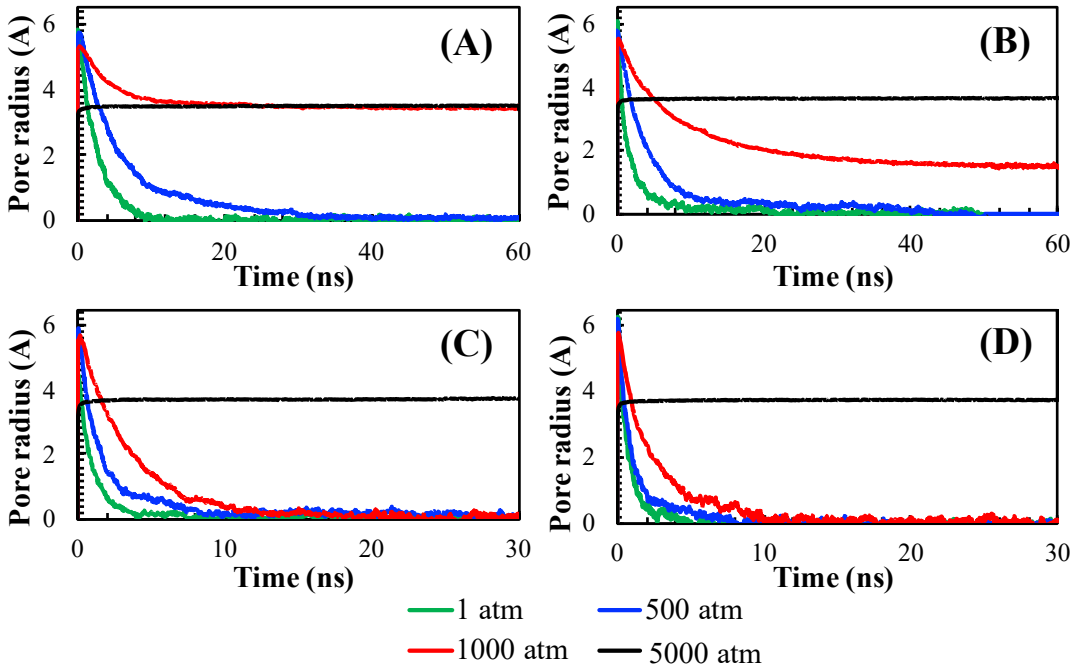

FIGURE 4.9. Time evolution of pore radius at (A) 288 K, (B) 308 K, (C) 328 K and (D) 348 K.

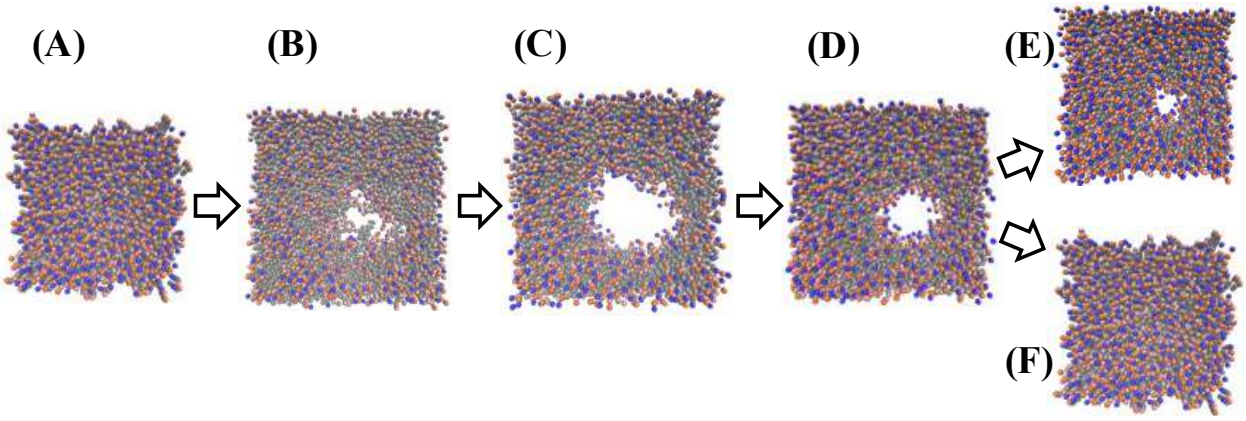

FIGURE 4.10. Snapshots depicting the transformations observed in the system: (A) Initial lipid bilayer, (B) pore formation, (C) pore stabilization, (D) pore resealing, (E) stabilization of a pore with a characteristic radius and (F) complete pore recovery.

structure (Fig. 4.10.F). These behaviors indicate a tendency towards irreversible or reversible electroporation. As can be seen in Figure 4.9, a propensity to irreversibility occurs at high pressures (1000 and 5000 atm), with a residual pore persisting until the end of the simulations. This may be an interesting feature to be explored, for example, in the food industry, where technologies using low electric fields (e.g., ohmic heating) generally result in reversible electroporation. According to the present results, the pro-

cess can become irreversible at high pressures, which can improve the inactivation rate of microorganisms in such systems. Indeed, a synergistic effect of pulsed electric field (PEF) application and high hydrostatic pressure (HHP) was observed in a study on microbial inactivation (PYATKOVSKYY et al., 2018), suggesting that higher pressures may indeed enhance irreversible electroporation.

The kinetic behavior described has been quantitatively and qualitatively reported in other experimental and simulation studies (TEISSIE et al., 2005; KRASSOWSKA; FILEV, 2007). According to the mechanism proposed by Teissie et al. (2005), two stages were not observed in the simulations: the induction step (i.e., the establishment of the transmembrane potential) and the memory effects (changes on the bilayer structure after hours before the resealing stage). The induction step was not visualized because the simulation setup for the analyzed system assumed that the ionic imbalance had already occurred prior to the simulation start, while the memory effects were not observed due to the limited simulation time scale. Table 4.1 shows some characteristic parameters of the pore kinetics, and the results of the statistical analysis. The plots of these variables as a function of temperature and pressure can be found in Figure 4.11. It can be emphasized that the mass diffusion rates predicted by the Martini model are generally faster compared to all-atom data due to the smoothed free energy landscape typical of mesoscale models (YESYLEVSKYY et al., 2010; STACHURA; KNELLER, 2013; ALESSANDRI et al., 2019). To obtain values consistent with those obtained in AA MD simulations for lipid membranes, the characteristic times presented in Table 4.1 should be corrected using a factor of 4, as suggested on the Martini website and validated in Section 4.3.3.

The maximum pore radius r_{max} is temperature dependent, especially in the gel phases (larger pores are found at higher temperatures). After the main transition, a temperature independent radius is observed. This behavior suggests that smaller defects are created in the gel phases, gradually increasing until the phase transition, at which point a stable maximum value is reached. The radius is also pressure dependent, with lower pressures leading to larger pores (radii of 6.04, 5.85 and 5.76 Å were observed in the L_α phase at 1, 500 and 1000 atm, respectively). At 5000 atm, a r_{max} of about 3.60 Å was observed, with a slight dependence on temperature. Stiffer membranes can inhibit pore formation by electroporation, as reported by Sun et al. (2011),

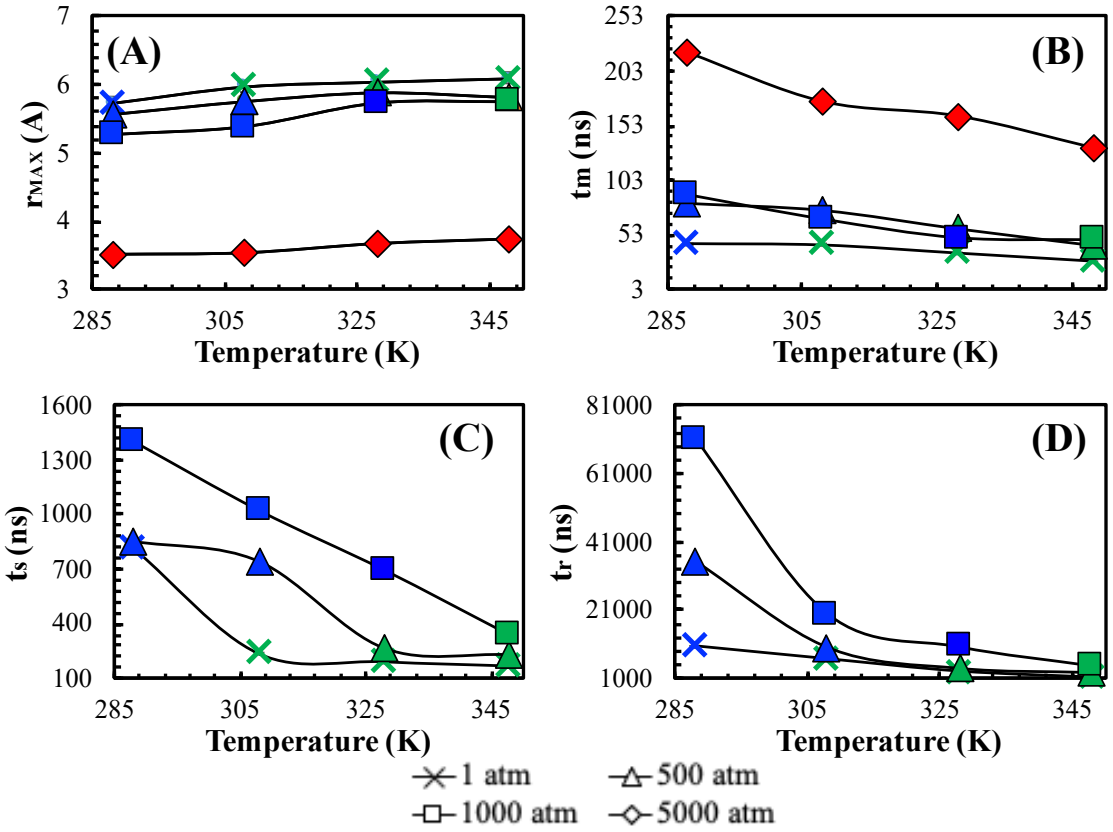

FIGURE 4.11. Kinetic parameters of pore formation and resealing (A) r_{MAX}, (B) t_m, (C) t_s, and (D) t_r as function of temperature for each applied pressure.

which agrees with the simulations once that the gel phases (characterized by a high ordering of acyl groups) presented smaller pore radii. Furthermore, the value of 5.72 Å at 1 atm/288 K is comparable to the results of Griese et al. (2002), who reported a radius of 5.6 Å using electro-optic and conductometric relaxation spectrometry at 293 K (deviation of 2.1 %), and to the results of Böckmann et al. (2008), who reported a radius of 5 Å using all-atom MD simulations.

In some cases, several smaller defects were formed instead of one large pore, which did not merge into each other because of a typically large distance between them. The results presented in Figure 4.9 and Table 4.1 consider a single effective radius containing all observed defects. This was performed by summing the area of all N defects (N_p), with subsequent application of the relation $\sum_1^{N_p} A_{pore} = \pi r^2$. Krassowska e Filev (2007) used a single-cell model at 1 atm/310 K to show that multiple pores with a wide radius distribution spectrum were formed under this condition. Only a few pores (2.2 %) were considered large (radius $>$ 1 Å), although they accounted for over

TABLE 4.1. Characteristic parameters of pore formation kinetics for varied T and P conditions.[1]

Condition	**Phase**	r_{MAX} **(Å)**	t_m **(ps)**	t_s **(ps)**	t_r **(ns)**
288 K/1 atm	$L_{\beta'}$	5.74±0.08^{d}	45.8±2.6^{g,h}	821.3±4.5^{c,d}	10.3±1.1^{d}
308 K/1 atm	L_{α}	5.98±0.08^{a,b}	44.6±4.0^{g,h}	241.7±14.0^{g}	6.7±2.4^{e}
328 K/1 atm	L_{α}	6.05±0.08^{a}	37.1±1.4^{h}	197.5±5.7^{h}	3.2±0.2^{g,h}
348 K/1 atm	L_{α}	6.10±0.09^{a}	29.6±1.9^{i}	173.8±13.0^{h}	1.5±0.2^{i}
288 K/500 atm	$L_{\beta'}$	5.56±0.12^{e}	82.1±2.9^{d,e}	854.6±18.8^{c}	35.3±2.8^{b}
308 K/500 atm	$L_{\beta'}$	5.75±0.09^{d,e}	75.7±8.0^{d,e,f}	745.0±66.3^{d,e}	10.1±5.2^{d}
328 K/500 atm	L_{α}	5.88±0.10^{b,c}	59.2±6.2^{g}	264.2±20.1^{g}	4.0±0.5^{f,g}
348 K/500 atm	L_{α}	5.81±0.06^{c,d}	44.2±2.6^{g,h,i}	227.1±23.2^{g,h}	2.8±0.2^{h}
288 K/1000 atm	$L_{\beta'}$	5.26±0.04^{f}	90.8±6.3^{d}	1398.8±171.8^{a}	71.4±3.6^{a}
308 K/1000 atm	$L_{\beta'}$	5.38±0.08^{f}	67.9±6.3^{e,f}	1021.7±58.3^{b}	20.0±2.1^{c}
328 K/1000 atm	$L_{\beta'}$	5.74±0.02^{d}	50.3±1.8^{g,h}	696.4±24.6^{e}	10.3±0.8^{d}
348 K/1000 atm	L_{α}	5.76±0.05^{c,d}	48.5±0.9^{g,h}	341.3±5.7^{f}	4.7±0.6^{e,f}
288 K/5000 atm	HP	3.53±0.07^{i}	220.0±21.0^{a}	NA	NA
308 K/5000 atm	HP	3.55±0.04^{h,i}	175.0±18.9^{b}	NA	NA
328 K/5000 atm	HP	3.67±0.12^{g,h}	161.7±9.7^{b}	NA	NA
348 K/5000 atm	HP	3.73±0.03^{g}	127.9±13.8^{c}	NA	NA

[1] r_{MAX} is the maximum pore radius, t_m is the time to reach the maximum radius, t_s is the time of stabilization at $r = r_{MAX}$ and t_r is the resealing time. Results with the same superscript are not significantly different from each other ($p > 0{,}05$). NA = Non Applicable.

95.3 % of the total pore area; the maximum individual pore radius observed by the authors was 4.1 Å. This behavior agrees with the simulated structures at 308 K/1 atm, which featured pores with radii ranging from 1.0 to 3.5 Å.

A significant decrease in the time required to reach the maximum radius (t_m) was found at 1 atm and 348 K. A qualitatively similar behavior was observed in all-atom simulations (SUN et al., 2011), suggesting that the increased thermal agitation of lipids at higher temperatures has catalyzed the formation of defects in the membrane (i.e., the higher the temperature, the faster the pore formation). These authors found that the formation time at 283, 298 and 310 K was approximately 40 ps, which agrees well with the average results obtained within this temperature range (42.5 ps). It was also observed that t_m decreased to 15 ps at 347 K, which differs from the present value of 29.6 ps at 348 K, although the qualitative behavior was similar (decrease in t_m at temperatures near 350 K). At 500 atm, statistically equivalent values were observed within the $L_{\beta'}$ phase, but a significant decrease in t_m was observed after the main transition; in the L_{α} phase, the results were temperature independent. At 1000 atm, the results were statistically equivalent only at 328 and 348 K. At 5000 atm, a decrease with temperature

was also observed, and t_m was considerably higher in this condition compared to the $L_{\beta'}$ and L_α phases. Lebar et al. (2021) stated that pores are more easily formed in disordered bilayers, which agrees with the present simulations where liquid crystalline bilayers had lower values of t_m at all pressures analyzed.

Regarding the stabilization time (t_s), the simulations showed that this variable strongly depends on the bilayer phase: while the pore remained at its maximum value for longer periods in the gel state, a significant decrease was observed after the main transition temperature T_m. In the L_α phase, t_s decreases less with temperature (as indicated by the statistically equivalent values at 308, 328 and 348 K and 1 atm and at 328 and 348 K at 500 atm), in comparison with the significant reductions observed within the $L_{\beta'}$ phase. Furthermore, it was not possible to calculate t_s at 5000 atm, as the pore maintained its maximum value throughout the simulation. This indicates that the time scale analyzed is lower than the one required for membrane resealing under such conditions, or that irreversibility is favored in high-pressure phases. Regarding the resealing time (t_r), it is observed that higher temperatures lead to faster healing of the porous structure. An opposite trend was observed when the pressure was increased. It should be noted that this variable could not be measured at 5000 atm as well, since the bilayers were not healed under these conditions. Moreover, at higher pressures and lower temperatures, the pores did not heal completely, but stabilized at a characteristic diameter. This was observed at 1000 atm/288 K ($r = 3.5$ Å) and 1000 atm/308 K ($r = 1.5$ Å).

Weaver e Chizmadzhev (1996) stated that planar lipid bilayers could be considered as metastable states since porous membranes have lower free energies. Therefore, several properties of these structures can be estimated using the Gibbs approach, which treats pore formation as a phase transition modeled as an exponential function of the reciprocal temperature ($property = C_1 \exp(C_2/T)$). The present results align well with this theory, as indicated by the plot of $1/t_m \times 1/T$ provided in the Appendix A. Additionally, plots for $1/t_s \times 1/T$ and $1/t_s \times 1/T$ are also provided in the same figure. These results underscore how various aspects of electroporation can be understood within the framework of classical kinetics of biomolecular reactions. Specifically, increases in temperature and decreases in pressure tend to shorten the time for pore formation, stabilization, and recovery. Several studies have used the Arrhenius law

to describe the electroporation kinetics dependence with temperature (SHAFIEE et al., 2009; GARCIA et al., 2011; AGNASS et al., 2020), which is consistent with the general trends of the present simulations.

According to Chiapperino et al. (2019), the time dependence of the pore radius can be calculated by Eq. 4.8:

$$\frac{dr}{dt} = \frac{D}{k_b T}\left(\frac{V_m^2 F_{max}}{1 + r_h/(r + r_t)} + 4\beta\left(\frac{r_*}{r}\right)^4 \frac{1}{r} + 2\pi\gamma + 2\pi\lambda effr\right) \tag{4.8}$$

where D is the diffusion coefficient for pore radius, T is the absolute temperature, k is the Boltzmann constant, V_m is the transmembrane potential, F_{max} is the maximum electric force per voltage squared, r_h and r_t are constants of advection velocity, β is the steric repulsion energy, r_* is the minimum radius of pores, γ is the edge energy and σ_{eff} is the effective tension of the membrane, calculated by $\sigma_{eff} = 2\sigma' - (2\sigma' - \sigma_0)/(1 - A_p/A)^2$, where σ_0 is the tension of the membrane without pores, σ' is the energy per area of the membrane/solvent interface, A_p is the pore area and A is the cell surface area. In the equation, the first term accounts for the electric force, the second for the steric repulsion of the lipid heads, the third for the line tension acting on the pore perimeter and the fourth for the surface tension of the cell membrane. From the equation, it can be seen that pore formation is a complex process that depends on the electrical and mechanical properties of the bilayer. This is in good agreement with the simulations results where dependence on temperature and pressure was observed for a fixed potential difference (i.e., the first term of the equation is maintained almost constant, even though some variations in the resulting electric field were observed and discussed in Section 4.3.2.3). The pressure effects in the bilayer recovery are related to the increase in phospholipid molecules line and surface tension, while the temperature effects are categorized in the overall constant ($D/(kT)$) and in the strength of the steric repulsion of the lipid heads (which increase with temperature as showed by neutron scattering experiments (PABST et al., 2002)).

Since a coarse-grained model was used, the results discussed must be understood qualitatively (or semi-quantitatively) once the degrees of freedom of the atomistic details are omitted in this representation. However, several kinetic parameters agree with previous experimental and all-atom studies. The next section will discuss the effects of these kinetic characteristics on the ion migration, aiming to improve the knowledge of how pore formation affects these process

4.3.2.2 Ion migration

One of the most important applications of electroporation is enhancing mass transfer operations, such as the extraction of intracellular compounds or the introduction of molecules into cells. This section focuses on ion migration across the membrane, helping to explain the dependence of ion flux on the bilayer temperature and pressure. Figure 4.12 shows the time evolution of the number of Na^+ and Cl^- ions in the simulation box region that initially contained only Cl^- (i.e., region I as depicted in Fig. 4.1). Overall, it can be seen that indeed the number of Na^+ ions was 0 at $t = 0$, and increased to a maximum value in which it stabilized. The number of Cl^- ions was 178 at the beginning and then decreased; this behavior is expected due to the initial simulation setup, as described in Sec. 4.2.3. Simultaneous plots for Na^+ and Cl^- ions at various temperature-pressure combinations can be found in Figure A.3 of Appendix A. Table 4.2 shows some key parameters of ion migration computed from the aforementioned curves, along with their statistical analysis.

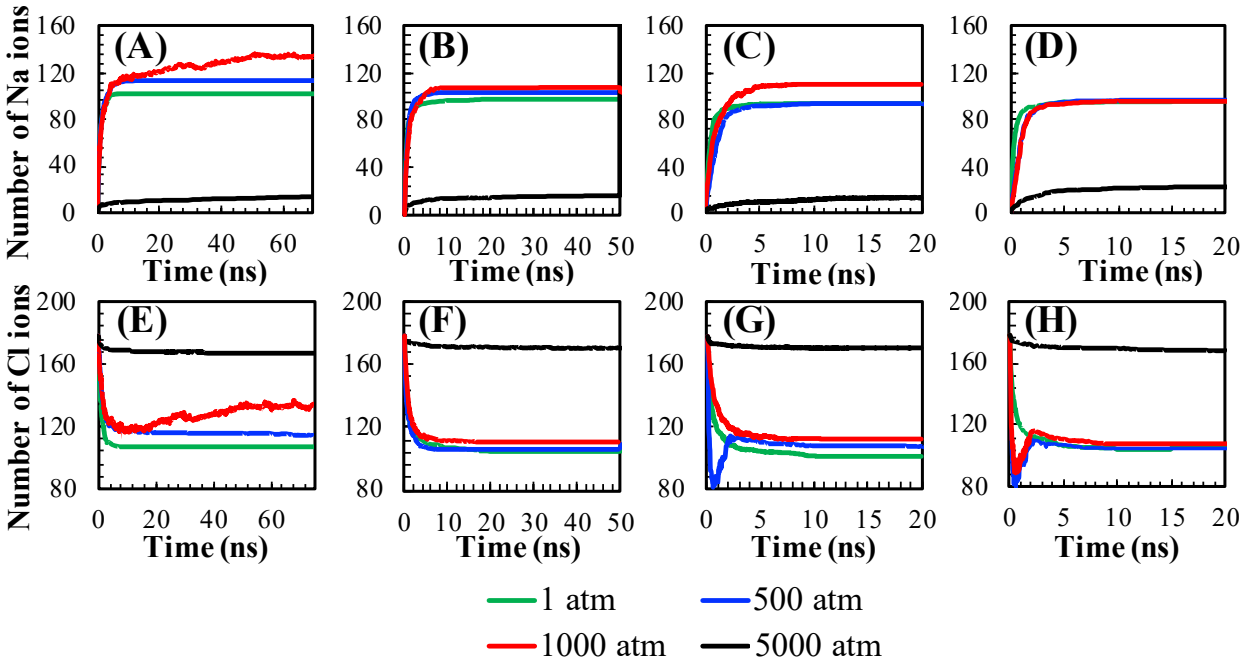

FIGURE 4.12. Number of sodium ions in the compartment I at (A) 288 K, (B) 308 K, (C) 328 K and (D) 348 K, and number of chloride ions in the compartment I at (E) 288 K, (F) 308 K, (G) 328 K and (H) 348 K.

Overall, higher migration rates of ions towards region I were obtained at 1000

TABLE 4.2. Characteristic parameters of ion migration.[1]

Condition	**Phase**	n_{Na}	n_{Cl}	t_{eq} **(ps)**
288 K/1 atm	$L_{\beta'}$	$102\pm4^{c,d,e}$	$107\pm3^{c,d,e}$	4.13 ± 0.33^{b}
308 K/1 atm	L_{α}	$98\pm4^{d,e,f}$	$105\pm5^{d,e}$	$2.41\pm0.16^{c,d}$
328 K/1 atm	L_{α}	95 ± 3^{f}	101 ± 4^{e}	$1.89\pm0.15^{d,e}$
348 K/1 atm	L_{α}	$96\pm1^{e,f}$	$104\pm2^{d,e}$	1.38 ± 0.31^{e}
288 K/500 atm	$L_{\beta'}$	113 ± 2^{b}	103 ± 3^{e}	4.36 ± 0.50^{b}
308 K/500 atm	$L_{\beta'}$	$103\pm3^{c,d}$	$106\pm3^{c,d,e}$	2.97 ± 0.23^{c}
328 K/500 atm	L_{α}	94 ± 4^{f}	$107\pm5^{c,d,e}$	$2.39\pm0.15^{c,d}$
348 K/500 atm	L_{α}	$97\pm3^{e,f}$	$105\pm9^{d,e}$	2.12 ± 0.28^{d}
288 K/1000 atm	$L_{\beta'}$	136 ± 10^{a}	135 ± 8^{b}	NA
308 K/1000 atm	$L_{\beta'}$	$108\pm2^{b,c}$	111 ± 2^{c}	5.24 ± 0.50^{a}
328 K/1000 atm	$L_{\beta'}$	110 ± 3^{b}	112 ± 1^{c}	4.18 ± 0.39^{b}
348 K/1000 atm	L_{α}	$96\pm4^{e,f}$	$108\pm3^{c,d}$	2.75 ± 0.47^{c}
288 K/5000 atm	HP	15 ± 2^{i}	168 ± 1^{a}	NA
308 K/5000 atm	HP	$20\pm3^{h,i}$	167 ± 4^{a}	NA
328 K/5000 atm	HP	$23\pm1^{g,h}$	167 ± 1^{a}	NA
348 K/5000 atm	HP	27 ± 4^{g}	162 ± 3^{a}	NA

[1] n_{Na} and n_{Cl} are the number of sodium and chloride ions at equilibrium and t_{eq} is the time where the ion migration stopped. Results with the same superscript are not significantly different from each other ($p > 0{,}05$). NA = Non Applicable.

atm, suggesting that higher pressures triggered a stronger ion flux. This is especially true for the $L_{\beta'}$ phase (in L_{α} bilayers, the differences were smaller or even not significant and in the HP phase the ion flux was almost null). Moreover, for the same pressure and phase, the best results were observed at low temperatures, and the highest ion migration was obtained at 288 K/1000 atm. Figure 4.9 shows that in this condition the pore was not closed within the simulated time scale, giving the ions a longer time to distribute themselves more homogeneously between the 2 compartments. In addition, the Cl^- migration profile at 328 K/500 atm, 348 K/500 atm and 348 K/1000 atm showed a sharp decrease in the earlier time steps of the simulation, with a further counter-diffusion to compensate the resulting concentration gradient. This behavior was visualized when the simulations at these pressures led to the L_{α} phase. Bi et al. (2018) found that negative ions are more affected in the early stages of electroporation, since the outermost part of the DPPC bilayer consists of the positively charged head-group (C_3N^+), which may explain why only Cl^- ions showed this behavior.

Notably, within the $L_{\beta'}$ phase, the number of Na^+ ions into region I was always higher than 100. In the L_{α} phase, an approximately constant number of ions was found,

regardless of the temperature and pressure ($\approx$ 96 Na^+ and $\approx$ 105 Cl^-). Some studies have analyzed electroporation guided extraction at different temperatures, mostly at ambient pressure. Haberl-Meglič et al. (2016) analyzed the extraction of proteins from *Escherichia coli* cells applying incubation temperatures from 277 to 318 K. A concentration of 26 μg l^{-1} was found at 277 K, compared to 6.56 μg l^{-1} at 318 K. Scherer et al. (2019) found that the protein extraction from *Chlorella vulgaris* was twice as high in the temperature range of 293-313 K compared to 323 K. The simulations showed that the pore resealing kinetics is considerably slower in the $L_{\beta'}$ phase, which presented higher values for t_m, t_s and t_r as seen in Table 4.2. This effect can result in longer times for the extraction of intramolecular molecules, helping to explain the aforementioned experimental results. On the other hand, Gianpiero et al. (2019) examined the extraction of carotenoids from tomato wastes using a PEF pre-treatment at 293, 308 and 323 K and found no significant differences between the different temperatures. This result suggests that the temperature effects on the extraction of intracellular compounds occur only under certain conditions. In this case, it can be hypothesized that the molecule size could play an important role in the extraction: for larger molecules, the increase in r_{MAX} observed in the L_α phase may contribute for the extraction, compensating the faster membrane resealing computed for these conditions.

Studies analyzing the practical effects of pressure during electroporation are still scarce in the literature. The effect of the combination between PEF and mechanical compression on the permeability and structure of the micro-algae *Chlamydomonas reinhardtii* has been analyzed using transmission electron microscopy (BENSALEM et al., 2020). The authors showed that more dextran molecules were extracted when the system was under compression. Pyatkovskyy et al. (2018) combined PEF (10-30 kV/cm) and HHP (200 MPa/25°C and 400 MPa/35°C) for the inactivation of *Listeria innocua* in water. The authors found a synergistic effect resulting from the combination of high pressures with electric fields. Interestingly, the authors did not observe this effect when the HHP was applied after the PEF treatment. The previously reported kinetic behavior may help to explain this: once PEF is applied under atmospheric pressure, a faster resealing of the membrane is observed, so the integrity of the bilayer might already be restored when the HHP was applied, hindering the synergistic effects. Similarly, no synergistic effect occurred when HHP (200 MPa) was applied, for 5 min or less, prior to PEF (25 kV/cm, T = 22°C)(HEINZ; KNORR, 2000).

These results suggest that ion flux is influenced by the membrane phase as well as by temperature and pressure. At 5000 atm, a significantly slower migration occurred and, as shown in the previous section, an almost constant pore radius of 3.5 Å was observed at 5000 atm in all temperatures, which was not closed within the simulated time scale. This pore radius is much narrower than the radius observed at lower pressures, which may indicate that a radius below a certain critical value does not cause massive ion flow in the bilayer. In addition, the slower ion flux may be caused by other possibilities such as: (i) the time scale analyzed was not sufficient to observe complete ion migration at 5000 atm; (ii) HP gels might be unfavorable for ion flux; or (iii) the use of a coarse-grained model may not be appropriate for representing electroporation in HP phases. A comparison with AA-MD results for a smaller system in Section 4.3.3 demonstrates that ion migration is indeed lower at 5000 atm. However, the AA model predicts higher rates compared to the coarse-grained representation. Therefore, HP gels are probably unfavorable for ion flux, although this effect is slightly overestimated by the Martini representation.

To check if the ion migration stops before the pore full recovery, the time at which the ion transport stopped (t_{eq}) can be compared with the kinetic parameters reported in the previous section. According to the discussion in section 4.3.2.1, t_{eq} decreased with temperature and increased with pressure. A comparative analysis of the results of Tables 4.1 and 4.2 show that the ion migration stops before the complete recovery of the membrane (i.e., $t_{eq} < t_r$). This can be illustrated by analyzing the results at 308 K/1000 atm, where a pore of 1.5 Å persisted even after the simulations ended, but the ion flux stopped after approximately 5.2 ps. This suggests that pore formation is a necessary but not sufficient condition for ion migration, which is a critical aspect to be considered in industrial applications on which larger molecules (rather than single ions) are extracted from cells.

4.3.2.3 Electrostatic aspects

Figure 4.13 shows the instantaneous electric field profiles in times up to 10 ns for each combination of T/P. Dimensionless coordinates were used in the x-axis (length); this was done to improve the visualization of the profiles once the bilayer stretches under the field application, which would affect the data representation. The initial

profile is similar to that obtained by Muralidharan et al. (2021) using experimental (fluorescence imaging) and numerical (heat and mass transfer models) techniques. At $t = 0$, a consistent field distribution is found for all cases. As time progresses and the ion concentration gradient decreases, the electric field decreases to practically zero. This was not the case at 5000 atm pressure, where a remaining field of 4 V/nm was seen at the end of the simulations. This phenomenon is attributed to the slower recovery kinetics at this pressure, which resulted in a slower ion flux and, consequently, a slower decrease in the electrostatic potential.

In the plots of Figure 4.13, despite the same initial ion concentration, the initial electric field was slightly different in each bilayer phase. Figure 4.14 shows a two-dimensional electric field distribution for each phase at $t = 0$. Overall, the gel states yielded higher initial fields, as indicated by the darker shading of the profiles in Figure 4.14. It can be noticed on Eq. 4.6 that the field profile is essentially affected by the system dimensions and ρ. As previously discussed, lipid bilayers in gel phases exhibit a larger thickness and thus an increase in the z dimension of the simulation box is observed. By increasing the length, the Equation 4.6 holds that the corresponding field will be higher, provided that the charge density remains constant. The bilayer thickness was approximately 3.9 and 4.7 Å in the L_α and $L_{\beta'}$ phases, respectively. Assuming that the water is incompressible, the system z-axis is stretched by about 16.7%. Under the same conditions, the field increased by about 19.4%, corroborating that the increase in the bilayer thickness was responsible for the increase in the initial electric field.

At 5000 atm, the bilayer thickness was similar to the liquid crystalline state. Thus, assuming that only thickness influences the electric field, a value similar to the L_α phase would be expected. Water increases its compressibility as pressure increases, and at 5000 atm its density is considerably higher than in other conditions (at 288 K, the specific mass of water is 999, 1021, 1041 and 1152 kg/m^3 at 1, 500, 1000 and 5000 atm, respectively). Therefore, a decrease in volume is expected, which increases the charge density. In addition, higher electric fields were found in the same phase when pressure was increased (as shown in Figure 4.15), confirming that water compressibility plays a role in the electrostatic aspects of electroporation. An increase in electric field effects at higher pressures has already been reported in some experimental studies in physics (JORNADA; ZAWISLAK, 1979; PARK et al., 2021), which is consistent with the behavior reported in the present work for lipid bilayers.

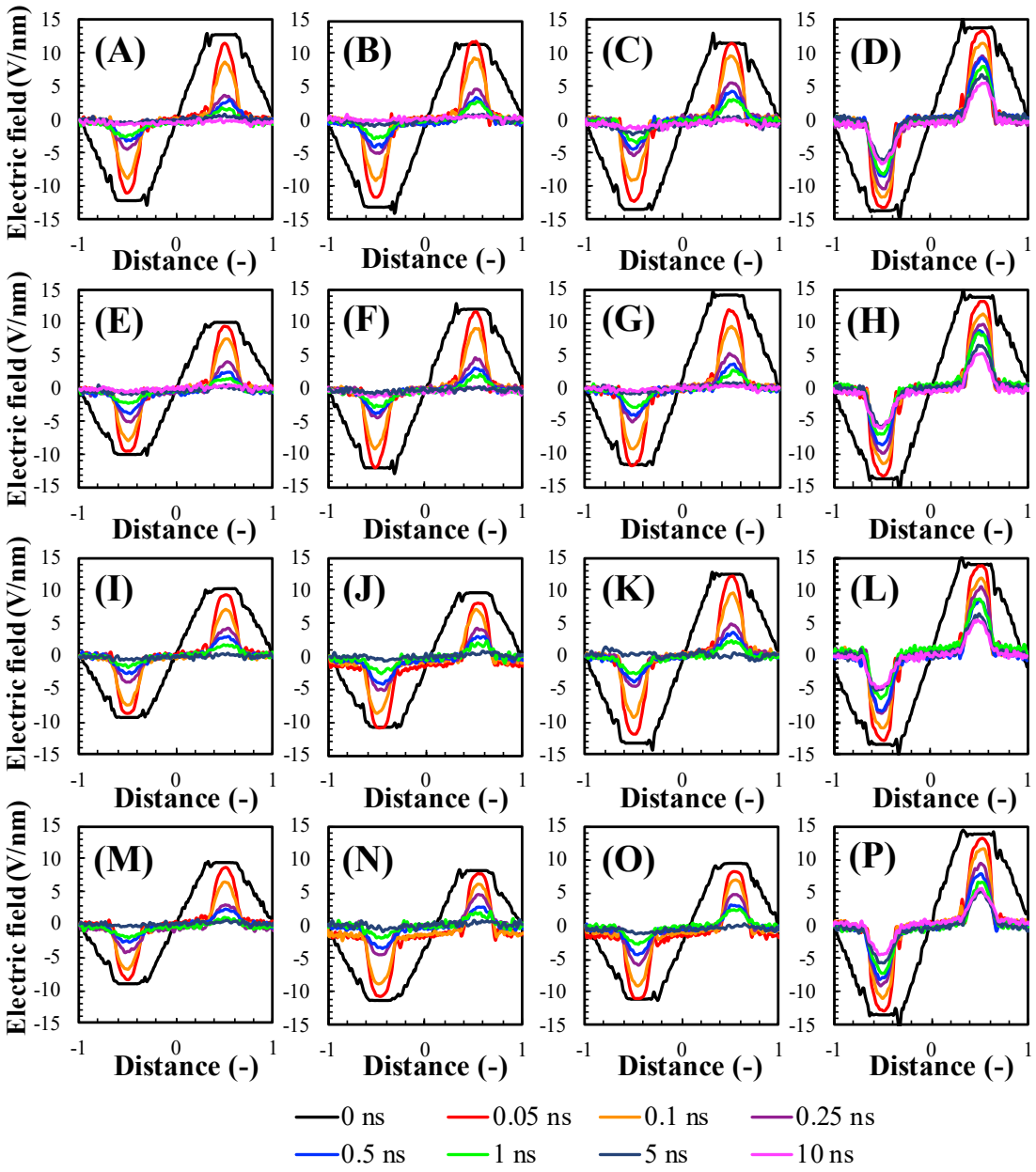

FIGURE 4.13. Time evolution of electric field profiles at (A) 288 K/1 atm, (B) 288 K/500 atm, (C) 288 K/1000 atm, (D) 288 K/5000 atm, (E) 308 K/1 atm, (F) 308 K/500 atm, (G) 308 K/1000 atm, (H) 308 K/5000 atm, (I) 328 K/1 atm, (J) 328 K/500 atm, (K) 328 K/1000 atm, (L) 328 K/5000 atm, (M) 348 K/1 atm, (N) 348 K/500 atm, (O) 348 K/1000 atm and (P) 348 K/5000 atm.

4.3.3 Comparison with all-atom simulations

Figure 4.16 illustrates the electroporation kinetics for both the AA representation and a corresponding Martini system with the same size and composition. The

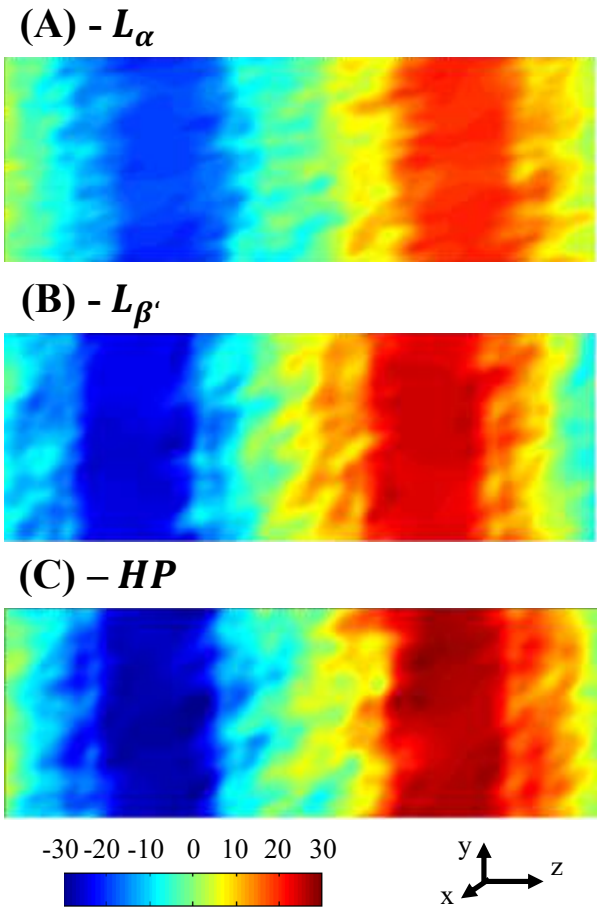

FIGURE 4.14. 2D electric field profiles (V nm^{-1}) for the (A) L_α, (B) $L_{\beta'}$ and (C) high pressure phases.

traditional stages of electroporation, including pore formation, stabilization, and resealing, are apparent in both representations, and the maximum pore sizes are also quite similar. Moreover, the qualitative behavior is also the same (faster resealing at low pressure and incomplete recovery of the pore at 5000 atm). However, there is a notable difference in the time scale along the x-axis of the figure, with the AA simulations showing slower formation and recovery. This is a well-documented artifact of the Martini force field due to an effective acceleration factor in the diffusion dynamics of Martini water compared to real water. To correct the characteristic time scales, the Martini developers recommend in their website the use of a standard conversion factor of 4 for kinetic processes occurring in lipid bilayers. Table 4.3 provides the computed AA kinetic parameters alongside the CG ones with the correction factor applied, demonstrating good agreement between atomistic and coarse-grained representations.

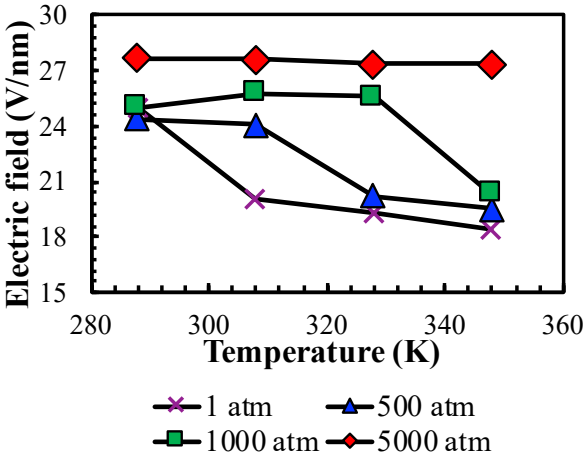

FIGURE 4.15. Initial electric field as function of temperature for each applied pressure.

TABLE 4.3. Characteristic parameters of pore formation of the AA and CG representation at $T = 348K$ for varied P conditions.[1]

Condition	r_{MAX} **(Å)**	t_m **(ns)**	t_s **(ns)**	t_r **(ns)**
1 atm/CG	1.35	0.10	1.22	15.63
500 atm/CG	1.36	0.15	1.45	16.28
1000 atm/CG	1.35	0.17	1.68	26.02
5000 atm/CG	0.65	0.81	NA	NA
1 atm/AA	1.38	0.22	1.41	13.68
500 atm/AA	1.36	0.29	1.67	14.64
1000 atm/AA	1.34	0.31	1.79	29.70
5000 atm/AA	0.74	0.89	NA	NA

[1] r_{MAX} is the maximum pore radius, t_m is the time to reach the maximum radius, t_s is the time of stabilization at $r = r_{MAX}$ and t_r is the resealing time. NA = Non Applicable.

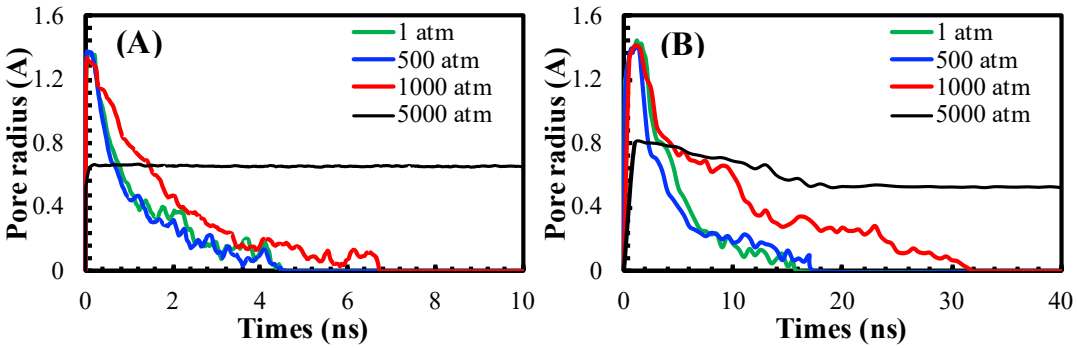

FIGURE 4.16. Time evolution of pore radius at 348 K for the (A) AA representation and (B) CG representation.

A comparison of ion migration for both representations is also shown in Figure

4.17. For the pressures of 1, 500 and 1000 atm, the Martini simulations agreed well with the AA parameters. At 5000 atm, a qualitatively similar description is observed (lower number of migrating ions); however, the total number of ions that crossed the membrane is higher in the atomistic representation. This deviation at 5000 atm might be due to a deficiency of the Martini CG to describe properly the HP gel state, as previously discussed.

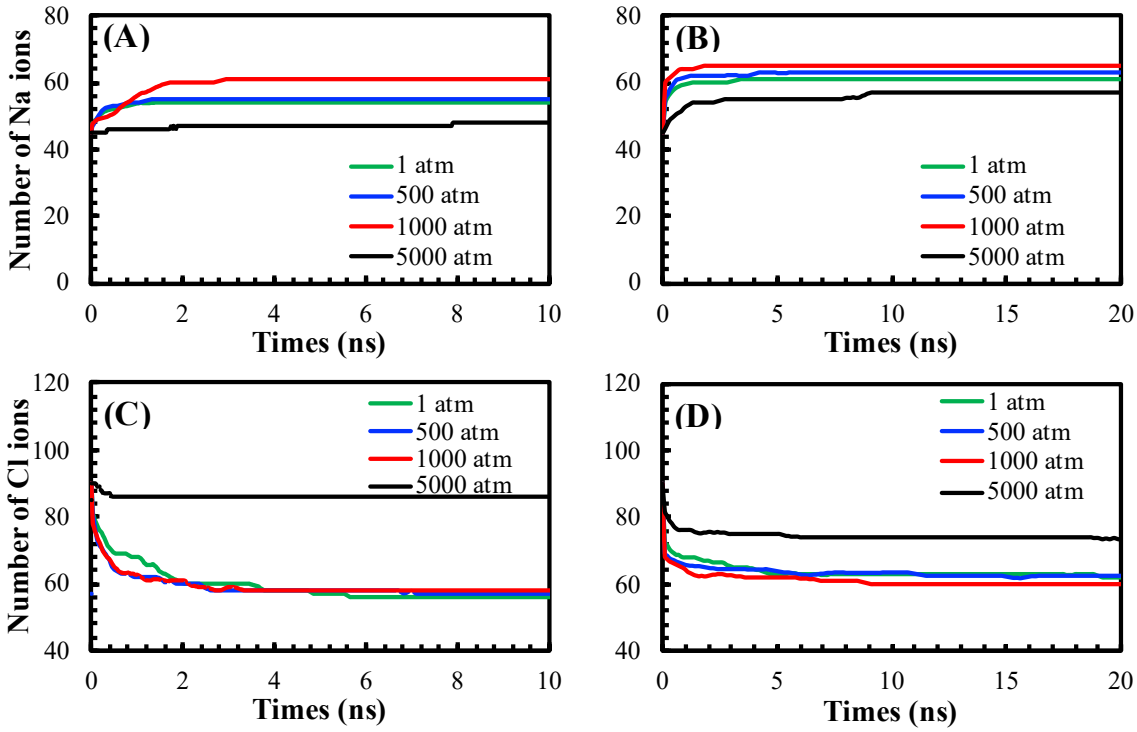

FIGURE 4.17. Number of sodium ions in the compartment I at 348 K using (A) AA representation, (B) CG representation, and number of chloride ions in the compartment I at (C) AA representation, (D) CG representation.

4.4 Conclusion

The aim of this study was to analyze the phenomenon of electroporation using molecular dynamics simulations. The bilayers were correctly described by the Martini force field and agreed with both experimental and all-atom studies. The pore formation kinetics was found to be affected by temperature and pressure, with lower temperatures and higher pressures leading to slower resealing of the membrane structure. In the $L_{\beta'}$ gel state, this phenomenon resulted in an increase in ion migration. However,

at the highest applied pressure, the formed gel phase exhibited limited ion transport capabilities due to its highly compressed nature, restricting the movement of molecular components. The results presented can help improve the performance of the electroporation in various applications of this technique, such as extraction of intracellular compounds, inactivation of microorganisms and, recently, in cancer research.

Chapter 5

Computational analysis of the simultaneous application of ultrasound and electric fields in a lipid bilayer

The findings of the study *Computational Analysis of Simultaneous Ultrasound and Electric Field Application in a Lipid Bilayer* are presented in this chapter. The research utilized all-atom molecular dynamics simulations to investigate the synergistic effects of these two processes. The outcomes contribute significantly to the comprehension of their intricate interplay, particularly shedding light on the pivotal role played by cavitation in driving these synergistic phenomena. Additionally, the study delves into the underlying mechanisms governing the combined impact of ultrasound and electric fields on the lipid bilayer, offering valuable insights for potential applications in various fields such as microbial inactivation and medical technology.

Chapter 6

Unraveling the Phase Behavior, Mechanical Stability, and Protein Reconstitution Properties of Polymer-Lipid Hybrid Vesicles

The results of the study *Unraveling the Phase Behavior, Mechanical Stability, and Protein Reconstitution Properties of Polymer–Lipid Hybrid Vesicles* are presented in this chapter. This comprehensive study employed coarse-grained molecular dynamics simulations to analyze several attributes encompassing physicochemical, mechanical, and biochemical aspects of lipid/polymer hybrid vesicles. This investigation was done in collaboration with the Macromolecular Biochemistry group at the University of Leiden, Netherlands, and also included experiments using the dynamic light scattering and fluorescence spectroscopy techniques to further elucidate the vesicles' characteristics. This study has been published in the journal *Biomacromolecules* (DOI: <https://doi.org/10.1021/acs.biomac.3c00498>).

Abstract: Hybrid vesicles consisting of natural phospholipids and synthetic amphiphilic copolymers have shown remarkable material properties and potential for biotechnology, combining the robustness of polymers with the biocompatibility of phospholipid membranes. To predict and optimize the mixing behavior of lipids and copolymers, as well as understand the interaction between the hybrid membrane and macromolecules like membrane proteins, a comprehensive understanding at the molecular level is essential. This can be achieved by a combination of molecu-

lar dynamics simulations and experiments. Here, simulations of POPC and PBD_{22}-*b*-PEO_{14} hybrid membranes are shown, uncovering different copolymer configurations depending on the polymer-to-lipid ratio. High polymer concentrations created thicker membranes with an extended polymer conformation, while high lipid content led to the collapse of the polymer chain. High concentration of polymer further correlated with a decreased area compression modulus and altered lateral pressure profiles, hypothesized to result in the experimentally-observed improvement in membrane protein reconstitution and resistance towards destabilization by detergents. Finally, simulations of a WALP peptide embedded in the bilayer showed that only membranes with up to 50% polymer content favored a transmembrane configuration. These simulations correlate with previous and new experimental results and provide a deeper understanding of the properties of lipid-copolymer hybrid membranes.

Keywords: Polymersomes; Liposomes; Biomembranes; Molecular Dynamics; Martini.

6.1 Introduction

Phospholipids vesicles, or liposomes, have many biotechnological applications, including in delivery of drugs and vaccines (SERCOMBE et al., 2015; REIMHULT; VIRK, 2021), improvement of food quality (LIU et al., 2020), diagnostic imaging (LAMICHHANE et al., 2018), biosensors (MAZUR et al., 2017) and as nanoreactors (GUDLUR et al., 2015). A key drawback of these vesicles is their limited stability, which is caused by various factors, including the formation of transient pores in the lipid bilayer and oxidation of the acyl chains (GRIT; CROMMELIN, 1993). To address this, polymersomes (formed by the spontaneous self-assembly of amphiphilic copolymers) have been proposed as an alternative in recent decades (ZHAO, 2017; LIU et al., 2020). Polymersomes are usually more resistant and exhibit a wider range of physicochemical properties due to the diversity of polymers that can be used to form them. However, besides some notable exceptions (STOENESCU et al., 2004; KUMAR et al., 2012; HABEL et al., 2015), polymer bilayers are not suitable for the functional incorporation of membrane proteins (MUHAMMAD et al., 2011; KHAN et al., 2016), which

evolved to be biocompatible with phospholipids and not with copolymers. Hence, genetic modifications of the proteins or changes in the membrane structure are necessary to make polymersomes a more viable option for biotechnological applications.

In the past decade, hybrid vesicles (HVs) composed of mixtures of phospholipids and copolymers have been studied, aiming to combine the best properties of both components: the biocompatibility of liposomes and the robustness of polymersomes (ZHU et al., 2017; WANG et al., 2018; LEONE et al., 2020). HVs composed of 1-palmitoyl-2-oleoyl-sn-glycero-3-phosphocholine (POPC) and poly(1,2-butadiene)-*b*-poly(ethylene oxide) (PBD_{22}-*b*-PEO_{14}) were found to efficiently incorporate cytochrome bo_3, with a 50/50 mol% ratio providing the best cost-benefit scenario considering the balance between long-term stability and initial activity of the protein (KHAN et al., 2016; SENEVIRATNE et al., 2018). Also, when reconstituting cytochrome bo_3 from styrene-maleic-acid lipid particles (SMALPs), no surfactants were required for hybrid vesicles, whereas pure liposomes necessitated the addition of a detergent to effectively incorporate this protein (CATANIA et al., 2022). The addition of PBD_{22}-*b*-PEO_{14} in a DOPC vesicle has been shown to also improve the efficiency of protein folding and reconstitution into the membrane (JACOBS et al., 2019). Enhanced protein activity in PDMS-*g*-PEO and soy-PC HVs was also reported (OTRIN et al., 2017). Therefore, despite the distinct structural characteristics of lipids and copolymers, HVs have demonstrated various examples of equivalent/superior performance when compared to pure liposomes and polymersomes, showcasing their unique advantages. These observations have led to an increased interest in the mixing behavior of lipids and polymers (BEALES et al., 2017; REIMHULT; VIRK, 2021; SENEVIRATNE et al., 2023), and a need to optimize the vesicle environment through a better understanding of the relationship between a hybrid membrane's chemical composition and its material properties.

Experimental techniques have been widely used to explore the physicochemical properties of pure and hybrid membranes, but some phenomena are not easily understood through experiments alone. Molecular dynamics (MD) simulations allow for the analysis of atomistic trajectories, providing valuable insights that can complement experimental data and offer a deeper understanding of relevant phenomena at the molecular level (RAPAPORT, 2004). Although the use of MD applied to hybrid

vesicles holds great potential, the use of computational techniques in the study of these membranes is still in its early stages of development. Recently, all-atom (AA) MD simulations were performed to investigate HVs composed of DOPC and PBD-*b*-PEO, with polymer fractions of 10 and 20 mol% (STEINKÜHLER et al., 2022). These simulations offered valuable insights into the molecular structure of these vesicles. However, atomistic simulations face limitations in their ability to analyze systems with more than hundreds of thousands of atoms (a common occurrence in biochemistry (CHEN et al., 2018)) over long time scales. To overcome this limitation, coarse-graining (CG) techniques can be utilized to access longer time and length scales by simplifying some of the atomistic degrees of freedom, which has not been employed in the context of hybrid membranes up to now.

The objective of this study is to obtain a deeper understanding of the structure and properties of hybrid vesicles, in particular POPC and PBD_{22}-*b*-PEO_{14} HVs, by combining experiments and mesoscale MD simulations. The POPC/PBD_{22}-*b*-PEO_{14} system was chosen due to its extensive previous characterization using various experimental techniques, such as small-angle X-ray scattering (SAXS) and cryo-electron tomography (SENEVIRATNE et al., 2023), general polarisation measurements of Laurdan (SENEVIRATNE et al., 2022), confocal fluorescence microscopy (NAM et al., 2010) and flow cytometry (LIM et al., 2013), which raised several questions regarding the observed phenomena that can benefit from MD simulations. A coarse-graining method using the Martini force field (FF) was employed following its widespread use for biomolecules. As Martini currently lacks a parameterization for the analyzed copolymer, a model for this molecule was first developed. Qualitative and quantitative metrics were evaluated to study the fundamental interactions of lipids and copolymers within the HVs. Furthermore, the incorporation of a WALP peptide in HVs was assessed to investigate peptide/membrane interactions. Fluorescence experiments were performed to evaluate the leakage of hybrid vesicles in the presence of detergent, aiming to determine if increasing the concentration of polymers enhances the stability of the membrane when surfactants are added. The comparison between simulation and experimental results allowed the examination of diverse phenomena in HVs, such as the presence of different spatial configurations in homogeneous membranes (SENEVIRATNE et al., 2023) and improved incorporation of membrane proteins into HVs (JACOBS et al., 2019; CATANIA et al., 2022).

6.2 Computational Methods

Because of the characteristic length scale of biological membranes, a CG approach was adopted to study the hybrid vesicles. The Martini 3 force field (SOUZA et al., 2021) was applied due to its success in reproducing key aspects of POPC membranes (JING et al., 2020; JUNQUEIRA et al., 2021). Additionally, the Martini 3 version has demonstrated notable advancements in accurately describing the behavior of peptides and transmembrane proteins within bilayers (SOUZA et al., 2021). A cutoff of 1.2 nm was employed for both electrostatic and nonbonded interactions. All simulations were performed using the open-source Gromacs package (LINDAHL et al., 2021), with periodic boundary conditions in all dimensions.

6.2.1 Parametrization of PBD-*b*-PEO

The Martini 3 force field lacks an established model for PBD and, consequently, for the PBD-*b*-PEO copolymer. Although Grillo et al. (2017) previously analyzed a similar system with this force field, they focused on the linear configuration of PBD, while the present study examines the vinyl isomer. The selected isomeric conformation was parametrized following best practices outlined on the Martini website and in relevant publications (MARRINK et al., 2007; SOUZA et al., 2021). The next sections provide a detailed explanation of how the model was derived.

6.2.1.1 Beads choice and non-bonded parameters

In the CG scale, polymers are typically modeled using a single particle corresponding to each monomer (GRILLO et al., 2017; LEE et al., 2009; ROSSI et al., 2011; ROSSI et al., 2012; GRUNEWALD et al., 2018), and the initial proposed model followed this approach. Martini particles typically use a 4-1 strategy (i.e., four heavy atoms and their bonded hydrogen atoms are represented by a regular *R* bead). For increased resolution, 3-1 small beads *S* and 2-1 tiny beads *T* can also be used. The C4 bead was selected because it represents nonpolar chains with double bonds, while the SN3a bead

was chosen because it represents ether groups. As PEO only has three heavy atoms, a *S* bead was used to model this monomer.

Although this representation resulted in a satisfactory description of the PBD-*b*-PEO all-atom (AA) structure, when polymers and phospholipids were mixed to form hybrid bilayers, a phase separation was observed (Figure 6.1.A). This outcome conflicted with the expectation of homogeneous dispersion, as shown by Seneviratne et al. (2022), indicating that the interactions between the molecules were not accurately computed. To determine which part of the molecule needed to be better modeled, tests were conducted by altering the Lennard-Jones parameters of the C4 and SN3a beads. It was found that the C4 beads exerted a considerable repulsion on the acyl chains of the phospholipids, which caused the observed separation.

To address this issue, a two-bead parameterization using Tiny Martini beads was proposed for PBD. The main chain, which consists of two bonded carbon atoms, was represented by the TC2 bead while the side chain, composed of two double bonded carbons, was represented by TC4 (Polybutadiene - Model 2 in Figure 6.1.B). *T* beads were used for this polymer since each particle contains only two heavy atoms. This adjustment was capable of forming membranes without phase separation. Despite the higher computational cost, this approach produced well-mixed hybrid bilayers (Figure 6.1.B). An illustration of the resulting PBD-*b*-PEO chain is illustrated in Figure 6.1.C, along with the two models considered for representing the PBD monomer.

Martini beads can be further divided into attractive, normal and repulsive beads, and all different conformations were tested. Electron density profiles were compared with experimentally obtained ones by Seneviratne et al. (2023). The normal version of the SN3a, along with the repulsive versions of the TC2 and TC4 beads (TC2r and TC4r) were used, which resulted in electron density profiles very similar to the observed in experiments. The developed model also introduced a small amount of hydrophilic PEO beads into the hydrophobic core. This contradicts experimental findings (SRINIVAS et al., 2004), and a similar issue had been previously reported in another study that used the Martini force field to model a linear conformation of the PBD-*b*-PEO polymer (GRILLO et al., 2017). To address this issue, Grillo et al. (2017) reduced the ϵ parameter describing the interactions between PBD and PEO beads by

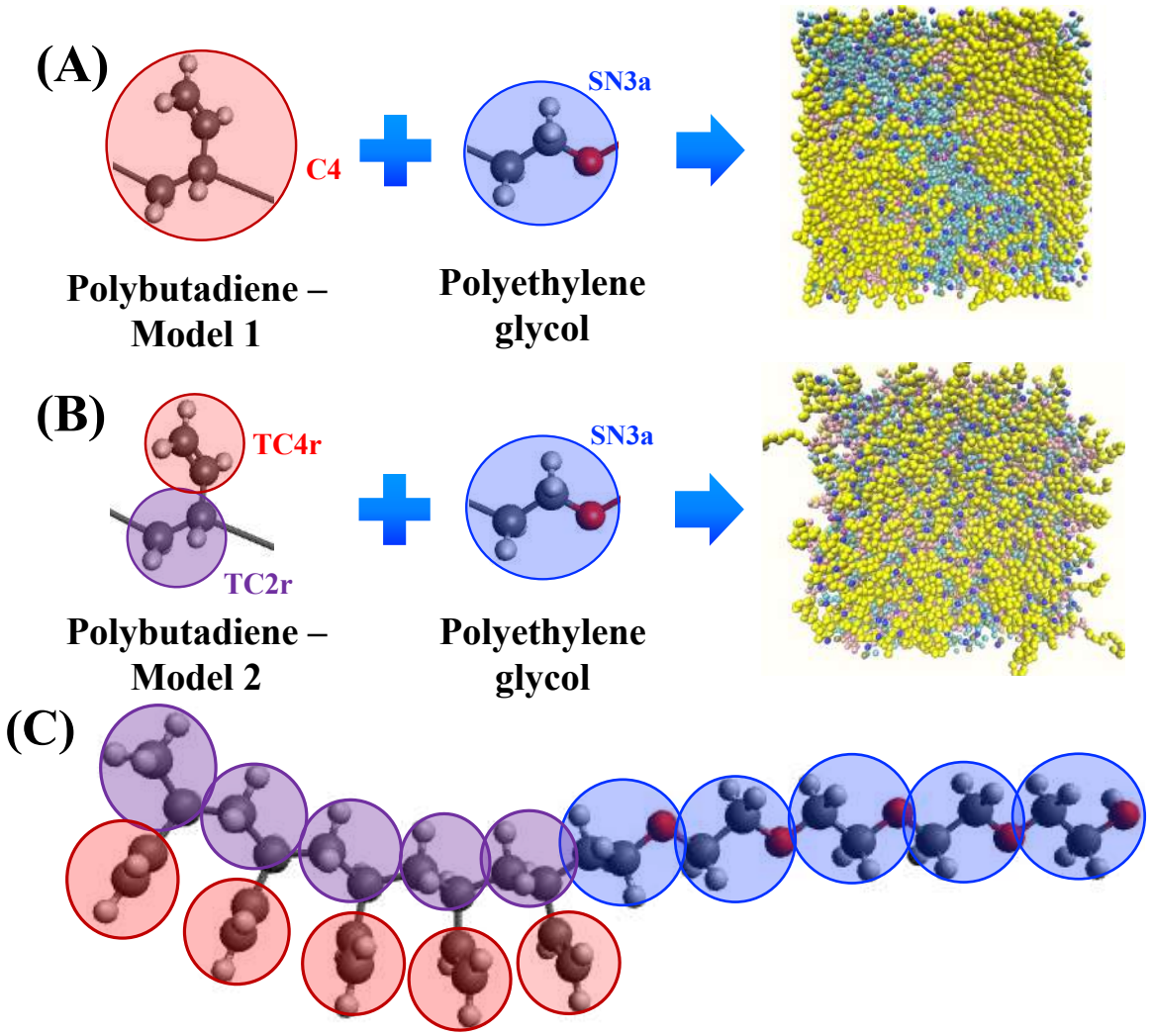

FIGURE 6.1. Coarse-grained representation of the PBD-*b*-PEO polymer, where (A) and (B) shown models I and II for the PBD molecule and (C) the molecule PBD_5-*b*-PEO_5.

11.4 %. Following a similar approach, this parameter was decreased by ≈ 9 %, resulting in $\epsilon_{TC2r-SN3a}$ changing from 1.6 to 1.45 kJ/mol and $\epsilon_{TC4r-SN3a}$ changing from 1.75 to 1.6 kJ/mol. This small adjustment was sufficient to achieve proper separation of hydrophobic and hydrophilic polymer regions.

6.2.1.2 Bonded parameters

The bonded parameters were derived by comparing the distributions of the CG beads with those from all-atom (AA) simulations and further refined to represent experimental features visualized in experiments. PBD and PEO chains with 10

monomers were analyzed to derive parameters for the pure polymers, while PBD_5-*b*-PEO_5 was used to derive parameters for the copolymer hydrophobic-hydrophilic interface. The AA simulations were carried out in the NPT ensemble (T= 310 K, P = 1 atm) with OPLS-AA FF force field, using the Nosé-Hoover barostat and thermostat to control pressure and temperature, respectively. Each polymer chain was solvated with 8000 TIP3P water molecules, using 1.4 nm cut-offs for both nonbonded and electrostatic potentials, and PPPM for long-range electrostatic interactions. The simulations included a 50 ns equilibration and a 100 ns data collection run. The CG representations were generated from AA structures using the CG builder tool <https://jbarnoud.github.io/cgbuilder/>. For PEO, bonds, angles, and dihedrals were parametrized, while only bonds and angles were used for PBD due to the lack of a well-defined dihedral distribution for this monomer. PEO models have been previously developed for the Martini force field, and initial parameters for this molecule were adopted from the literature (GRILLO et al., 2017; GRÜNEWALD et al., 2022; ROSSI et al., 2012) and refined based on the simulation results. To match the AA bonded parameters with the CG representation, a combination of optimization algorithms and trial and error was employed until the CG distributions were in close agreement with those of the AA simulations.

The harmonic potential was used to model the bonds following the Martini force-field formulation. Bond distributions of the simulated polymers are shown in Figure 6.2, indicating good agreement between the CG and AA simulations. However, the bonds between TC2r-TC2r and TC2r-SN3a beads showed a bimodal behavior in the AA representation which was not captured by the CG model. As a result, the two configurations were combined into one due to the simplified phase-space sampling typical of mesoscale models. The use of non-charged Martini 3 beads in modeling can lead to underestimation of structural properties when using bond distances directly from atomistic simulations, as their attractive interactions are slightly underestimated (GRUNEWALD et al., 2018). To address this issue, bond lengths can be adjusted for a more accurate representation. One proposed solution is to slightly increase ($\approx 15\,\%$) the atomically adjusted bond length of main chains (GRUNEWALD et al., 2018). Following this suggestion, this correction was applied for SN3a-SN3a bonds and TC2r-TC2r bonds.

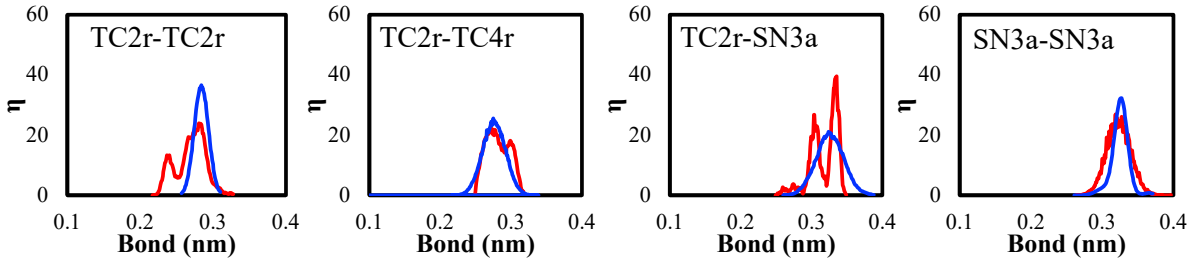

FIGURE 6.2. AA (red) and CG (blue) bond length distributions.

The angles were also modeled using a harmonic potential, and the results are depicted in Figure 6.3, which shows close agreement with the atomistic reference data. Five different types of angle were considered, including main chain angles (TC2r-TC2r-TC2r, TC2r-TC2r-SN3a, TC2r-SN3a-SN3a, SN3a-SN3a-SN3a) and the main and side chain of a PBD bead with its neighboring particle (TC4r$_i$-TC2r$_i$-TC2r$_{i+1}$). Again, angular distribution that exhibited a bimodal behavior were combined into a single distribution in the CG scale. Simulations became unstable when the SN3a-SN3a-SN3a angles approach 180° if only an harmonic potential is used, as also reported elsewhere (ROSSI et al., 2012; GRUNEWALD et al., 2018). To correct this, the constrained bending potential developed by Bulacu *et al.* (BULACU et al., 2013) was applied along with the harmonic potential for this angle. With this correction, a timestep of 2 femtoseconds could be used, whereas without it, only a step of 1 femtosecond could be applied.

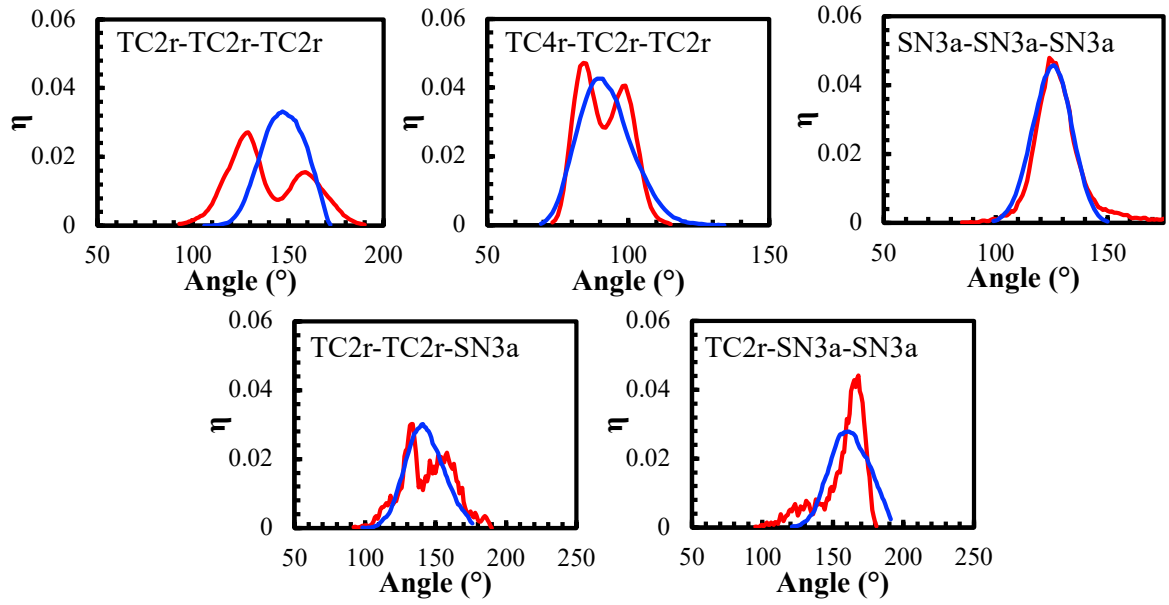

FIGURE 6.3. AA (red) and CG (blue) angle distribution.

The dihedral distribution of PBD did not exhibit a well-defined behavior, and therefore dihedral terms were not included for these beads. Regarding PEO, there are some peculiarities in modeling this term, such as bimodalities, and for simplicity the CG dihedral model implemented in the Poliply Python suite was used (GRÜNEWALD et al., 2022). A summary of all the bonded parameters is provided in Table 6.1.

TABLE 6.1. Bonded parameters for PBD-*b*-PEO copolymer.

Bonds parameters ($E_B = k_b(r - r_0)^2$)			
Bond type	r_0 (nm)	k_b (kJ mol^{-1} nm^{-2})	
TC2r - TC2r	0.332	50,000	
TC2r - TC4r	0.272	10,000	
TC2r - SN3a	0.330	7,000	
SN3a - SN3a	0.370	7,000	
Angles parameters ($E_\theta = k_\theta(\theta - \theta_0)^2$)			
Angle type	θ_0 (deg)	k_a (kJ mol^{-1} rad^{-2})	
TC2r - TC2r - TC2r	170	150	
TC4r - TC2r - TC2r	90	50	
TC2r - TC2r - SN3a	146	100	
TC2r - SN3a - SN3a	165	75	
SN3a - SN3a - SN3a (*constrained bending potential*)	135	50	
Dihedral parameters ($E_\phi = k_m(1 + \cos(m\phi + \phi_0))$)			
Dihedral type	ϕ_0 (deg)	k_m (kJ mol^{-1})	m
SN3a - SN3a - SN3a - SN3a	180	1.96	1
	0	0.18	2
	0	0.33	3
	0	0.12	4

6.2.1.3 Validation of the proposed model

To validate the efficacy of the proposed parameterization, calculations of the radius of gyration (R_g) and surface area of available solvent (SASA) for both the AA and CG representations were conducted. The SASA was calculated based on the system used for parameterization, as it represents the polymers fully immersed in water.

Meanwhile, the R_g was calculated through independent simulations of 30 polymer chains in a simulation box to assess the ability of the proposed model to capture the degree of packing of the bulk polymer. As both bonded and non-bonded parameters can impact the R_g and SASA, the presented results are based on the final set of parameters utilized in the simulations.

The radius of gyration is a measure of the overall size of the molecule as discussed in Section 3.2.4. Figure 6.4 illustrates the radius of gyration of the three polymer chains systems studied during parameterization. The good agreement between the distributions of the AA and CG trajectories suggests that the Martini parameterization proposed in this work accurately represents the overall size of the molecule.

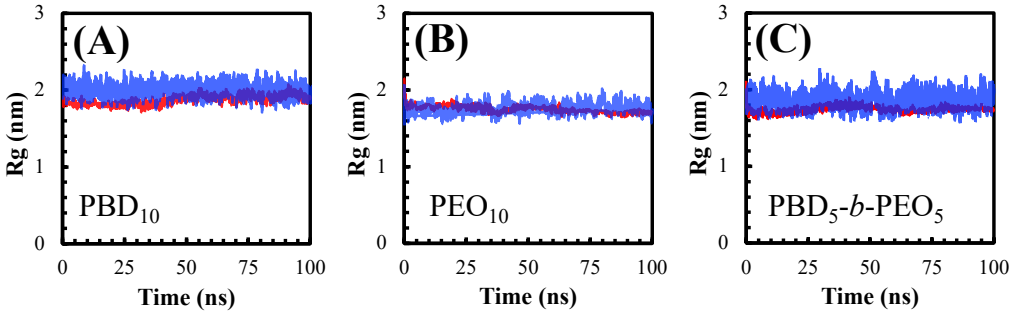

FIGURE 6.4. Radius of gyration of AA (blue) and CG (red) representations of (A) PBD_{10}, (B) PEO_{10}, and (C) PBD_5-*b*-PEO_5.

SASA measures the area of a molecule available to establish contact with its surrounding solvent or media as also discussed in Section 3.2.4. The SASA distributions of the three polymers were evaluated for both their AA and CG representations (Figure 6.5). In general, the CG model underestimated the SASA values by about 5 %, which is in good agreement with the trends reported by the Martini developers (SOUZA et al., 2021). As this is a small deviation, the analysis of the radius of gyration (R_g) and SASA provides strong evidence that the CG model is a good representation of the AA structure.

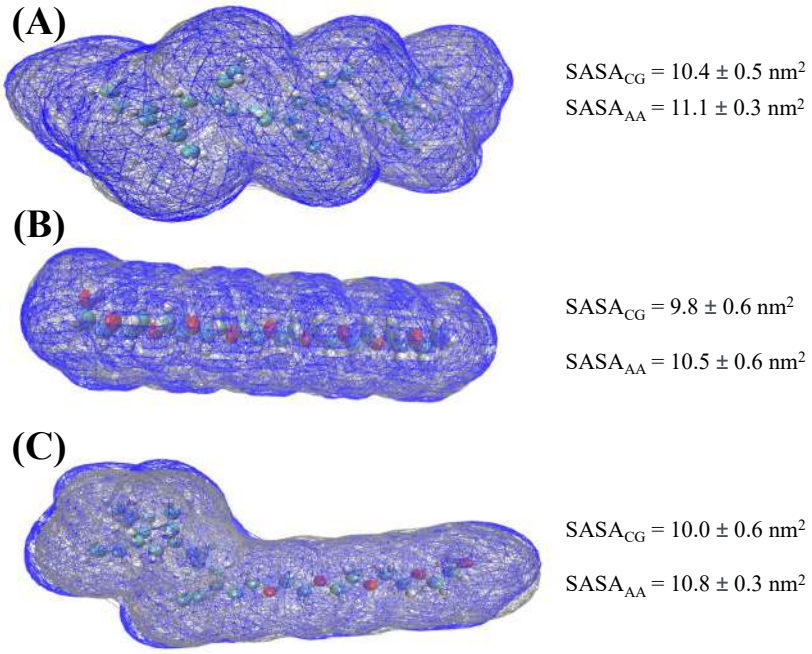

FIGURE 6.5. Connolly surfaces of (A) PBD, (B) PEO, and (C) PBD-*b*-PEO, where the blue and gray contours represent the estimated areas for the AA and CG models.

6.2.2 Initial system setup and analysis

Different systems were built by randomly placing Martini water beads and POPC and/or PBD_{22}-*b*-PEO_{14} in a simulation box as showed in Figure 6.6. To analyze bilayers with different polymer/lipid ratios, the concentration of polymer was systematically altered in increments of 25% from 0 to 100% (mol %). The initial structure of the POPC molecule was obtained directly from the Martini website (<http://cgmartini.nl/index.php>), while the initial structure of the polymer was obtained according to the procedures described in the previous section.

To verify that the developed parameterization is capable of spontaneously forming bilayers, 500 lipids and/or polymers were mixed with 10^4 water beads, corresponding to a fully hydrated condition ($\geq$ 40 real water molecules per lipid/copolymer (ZHANG et al., 2022)). These systems were energy-minimized using the steepest descent algorithm, followed by a 200 ns equilibration at 4 independent temperatures (290 to 350 K with increments of 20 K) in the isobaric isothermal ensemble (NPT, P = 1 atm) with isotropic pressure coupling. A time step of 10 fs was applied during equilibration to avoid instabilities during the initial stages of the simulations. Spontaneously self-

assembled bilayers (as illustrated in Figure 6.6) were obtained at all temperatures and polymer fractions. Due to the spontaneous formation of the bilayers, there was a slight discrepancy in the number of POPC and/or PBD_{22}-*b*-PEO_{14} molecules on each leaflet ($\leq 3\%$). Since the observed difference was minor and probably caused by random events during self-assembly, a Matlab 2012b code was applied to adjust the molecular distribution and achieve a fully symmetric bilayer after the initial equilibration. This approach was used to standardize the simulation results and ensure that the bilayer would not have any residual stress related to uneven distribution between leaflets (CHAISSON et al., 2023).

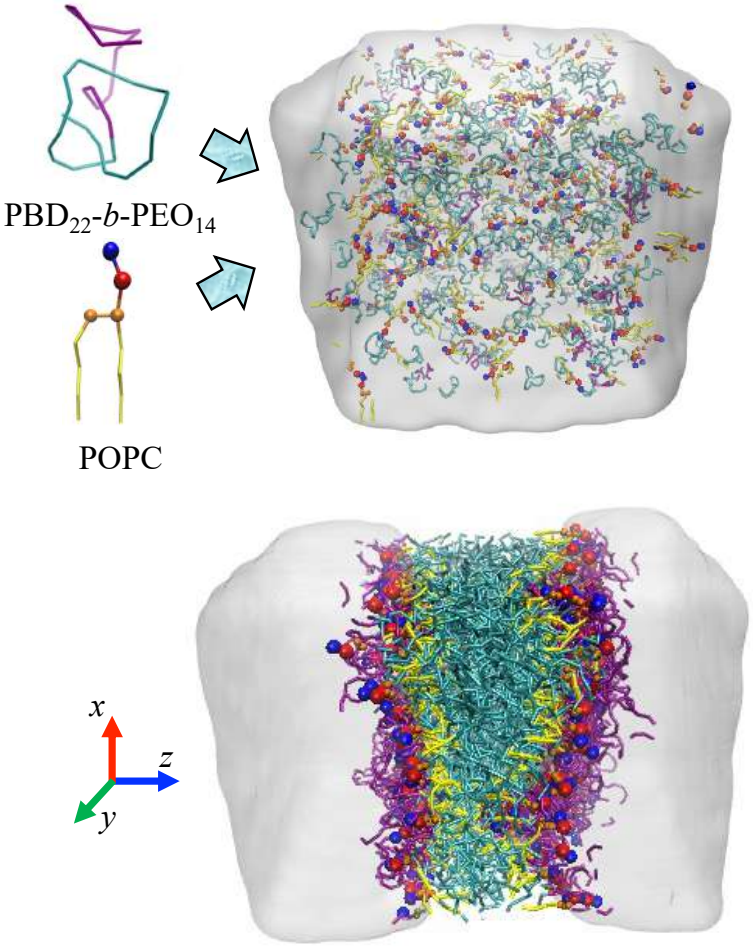

FIGURE 6.6. System representation and workflow of the simulations: POPC and PBD_{22}-*b*-PEO_{14} were randomly distributed in a solvent medium and spontaneously assembled into organized bilayers/vesicles.

The formed bilayers were under non-zero stress due to the isotropic pressure coupling scheme. To address this, semi-isotropic pressure coupling was applied in the sequence with a further 100 ns equilibration. Runs for data collection were performed for at least 10 μs with a 20 fs time step, and absence of significant variations in the properties for at least 3 μs was considered as the convergence criterion. Particle trajectories were analyzed using the Visual Molecular Dynamics (VMD) software (HUMPHREY et al., 1996), Gromacs built-in tools, Martini scripts available on its official website and in-house codes. The systems were characterized in terms of membrane thickness, lateral area, mass diffusivity, order parameter of the POPC acyl chains, electron density profiles, pressure profiles, Gaussian curvature modulus, bending modulus and area compressibility modulus. In addition, the ability of the polymer model to form whole vesicles under appropriate conditions was also evaluated. For this, 2000 POPC and/or polymer molecules were added along with 100,000 water molecules. Formation of vesicles was observed for all combinations of composition/temperature, similar to what is observed experimentally. The formation of a vesicle composed of equal molar fractions of lipids and polymers is illustrated in Figure 6.7.

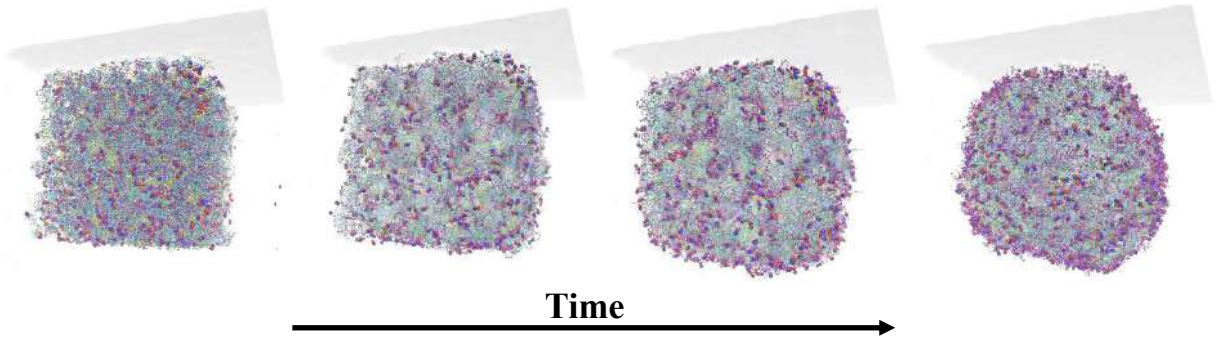

FIGURE 6.7. Spontaneous self-assembly of hybrid vesicles.

6.2.3 Structural analysis

Several physical-chemical and mechanical properties were evaluated to analyze the studied systems, aiming to compare their values with experimental results and assess their structural properties. The lateral area, mass diffusivity, order parameter, and pressure profile were measured following the methodology outlined in section 4.2.2, and will not be detailed again. For the electron density profile, the number of electrons

of each CG particle is considered for the measurement of the profiles, contrasting with the mass in conventional density profiles. To analyze the degree of membrane interdigitation, the MembPlugin developed by Guixà-González et al. (2014) was used. This tool employs a correlation-based approach to evaluate the overlap of the mass distribution of the two leaflets along the membrane normal. The fraction of overlap, denoted by the symbol I_ρ, is computed using the equation $I_\rho^2 = 4\int \rho_a(z)\rho_b(z)dz / \int[\rho_a(z) + \rho_b(z)]^2 dz$, where ρ_a and ρ_b represent the density profiles of the two leaflets

The distance between the peaks of the phosphate groups in the density profile cannot be used to analyze the thickness of hybrid membranes, as this method would not be applicable to membranes with a high concentration of polymers. Additionally, the high flexibility of the polymer chains makes it difficult to select a single polymer particle as an indicator of the bilayer thickness. Finally, it was observed that hybrid membranes have high local thickness fluctuations, making the analysis even more difficult. The average thickness of the bilayer was obtained by subtracting the volume occupied by the water from the total volume of the simulation box, and dividing the result by the area of the box parallel to the bilayer plane ($h = (V_{box} - V_{water})/A_{xy}$), as done in Wang et al. (2016).

The area compressibility modulus is an elastic property that describes how easily the lateral area of a bilayer can be compressed or expanded in response to external forces or tensions. To evaluate the area compressibility modulus, a lipid bilayer is considered to undergo infinitesimal deformations in its area due to tangential stresses and, according to Doktorova et al. (2019), the elastic compression energy can be described by:

$$E = \frac{1}{2} k_A \frac{(A - A_0)^2}{A_0} \tag{6.1}$$

Where A is the deformed area and A_0 is the equilibrium area. The area compressibility constant, k_A, is used to relate the energy with the deformation suffered by the lipid bilayer. Assuming that the compression energy is independent of the other energies that describe membrane mechanics (such as curvature and flexion energies), k_A can be calculated by evaluating only the area fluctuations caused by thermal effects. According to the equipartition theorem, $\langle E \rangle = \frac{1}{2} k_b T$, and by equating the two energy expressions:

$$k_A = k_b T \left(\frac{A_0}{\langle (A - A_0)^2 \rangle} \right) \tag{6.2}$$

The Gaussian curvature modulus, κ_G, is related to the amount of energy required to deform the membrane without altering its mean curvature. This modulus can be obtained from the lateral pressure profile (τ) of the membrane, which is closely related to its mechanical properties as described by Helfrich's theory (HU et al., 2013). For the case of a bilayer, the following relation is obtained:

$$\kappa_G = \int_{-\infty}^{\infty} dz \tau(z)(z - z_0)^2 \tag{6.3}$$

Equation 6.3 is defined as the second moment of the stress profile. If the sum of stresses in the membrane is zero ($\sum = \int dz\tau(z) = 0$), the analysis of the first moment of the stress profile ($-\kappa_m K_0 = \int dz\tau(z)(z - z_0)$) shows that the value of κ_G is independent of z_0. The summations of stresses are presented in Table 6.2, indicating that this sum is close to zero for all analyzed membranes in the present study, which indicates that the results are independent of z_0. Thus, the modulus was measured solely by $\kappa_G = \int_{-\infty}^{\infty} dz\tau(z)z^2$.

TABLE 6.2. First moment of pressure profiles for all temperatures and membrane compositions.

	0:100	25:75	50:50	75:25	100:0
290	-0.016	-0.055	-0.027	0.057	0.025
310	-0.015	-0.133	0.035	0.201	0.483
330	-0.010	0.280	0.116	-0.148	-0.293
350	-0.039	0.028	0.002	-0.293	0.184

Finally, the bending modulus refers to the energy required to bend the membrane. This metric was analyzed using compressed bilayers subjected to a tension $\lambda = (L_0 - L_{compressed})/L_0$. These membranes were formed by applying stress in the desired direction (in this case, in the x-axis), while keeping the length of the remaining dimensions (y and z) constant. After reaching the desired deformation (in this study, $\lambda = 0{,}2$), the system undergoes additional simulations with restricted dimensions in x and y, and pressure coupling in the z direction. The force required to maintain the deformed membrane is calculated using the xx component of the stress tensor

($F_x = P_{xx}A_yA_z$). Moreover, Diggins e Deserno (2013) showed through the analytical solution of the stress-strain relation that this force is also equivalent to:

$$F = 4\pi^2 k_c \frac{L_y}{L} \sum_{i=0}^{\infty} b_i \lambda^i \tag{6.4}$$

where k_c is the bending modulus, L_y is the y dimension of the box, L is the x dimension of the initial box (before applying deformation), and b_i are coefficients proposed by Diggins e Deserno (2013). The infinite series represents the analytical solution by series expansion of the Helfrich Hamiltonian, which was truncated at its tenth term, since changes on the order of 10^{-6} were observed for higher values of i. The effects of thermal fluctuations were included in the overall force by addition of a term $\sigma F = -1{,}5 k_B T \sum_{i=0}^{\infty} d_i \lambda^i / L_x$, where σF are the contribution of thermal undulations to the force and d_i are coefficients published by Diggins e Deserno (2013). It should be noted that this method is highly dependent to the size of the system. For this purpose, larger membranes (consisting of 1000 molecules) were assembled in a $32 \times 8 \times 20$ nm^3 simulation box containing 35516 water molecules. The reason for using a larger system was to address convergence issues that were previously reported when applying this method to smaller membranes (EID et al., 2020).

6.2.4 Analysis of the interactions between HVs and a WALP peptide

One of the advantages of HVs compared to pure polymersomes is the functional incorporation of proteins, as discussed in Section 2.4.3. To understand thermodynamic aspects that favor protein reconstitution in these bilayers, simulations of a WALP peptide incorporated into the membrane were performed. WALP is a helical peptide composed of glycine, tryptophan, alanine and leucine that is widely used in computational biology as a model for transmembrane proteins (BEREAU et al., 2015; SOUZA et al., 2021; SPINTI et al., 2023). The dynamics of WALP in bilayers can be accurately described by Martini 3 as shown before (SPINTI et al., 2023), provided that the peptide length is not too short ($\leq$ 12 amino acids). Considering this, and the fact that transmembrane α-helices usually span between 17 to 25 amino acids (CHEN; ROST, 2009), the peptide WALP$_{23}$ was used, depicted in Figure 6.8. The CG model of WALP$_{23}$ was generated as follows: an AA representation was created using the Avogadro software,

with each residue assumed to adopt an α-helical conformation. Next, Martini beads with bonded parameters were assigned to each amino acid using the Insane python script (WASSENAAR et al., 2015). The peptide was then aligned and inserted into a pre-equilibrated membrane, and the system was subjected to an energy minimization using a steepest descent algorithm.

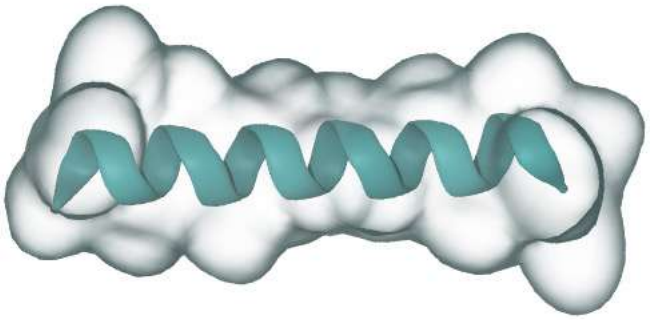

FIGURE 6.8. All-atom representation of the $WALP_{23}$ peptide.

To examine the interaction of the peptide with membranes of varied compositions, umbrella sampling (US) simulations were conducted. US is a sampling technique that allows the free energy calculation of complex systems and is useful when the system presents multiple thermodynamic states or energy barriers that prevent transitions between states. The method involves biasing the system along a specific reaction coordinate by adding an external potential energy term (umbrella potential). After performing US simulations at different points along the desired reaction coordinate, the data is combined to reconstruct the unbiased potential of mean force (PMF). The PMF represents the free energy profile along the chosen reaction coordinate and provides valuable insights into the thermodynamic behavior of the system. US simulations have already been conducted to analyze the dynamics of various peptides in lipid membranes (BEREAU et al., 2015; SOUZA et al., 2021), and are used in this study to assess the change in free energy that occurs when the peptide is pulled through HVs with different lipid/polymer compositions.

For the umbrella sampling analyzis, multiple configurations were generated, with the peptide gradually moved in increments of 0.1 nm along the z-axis towards the outer side of the bilayer, until it was fully immersed in water and no longer interacting with the membrane. A representation of the system and the histogram of the

umbrella sampling windows can be seen in Figure 6.9. In each configuration, a harmonic potential with an energy constant of 1000 kJ mol^{-1} nm^{-2} was applied to restrict the center of mass of the peptide in a given position. For each configuration (window), an energy minimization was performed followed by 50 ns equilibration on the isobaric-isothermal ensemble (NPT, P = 1 atm, T = 300 K). Data acquisition simulations were performed for 200 ns for each window. The PMFs were calculated using the weighted histogram analysis method (WHAM) (KUMAR et al., 1995) as implemented in the Gromacs tool *gmx wham*. The results were found to be consistent with equilibrium simulations by performing additional runs without restrictions on the peptide. The final position of the molecule was in agreement with the point of minimum energy in the PMF analysis for all cases.

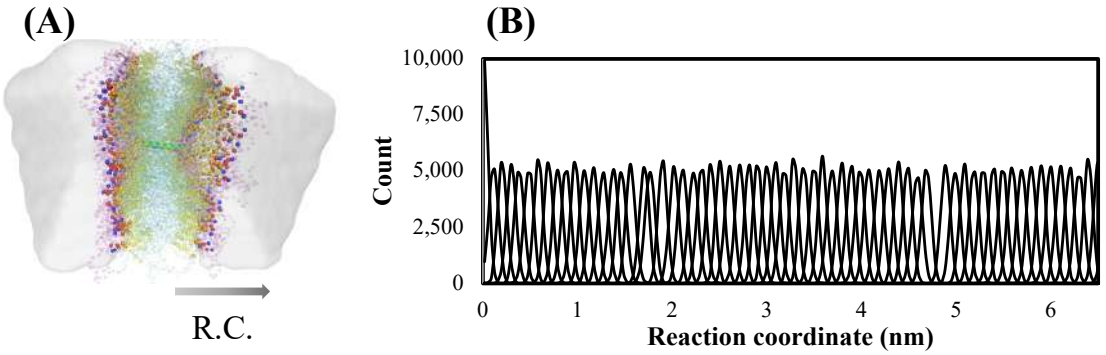

FIGURE 6.9. (A) Representation of a system used in the US simulations and (B) Histogram showing the overlap between adjacent windows.

Systems that showed an energy minimum when the peptide was in a transmembrane configuration were further examined in 5 μs simulations, which were conducted without restriction potentials for all four temperatures described previously. 2D profiles were analyzed to access the local impact of peptide insertion on different membrane compositions. The thickness and density of the membrane, as well as the order parameter of the lipid acyl chains, were calculated. Profiles were obtained by discretizing the membrane in a 0.5 nm grid along the x and y directions. To ensure that no empty cells were present, the non-local weighted-averaging method proposed by (CHAURASIA et al., 2018) was employed. This approach involves determining the local value of a variable by averaging the values of that property for all molecules within a radius of σ from the center of the cell, known as the horizon. The local value of a

generic variable $f(x_i)$ is then determined by the following relation:

$$f(\bar{x}_i) = \frac{1}{\sum_{j=1}^{N_c} w(r_{x_j})} \left[\sum_{j=1}^{N_c} w(r_{x_j}) f(x_j) \right] \tag{6.5}$$

where $w(r_{x_j})$ is the weight assigned to a particle at radius r_{x_j} away from the center of the element $\bar{x}_i$, $f(x_j)$ is the value of the measured property for this particle and N_c is the number of particles that lie within the horizon. The weights assigned to each molecule are given by 6.6:

$$w(r_{x_j}) = \frac{1}{1 - e^{-\alpha}} \left[e^{-\alpha r_{x_j}/\delta} - e^{-\alpha} \right] \tag{6.6}$$

It can be observed that the average weight of molecules decreases exponentially with distance from the center at a rate defined by α. The value of α can be adjusted to achieve a desired level of resolution and, in this study, $\alpha = 8$ and $\delta = 0{,}5$ nm, which have been found to provide an adequate sampling by preventing empty cells.

6.3 Experimental Methods

6.3.1 Hybrid Vesicles formation

The protocol for preparing pure and hybrid vesicles is similar to the previously published method of Seneviratne et al. (2018) and briefly described here. Initially, the PBD$_{22}$-*b*-PEO)$_{14}$ polymer was dissolved in chloroform to obtain a polymer suspension with concentration of 6.6 mM. Vesicles with different compositions were prepared by mixing corresponding aliquots of this suspension with 33 mM of POPC (Avanti Polar Lipids) dissolved in $CHCl_3$:MeOH. The procedure was performed in glass containers to avoid the incorporation of molecules from plastic containers into the solution. The mixture was then dehydrated in a vacuum desiccator for 6 hours, forming a multi-layered film of lipids/polymers, which was rehydrated with 1 mL of 20 mM HEPES buffer solution (Thermo Scientific, pH 7) containing 50 mM of the fluorescent dye 5(6)-carboxyfluorescein (Novabiochem).

Multilamellar vesicles were formed by heating cycles of 50°C for 5 minutes followed by vigorous vortex agitation for 1 minute, until the films were completely dissolved in the buffer. The resulting suspension was frozen in liquid nitrogen and heated

to 60°C, followed by vigorous agitation for 15 seconds. This cycle was repeated 5 times and is necessary to ensure the formation of vesicles for compositions with high polymer content, where the system dynamics evolves more slowly. To obtain unilamellar vesicles with reproducible size, the aliquots were subjected to 11 cycles of extrusion through a 100 nm polycarbonate membrane using an Avanti mini extruder. The extrusion was conducted at 60°C to facilitate sample extraction.

Vesicle formation was confirmed through dynamic light scattering (DLS) measurements, a technique that is based on the Brownian motion of particles suspended in a liquid. In this method, the sample is placed in a cuvette and exposed to a polarized laser beam. As light passes through the sample, it interacts with the suspended particles, leading to fluctuations in the intensity of the scattered light. These fluctuations are directly related to the movement and size of the particles (smaller particles exhibit faster fluctuations since they diffuse faster). The scattering light fluctuations are analyzed using an autocorrelation function, which correlates the scattered intensity at different time intervals. This autocorrelation function is employed to calculate the translational diffusion coefficient (D). Larger particles have lower diffusion rates, resulting in a longer correlation time and a faster decrease in the autocorrelation function. Conversely, smaller particles exhibit the opposite behavior. To determine the average hydrodynamic diameter of the particles (d), the value of D can be converted using the Einstein-Stokes relation: $d = \frac{k_b T}{6\pi\nu D}$, where k_b is Boltzmann's constant, T is the temperature, and ν is the viscosity of the liquid. The particle size distributions, as shown in Figure 6.10, indicate that the average vesicle size is approximately 100 nm, which is in line with the size of the filter used in the extrusion process.

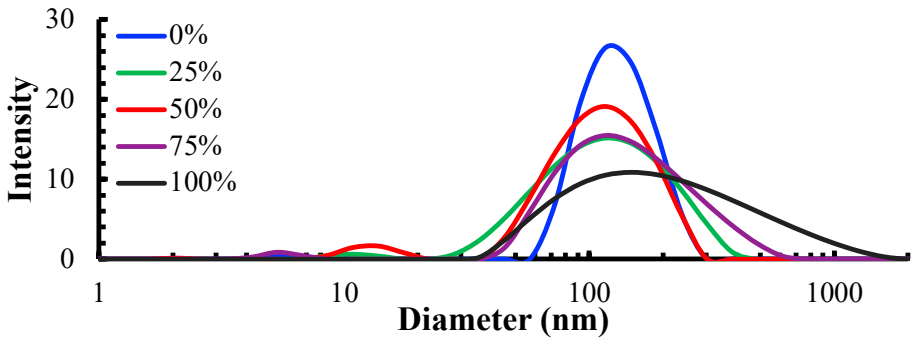

FIGURE 6.10. Vesicle diameter distribution for various polymer concentrations.

6.3.2 Fluorescence spectroscopy

The vesicles were formed in a solution containing carboxyfluorescein, which was then encapsulated. The excess of dye outside the vesicles was removed from the solution through size exclusion chromatography using a NAP-5 column (Cytiva) according to the manufacturer instructions. Therefore, almost all carboxyfluorescein was contained inside the vesicles. To evaluate the mechanical stability of these structures, fluorescence spectroscopy experiments were performed with the addition of detergent molecules. Detergents have the ability to destabilize the vesicles, resulting in the formation of micelles and the release of encapsulated dye molecules when the detergent concentration is high enough, which results in an increase in the fluorescence of the sample.

For this purpose, vesicle aliquots were diluted 100 times and exposed to varying concentrations of Triton X-100 (Sigma-Aldrich). Fluorescence measurements were conducted using a FLUOstar Omega plate reader with excitation and emission wavelengths set at 485 nm and 520 nm, respectively. The FLUOstar Omega plate reader employs a light source and a monochromator filter to separate the desired wavelengths, which are then directed onto the vesicle suspensions. During the measurements, the excitation light interacts with the fluorescent molecules in the dye, causing these molecules to absorb photons and elevate their energy levels. When the fluorescent molecules return to their ground state, they release the excess energy in the form of emitted light (fluorescence). Therefore, the fluorescence curves obtained are directly related to the released dye concentration and consequently, to the proportion of destabilized vesicles. The experiments were conducted at two different temperatures, 298 K and 318 K.

To obtain normalized curves, the fluorescence of the original samples was considered as 0 and the complete rupture caused by the addition of 10% Triton (m/v) was considered as 1. The collected data were fitted to a fourth-order logistic model (4PL), represented by the equation $F = d + (a - d)/[1 + ([T]/c)^b]$, where a is the theoretical response at zero concentration, b is the slope factor, c is the intermediate concentration (inflection point), and d is the theoretical response at infinite concentration. As the data were normalized, the values of a and d were fixed at 0 and 1, respectively, while the

remaining parameters were estimated using a Matlab code.

6.4 Results and discussion

6.4.1 Structural properties

Recently, the electron density profiles (EDPs) of hybrid vesicles composed of POPC and PBD_{22}-*b*-PEO_{14} were determined using SAXS and cryo-electron tomography techniques (SENEVIRATNE et al., 2023). To validate the simulation results, the EDPs at different temperatures were compared with the experimental data. The density profiles of both leaflets were found to be symmetrical and in agreement with the experiments, as depicted in Figure 6.11. Minor asymmetries were experimentally reported, and attributed to curvature effects at the membrane (SENEVIRATNE et al., 2023); as the simulation profiles are based on planar bilayers, this behavior was not seen, supporting the hypothesis of the authors. As the polymer fraction increases, the peak-to-peak distance becomes longer, indicating a larger membrane thickness. The peak-to-peak distance of a POPC membrane was reported to be 36.4 Å in SAXS experiments, while a cryo-electron microscopy analysis using a fast Fourier transform (cryo-FFT) showed a distance of 35 Å, in very good agreement with the value of 36.9 Å predicted in the simulations. Particular attention can be paid to the pure polymer membrane, as the present study aims to provide a reliable CG model for PBD-*b*-PEO. In this case, both SAXS and cryo-FFT reported a peak-to-peak distance of 108 Å, which is in close agreement with the simulation prediction of 106 Å.

Experimental observations have shown the existence of two distinct populations of 50:50 HVs, with different membrane thicknesses (SENEVIRATNE et al., 2023). One of these has an EDP similar to that of polymersomes ('thick' membrane), while the other resembles that of pure liposomes ('thin' membrane). This is an interesting observation given that earlier fluorescence studies have shown that POPC and PBD_{22}-*b*-PEO_{14} form well mixed and homogeneous vesicles containing both polymers and lipids in their composition (SENEVIRATNE et al., 2022). It was previously hypothesized that the coexistence of these two distinct membrane structures in otherwise homogeneously mixed membranes indicates that the thin and thick structures have

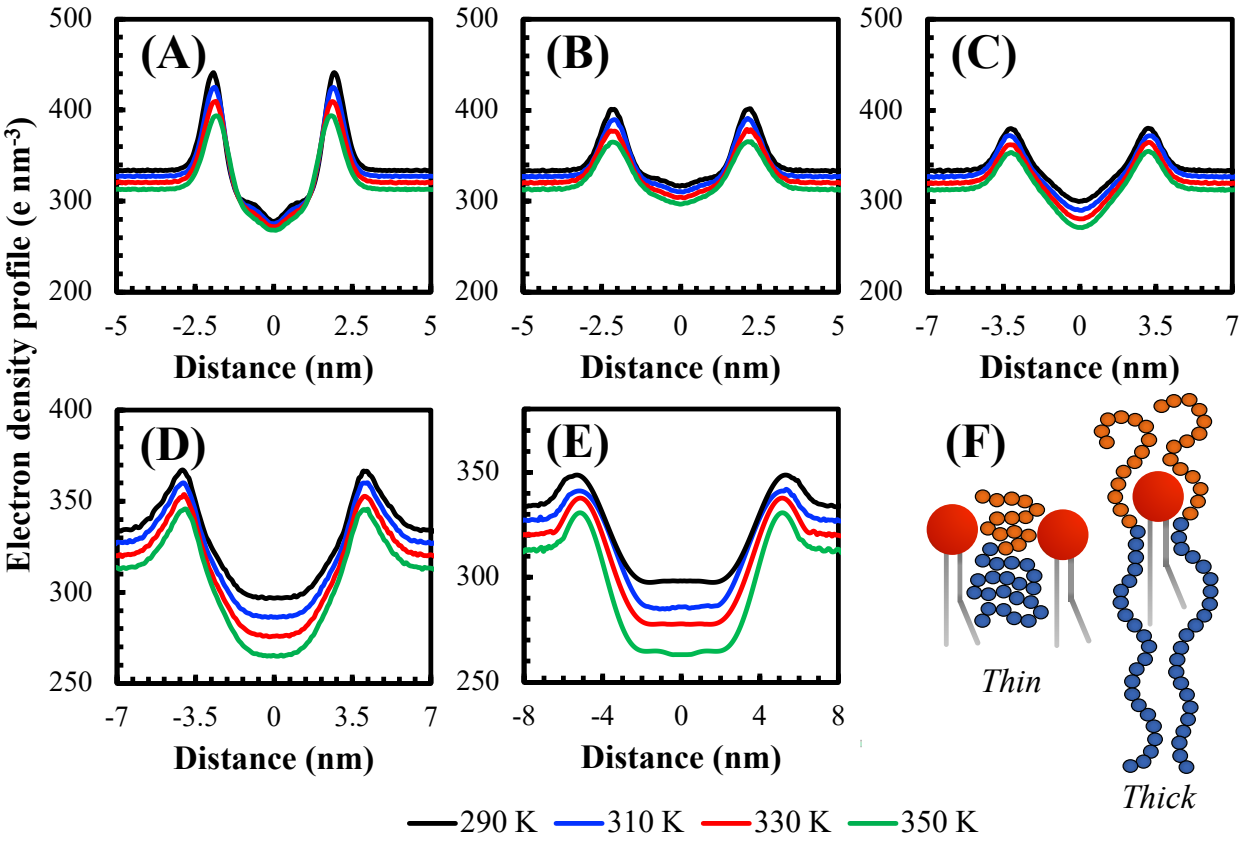

FIGURE 6.11. Electron density profiles as a function of distance from the bilayer center of mass obtained from MD simulations. (A) pure liposome, (B) 25% polymer:75% phospholipid HV, (C) 50:50 HV, (D) 75:25 HV and (E) pure polymersome. Proposed configurations for the thick and thin regions are shown in (F), where red, orange, and blue beads represent phospholipid headgroups, PEO monomers, and PBD monomers, respectively. The lines correspond to the lipid acyl chain.

comparable free energies, while intermediate structures are energetically unfavorable (SENEVIRATNE et al., 2023). The CG representation in the present study appears to accurately model the two distinct populations of HVs. Both lipid-only membranes and the 25 % polymer:75 % phospholipid HVs showed qualitatively similar EDPs and thin membranes (Figure 6.11.A and B and Figure 6.14.A). The same is true for the 75:25 HVs and pure polymersomes (Figure 6.11.D and E), which both show thick membranes. In the 50:50 simulations, the average membrane thickness falls between those of the two observed conformations (Figure 6.11.C and Figure 6.14.A), but closer inspection shows the coexistence of thicker and thinner regions (Figure 6.6). The co-existence of both phases for this particular composition was previously reported (SENEVIRATNE et al., 2023), which supports the accuracy of the present CG parametrization to model HVs.

While the existence of two different conformations is not readily visible in the average electron density profiles shown in Figure 6.11.C, Figure B.6 of the Appendix B shows separated profiles for each component in the system. This analysis reveals the presence of acyl chains both at the center and at the extremities of the bilayer, providing additional evidence of two configurations in the simulations. This can also be seen in Figure 6.12, which depicts the spatial distribution of the phosphate-phosphate distance between the leaflets for a 50:50 HV. The plot in Figure 6.12 shows distinct regions with a thickness comparable to that of POPC ($\approx$ 40 Å) surrounded by domains of thicker conformations ($\approx$ 70 Å). On average, approximately 20% of the membrane was in the thin configuration (defined here as having a thickness of 50 Å or less). Experiments (PERERA et al., 2022) and AA MD simulations (STEINKÜHLER et al., 2022) also revealed the presence of different conformations related to changes in the copolymer chain lengths and concentration.

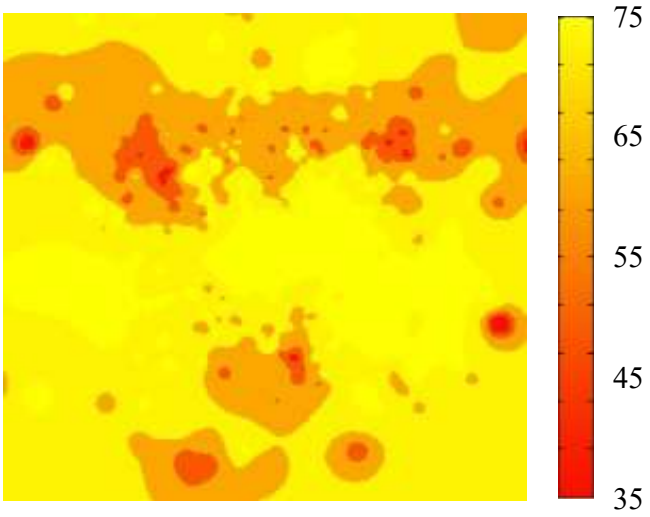

FIGURE 6.12. Membrane thickness profile for a 50:50 HV at 330 K showing the 'thin' and 'thick' regions.

As an effort to understand the nature and origin of these different bilayer conformations, a more detailed description of the regions with thinner and thicker conformations is presented. The bottom part of the membrane showed in Figure 6.6 displays the thinner conformation, where the phospholipids in opposite leaflets are closely packed, as observed in pure lipid membranes. The elastic chains of polymers are able to adjust

to this configuration by becoming more entangled and bending towards the lateral regions, as depicted in Figure 6.11F. Moreover, the apolar part of the polymers tend to interdigitate more tightly in this region to conform to its intricate topographical features, as shown in Figure 6.13. The polar part of the copolymer adopts a mushroom-like structure to conform to the choline and phosphate groups of the phospholipid head group. In general, mushroom-like structures are formed at low polymers density (BACKMANN et al., 2010), and therefore the thin region may result from a slightly lower local polymer concentration in the bilayer. Figure 6.14.B supports this conclusion by showing that the lateral areas of lipid/polymer mixtures increases in 25:75 HVs, which is expected when a collapsed structure is present. In the case of the thicker conformation at the top part of the membrane depicted in Figure 6.6, a locally high polymer density results in a extended polymeric structure, with a more elongated configuration for both the polar and apolar units (as also seen in Figure 6.11.F) and reduced degree of polymer interdigitation (Figure 6.13). The phospholipids in both leaflets are then located at the hydrophobic-hydrophilic interface of the copolymer, with minimal interaction between the phospholipids in opposite leaflets.

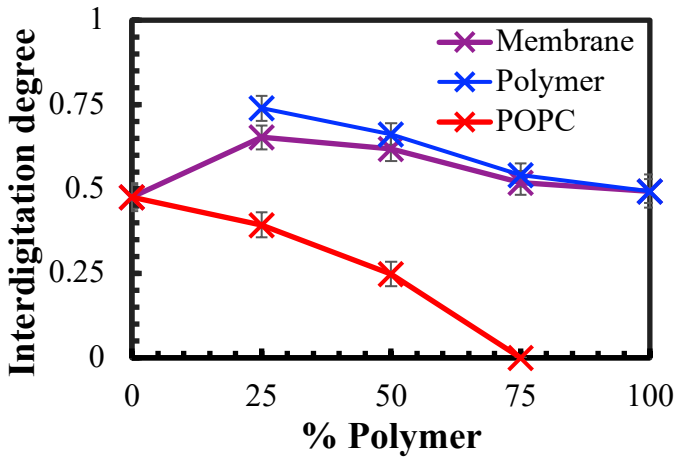

FIGURE 6.13. Fraction of overlap between leaflets for different HVs at 330 K.

Seneviratne et al. (2023) previous study did not find different membrane configurations within the same vesicle, but vesicles exhibiting either thicker or thinner conformations. In the simulations, both conformations were observed within the same membrane for 50:50 HVs. This deviation can be understood by a more in-depth analysis of the lipids/polymers concentration at each phase. In the thinner region, the

polymer-lipid ratio was slightly lower (at around 40% polymer and 60% lipid), causing the polymer to conform to the lipid structure. This conformation was caused by the polymer adopting a more entangled structure and a higher degree of interdigitation, as discussed in the previous paragraph. On the other hand, when the polymer concentration was slightly higher, the phospholipid adapted to the elongated structure of the polymer. This observation suggest that, even though the vesicle preparation in experiments use a 50:50 ratio, slightly different compositions between individual vesicles might drive the complete vesicle towards either a thin or thick conformation. In the simulations, an exact 50:50 proportion was used, and therefore the different configurations resulted from local fluctuations in the polymer-lipid concentration within a region of the same membrane.

The average lateral area, membrane thickness, order parameters of the acyl chains and lateral diffusion coefficient at various temperatures and membrane compositions obtained from the simulations are presented in Figure 6.14. Small angle neutron scattering experiments measured average lateral areas of POPC, which ranged from 0.627 to 0.681 $\pm$ 0.013 nm^2 for a temperature range of 293 to 333 K (KUČERKA et al., 2011). These results agree well with the present simulations, which predicted values between 0.635 and 0.689 nm^2 for similar temperature conditions (290 to 330 K) as shown in Figure 6.14.B. Varied estimates for this variable have been reported for copolymers, depending on the level of analysis and whether experiments or simulations were analyzed. For a slightly longer chain (PBD_{23}-*b*-PEO_{16}), cryo-TEM measurements by Kowalik et al. (2017) reported a lateral area of 0.65 $\pm$ 0.05 nm^2. The authors also proposed a CG model for this slightly longer molecule, which predicted a lateral area of 0.77 nm^2 at 323 K. An AA model was proposed for PBD_{22}-*b*-PEO_{14} using the CHARMM FF and found an area of 0.87 nm^2 (STEINKÜHLER et al., 2022). The results of the present study are lower than those reported in previous simulation studies, but are in better agreement with cryo-TEM results (KOWALIK et al., 2017). Bermudez et al. (2002) developed a mathematical model based on experimental measurements to estimate the lateral area of diblock copolymers as a function of the molecular weigth of the hydrophobic block. Using the parameters for hydrophobic chains with intermediate to high molecular masses ($>$ 1 kg mol^{-1}), the expected area of PBD_{22}-*b*-PEO_{14} is of 0.63 nm^2, in agreement with the cryo-TEM measurements. The presented results agree well with these experimental observations and tend to slightly underestimate it

by $\approx 6\%$.

Although the lateral area of the pure polymer membrane is smaller than that of the pure phospholipid, the addition of a small amount of polymers (25%) to a POPC membrane leads to an increase in this area. This supports the hypothesis of a collapsed polymer structure at low polymer concentrations, as discussed earlier. Moreover, the lateral area exhibits a similar qualitative trend as experimentally-obtained permeability profile of these vesicles (permeability increases for 25:75 HVs and decreases at higher polymer concentrations) (SENEVIRATNE et al., 2018). Previous researches on phospholipids have established a correlation between permeability and lateral area. Specifically, membranes with higher lateral area exhibit higher permeability due to the formation of local defects such as gaps or disordered regions (MATHAI et al., 2007; LEONTIADOU et al., 2004). These defects can serve as pathways for molecules or ions to cross the lipid bilayer, ultimately resulting in higher permeability. Given these findings and the aforementioned similar trend between the simulations results and previous experimental reports (SENEVIRATNE et al., 2018), it is possible to infer that the same relationship holds for hybrid vesicles. In addition, the lateral area increased with temperature, likely due to the increased mobility of the molecules, which reduces the packing density of the membrane and increases its lateral area.

The order parameter of phospholipids is shown in Figure 6.14.C and an interesting trend is found: as the polymer content increases, S_{cd} decreases, indicating that the entropy of the acyl chains of phospholipids rises at higher polymer concentrations. In addition, S_{cd} offers information about the state of the lipids, with lower and higher values indicating a more fluid or gel-like state, respectively. This observation may help explain some previous experimental reports related to the incorporation of membrane proteins into HVs, specifically with respect to the more amenable reconstitution into these structures (JACOBS et al., 2019; CATANIA et al., 2022). Given that increased fluidity can increase the permeability of membranes (SASTRE et al., 2020), the elevated entropy of the side chains may be a plausible explanation for this phenomenon. It is worth noting that S_{cd} applies only to the lipids and not to a broader effect throughout the entire membrane. Diblock copolymers often exhibit high viscosity (DIMOVA et al., 2002), which may lead to a general increase in membrane adhesion forces, as confirmed by fluorescence anisotropy measurements (JACOBS et al., 2019). Furthermore,

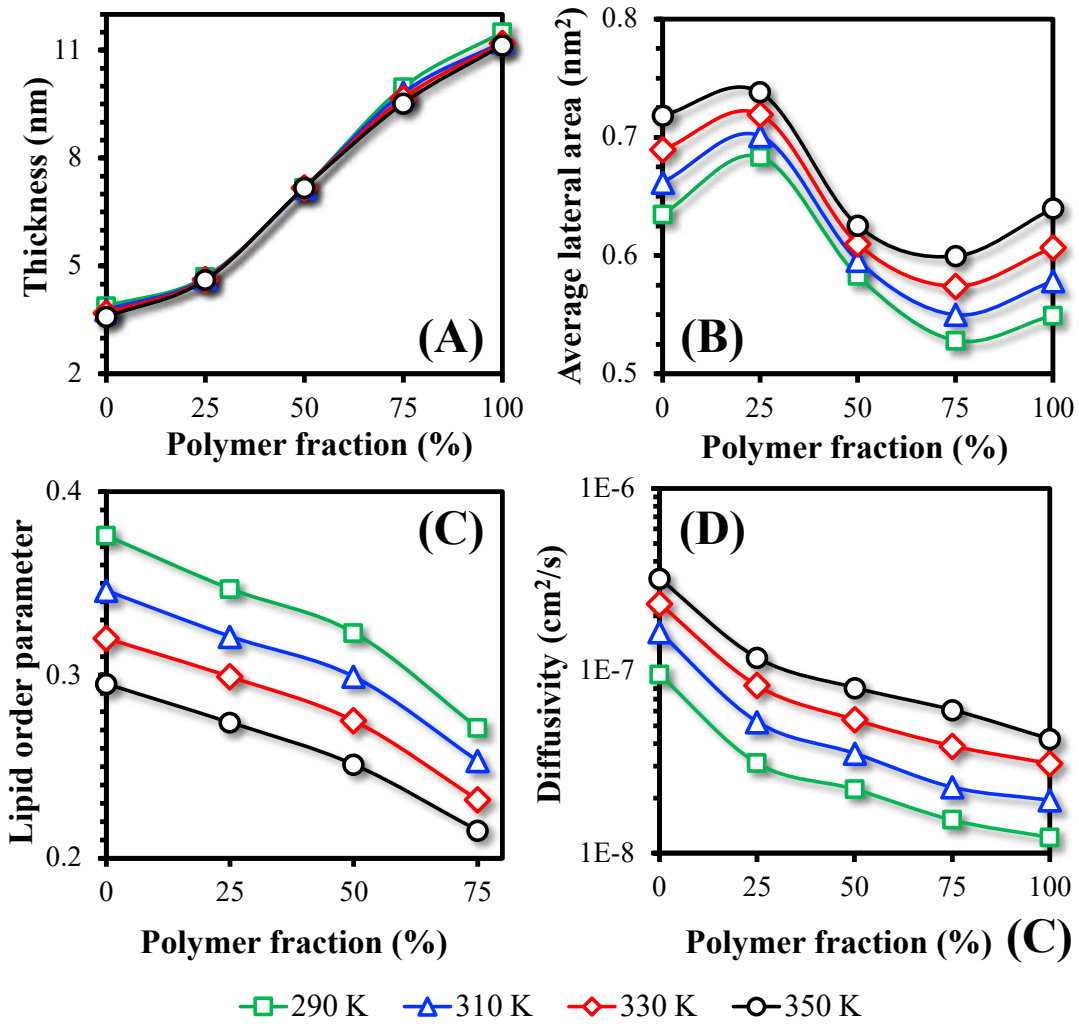

FIGURE 6.14. HVs (A) thickness, (B) lateral area, (C) lipid order parameter and (D) mass diffusivity as function of polymer composition for varied temperatures, computed from the simulations.

an increase in temperature causes a corresponding increase in the entropy of the acyl chains, reducing the order parameter and increasing the membrane fluidity.

Figure 6.14.D shows the average lateral mass diffusion coefficient of the membranes at different temperatures, whereas the lateral mass diffusion coefficients for both lipids and polymers separately is depicted in Figure 6.15, which agree with previous fluorescence recovery after photobleaching measurements (SENEVIRATNE et al., 2022). The simulations show that the overall diffusion coefficient of the membrane increases significantly with temperature, while it decreases with polymer content. This indicates that indeed a decrease in fluidity is observed in the membranes

with higher polymer concentration, as suggested in the previous paragraph. Additionally, fluorescence experiments revealed that HVs of POPC and a polymer with a longer chain (PBD_{48}-*b*-PEO_{30}) also exhibited decreased fluidity as the polymer content increases (NAM et al., 2010). This observation suggests that the addition of this type of block copolymer may generally reduce membrane fluidity. The individual diffusivity of POPC in the simulations is higher than that of PBD-*b*-PEO, which is expected due to the reduced free volume required for lipids to hop laterally between sites in the membrane matrix (SENEVIRATNE et al., 2022). Moreover, higher temperatures lead to more fluid membranes as a result of decreased viscosity and increased molecular mobility (SAFFMAN; DELBRüCK, 1975). The simulated values are in good agreement with the diffusivity range measured experimentally for pure POPC membranes at room temperature using NMR ($3{,}2\times10^{-8}$ - $1{,}9\times10^{-7}$ $cm^2\ s^{-1}$) (GAEDE; GAWRISCH, 2003; SALEEM et al., 2012).

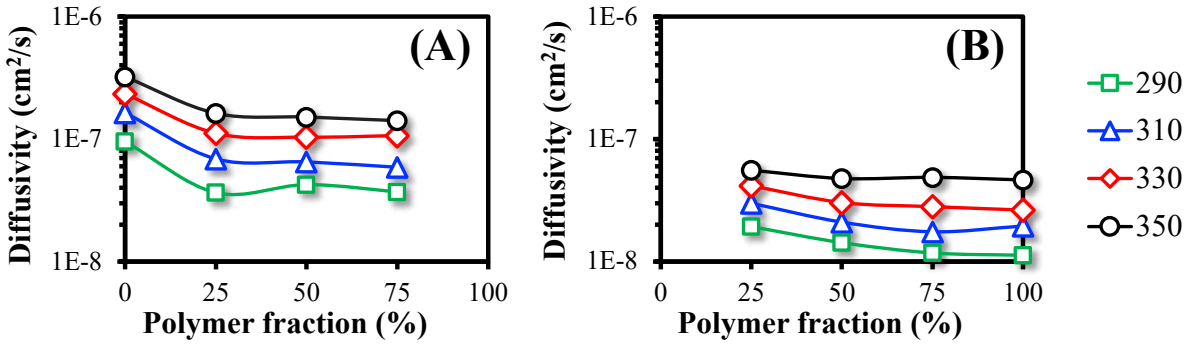

FIGURE 6.15. Lateral diffusion coefficient at varied temperatures for (A) POPC and (B) PBD_{22}-*b*-PEO_{14}.

The results of this subsection helped to shed some light into HV-related phenomena, such as the reasons behind the presence of two distinct membrane conformations despite the absence of clear phase separation between polymers and lipids. Additionally, the structural properties predicted by the proposed model are in very good agreement with previous experimental results for both pure liposomes/polymersomes and HVs. The dependence of several of these properties with the polymer content potentially enables tuning the membrane environment for several practical applications of HVs, as discussed elsewhere for drug delivery and synthetic biology (KHAN et al., 2020; MARUŠIČ et al., 2022; BRODSZKIJ et al., 2022). One of the most noteworthy

benefits of incorporating polymers in lipid membranes is the enhancement of vesicle robustness, which is closely tied to their mechanical properties, addressed in the next section.

6.4.2 Mechanical behavior

The lateral pressure profiles of the simulated bilayers under all conditions studied are presented in Figure 6.16, providing valuable insight into membrane interactions by revealing the relationship between stress and strain on these structures. The pressure in all curves approaches zero at the edges of the simulation box, demonstrating that the systems are fully hydrated. Positive and negative peaks indicate areas where expansion and contraction forces are dominant, respectively. Importantly, these forces decrease with increasing polymer content, suggesting that polymer-based membranes are subjected to lower local stresses.

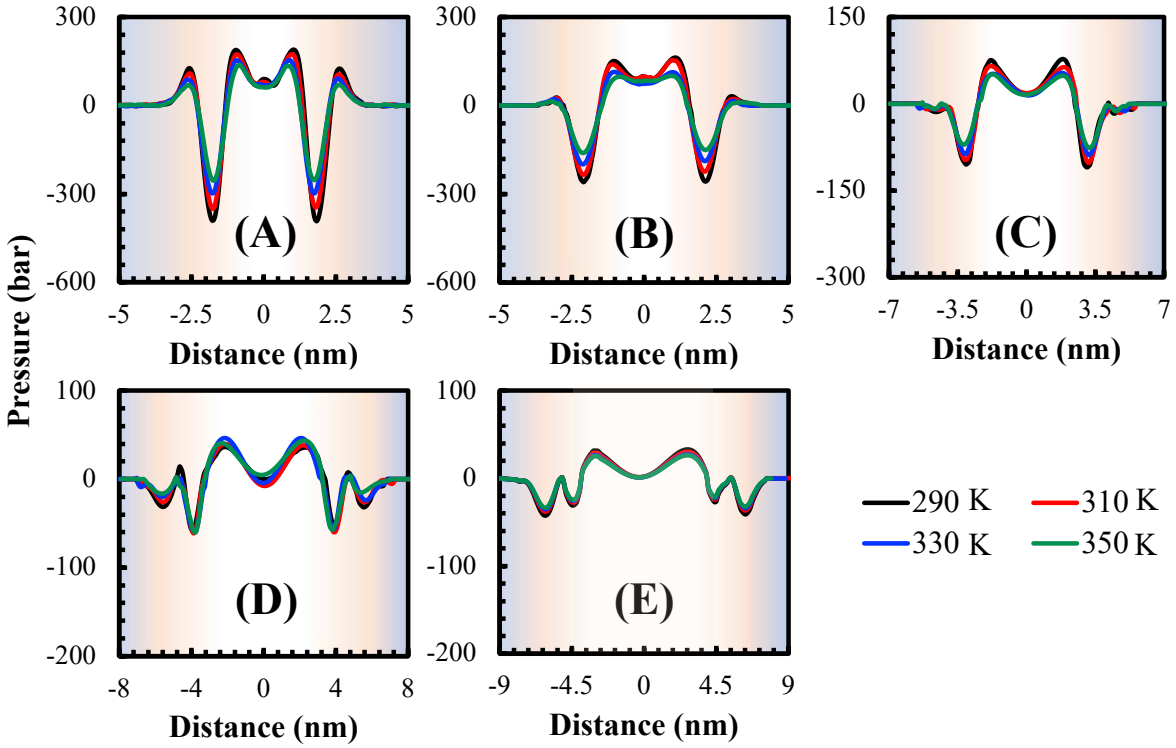

FIGURE 6.16. Lateral pressure profile as a function of the distance to the bilayer center of mass at varied temperatures for (A) pure liposome, (B) 25 polymer:75 phospholipid HV, (C) 50:50 HV, (D) 75:25 HV and (E) pure polymersome. The colored regions correspond to the water (extremities), hydrophilic region and hydrophobic core (center).

In lipid bilayers, the two positive peaks at the extremities are associated with the polar head-groups, where repulsive electrostatic interactions and steric effects at the membrane-water interface generate an expansion force at the bilayer. There is also a positive peak in the hydrophobic core region, which is slightly decreased in the center of the membrane where cohesion between lipids takes place. To counterbalance these repulsive forces, the glycerol groups at the hydrophilic/hydrophobic interface exert an attractive compressive force. These results are consistent with profiles reported previously for POPC membranes (DOMINGUEZ et al., 2016; ARYAL et al., 2017). The first moment of the stress profile ($\int_{-\infty}^{\infty} \tau dz = 0$) is close to zero, as shown in Table 6.2, indicating that the compressive and expansive forces are in balance, as expected for stress-free bilayers.

The pressure profiles observed for HVs show a dependence on the polymer-to-lipid ratio. At 25:75, the profile is similar but smoother when compared to pure lipid bilayers, suggesting a reduction in the intensity of local forces as polymers are incorporated into the membrane. For 50:50 HVs, a negative peak starts to appear at the edges of the bilayer, followed by a decrease in the positive peak related to the hydrophobic core. At a 75:25 ratio, this behavior is even more pronounced. These results suggest that PEO contributes to the cohesion of the bilayer, replacing the compression forces previously exerted by the glycerol groups. Indeed, in pure polymer membranes, there is no positive peak in the hydrophilic core, but only two negative peaks, indicating that the attraction force is caused mainly by the hydrophilic chain and its interactions with water (first negative peak) and the hydrophilic core (second negative peak). As for the effects of temperature, a slight decrease in the stress profiles is observed for the same composition as T increases, suggesting that the mechanisms described above are similar at different T conditions. Similar qualitative/quantitative profiles for polymer membranes have been also reported before (GRILLO et al., 2018).

The pressure profiles results for HVs have implications for the reconstitution of membrane proteins. High pressures in hydrocarbon cores can hinder the insertion of proteins into these environments (FIEDLER et al., 2010). The simulations indicate that an increase in the polymer concentration may reduce the intensity of the repulsion in the hydrophobic core, potentially making it easier for proteins to be incorporated. This aspect will be addressed in the next section. To gain a more comprehensive un-

derstanding of the mechanical properties of HVs, a combination of simulations with experiments was performed. The results are presented in Figure 6.17, which illustrates the elastic moduli obtained from simulations, as well as the mechanical stability of the vesicles following the addition of Triton X-100 in experiments.

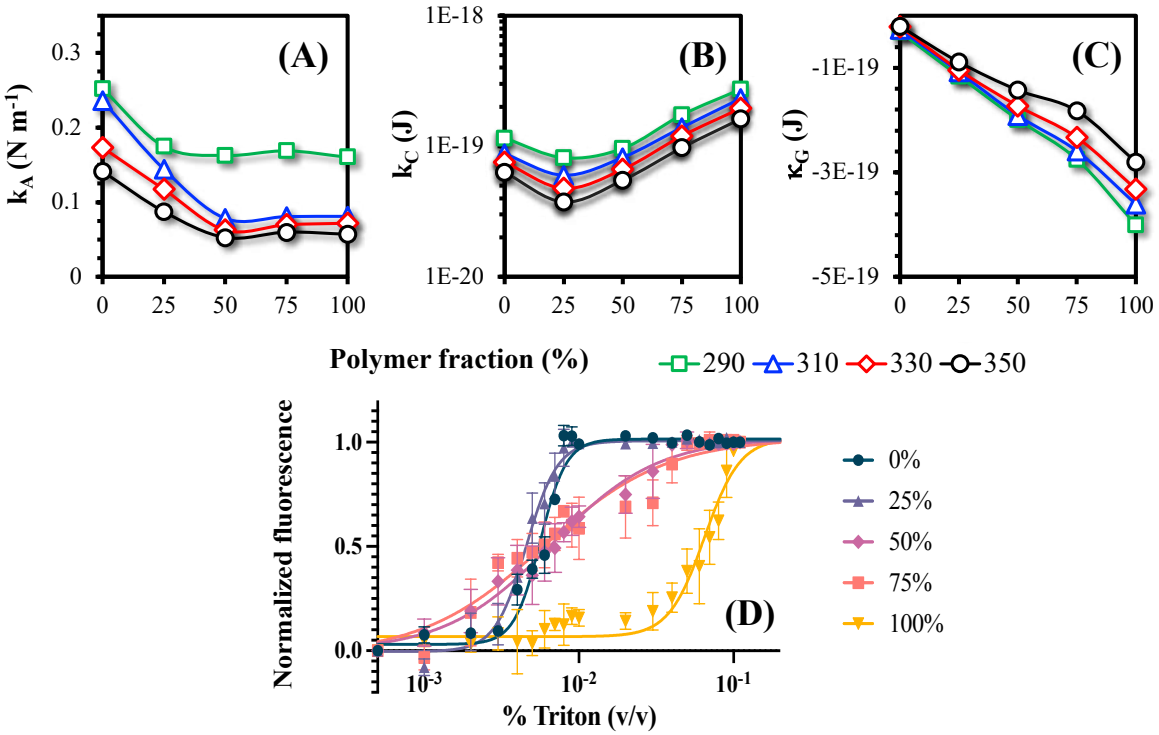

FIGURE 6.17. HVs (A) area compression, (B) bending, and (C) Gaussian curvature modulus as function of polymer composition for varied temperatures, as computed from the simulations; (D) Triton X-100 destabilization profile at 25°C for varied polymer concentrations measured in the experiments.

It can be seen that the area compressibility modulus k_A tends to decrease with increasing polymer content, indicating that lower stresses are needed to expand or compress the bilayer, in line with the obtained pressure profiles. The values for 50:50 and 75:25 HVs and polymersomes were almost identical, suggesting that this moduli can be significantly reduced by just adding 50% polymers into a lipid bilayer. This reduction of k_A (along with the increased POPC side-chain entropy reported in the previous section) can contribute to the easier insertion of peptides in HVs compared to pure phospholipids. This hypothesis was previously suggested in by Jacobs et al. (2019), who experimentally determined a $k_A = 0{,}103 \pm 0{,}005$ J m^{-2} for PBD-*b*-PEO at

room temperature, which is in good agreement with the averaged value obtained in the simulations on the 290-330 K range of 0.105 J m^{-2} (error = 1.9%). Furthermore, a decrease in k_A for POPC/PBD_{44}-*b*-PEO_{30} hybrid vesicles was previously reported (NAM et al., 2010), which further supports the simulation results. Higher temperatures resulted in lower k_A values, which is consistent with experimental observations, and is related to the increased thermal fluctuations of bilayers at higher T, as predicted by statistical thermodynamics theory (HEIMBURG, 1998). Moreover, experimental values for pure lipid bilayers range from 0.15 - 0.25 J m^{-2}, with a value of 0.21 J m^{-2} for POPC (WEBER et al., 2014), which is in good agreement with the average value of 0.2 J m^{-2} from the simulations.

The bending modulus k_C is a crucial mechanical parameter of lipid bilayers, as it quantifies the energy required to deform the membrane from its natural curvature to a different shape. The results are shown in Figure 6.17.B and, in general, as the polymer fraction increases, the bending modulus increases as well. However, an exception is observed in the 25:75 case, where a decrease is observed instead. Generally, a higher polymeric content results in vesicles with higher stiffness (CZERNOHLAVEK; SCHUSTER, 2020), and hence a higher k_C is expected in these structures, in line with the simulation results. The deviant behavior in the 25:75 case may be due to the increase in lateral area under these conditions (as shown in Figure 6.14.B). In general, larger bilayers are more flexible and easier to bend (SEIFERT, 1997), so the slight decrease in k_C in this case may be attributed to the higher surface area in these conditions. Regarding temperature effects, higher T increases the thermal energy of the system, causing the molecules in the bilayer to become more disordered and undergo greater thermal fluctuations. This effect makes the membrane more easily deformable and reduces the bending modulus of the bilayer (PAN et al., 2008). This behavior was observed in all lipid/polymer mixtures studied.

The Gaussian curvature modulus κ_G describes the energy cost of changing the Gaussian curvature of a surface while preserving its mean curvature, in contrast to k_C, which describes the energy cost of deforming a surface to change its mean curvature. Increasing the polymer content and temperature leads to a lower Gaussian curvature modulus, as shown in Figure 6.17.C. The negative values obtained indicate that, for all the lipid compositions studied, the formation of a vesicles is favored. Conversely,

positive values indicate that other conformations such as tubular or inverted hexagonal structures are preferred (as opposed to vesicles). The elastic ratio k_C/κ_G is a useful parameter for characterizing the how easily the structures of those vesicles can be changed, as it combines information from both the bending and Gaussian moduli. Stable vesicles have elastic ratios below 0 (TEMPLER et al., 1998), which is observed in all cases. However, the values of the elastic ratios vary between $\approx$ -0.3 for pure POPC and $\approx$ -1.6 for pure polymer vesicles. This suggests that although vesicular structures are thermodynamically favored in both cases (elastic ratio ≤ 0), pure POPC membranes are more susceptible to destabilization (formation of micelles or disorganized structures).

While these elastic moduli and their relationships provide valuable insights into the mechanical properties of the bilayers, they do not directly translate into quantitative assessments of the mechanical stability. Assessing stability through molecular dynamics simulations is challenging due to limitations in the simulation time scales (up to ns-μs). Lim et al. (2013) used fluorescence experiments to investigate the disruption of vesicles caused by naturally occurring pores on the membrane surface. They found that the addition of polymer significantly delayed the natural release of dye, and in the case of pure polymersomes, the release was less than 10% even after five days. However, it is unclear whether this stability persists under adverse conditions. Based on the previous discussion of the elastic ratio, it can be predicted that polymer-rich membranes will lead to more stable vesicles even under increased mechanical stress.

To confirm this hypothesis, fluorescent experiments on vesicle stability were conducted, exposing them to different detergent concentrations at two temperatures (298 K and 323 K). The results at 298 K are presented in Figure 6.17.D. Overall, the results of the detergent destabilization experiments corroborated an important characteristic of HVs: improved mechanical stability compared to pure liposomes. For pure liposomes, when the detergent concentration reached 0.003 % (v/v), the encapsulated carboxyfluorescin started to be released and, at a concentration of 0.009 %, the encapsulated dye was already fully released. Similar results were obtained at 45°C, although the fluorescence reached its maximum value more quickly (C = 0.008 %), indicating that the kinetics of lipid destabilization is accelerated at higher temperatures. A similar behavior in 25:75 HVs was observed, and a comparison of the 4PL model parameters provided in Table 6.3 shows that the kinetic behavior in both cases is indeed

similar.

TABLE 6.3. 4PL parameters and regression coefficient for varied polymer/lipid ratios.

	b	c	R^2
0:100	0.0058	5.89	0.979
25:75	0.0045	4.10	0.990
50:50	0.0069	1.29	0.991
75:25	0.0073	1.06	0.962
100:0	0.0667	4.11	0.978

At higher polymer concentrations, the destabilization rate was considerably slower, with complete leakage occurring only at detergent concentrations of 0.05 and 0.07 $\%$ for 50:50 and 75:25 compositions, respectively. This indicates a nearly tenfold increase in detergent concentration necessary to completely disrupt vesicles with higher polymer concentration. This can also be seen by the logistic model parameter b on Table S3 of the Supporting Information, which shows that higher Triton concentration is required to achieve 50$\%$ of the maximum leakage in polymer-rich HVs compared to pure liposomes and 25:75 HVs. Furthermore, the lower c parameter observed for the 50:50 and 75:25 vesicles, compared to pure liposomes, suggests slower disruption kinetics in these cases. These findings are in agreement with a previous study by Nam et al. (2012), which reported that the addition of detergent primarily affects lipid-rich domains, but leakage is prevented by the presence of surrounding polymer molecules that cover the resulting pores. For pure polymersomes, complete disruption was achieved at detergent concentration of 0.09 $\%$, but the leakage only began when $C_{Triton} = 0{,}01\%$. These results indicate a substantial increase in vesicle stability upon the addition of PBD_{22}-*b*-PEO_{14}, which is in good agreement with the aforementioned simulation results of lower elastic ratios in such conditions.

In conclusion, the addition of polymers has an impact on all measured mechanical properties. Lateral pressure profiles and the area compression-expansion modulus from the simulations indicate that the forces required to stretch the membrane are significantly lower in polymer-rich vesicles. The combined effect of the bending and Gaussian curvature moduli indicates that polymer-rich membranes result in more stable vesicles, as confirmed by the fluorescence leakage experiments under addition of

detergent. Therefore, as noted in several publications (KHAN et al., 2016; SENEVIRATNE et al., 2018; JACOBS et al., 2019; CATANIA et al., 2022; SENEVIRATNE et al., 2022; SENEVIRATNE et al., 2023; STEINKÜHLER et al., 2022), HVs are robust structures that can be used as effective alternatives to pure polymersomes and liposomes. This set of mechanical parameters shows that HVs have a potential advantage over pure liposomes/polymersomes when applied in the release of encapsulated compounds. In the context of drug delivery, it is crucial for vesicles to withstand the high osmotic pressure and shear flow in blood vessels without leakage. This property can be finely tuned by controlling the polymer/lipid ratio (MEINS et al., 2013). While lipids tend to destabilize rapidly, polymersomes are often too stable and do not provide a sufficiently quick release (REIMHULT; VIRK, 2021). The calculated moduli and detergent stabilization profiles highlight the potential of HVs to modulate drug release, as supported by Reimhult e Virk (2021). To explore the interaction of HV with membrane proteins, the following section will focus on the dynamics of pure and hybrid vesicles with the $WALP_{23}$ peptide.

6.4.3 Incorporation of WALP peptide

The free energy profiles of the $WALP_{23}$ peptide as it is extracted from the bilayer starting from the N-terminus (computed from US simulations) are depicted in Figure 6.18. As the free energy of solvation of the peptide in water is equal for all membranes, the aqueous region that is far from the membrane's surface was chosen as reference point. In other words, this region serves as a baseline where the PMF value is equal to 0 kJ mol^{-1}.

For the 50:50 HVs, two scenarios were analyzed: the peptide starting from either the thin or the thick region (as defined and discussed previously). It is evident that the PMFs vary significantly among different membrane compositions. In pure liposomes and 25:75 HVs, the lowest energy is found at the center of the bilayer and energy gradually increases as the peptide moves away from the membrane and into the solvent, indicating that the transmembrane orientation of the peptide is thermodynamically favored, as previously reported (SPINTI et al., 2023; YUE et al., 2016). As the peptide moves away from the center, energy increases due to the increased repulsive interac-

tion between the hydrophobic helix core and the membrane hydrophilic region. At the same time, the C-terminus is moved into the hydrophobic core of the bilayer, also contributing to the energy increase. When the peptide reaches the hydrophilic area of the membrane, it aligns along the x-y plane to minimize surface contact between its charged ends and the acyl chains of the bilayer, and in this region the energy remains almost constant. After the peptide is fully removed from the bilayer, its charged termini are still attracted to the POPC head groups via electrostatic interactions, causing the system's energy to increase as the peptide moves away from the membrane. Once the peptide-bilayer distance exceeds the electrostatic cutoff (i.e., the peptide is sufficiently far from the membrane surface), the free energy of the system remains constant.

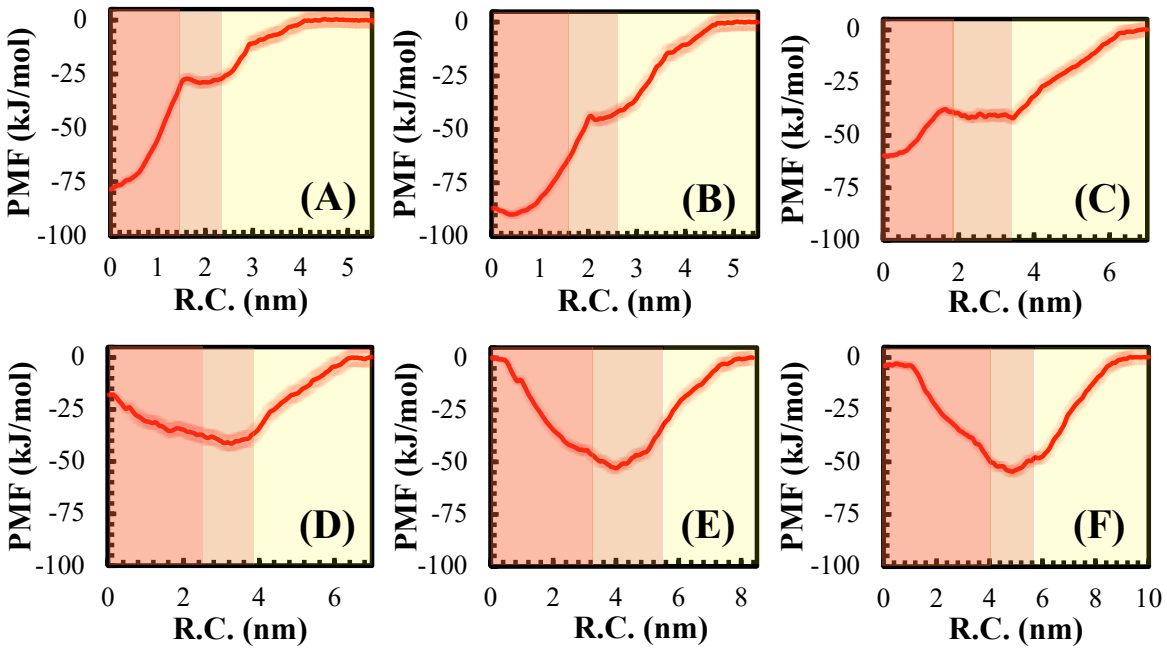

FIGURE 6.18. Potential of mean force as a function of the reaction coordinate for (A) pure liposomes, (B) 25:75 HV, (C) 50:50 HV with the peptide in the thin region, (D) 50:50 HV with the peptide in the thick region, (E) 75:25 HV and (F) pure polymersome. The colored regions, from left to right, correspond to the hydrophobic core, hydrophilic region, and water, respectively.

For 50:50 HV bilayers, the behavior of the peptide depends on its starting location (thin or thick region). If it starts within the thin region, a profile similar to that seen for lower polymer fractions is observed (Figure 6.18.C), although the differ-

ence in free energies between the transmembrane and fully solvated configurations is slightly smaller, indicating that less energy is required to extract the peptide from the membrane. Notably, the energy difference between the bulk water and the initial interaction with the membrane hydrophilic part is larger than in the case of pure lipid membranes. This suggests that the initial interaction of the peptide with the protein is more favorable for 50:50 HVs, which could help to explain why proteins insert more readily into HVs than into liposomes, as observed in *in vitro* reconstitution studies (JACOBS et al., 2019; CATANIA et al., 2022). Conversely, when the peptide starts within the thick region of the 50:50 HVs, a different profile is obtained, with the energy minimum shifted to the hydrophilic part of the membrane. In this case, the charged termini of the peptide cannot reach the hydrophilic regions of the membrane due to the significant size difference between the thickness of the bilayer and the length of the peptide. As the peptide moves closer to the hydrophilic core, the energy decreases and reaches a minimum when the peptide is parallel to the bilayer plane and fully inserted into the hydrophilic region, where electrostatic interactions between the polar components of the membrane and the charged termini of the peptide are minimized. Upon removal from the bilayer, the energy increases again due to the electrostatic attraction to the membrane, as previously mentioned. Similar behavior is also observed for 75:25 HV and pure polymersomes (Figure 6.18.E and 6.18.F, respectively).

The PMF results presented demonstrate that the composition of hybrid vesicles can impact the behavior of peptides in the membrane. Cytochrome bo_3 exhibited higher initial activity when embedded in a pure liposome, with 95 ± 5 and 81 ± 11 % of this activity being maintained in 25:75 and 50:50 HVs, respectively (KHAN et al., 2016). In contrast, only 34 ± 5 and 5 ± 1 % of this activity was retained in 75:25 and pure polymersomes. The simulation results support these experimental findings, as the peptide was found to have an energy minimum in a transmembrane configuration only when the bilayer composition consisted of up to 50% polymer. To further analyze the membrane arrangements near the peptide, Figure 6.19 provides a visual representation of the membrane thickness, density, and order parameter of phospholipid acyl chains for the mixtures in which a transmembrane peptide was found to be energetically stable (0, 25, and 50% collapsed polymer fraction). The results are displayed as contour plots in the bilayer plane, which is perpendicular to the axis of peptide insertion. To facilitate analysis, the peptide was positioned at the center of the simulation

box. The results are presented for a temperature of 310 K, with additional profiles for other temperatures available in Figures B.1-B.5 of Appendix B.

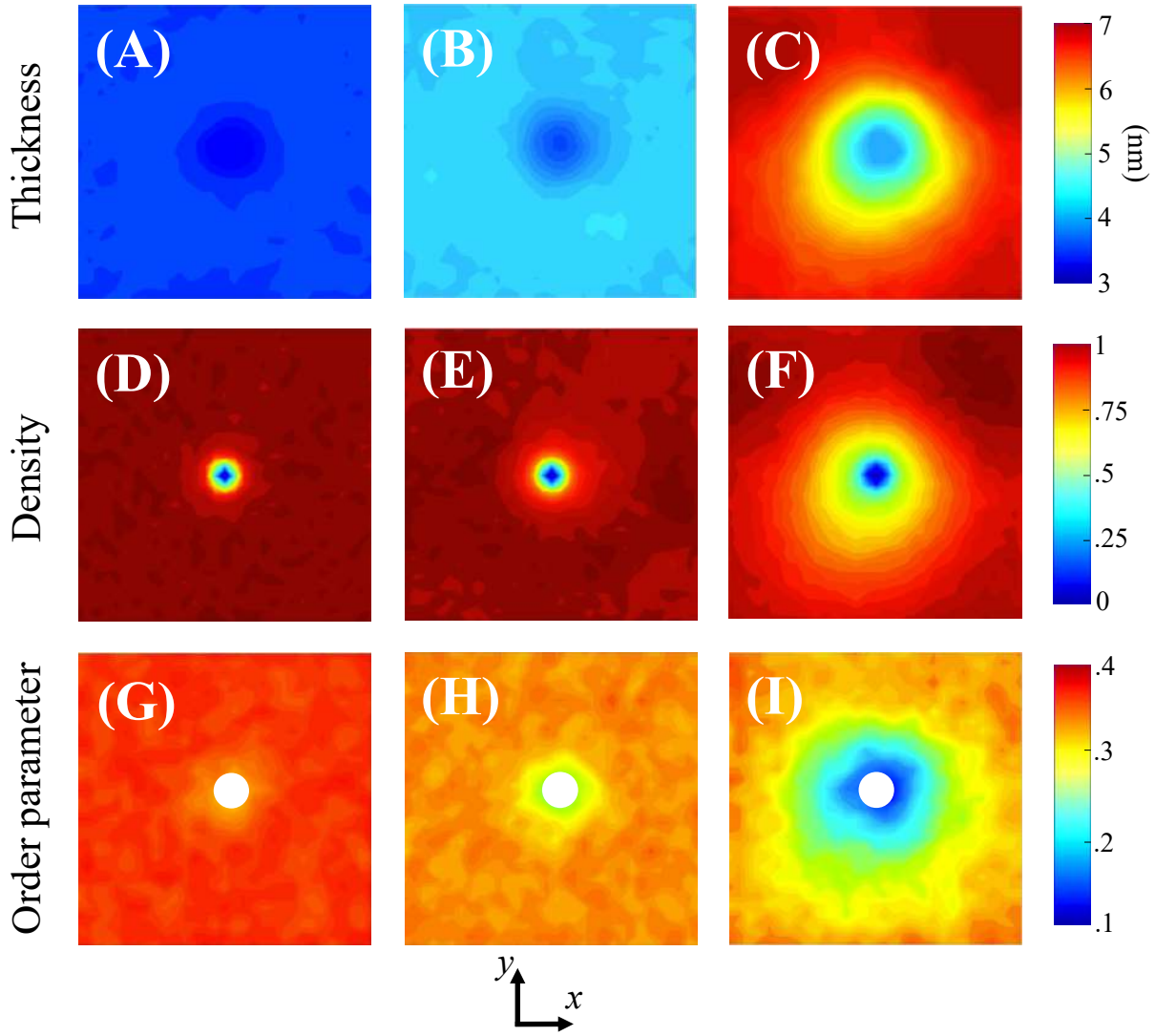

FIGURE 6.19. Contour plots showing local measurements of various properties on the membrane's lateral area as seen in the simulations, including thickness for (A) pure liposomes, (B) 25:75 HV, (C) 50:50 HV (peptide starting in the thin conformation); membrane normalized density for (D) pure liposomes, (E) 25:75 HV, (F) 50:50 HV; acyl chains order parameter for (G) pure liposomes, (H) 25:75 HV, (i) 50:50 HV. The color scale for each variable is displayed in the right-hand side detail.

The membrane thickness decreases near the peptide, particularly for the 50:50 HV composition, where a larger decrease is observed. This pronounced behavior in 50:50 membranes is related to the thin and thick phases observed both experimentally

and in simulations. Distinct patterns are also observed for the density when comparing the different compositions. In the lipid bilayer and 25:75 HVs, the membrane density increases rapidly right after the point where the peptide is inserted. However, the membrane with 50:50 composition exhibits a larger zone of decreased density. Separate density profiles for the POPC and the polymer can be found in Figure B.2 and B.3 of Appendix B. Comparison of the density profiles for the POPC and the polymer reveals that the decrease in density near the peptide in the 50:50 HV composition corresponds to a local higher concentration of phospholipids and a lower concentration of polymer. These differences do not result in lipid/copolymer phase separation, but they are significant enough to be visualized. This observation supports the hypothesis presented earlier that a local decrease in polymer concentration promotes a collapsed polymeric configuration and reduces the thickness of the bilayer (as seen in Figure 6.19 C). These findings suggest that locally increased phospholipid density may contribute to protein/peptide insertion in HVs, which, together with the thermodynamics analysis by the umbrella sampling technique, may help to explain why bioactivity is only preserved at specific polymer-to-lipid ratios.

In addition, Figures 6.19G-I also suggest a remarkable difference in the distribution of order parameters between pure liposomes and HVs. While the S_{cd} in pure liposomes show a homogeneous and space-independent value, which decreases with temperature as seen in B.5 of Appendix B, the addition of polymers to the lipid bilayer results in a local shell of decreased order parameter around the peptide. This behavior is observed across all temperatures, as evidenced by the data in the Appendix. This provides further evidence that the addition of polymers tends to increase the entropy of the acyl chains of phospholipids, making the hydrophobic core more disordered and favorable for protein incorporation.

The results presented in this study regarding the dynamics of a WALP peptide within various HVs formulations have significant implications for practical purposes. The successful integration of proteins into vesicles is crucial for a wide range of biotechnological purposes, such as the development of transmembrane channels for drug delivery (MAJD et al., 2010), energy transduction (RIGAUD et al., 1995), improvement of food quality (LIU et al., 2020) and synthetic cell studies (PAPAHADJOPOULOS; KIMELBERG, 1974). While these operations are typically carried out using liposomes,

the present findings align well with prior research on hybrid vesicles (KHAN et al., 2016; SENEVIRATNE et al., 2018; OTRIN et al., 2017; JACOBS et al., 2019), suggesting that HVs, with the addition of low to moderate amounts of polymers, can effectively perform similar functions. Furthermore, the reconstitution process in the absence of detergent might be enhanced in hybrid membranes (CATANIA et al., 2022), facilitating protein incorporation in vesicles.

6.5 Conclusion

In this study, hybrids vesicles composed by POPC and PBD_{22}-*b*-PEO_{14} were analyzed with computational techniques and the results contrasted with existing and new experimental data. The structural and mechanical properties of these membranes were investigated along with their biophysical behavior in the presence of a $WALP_{23}$ peptide using coarse-grained MD simulations (with a new parameterization for the copolymer) and the umbrella sampling technique. The simulations results helped to shed some light on the different conformations adopted by lipids and copolymers depending on the polymer-to-phospholipid ratio. When the lipid concentration is low, an elongated arrangement is taken by the copolymers, and POPC molecules are positioned at the hydrophilic/hydrophobic interface of the membrane. This leads to an increased thickness and decreased lateral area on the membrane. Conversely, at high lipid concentration, the polymer adapts to the phospholipid configuration by adopting a collapsed structure, with decreased thickness and increased lateral area. These structural observations were in good agreement with recent reports about the phase behavior in HVs.

The calculated mechanical modulus showed that the energy required to stretch the membrane is significantly reduced by polymer addition. Furthermore, the addition of polymers tended to increase the fluidity of the POPC acyl chains. These two findings help to explain why proteins are more easily reconstituted in hybrid vesicles (HVs) than in pure liposomes. Additionally, the relationship between the bending and Gaussian curvature elastic moduli supports previous findings that HVs become more stable as polymer content increases. This conclusion is also supported by fluorescence experiments that measure leakage in the presence of detergent. Umbrella sampling

simulations revealed that the $WALP_{23}$ peptide is only thermodynamically stable in a transmembrane configuration when polymer concentrations are up to 50%, helping to explain why high polymer concentration may not favored active incorporation of proteins. The present findings are consistent with previous studies and provide new insights into the behavior of hybrid vesicles that can be helpful to modify and optimize these structures for their various biotechnological applications.

Chapter 7

Final Considerations

Understanding the emerging technologies impact on diverse nutrients relevant to the food industry is crucial for the application of these processes as alternatives to conventional methods. Experimental characterization techniques, such as NMR and cryo-EM, are extremely useful for this purpose, although, in general, they present three limitations: (i) the high equipment cost; (ii) the analysis resolution; and (iii) the difficulty in evaluating mechanisms. This thesis aimed to analyze the application of emerging technologies through a different approach, the use of molecular dynamics simulations. It may be stated that the roles of experiments and simulations are distinct, yet complementary. Experimental techniques provide measurements of physicochemical parameters and structural details for the systems under investigation. On the other hand, MD simulations detail the dynamic evolution of structures during processes, allowing the computational modeling of several systems and providing a fundamental perspective on phenomena observed in experiments. The synergy between these two approaches is therefore a powerful tool for the comprehensive examination of phenomena in food science.

Through the computational evaluation of various technologies and systems, the present work aimed to contribute to the field offering a multifaceted perspective on how molecular simulations can be applied in the context of food science. Possibly the most straightforward example of this objective is found in Chapter 3, where the effects of continuous and alternating electric fields on the ovalbumin molecule were studied. As this protein has several technological applications in the food industry, this chapter shows how molecular simulations can be used to analyze molecules relevant to food science. Despite the restriction in temporal and spatial scales, the simulations

demonstrated the ability to reproduce relevant phenomena that were experimentally reported by other authors. Furthermore, the simulations enabled the explanation of various properties of egg-based products by establishing correlations between experimental behaviors with properties measured at a molecular scale.

The studies addressed in Chapters 4, 5, and 6 also find several applications in the food industry, either by explaining the synergy obtained by the simultaneous application of two emerging technologies or by analyzing properties of microencapsulation systems. However, it is important to note that these results have applications beyond the food industry. For example, hybrid vesicles can serve as nanoreactors in the chemical industry, while the combination of electric field with high-pressure or ultrasound can be employed in drug delivery by the pharmaceutical industry. Thus, a broader range of phenomena is explained in these studies. This fact illustrates the possibility of interdisciplinarity in the simulation results, enhancing mutual advances across different areas of knowledge.

Regarding the research objectives presented in the Introduction section, the first objective, concerning the influence of electric field applications on the structural, solubility, and electrical properties of the ovalbumin molecule, was addressed in Chapter 3. During the application of electric fields, the preservation of helical structures was observed. This phenomenon possibly arises from the increase in salt bridges in ovalbumin under the influence of external electric fields. Furthermore, it was found that both continuous and alternating electric fields caused an increase in the radius of gyration, dipole moment, and available surface area for contact with the solvent. These results indicate that the application of electric fields has the potential to alter the technological properties of this protein. The increase in electrostatic interactions and dipole-dipole forces under these conditions is in accordance with experimentally reported results in the literature. Additionally, these findings were helpful in elucidating the underlying mechanism of some non-thermal effects experimentally reported in egg-based products, such as the increase in viscosity, emulsification, and gel formation.

The second study used mesoscale simulation techniques (where some atoms with similar properties are grouped into an effective particle) to analyze the electroporation phenomenon in a lipid bilayer composed of DPPC, aiming to address the

second specific objective (to investigate the effect of temperature and pressure on electroporation). Results showed that the time for pore formation and resealing increased with pressure and decreased with temperature, whereas the maximum pore radius increased with temperature and decreased with pressure. This behavior influenced the ion migration through the bilayer, and the higher ionic mobility was obtained in the 288 K/1000 atm simulations, i.e., a combination of low temperature and (not excessively) high pressure. These results were used to discuss some experimental observations regarding the extraction of intracellular compounds.

The third objective, which involves the analysis of synergistic effects between electric fields and ultrasound, was addressed in Chapter 5. The study demonstrated that synergistic effects do not occur in the absence of cavitation if electroporation alone is capable of forming pores. However, the shock wave leads to a reduction in the thickness of the lipid bilayer, and this mechanism can result in pore formation for lower electric fields (when the transmembrane potential is below the membrane rupture threshold). In the presence of cavitation, synergistic effects were observed at the highest studied velocities. In this scenario, a nanojet caused by the collapse of the cavitation bubble causes initial damage to the membrane, which is quickly amplified by the electroporation effect. Therefore, ultrasound can catalyze and direct the pore formation by electroporation.

The evaluation of physicochemical, mechanical, and biochemical properties of lipid-polymer hybrid vesicles, was addressed in Chapter 6 and is related to the final objective of this thesis. This study was carried out in collaboration with the Macromolecular Biochemistry group at the University of Leiden in Leiden, the Netherlands, through a scholarship provided by the CAPES-PRINT internationalization program. This collaboration also allowed for the application of experimental characterization techniques in conjunction with molecular dynamics simulations. This hybrid approach proved to be crucial in understanding several properties of these systems. In general, it was observed that hybrid membranes with low to medium polymer concentrations were able to combine the best characteristics of both constituents, namely the robustness of the polymers and the bioactivity of the lipids. The loss of activity in vesicles with high polymer concentrations was mainly due to the hydrophobic size mismatch between the apolar fractions of the membrane and proteins, making these membranes

less suitable for biotechnological applications.

In conclusion, this thesis has contributed to a deeper understanding of the impact of emerging technologies on some nutrients relevant to the food industry. By employing computational techniques, insights were obtained into fundamental processes that are often challenging to investigate through experiments. The findings from this thesis have the potential to be used by several industries, fostering innovation and advancing the use of emerging technologies in practical applications. As this field continues to evolve, the interplay between computational simulations and experimental investigations will become increasingly critical for solving complex challenges and driving progress in this scientific domain.

7.1 Perspectives for Future Work

The present work investigated phenomena relevant in food science through the use of molecular dynamics simulations. However, there are a number of possible technologies to be studied and several computational methodologies available. Considering this, some suggestions for future work in this area are presented as follows.

- Investigate the dissolution of ozone in water and its reaction kinetics with foodborne pathogens, enzymes, and other food constituents at the atomistic level using, for example, reactive molecular dynamics.

- Investigate at the mesoscale the fouling mechanisms in membranes used in food processing, such as ultrafiltration and microfiltration, contributing to the development of strategies for fouling mitigation.

- Explore the behavior of carbohydrates or lipids in high pressure and PEF processing, since most studies focus on the molecular analysis of proteins.

- Investigate the stability of nanoparticles used in food applications (e.g., nanoemulsions, nanocapsules) at the molecular level, to optimize their long-term performance and controlled release properties.

- Utilize density functional theory calculations to predict the binding energies and interactions of flavor molecules with food matrices, which impact flavor release and sensorial perception.
- Simulate the interactions between nanomaterials and food molecules to optimize barrier properties, antimicrobial activity and controlled release.

These examples show how simulations can be applied to address various challenges in emerging food processing technologies. Depending on the specific problem and research goals, these computational methods can provide insights into molecular-level mechanisms and interactions, that are essential for optimizing the different use of food processing techniques.

Bibliography

AGANOVIC, K.; HERTEL, C.; VOGEL, R. F.; JOHNE, R.; SCHLÜTER, O.; SCHWARZENBOLZ, U.; JÄGER, H.; HOLZHAUSER, T.; BERGMAIR, J.; ROTH, A.; SEVENICH, R.; BANDICK, N.; KULLING, S. E.; KNORR, D.; ENGEL, K.-H.; HEINZ, V. Aspects of high hydrostatic pressure food processing: Perspectives on technology and food safety. *Comprehensive Reviews in Food Science and Food Safety*, Wiley, v. 20, n. 4, p. 3225–3266, 2021. Disponível em: <https://doi.org/10.1111/1541-4337.12763>.

AGHAZADEH, H.; KOLI, M. G.; RANJBAR, R.; BAGHERI, K. P. Interactions of GF-17 derived from LL-37 antimicrobial peptide with bacterial membranes: a molecular dynamics simulation study. *Journal of Computer-Aided Molecular Design*, Springer Science and Business Media LLC, v. 34, n. 12, p. 1261–1273, 2020. Disponível em: <https://doi.org/10.1007/s10822-020-00348-4>.

AGNASS, P.; VELDHUISEN, E. van; GEMERT, M. J. C. van; GELD, C. W. M. van der; LIENDEN, K. P. van; GULIK, T. M. van; MEIJERINK, M. R.; BESSELINK, M. G.; KOK, H. P.; CREZEE, J. Mathematical modeling of the thermal effects of irreversible electroporation for in vitro, in vivo, and clinical use: a systematic review. *International Journal of Hyperthermia*, Informa UK Limited, v. 37, n. 1, p. 486–505, 2020. Disponível em: <https://doi.org/10.1080/02656736.2020.1753828>.

ALESSANDRI, R.; SOUZA, P. C. T.; THALLMAIR, S.; MELO, M. N.; VRIES, A. H. de; MARRINK, S. J. Pitfalls of the Martini model. *Journal of Chemical Theory and Computation*, American Chemical Society (ACS), v. 15, n. 10, p. 5448–5460, 2019. Disponível em: <https://doi.org/10.1021/acs.jctc.9b00473>.

ALKANAN, Z. T.; ALTEMIMI, A. B.; AL-HILPHY, A. R. S.; WATSON, D. G.; PRATAP-SINGH, A. Ohmic heating in the food industry: Developments in concepts and applications during 2013–2020. *Applied Sciences*, MDPI AG, v. 11, n. 6, p. 2507, 2021. Disponível em: <https://doi.org/10.3390/app11062507>.

ALKHALAF, W.; PIARD, J.-C.; SODA, M. E.; GRIPON, J.-C.; DESMAZEAUD, M.; VASSAL, L. Liposomes as proteinase carriers for the accelerated ripening of saint-paulin type cheese. *Journal of Food Science*, Wiley, v. 53, n. 6, p. 1674–1679, 1988. Disponível em: <https://doi.org/10.1111/j.1365-2621.1988.tb07813.x>.

ALLEONI, A. C. C. Albumen protein and functional properties of gelation and foaming. *Scientia Agricola*, FapUNIFESP (SciELO), v. 63, n. 3, p. 291–298, 2006. Disponível em: <https://doi.org/10.1590/s0103-90162006000300013>.

ALLISON, A.; FOULADKHAH, A. Sensitivity of *Salmonella serovars* and natural microflora to high-pressure pasteurization: Open access data for risk assessment and practitioners. *Data in Brief*, Elsevier BV, v. 21, p. 480–484, 2018. Disponível em: <https://doi.org/10.1016/j.dib.2018.09.071>.

ALLOTT, A.; MINDORFF, D. *Ib Biology Course Book: 2014 Edition: Oxford Ib Diploma Program*. USA: Oxford University Press, 2014.

ÁLVAREZ, I.; HEINZ, V. Hurdle technology and the preservation of food by pulsed electric fields. In: *Food Preservation by Pulsed Electric Fields*. Elsevier, 2007. p. 165–177. Disponível em: <https://doi.org/10.1533/9781845693831.2.165>.

AMARAL, P. H. R. do; ANDRADE, P. L.; CONTO, L. C. de. Microencapsulation and its uses in food science and technology: A review. In: *Microencapsulation - Processes, Technologies and Industrial Applications*. IntechOpen, 2019. Disponível em: <https://doi.org/10.5772/intechopen.81997>.

ANDREWS, L. S.; AHMEDNA, M.; GRODNER, R. M.; LIUZZO, J. A.; MURANO, P. S.; MURANO, E. A.; RAO, R. M.; SHANE, S.; WILSON, P. W. Food preservation using ionizing radiation. In: *Reviews of Environmental Contamination and Toxicology*. New York, USA: Springer New York, 1998. p. 1–53. Disponível em: <https://doi.org/10.1007/978-1-4612-2208-8_1>.

ARYAL, P.; JARERATTANACHAT, V.; CLAUSEN, M. V.; SCHEWE, M.; MCCLENAGHAN, C.; ARGENT, L.; CONRAD, L. J.; DONG, Y. Y.; PIKE, A. C.; CARPENTER, E. P.; BAUKROWITZ, T.; SANSOM, M. S.; TUCKER, S. J. Bilayer-mediated structural transitions control mechanosensitivity of the TREK-2 k2p channel. *Structure*, Elsevier BV, v. 25, n. 5, p. 708–718.e2, 2017. Disponível em: <https://doi.org/10.1016/j.str.2017.03.006>.

ASTRAKAS, L.; GOUSIAS, C.; TZAPHLIDOU, M. Electric field effects on chignolin conformation. *Journal of Applied Physics*, AIP Publishing, v. 109, n. 9, 2011. Disponível em: <https://doi.org/10.1063/1.3585867>.

ASTRAKAS, L. G.; GOUSIAS, C.; TZAPHLIDOU, M. Structural destabilization of chignolin under the influence of oscillating electric fields. *Journal of Applied Physics*, AIP Publishing, v. 111, n. 7, p. 074702, 2012. Disponível em: <https://doi.org/10.1063/1.3699389>.

ATUONWU, J. C.; LEADLEY, C.; BOSMAN, A.; TASSOU, S. A. High-pressure processing, microwave, ohmic, and conventional thermal pasteurization: Quality aspects and energy economics. *Journal of Food Process Engineering*, Wiley, v. 43, n. 2, 2019. Disponível em: <https://doi.org/10.1111/jfpe.13328>.

AYCOCK, K. N.; DAVALOS, R. V. Irreversible electroporation: Background, theory, and review of recent developments in clinical oncology. *Bioelectricity*, Mary Ann Liebert Inc, v. 1, n. 4, p. 214–234, 2019. Disponível em: <https://doi.org/10.1089/bioe.2019.0029>.

BACKMANN, N.; KAPPELER, N.; BRAUN, T.; HUBER, F.; LANG, H.-P.; GERBER, C.; LIM, R. Y. H. Sensing surface PEGylation with microcantilevers. *Beilstein Journal of Nanotechnology*, Beilstein Institut, v. 1, p. 3–13, 2010. Disponível em: <https://doi.org/10.3762/bjnano.1.2>.

BALDI, G.; D'ELIA, F.; SOGLIA, F.; TAPPI, S.; PETRACCI, M.; ROCCULI, P. Exploring the effect of pulsed electric fields on the technological properties of chicken meat. *Foods*, MDPI AG, v. 10, n. 2, p. 241, 2021. Disponível em: <https://doi.org/10.3390/foods10020241>.

BALGAVÝ, P.; DUBNIČKOVÁ, M.; KUČERKA, N.; KISELEV, M. A.; YARADAIKIN, S. P.; UHRÍKOVÁ, D. Bilayer thickness and lipid interface area in unilamellar extruded 1, 2-diacylphosphatidylcholine liposomes: a small-angle neutron scattering study. *Biochimica et Biophysica Acta (BBA) - Biomembranes*, Elsevier BV, v. 1512, n. 1, p. 40–52, 2001. Disponível em: <https://doi.org/10.1016/s0005-2736(01)00298-x>.

BARBA, F.; PARNIAKOV, O.; WIKTOR, A. *Pulsed Electric Fields to Obtain Healthier and Sustainable Food for Tomorrow*. Elsevier, 2020. Disponível em: <https://doi.org/10.1016/c2018-0-00129-2>.

BARSOTTI, L.; DUMAY, E.; MU, T. H.; DIAZ, M. F.; CHEFTEL, J. Effects of high voltage electric pulses on protein-based food constituents and structures. *Trends in Food Science & Technology*, Elsevier BV, v. 12, n. 3-4, p. 136–144, 2001. Disponível em: <https://doi.org/10.1016/s0924-2244(01)00065-6>.

BEALES, P. A.; KHAN, S.; MUENCH, S. P.; JEUKEN, L. J. Durable vesicles for reconstitution of membrane proteins in biotechnology. *Biochemical Society Transactions*, Portland Press Ltd., v. 45, n. 1, p. 15–26, 2017. Disponível em: <https://doi.org/10.1042/bst20160019>.

BEHRUZIAN, A.; SAMANI, B. H.; ROSTAMI, S.; LORIGOOINI, Z.; BEHRUZIAN, M. The effect of combined AC electric field and ultrasound on the chemical compositions and *Escherichia coli* content of spearmint aromatic water. *Journal of Food Process Engineering*, Wiley, v. 41, n. 2, p. e12650, 2017. Disponível em: <https://doi.org/10.1111%2Fjfpe.12650>.

BELITZ, H. D.; GROSCH, W.; SCHIEBERLE, P. *Food Chemistry*. Berlin, Germany: Springer Berlin Heidelberg, 2009. Disponível em: <https://doi.org/10.1007/978-3-540-69934-7>.

BENSALEM, S.; PAREAU, D.; CINQUIN, B.; FRANÇAIS, O.; PIOUFLE, B. L.; LOPES, F. Impact of pulsed electric fields and mechanical compressions on the permeability and structure of *Chlamydomonas reinhardtii* cells. *Scientific Reports*, Springer Science and Business Media LLC, v. 10, n. 1, 2020. Disponível em: <https://doi.org/10.1038/s41598-020-59404-6>.

BEREAU, T.; BENNETT, W. F. D.; PFAENDTNER, J.; DESERNO, M.; KARTTUNEN, M. Folding and insertion thermodynamics of the transmembrane WALP peptide. *The Journal of Chemical Physics*, AIP Publishing, v. 143, n. 24, p. 243127, 2015. Disponível em: <https://doi.org/10.1063/1.4935487>.

BERMUDEZ, H.; BRANNAN, A. K.; HAMMER, D. A.; BATES, F. S.; DISCHER, D. E. Molecular weight dependence of polymersome membrane structure, elasticity, and stability. *Macromolecules*, American Chemical Society (ACS), v. 35, n. 21, p. 8203–8208, 2002. Disponível em: <https://doi.org/10.1021/ma020669l>.

BEST, R. B.; ZHU, X.; SHIM, J.; LOPES, P. E. M.; MITTAL, J.; FEIG, M.; MACKERELL, A. D. Optimization of the additive CHARMM all-atom protein force field targeting improved sampling of the backbone ϕ, ψ and side-chain χ1 and χ2 dihedral angles. *Journal of Chemical Theory and Computation*, American Chemical Society (ACS), v. 8, n. 9, p. 3257–3273, 2012. Disponível em: <https://doi.org/10.1021/ct300400x>.

BI, H.; WANG, X.; HAN, X.; VOïTCHOVSKY, K. Impact of electric fields on the nanoscale behavior of lipid monolayers at the surface of graphite in solution. *Langmuir*, American Chemical Society (ACS), v. 34, n. 32, p. 9561–9571, 2018. Disponível em: <https://doi.org/10.1021/acs.langmuir.8b01631>.

BÖCKMANN, R. A.; GROOT, B. L. de; KAKORIN, S.; NEUMANN, E.; GRUBMÜLLER, H. Kinetics, statistics, and energetics of lipid membrane electroporation studied by molecular dynamics simulations. *Biophysical Journal*, Elsevier BV, v. 95, n. 4, p. 1837–1850, 2008. Disponível em: <https://doi.org/10.1529/biophysj.108.129437>.

BOUALEM, K.; SUBIRADE, M.; DESJARDINS, Y.; SAUCIER, L. Development of an encapsulation system for the protection and controlled release of antimicrobial nisin at meat cooking temperature. *Journal of Food Research*, Canadian Center of Science and Education, v. 2, n. 3, p. 36, 2013. Disponível em: <https://doi.org/10.5539/jfr.v2n3p36>.

BOWEN, A. J.; GRYGORCZYK, A. Challenges and opportunities for sensory and consumer science in new cultivar development and fresh produce marketing. *Current Opinion in Food Science*, Elsevier BV, v. 41, p. 152–158, 2021. Disponível em: <https://doi.org/10.1016/j.cofs.2021.04.009>.

BOZKURT, H.; ICIER, F. The change of apparent viscosity of liquid whole egg during ohmic and cnventional heating. *Journal of Food Process Engineering*, Wiley, v. 35, n. 1, p. 120–133, 2011. Disponível em: <https://doi.org/10.1111/j.1745-4530.2010.00575.x>.

BRAUN, E.; GILMER, J.; MAYES, H. B.; MOBLEY, D. L.; MONROE, J. I.; PRASAD, S.; ZUCKERMAN, D. M. Best practices for foundations in molecular simulations. *Living Journal of Computational Molecular Science*, University of Colorado at Boulder, v. 1, n. 1, 2019. Disponível em: <https://doi.org/10.33011/livecoms.1.1.5957>.

BRODSZKIJ, E.; WESTENSEE, I. N.; HOLLEUFER, S. F.; ADE, C.; ANDRES, P. D. D.; PEDERSEN, J. S.; STÄDLER, B. Membrane composition of polymer-lipid hybrid vesicles. *Applied Materials Today*, Elsevier BV, v. 29, p. 101549, 2022. Disponível em: <https://doi.org/10.1016/j.apmt.2022.101549>.

BROOKS, B. R.; BRUCCOLERI, R. E.; OLAFSON, B. D.; STATES, D. J.; SWAMINATHAN, S.; KARPLUS, M. CHARMM: A program for macromolecular energy, minimization, and dynamics calculations. *Journal of Computational Chemistry*, Wiley, v. 4, n. 2, p. 187–217, 1983. Disponível em: <https://doi.org/10.1002/jcc.540040211>.

BUI, T. Q.; NGO, H. T. M.; TRAN, H. T. Surface-protective assistance of ultrasound in synthesis of superparamagnetic magnetite nanoparticles and in preparation of mono-core magnetite-silica nanocomposites. *Journal of Science: Advanced Materials and Devices*, Elsevier BV, v. 3, n. 3, p. 323–330, 2018. Disponível em: <https://doi.org/10.1016/j.jsamd.2018.07.002>.

BULACU, M.; GOGA, N.; ZHAO, W.; ROSSI, G.; MONTICELLI, L.; PERIOLE, X.; TIELEMAN, D. P.; MARRINK, S. J. Improved angle potentials for coarse-grained molecular dynamics simulations. *Journal of Chemical Theory and Computation*, American Chemical Society (ACS), v. 9, n. 8, p. 3282–3292, 2013. Disponível em: <https://doi.org/10.1021%2Fct400219n>.

BURBACH, B. J.; O'FLANAGAN, S. D.; SHAO, Q.; YOUNG, K. M.; SLAUGHTER, J. R.; ROLLINS, M. R.; STREET, T. J. L.; GRANGER, V. E.; BEURA, L. K.; AZARIN, S. M.; RAMADHYANI, S.; FORSYTH, B. R.; BISCHOF, J. C.; SHIMIZU, Y. Irreversible electroporation augments checkpoint immunotherapy in prostate cancer and promotes tumor antigen-specific tissue-resident memory CD8 + t cells. *Nature Communications*, Springer Science and Business Media LLC, v. 12, n. 1, 2021. Disponível em: <https://doi.org/10.1038/s41467-021-24132-6>.

CARACCIOLO, F.; EL-NAKHEL, C.; RAIMONDO, M.; KYRIACOU, M. C.; CEMBALO, L.; PASCALE, S. D.; ROUPHAEL, Y. Sensory attributes and consumer acceptability of 12 microgreens species. *Agronomy*, MDPI AG, v. 10, n. 7, p. 1043, 2020. Disponível em: <https://doi.org/10.3390/agronomy10071043>.

CARDOSO, R. M.; MARTINS, P. A.; RAMOS, C. V.; CORDEIRO, M. M.; LEOTE, R. J.; NAQVI, K. R.; VAZ, W. L.; MORENO, M. J. Effect of dipole moment on amphiphile solubility and partition into liquid ordered and liquid disordered phases in lipid bilayers. *Biochimica et Biophysica Acta (BBA) - Biomembranes*, Elsevier BV, v. 1862, n. 3, p. 183157, 2020. Disponível em: <https://doi.org/10.1016/j.bbamem.2019.183157>.

CARTER, M.; SHIEH, J. *Guide to Research Techniques in Neuroscience*. Cambridge, UK: Elsevier, 2015. Disponível em: <https://doi.org/10.1016/c2013-0-06868-5>.

CARULLO, D.; ABERA, B. D.; CASAZZA, A. A.; DONSÌ, F.; PEREGO, P.; FERRARI, G.; PATARO, G. Effect of pulsed electric fields and high pressure homogenization on the aqueous extraction of intracellular compounds from the microalgae *Chlorella*

vulgaris. *Algal Research*, Elsevier BV, v. 31, p. 60–69, 2018. Disponível em: <https://doi.org/10.1016/j.algal.2018.01.017>.

CASTRO, A. J.; BARBOSA-CÁNOVAS, G. V.; SWANSON, B. G. Microbial inactivation of foods by pulsed electric fields. *Journal of Food Processing and Preservation*, Wiley, v. 17, n. 1, p. 47–73, 1993. Disponível em: <https://doi.org/10.1111/j.1745-4549.1993.tb00225.x>.

CATANIA, R.; MACHIN, J.; RAPPOLT, M.; MUENCH, S. P.; BEALES, P. A.; JEUKEN, L. J. C. Detergent-free functionalization of hybrid vesicles with membrane proteins using SMALPs. *Macromolecules*, American Chemical Society (ACS), v. 55, n. 9, p. 3415–3422, 2022. Disponível em: <https://doi.org/10.1021/acs.macromol.2c00326>.

CHAISSON, E. H.; HEBERLE, F. A.; DOKTOROVA, M. Building asymmetric lipid bilayers for molecular dynamics simulations: What methods exist and how to choose one? *Membranes*, MDPI AG, v. 13, n. 7, p. 629, 2023. Disponível em: <https://doi.org/10.3390/membranes13070629>.

CHAURASIA, A. K.; RUKANGU, A. M.; PHILEN, M. K.; SEIDEL, G. D.; FREEMAN, E. C. Evaluation of bending modulus of lipid bilayers using undulation and orientation analysis. *Physical Review E*, American Physical Society (APS), v. 97, n. 3, p. 032421–1–032421–12, 2018. Disponível em: <https://doi.org/10.1103/physreve.97.032421>.

CHÁVEZ-MARTÍNEZ, A.; REYES-VILLAGRANA, R. A.; RENTERÍA-MONTERRUBIO, A. L.; SÁNCHEZ-VEGA, R.; TIRADO-GALLEGOS, J. M.; BOLIVAR-JACOBO, N. A. Low and high-intensity ultrasound in dairy products: Applications and effects on physicochemical and microbiological quality. *Foods*, MDPI AG, v. 9, n. 11, p. 1688, 2020. Disponível em: <https://doi.org/10.3390/foods9111688>.

CHEMAT, F.; HUMA, Z. e; KHAN, M. K. Applications of ultrasound in food technology: Processing, preservation and extraction. *Ultrasonics Sonochemistry*, Elsevier BV, v. 18, n. 4, p. 813–835, 2011. Disponível em: <https://doi.org/10.1016/j.ultsonch.2010.11.023>.

CHEMIN, M.; BRUN, P.-M.; LECOMMANDOUX, S.; SANDRE, O.; MEINS, J.-F. L. Hybrid polymer/lipid vesicles: fine control of the lipid and polymer distribution in the binary membrane. *Soft Matter*, Royal Society of Chemistry (RSC), v. 8, n. 10, p. 2867, 2012. Disponível em: <https://doi.org/10.1039/c2sm07188f>.

CHEN, C. P.; ROST, B. Long membrane helices and short loops predicted less accurately. *Protein Science*, Wiley, v. 11, n. 12, p. 2766–2773, 2009. Disponível em: <https://doi.org/10.1110/ps.0214602>.

CHEN, G.; HUANG, K.; MIAO, M.; FENG, B.; CAMPANELLA, O. H. Molecular dynamics simulation for mechanism elucidation of food processing and safety: State of the art. *Comprehensive Reviews in Food Science and Food Safety*, Wiley, v. 18, n. 1, p. 243–263, 2018. Disponível em: <https://doi.org/10.1111/1541-4337.12406>.

CHEN, L.; HE, J. Outlier profiles of atomic structures derived from X-ray crystallography and from cryo-electron microscopy. *Molecules*, MDPI AG, v. 25, n. 7, p. 1540, 2020. Disponível em: <https://doi.org/10.3390/molecules25071540>.

CHEN, R.; POGER, D.; MARK, A. E. Effect of high pressure on fully hydrated DPPC and POPC bilayers. *The Journal of Physical Chemistry B*, American Chemical Society (ACS), v. 115, n. 5, p. 1038–1044, 2011. Disponível em: <https://doi.org/10.1021/jp110002q>.

CHIAPPERINO, M. A.; BIA, P.; LAMACCHIA, C. M.; MESCIA, L. Electroporation modelling of irregular nucleated cells including pore radius dynamics. *Electronics*, MDPI AG, v. 8, n. 12, p. 1477, 2019. Disponível em: <https://doi.org/10.3390/electronics8121477>.

CHO, H.-Y.; YOUSEF, A. E.; SASTRY, S. K. Kinetics of inactivation of *Bacillus subtilis* spores by continuous or intermittent ohmic and conventional heating. *Biotechnology and Bioengineering*, Wiley, v. 62, n. 3, p. 368–372, 1999. Disponível em: <https://doi.org/10.1002/(sici)1097-0290(19990205)62:3<368::aid-bit14>3.0.co;2-0>.

CHOUBEY, A.; VEDADI, M.; NOMURA, K. ichi; KALIA, R. K.; NAKANO, A.; VASHISHTA, P. Poration of lipid bilayers by shock-induced nanobubble collapse. *Applied Physics Letters*, AIP Publishing, v. 98, n. 2, 2011. Disponível em: <https://doi.org/10.1063/1.3518472>.

CRUM, L. Acoustic cavitation series: part five rectified diffusion. *Ultrasonics*, Elsevier BV, v. 22, n. 5, p. 215–223, 1984. Disponível em: <https://doi.org/10.1016/0041-624x(84)90016-7>.

CZERNOHLAVEK, C.; SCHUSTER, B. Formation and characteristics of mixed lipid/polymer membranes on a crystalline surface-layer protein lattice. *Biointerphases*, American Vacuum Society, v. 15, n. 1, p. 011002, 2020. Disponível em: <https://doi.org/10.1116/1.5132390>.

CZESLIK, C.; REIS, O.; WINTER, R.; RAPP, G. Effect of high pressure on the structure of dipalmitoylphosphatidylcholine bilayer membranes: a synchrotron-X-ray diffraction and FT-IR spectroscopy study using the diamond anvil technique. *Chemistry and Physics of Lipids*, Elsevier BV, v. 91, n. 2, p. 135–144, 1998. Disponível em: <https://doi.org/10.1016/s0009-3084(97)00104-7>.

DAGGETT, V.; LEVITT, M. Molecular dynamics simulations of helix denaturation. *Journal of Molecular Biology*, Elsevier BV, v. 223, n. 4, p. 1121–1138, 1992. Disponível em: <https://doi.org/10.1016/0022-2836(92)90264-k>.

DAMODARAN, S.; PARKIN, K. L. *Fennema's Food Chemistry, Fifth Edition*. Boca Raton, USA: CRC Press, 2017. Disponível em: <https://doi.org/10.1201/9781315372914>.

DANIEL, I.; OGER, P.; WINTER, R. Origins of life and biochemistry under high-pressure conditions. *Chemical Society Reviews*, Royal Society of Chemistry (RSC), v. 35, n. 10, p. 858, 2006. Disponível em: <https://doi.org/10.1039/b517766a>.

DARYAEI, H.; YOUSEF, A. E.; BALASUBRAMANIAM, V. M. Microbiological aspects of high-pressure processing of food: Inactivation of microbial vegetative cells and spores. In: *High Pressure Processing of Food*. Springer New York, 2016. p. 271–294. Disponível em: <https://doi.org/10.1007/978-1-4939-3234-4_14>.

DAVYDOV, S. Temperature effect on the dipole moment of adatoms. *Surface Science*, Elsevier BV, v. 364, n. 3, p. 477–480, 1996. Disponível em: <https://doi.org/10.1016/0039-6028(96)00656-5>.

DELORME, M. M.; GUIMARÃES, J. T.; COUTINHO, N. M.; BALTHAZAR, C. F.; ROCHA, R. S.; SILVA, R.; MARGALHO, L. P.; PIMENTEL, T. C.; SILVA, M. C.; FREITAS, M. Q.; GRANATO, D.; SANT'ANA, A. S.; DUART, M. C. K.; CRUZ, A. G. Ultraviolet radiation: An interesting technology to preserve quality and safety of milk and dairy foods. *Trends in Food Science & Technology*, Elsevier BV, v. 102, p. 146–154, 2020. Disponível em: <https://doi.org/10.1016/j.tifs.2020.06.001>.

DHINESHKUMAR, V. Review on membrane technology applications in food and dairy processing. *Journal of Applied Biotechnology & Bioengineering*, MedCrave Group, LLC, v. 3, n. 5, 2017. Disponível em: <https://doi.org/10.15406/jabb.2017.03.00077>.

DIGGINS, P.; DESERNO, M. Determining the bending modulus of a lipid membrane by simulating buckling. *The Journal of Chemical Physics*, AIP Publishing, v. 138, n. 21, p. 214110, 2013. Disponível em: <https://doi.org/10.1063/1.4808077>.

DIMOVA, R.; SEIFERT, U.; POULIGNY, B.; FÖRSTER, S.; DÖBEREINER, H.-G. Hyperviscous diblock copolymer vesicles. *The European Physical Journal E*, Springer Science and Business Media LLC, v. 7, n. 3, p. 241–250, 2002. Disponível em: <https://doi.org/10.1140/epje/i200101032>.

DING, W.; PALAIOKOSTAS, M.; SHAHANE, G.; WANG, W.; ORSI, M. Effects of high pressure on phospholipid bilayers. *The Journal of Physical Chemistry B*, American Chemical Society (ACS), v. 121, n. 41, p. 9597–9606, 2017. Disponível em: <https://doi.org/10.1021/acs.jpcb.7b07119>.

DOKTOROVA, M.; LEVINE, M. V.; KHELASHVILI, G.; WEINSTEIN, H. A new computational method for membrane compressibility: Bilayer mechanical thickness revisited. *Biophysical Journal*, Elsevier BV, v. 116, n. 3, p. 487–502, 2019. Disponível em: <https://doi.org/10.1016/j.bpj.2018.12.016>.

DOMINGUEZ, L.; FOSTER, L.; STRAUB, J. E.; THIRUMALAI, D. Impact of membrane lipid composition on the structure and stability of the transmembrane domain of amyloid precursor protein. *Proceedings of the National Academy of Sciences*, Proceedings of the National Academy of Sciences, v. 113, n. 36, p. E5281–E5287, 2016. Disponível em: <https://doi.org/10.1073/pnas.1606482113>.

DRISCOLL, D. A.; JONAS, J.; JONAS, A. High pressure 2H nuclear magnetic resonance study of the gel phases of dipalmitoylphosphatidylcholine. *Chemistry and Physics of Lipids*, Elsevier BV, v. 58, n. 1-2, p. 97–104, 1991. Disponível em: <https://doi.org/10.1016/0009-3084(91)90115-r>.

E.A., M.; EISS, A. H. A. Pulsed electric fields for food processing technology. In: *Structure and Function of Food Engineering*. London, UK: InTech, 2012. Disponível em: <https://doi.org/10.5772/48678>.

EID, J.; RAZMAZMA, H.; JRAIJ, A.; EBRAHIMI, A.; MONTICELLI, L. On calculating the bending modulus of lipid bilayer membranes from buckling simulations. *The Journal of Physical Chemistry B*, American Chemical Society (ACS), v. 124, n. 29, p. 6299–6311, 2020. Disponível em: <https://doi.org/10.1021/acs.jpcb.0c04253>.

ESPAÑOL, P.; WARREN, P. B. Perspective: Dissipative particle dynamics. *The Journal of Chemical Physics*, AIP Publishing, v. 146, n. 15, p. 150901, 2017. Disponível em: <https://doi.org/10.1063/1.4979514>.

FANG, H.; NI, K.; WU, J.; LI, J.; HUANG, L.; REIBLE, D. The effects of hydrogen bonding on the shear viscosity of liquid water. *International Journal of Sediment Research*, Elsevier BV, v. 34, n. 1, p. 8–13, 2019. Disponível em: <https://doi.org/10.1016/j.ijsrc.2018.10.008>.

FERNANDEZ-DIAZ, M. D.; BARSOTTI, L.; DUMAY, E.; CHEFTEL, J. C. Effects of pulsed electric fields on ovalbumin solutions and dialyzed egg white. *Journal of Agricultural and Food Chemistry*, American Chemical Society (ACS), v. 48, n. 6, p. 2332–2339, 2000. Disponível em: <https://doi.org/10.1021/jf9908796>.

FESMIRE, C. C.; PETRELLA, R. A.; FOGLE, C. A.; GERBER, D. A.; XING, L.; SANO, M. B. Temperature dependence of high frequency irreversible electroporation evaluated in a 3D tumor model. *Annals of Biomedical Engineering*, Springer Science and Business Media LLC, v. 48, n. 8, p. 2233–2246, 2020. Disponível em: <https://doi.org/10.1007/s10439-019-02423-w>.

FIEDLER, S.; BROECKER, J.; KELLER, S. Protein folding in membranes. *Cellular and Molecular Life Sciences*, Springer Science and Business Media LLC, v. 67, n. 11, p. 1779–1798, 2010. Disponível em: <https://doi.org/10.1007/s00018-010-0259-0>.

GAEDE, H. C.; GAWRISCH, K. Lateral diffusion rates of lipid, water, and a hydrophobic drug in a multilamellar liposome. *Biophysical Journal*, Elsevier BV, v. 85, n. 3, p. 1734–1740, 2003. Disponível em: <https://doi.org/10.1016/s0006-3495(03)74603-7>.

GALVÁN-D'ALESSANDRO, L.; CARCIOCHI, R. Fermentation assisted by pulsed electric field and ultrasound: A review. *Fermentation*, MDPI AG, v. 4, n. 1, p. 1, 2018. Disponível em: <https://doi.org/10.3390%2Ffermentation4010001>.

GARCIA, P. A.; NEAL, R. E.; SANO, M. B.; ROBERTSON, J. L.; DAVALOS, R. V. An experimental investigation of temperature changes during electroporation. In: *2011 XXXth URSI General Assembly and Scientific Symposium*. IEEE, 2011. p. 1–4. Disponível em: <https://doi.org/10.1109/ursigass.2011.6051310>.

GARNER, A. L. Pulsed electric field inactivation of microorganisms: from fundamental biophysics to synergistic treatments. *Applied Microbiology and Biotechnology*,

Springer Science and Business Media LLC, v. 103, n. 19, p. 7917–7929, 2019. Disponível em: <https://doi.org/10.1007/s00253-019-10067-y>.

GAVAHIAN, M.; MATHAD, G. N.; PANDISELVAM, R.; LIN, J.; SUN, D.-W. Emerging technologies to obtain pectin from food processing by-products: A strategy for enhancing resource efficiency. *Trends in Food Science & Technology*, Elsevier BV, v. 115, p. 42–54, 2021. Disponível em: <https://doi.org/10.1016/j.tifs.2021.06.018>.

GHOSH, T.; GARDE, S.; GARCÍA, A. E. Role of backbone hydration and salt-bridge formation in stability of α-helix in solution. *Biophysical Journal*, Elsevier BV, v. 85, n. 5, p. 3187–3193, 2003. Disponível em: <https://doi.org/10.1016/s0006-3495(03)74736-5>.

GIANPIERO, P.; DANIELE, C.; GIOVANNA, F. Effect of pef pre-treatment and extraction temperature on the recovery of carotenoids from tomato wastes. *Chemical Engineering Transactions*, AIDIC: Italian Association of Chemical Engineering, v. 75, p. 139–144, 2019. Disponível em: <https://doi.org/10.3303/CET1975024>.

GKEKA, P. *Molecular dynamics studies of peptide-membrane interactions: insights from coarse-grained models*. Tese (Doutorado) — The University of Edinburgh, 2010.

GOLBERG, A.; RUBINSKY, B. Mass transfer phenomena in electroporation. In: *Transport in Biological Media*. Elsevier, 2013. p. 455–492. Disponível em: <https://doi.org/10.1016/b978-0-12-415824-5.00012-6>.

GOMEZ-GOMEZ, A.; FUENTE, E. B. de la; GALLEGOS, C.; GARCIA-PEREZ, J.; BENEDITO, J. Combined pulsed electric field and high-power ultrasound treatments for microbial inactivation in oil-in-water emulsions. *Food Control*, Elsevier BV, v. 130, p. 108348, 2021. Disponível em: <https://doi.org/10.1016%2Fj.foodcont.2021.108348>.

GRIESE, T.; KAKORIN, S.; NEUMANN, E. Conductometric and electrooptic relaxation spectrometry of lipid vesicle electroporation at high fields. *Physical Chemistry Chemical Physics*, Royal Society of Chemistry (RSC), v. 4, n. 7, p. 1217–1227, 2002. Disponível em: <https://doi.org/10.1039/b108193b>.

GRILLO, D. A.; ALBANO, J. M. R.; MOCSKOS, E. E.; FACELLI, J. C.; PICKHOLZ, M.; FERRARO, M. B. Diblock copolymer bilayers as model for polymersomes: A coarse grain approach. *The Journal of Chemical Physics*, AIP Publishing, v. 146, n. 24, p. 244904, 2017. Disponível em: <https://doi.org/10.1063/1.4986642>.

GRILLO, D. A.; ALBANO, J. M. R.; MOCSKOS, E. E.; FACELLI, J. C.; PICKHOLZ, M.; FERRARO, M. B. Mechanical properties of drug loaded diblock copolymer bilayers: A molecular dynamics study. *The Journal of Chemical Physics*, AIP Publishing, v. 148, n. 21, p. 214901, 2018. Disponível em: <https://doi.org/10.1063/1.5028377>.

GRIT, M.; CROMMELIN, D. J. Chemical stability of liposomes: implications for their physical stability. *Chemistry and Physics of Lipids*, Elsevier BV, v. 64, n. 1-3, p. 3–18, 1993. Disponível em: <https://doi.org/10.1016/0009-3084(93)90053-6>.

GROTE, F.; LYUBARTSEV, A. P. Optimization of Slipids force field parameters describing headgroups of phospholipids. *The Journal of Physical Chemistry B*, American Chemical Society (ACS), v. 124, n. 40, p. 8784–8793, 2020. Disponível em: <https://doi.org/10.1021/acs.jpcb.0c06386>.

GRÜNEWALD, F.; ALESSANDRI, R.; KROON, P. C.; MONTICELLI, L.; SOUZA, P. C.; MARRINK, S. J. Polyply; a python suite for facilitating simulations of (bio-) macromolecules and nanomaterials. *Nature Communications*, v. 13, p. 68, 2022.

GRUNEWALD, F.; ROSSI, G.; VRIES, A. H. de; MARRINK, S. J.; MONTICELLI, L. Transferable MARTINI model of poly(ethylene oxide). *The Journal of Physical Chemistry B*, American Chemical Society (ACS), v. 122, n. 29, p. 7436–7449, 2018. Disponível em: <https://doi.org/10.1021%2Facs.jpcb.8b04760>.

GUDLUR, S.; SANDÉN, C.; MATOUŠKOVÁ, P.; FASCIANI, C.; AILI, D. Liposomes as nanoreactors for the photochemical synthesis of gold nanoparticles. *Journal of Colloid and Interface Science*, Elsevier BV, v. 456, p. 206–209, 2015. Disponível em: <https://doi.org/10.1016/j.jcis.2015.06.033>.

GUHA, S.; MAJUMDER, K.; MINE, Y. Egg proteins. In: *Encyclopedia of food chemistry*. Elsevier, 2019. p. 74–84. Disponível em: <https://doi.org/10.1016/b978-0-08-100596-5.21603-x>.

GUIXÀ-GONZÁLEZ, R.; RODRIGUEZ-ESPIGARES, I.; RAMÍREZ-ANGUITA, J. M.; CARRIÓ-GASPAR, P.; MARTINEZ-SEARA, H.; GIORGINO, T.; SELENT, J. MEMBPLUGIN: studying membrane complexity in VMD. *Bioinformatics*, Oxford University Press (OUP), v. 30, n. 10, p. 1478–1480, 2014. Disponível em: <https://doi.org/10.1093/bioinformatics/btu037>.

GUO, C.; ZHANG, Z.; CHEN, J.; FU, H.; SUBBIAH, J.; CHEN, X.; WANG, Y. Effects of radio frequency heating treatment on structure changes of soy protein isolate for protein modification. *Food and Bioprocess Technology*, Springer Science and Business Media LLC, v. 10, n. 8, p. 1574–1583, 2017. Disponível em: <https://doi.org/10.1007/s11947-017-1923-2>.

GUO, X.; YAN, H.; GUO, R. Interactions of ovalbumin with ionic surfactants. *Chinese Journal of Chemistry*, Wiley, v. 26, n. 9, p. 1589–1595, 2008. Disponível em: <https://doi.org/10.1002/cjoc.200890287>.

GUO, X.-Y.; PESCHEL, C.; WATERMANN, T.; RUDORFF, G.; SEBASTIANI, D. Cluster formation of polyphilic molecules solvated in a DPPC bilayer. *Polymers*, MDPI AG, v. 9, n. 12, p. 488, 2017. Disponível em: <https://doi.org/10.3390/polym9100488>.

HABEL, J.; HANSEN, M.; KYNDE, S.; LARSEN, N.; MIDTGAARD, S.; JENSEN, G.; BOMHOLT, J.; OGBONNA, A.; ALMDAL, K.; SCHULZ, A.; HÉLIX-NIELSEN, C. Aquaporin-based biomimetic polymeric membranes: Approaches and challenges. *Membranes*, MDPI AG, v. 5, n. 3, p. 307–351, 2015. Disponível em: <https://doi.org/10.3390/membranes5030307>.

HABERL-MEGLIČ, S.; LEVIČNIK, E.; LUENGO, E.; RASO, J.; MIKLAVČIČ, D. The effect of temperature and bacterial growth phase on protein extraction by means of electroporation. *Bioelectrochemistry*, Elsevier BV, v. 112, p. 77–82, 2016. Disponível em: <https://doi.org/10.1016/j.bioelechem.2016.08.002>.

HADRIOUI, N.; LEMAALEM, M.; DEROUICHE, A.; RIDOUANE, H. Physical properties of phospholipids and integral proteins and their biofunctional roles in pulmonary surfactant from molecular dynamics simulation. *RSC Advances*, Royal Society of Chemistry (RSC), v. 10, n. 14, p. 8568–8579, 2020. Disponível em: <https://doi.org/10.1039/d0ra00077a>.

HAN, Z.; CAI, M. jie; CHENG, J.-H.; SUN, D.-W. Effects of electric fields and electromagnetic wave on food protein structure and functionality: A review. *Trends in Food Science & Technology*, Elsevier BV, v. 75, p. 1–9, 2018. Disponível em: <https://doi.org/10.1016/j.tifs.2018.02.017>.

HANSON, S. M.; FORSYTH, B.; WANG, C. Combination of irreversible electroporation with sustained release of a synthetic membranolytic polymer for enhanced cancer cell killing. *Scientific Reports*, Springer Science and Business Media LLC, v. 11, n. 1, 2021. Disponível em: <https://doi.org/10.1038/s41598-021-89661-y>.

HARB, F.; SIMON, A.; TINLAND, B. Ripple formation in unilamellar-supported lipid bilayer revealed by FRAPP. *The European Physical Journal E*, Springer Science and Business Media LLC, v. 36, n. 12, 2013. Disponível em: <https://doi.org/10.1140/epje/i2013-13140-x>.

HASHEMI, S. M. B.; MAHMOUDI, M. R.; ROOHI, R.; TORRES, I.; SARAIVA, J. A. Statistical modeling of the inactivation of spoilage microorganisms during ohmic heating of sour orange juice. *LWT - Food Science and Technology*, Elsevier BV, v. 111, p. 821–828, 2019. Disponível em: <https://doi.org/10.1016/j.lwt.2019.04.077>.

HAYNES, L. C.; LEVINE, H.; OTTERBURN, M. S.; MATHEWSON, P. *Microwave browning composition*. US5089278A, 1989.

HEIMBURG, T. Mechanical aspects of membrane thermodynamics. estimation of the mechanical properties of lipid membranes close to the chain melting transition from calorimetry. *Biochimica et Biophysica Acta (BBA) - Biomembranes*, Elsevier BV, v. 1415, n. 1, p. 147–162, 1998. Disponível em: <https://doi.org/10.1016/s0005-2736(98)00189-8>.

HEINZ, V.; KNORR, D. Effect of pH, ethanol addition and high hydrostatic pressure on the inactivation of *Bacillus subtilis* by pulsed electric fields. *Innovative Food Science & Emerging Technologies*, Elsevier BV, v. 1, n. 2, p. 151–159, 2000. Disponível em: <https://doi.org/10.1016/s1466-8564(00)00013-8>.

HENDSCH, Z. S.; TIDOR, B. Do salt bridges stabilize proteins? A continuum electrostatic analysis. *Protein Science*, Wiley, v. 3, n. 2, p. 211–226, 1994. Disponível em: <https://doi.org/10.1002/pro.5560030206>.

HOVMÖLLER, S.; ZHOU, T.; OHLSON, T. Conformations of amino acids in proteins. *Acta Crystallographica Section D Biological Crystallography*, International Union of Crystallography (IUCr), v. 58, n. 5, p. 768–776, 2002. Disponível em: <https://doi.org/10.1107/s0907444902003359>.

HSIEH, C.-H.; LU, C.-H.; KUO, Y.-Y.; CHEN, W.-T.; CHAO, C.-Y. Studies on the non-invasive anticancer remedy of the triple combination of epigallocatechin gallate, pulsed electric field, and ultrasound. *PLOS ONE*, Public Library of Science (PLoS), v. 13, n. 8, p. e0201920, 2018. Disponível em: <https://doi.org/10.1371%2Fjournal.pone.0201920>.

HU, M.; JONG, D. H. de; MARRINK, S. J.; DESERNO, M. Gaussian curvature elasticity determined from global shape transformations and local stress distributions: a comparative study using the MARTINI model. *Faraday Discuss.*, Royal Society of Chemistry (RSC), v. 161, p. 365–382, 2013. Disponível em: <https://doi.org/10.1039/c2fd20087b>.

HU, Y.; CHEN, H.; XIAO, L.; CHU, L.; WANG, S.; WANG, H. Comparison of ovalbumin glycation by microwave irradiation and conventional heating. *LWT - Food Science and Technology*, Elsevier BV, v. 116, p. 108560, 2019. Disponível em: <https://doi.org/10.1016/j.lwt.2019.108560>.

HUANG, G.; CHEN, S.; DAI, C.; SUN, L.; SUN, W.; TANG, Y.; XIONG, F.; HE, R.; MA, H. Effects of ultrasound on microbial growth and enzyme activity. *Ultrasonics Sonochemistry*, Elsevier BV, v. 37, p. 144–149, 2017. Disponível em: <https://doi.org/10.1016/j.ultsonch.2016.12.018>.

HUANG, H.-W.; CHANG, Y. H.; WANG, C.-Y. High pressure pasteurization of sugarcane juice: Evaluation of microbiological shelf life and quality evolution during refrigerated storage. *Food and Bioprocess Technology*, Springer Science and Business Media LLC, v. 8, n. 12, p. 2483–2494, 2015. Disponível em: <https://doi.org/10.1007/s11947-015-1600-2>.

HUBER, G. A.; MCCAMMON, J. A. Brownian dynamics simulations of biological molecules. *Trends in Chemistry*, Elsevier BV, v. 1, n. 8, p. 727–738, 2019. Disponível em: <https://doi.org/10.1016/j.trechm.2019.07.008>.

HUMPHREY, W.; DALKE, A.; SCHULTEN, K. VMD: Visual molecular dynamics. *Journal of Molecular Graphics*, Elsevier BV, v. 14, n. 1, p. 33–38, 1996. Disponível em: <https://doi.org/10.1016/0263-7855(96)00018-5>.

IKEDA, Y.; NAKAMURA, H.; OHSAKI, S.; WATANO, S. Direct translocation of a negatively charged nanoparticle across a negatively charged model cell membrane. *Physical Chemistry Chemical Physics*, Royal Society of Chemistry (RSC), v. 23, n. 17, p. 10591–10599, 2021. Disponível em: <https://doi.org/10.1039/d0cp06278b>.

INDUCTIVELOAD. *Electromagnetic spectrum*. USA: [s.n.], 2007. Disponível em: <https://commons.wikimedia.org/wiki/File:EM_Spectrum_Properties.svg>.

JACOBS, L.; SMIDT, E. D.; GEUKENS, N.; DECLERCK, P.; HOLLEVOET, K. Electroporation outperforms in vivo-jetPEI for intratumoral DNA-based reporter gene transfer. *Scientific Reports*, Springer Science and Business Media LLC, v. 10, n. 1, 2020. Disponível em: <https://doi.org/10.1038/s41598-020-75206-2>.

JACOBS, M. L.; BOYD, M. A.; KAMAT, N. P. Diblock copolymers enhance folding of a mechanosensitive membrane protein during cell-free expression. *Proceedings of the National Academy of Sciences*, Proceedings of the National Academy of Sciences, v. 116, n. 10, p. 4031–4036, 2019. Disponível em: <https://doi.org/10.1073/pnas.1814775116>.

JIANG, F. Y.; BOURET, Y.; KINDT, J. T. Molecular dynamics simulations of the lipid bilayer edge. *Biophysical Journal*, Elsevier BV, v. 87, n. 1, p. 182–192, 2004. Disponível em: <https://doi.org/10.1529/biophysj.103.031054>.

JIANG, Z.; YOU, L.; DOU, W.; SUN, T.; XU, P. Effects of an electric field on the conformational transition of the protein: A molecular dynamics simulation study. *Polymers*, MDPI AG, v. 11, n. 2, p. 282, 2019. Disponível em: <https://doi.org/10.3390/polym11020282>.

JING, H.; WANG, Y.; DESAI, P. R.; RAMAMURTHI, K. S.; DAS, S. Lipid flip-flop and desorption from supported lipid bilayers is independent of curvature. *PLOS ONE*, Public Library of Science (PLoS), v. 15, n. 12, p. e0244460, 2020. Disponível em: <https://doi.org/10.1371/journal.pone.0244460>.

JO, S.; KIM, T.; IYER, V. G.; IM, W. CHARMM-GUI: A web-based graphical user interface for CHARMM. *Journal of Computational Chemistry*, Wiley, v. 29, n. 11, p. 1859–1865, 2008. Disponível em: <https://doi.org/10.1002/jcc.20945>.

JORNADA, J. A. H. da; ZAWISLAK, F. C. Effects of high pressure on the electric field gradient inspmetals. *Physical Review B*, American Physical Society (APS), v. 20, n. 7, p. 2617–2623, 1979. Disponível em: <https://doi.org/10.1103/physrevb.20.2617>.

JOSHI, R. P.; SCHOENBACH, K. H. Electroporation dynamics in biological cells subjected to ultrafast electrical pulses: A numerical simulation study. *Physical Review E*, American Physical Society (APS), v. 62, n. 1, p. 1025–1033, 2000. Disponível em: <https://doi.org/10.1103/physreve.62.1025>.

JUNQUEIRA, H.; SCHRODER, A. P.; THALMANN, F.; KLYMCHENKO, A.; MÉLY, Y.; BAPTISTA, M. S.; MARQUES, C. M. Molecular organization in hydroperoxidized POPC bilayers. *Biochimica et Biophysica Acta (BBA) - Biomembranes*, Elsevier BV, v. 1863, n. 10, p. 183659, 2021. Disponível em: <https://doi.org/10.1016/j.bbamem.2021.183659>.

KARAKATSANIS, P.; BAYERL, T. M. Diffusion measurements in oriented phospholipid bilayers byNMR1in a static fringe field gradient. *Physical Review E*, American Physical Society (APS), v. 54, n. 2, p. 1785–1790, 1996. Disponível em: <https://doi.org/10.1103/physreve.54.1785>.

KHAN, S.; LI, M.; MUENCH, S. P.; JEUKEN, L. J. C.; BEALES, P. A. Durable proteo-hybrid vesicles for the extended functional lifetime of membrane proteins in bionanotechnology. *Chemical Communications*, Royal Society of Chemistry (RSC), v. 52, n. 73, p. 11020–11023, 2016. Disponível em: <https://doi.org/10.1039/c6cc04207d>.

KHAN, S.; MCCABE, J.; HILL, K.; BEALES, P. A. Biodegradable hybrid block copolymer – lipid vesicles as potential drug delivery systems. *Journal of Colloid and Interface Science*, Elsevier BV, v. 562, p. 418–428, 2020. Disponível em: <https://doi.org/10.1016/j.jcis.2019.11.101>.

KIDDLE, J. J. Microwaves in organic and medicinal chemistry. *Journal of the American Chemical Society*, American Chemical Society (ACS), v. 128, n. 5, p. 1771–1772, 2006. Disponível em: <https://doi.org/10.1021/ja059814b>.

KIM, H.-J.; CHOI, Y.-M.; YANG, A. P. P.; YANG, T. C. S.; TAUB, I. A.; GILES, J.; DITUSA, C.; CHALL, S.; ZOLTAI, P. Microbiological and chemical investigation of ohmic heating of particulate foods using a 5 kW ohmic system. *Journal of Food Processing and Preservation*, Wiley, v. 20, n. 1, p. 41–58, 1996. Disponível em: <https://doi.org/10.1111/j.1745-4549.1996.tb00339.x>.

KIRSCH, S. A.; BÖCKMANN, R. A. Coupling of membrane nanodomain formation and enhanced electroporation near phase transition. *Biophysical Journal*, Elsevier BV, v. 116, n. 11, p. 2131–2148, 2019. Disponível em: <https://doi.org/10.1016/j.bpj.2019.04.024>.

KLAUDA, J. B.; VENABLE, R. M.; FREITES, J. A.; O'CONNOR, J. W.; TOBIAS, D. J.; MONDRAGON-RAMIREZ, C.; VOROBYOV, I.; MACKERELL, A. D.; PASTOR, R. W. Update of the CHARMM all-atom additive force field for lipids: Validation on six lipid types. *The Journal of Physical Chemistry B*, American Chemical Society (ACS), v. 114, n. 23, p. 7830–7843, 2010. Disponível em: <https://doi.org/10.1021/jp101759q>.

KNAPP, B.; OSPINA, L.; DEANE, C. M. Avoiding false positive conclusions in molecular simulation: The importance of replicas. *Journal of Chemical Theory and Computation*, American Chemical Society (ACS), v. 14, n. 12, p. 6127–6138, 2018. Disponível em: <https://doi.org/10.1021/acs.jctc.8b00391>.

KNORR, D.; FROEHLING, A.; JAEGER, H.; REINEKE, K.; SCHLUETER, O.; SCHOESSLER, K. Emerging technologies in food processing. *Annual Review of Food Science and Technology*, Annual Reviews, v. 2, n. 1, p. 203–235, 2011. Disponível em: <https://doi.org/10.1146/annurev.food.102308.124129>.

KOSHIYAMA, K.; KODAMA, T.; YANO, T.; FUJIKAWA, S. Structural change in lipid bilayers and water penetration induced by shock waves: Molecular dynamics simulations. *Biophysical Journal*, Elsevier BV, v. 91, n. 6, p. 2198–2205, 2006. Disponível em: <https://doi.org/10.1529/biophysj.105.077677>.

KOWALIK, M.; SCHANTZ, A. B.; NAQI, A.; SHEN, Y.; SINES, I.; MARANAS, J. K.; KUMAR, M. Chemically specific coarse-grained models to investigate the structure of biomimetic membranes. *RSC Advances*, Royal Society of Chemistry (RSC), v. 7, n. 86, p. 54756–54771, 2017. Disponível em: <https://doi.org/10.1039/c7ra10573h>.

KRASSOWSKA, W.; FILEV, P. D. Modeling electroporation in a single cell. *Biophysical Journal*, Elsevier BV, v. 92, n. 2, p. 404–417, 2007. Disponível em: <https://doi.org/10.1529/biophysj.106.094235>.

KRISHNAMURTHY, K.; KHURANA, H. K.; SOOJIN, J.; IRUDAYARAJ, J.; DEMIRCI, A. Infrared heating in food processing: An overview. *Comprehensive Reviews in Food Science and Food Safety*, Wiley, v. 7, n. 1, p. 2–13, 2008. Disponível em: <https://doi.org/10.1111/j.1541-4337.2007.00024.x>.

KUČERKA, N.; NIEH, M.-P.; KATSARAS, J. Fluid phase lipid areas and bilayer thicknesses of commonly used phosphatidylcholines as a function of temperature. *Biochimica et Biophysica Acta (BBA) - Biomembranes*, Elsevier BV, v. 1808, n. 11, p. 2761–2771, 2011. Disponível em: <https://doi.org/10.1016/j.bbamem.2011.07.022>.

KUMAR, M.; HABEL, J. E. O.; SHEN, Y. xiao; MEIER, W. P.; WALZ, T. High-density reconstitution of functional water channels into vesicular and planar block copolymer membranes. *Journal of the American Chemical Society*, American Chemical Society (ACS), v. 134, n. 45, p. 18631–18637, 2012. Disponível em: <https://doi.org/10.1021/ja304721r>.

KUMAR, S.; ROSENBERG, J. M.; BOUZIDA, D.; SWENDSEN, R. H.; KOLLMAN, P. A. Multidimensional free-energy calculations using the weighted histogram analysis method. *Journal of Computational Chemistry*, Wiley, v. 16, n. 11, p. 1339–1350, 1995. Disponível em: <https://doi.org/10.1002/jcc.540161104>.

KUMARI, B.; TIWARI, B. K.; HOSSAIN, M. B.; BRUNTON, N. P.; RAI, D. K. Recent advances on application of ultrasound and pulsed electric field technologies in the extraction of bioactives from agro-industrial by-products. *Food and Bioprocess Technology*, Springer Science and Business Media LLC, v. 11, n. 2, p. 223–241, 2017. Disponível em: <https://doi.org/10.1007%2Fs11947-017-1961-9>.

LAI, K.; WANG, B.; ZHANG, Y.; ZHANG, Y. High pressure effect on phase transition behavior of lipid bilayers. *Physical Chemistry Chemical Physics*, Royal Society of Chemistry (RSC), v. 14, n. 16, p. 5744, 2012. Disponível em: <https://doi.org/10.1039/c2cp24140d>.

LAMICHHANE, N.; UDAYAKUMAR, T.; D'SOUZA, W.; II, C. S.; RAGHAVAN, S.; POLF, J.; MAHMOOD, J. Liposomes: Clinical applications and potential for image-guided drug delivery. *Molecules*, MDPI AG, v. 23, n. 2, p. 288, 2018. Disponível em: <https://doi.org/10.3390/molecules23020288>.

LANGTON, M. J. Engineering of stimuli-responsive lipid-bilayer membranes using supramolecular systems. *Nature Reviews Chemistry*, Springer Science and Business Media LLC, v. 5, n. 1, p. 46–61, 2020. Disponível em: <https://doi.org/10.1038/s41570-020-00233-6>.

LARKIN, J.; SODEN, D.; COLLINS, C.; TANGNEY, M.; PRESTON, J.; RUSSELL, L.; MCHALE, A.; DUNNE, C.; O'SULLIVAN, G. Combined electric field and ultrasound therapy as a novel anti-tumour treatment. *European Journal of Cancer*, Elsevier BV, v. 41, n. 9, p. 1339–1348, 2005. Disponível em: <https://doi.org/10.1016%2Fj.ejca.2005.01.025>.

LEBAR, A. M.; MIKLAVČIČ, D.; KOTULSKA, M.; KRAMAR, P. Water pores in planar lipid bilayers at fast and slow rise of transmembrane voltage. *Membranes*, MDPI AG, v. 11, n. 4, p. 263, 2021. Disponível em: <https://doi.org/10.3390/membranes11040263>.

LEE, B.; RICHARDS, F. The interpretation of protein structures: Estimation of static accessibility. *Journal of Molecular Biology*, Elsevier BV, v. 55, n. 3, p. 379–IN4, 1971. Disponível em: <https://doi.org/10.1016/0022-2836(71)90324-x>.

LEE, B.-S.; MABRY, S. A.; JONAS, A.; JONAS, J. High-pressure proton NMR study of lateral self-diffusion of phosphatidylcholines in sonicated unilamellar vesicles. *Chemistry and Physics of Lipids*, Elsevier BV, v. 78, n. 2, p. 103–117, 1995. Disponível em: <https://doi.org/10.1016/0009-3084(95)02493-3>.

LEE, H.; VRIES, A. H. de; MARRINK, S.-J.; PASTOR, R. W. A coarse-grained model for polyethylene oxide and polyethylene glycol: Conformation and hydrodynamics. *The Journal of Physical Chemistry B*, American Chemical Society (ACS), v. 113, n. 40, p. 13186–13194, 2009. Disponível em: <https://doi.org/10.1021%2Fjp9058966>.

LEONE, S. D.; AVSAR, S. Y.; BELLUATI, A.; WEHR, R.; PALIVAN, C. G.; MEIER, W. Polymer–lipid hybrid membranes as a model platform to drive membrane Cytochrome c interaction and peroxidase-like activity. *The Journal of Physical Chemistry B*, American Chemical Society (ACS), v. 124, n. 22, p. 4454–4465, 2020. Disponível em: <https://doi.org/10.1021/acs.jpcb.0c02727>.

LEONTIADOU, H.; MARK, A. E.; MARRINK, S. J. Molecular dynamics simulations of hydrophilic pores in lipid bilayers. *Biophysical Journal*, Elsevier BV, v. 86, n. 4, p. 2156–2164, 2004. Disponível em: <https://doi.org/10.1016/s0006-3495(04)74275-7>.

LI, R.; KOU, X.; CHENG, T.; ZHENG, A.; WANG, S. Verification of radio frequency pasteurization process for in-shell almonds. *Journal of Food Engineering*, Elsevier BV, v. 192, p. 103–110, 2017. Disponível em: <https://doi.org/10.1016/j.jfoodeng.2016.08.002>.

LIM, S.; HOOG, H.-P. de; PARIKH, A.; NALLANI, M.; LIEDBERG, B. Hybrid, nanoscale phospholipid/block copolymer vesicles. *Polymers*, MDPI AG, v. 5, n. 3, p. 1102–1114, 2013. Disponível em: <https://doi.org/10.3390/polym5031102>.

LIMA, F.; VIEIRA, K.; SANTOS, M.; SOUZA, P. M. de. Effects of radiation technologies on food nutritional quality. In: *Descriptive Food Science*. London, UK: IntechOpen, 2018. Disponível em: <https://doi.org/10.5772/intechopen.80437>.

LIN, J.; ALEXANDER-KATZ, A. Probing lipid bilayers under ionic imbalance. *Biophysical Journal*, Elsevier BV, v. 111, n. 11, p. 2460–2469, 2016. Disponível em: <https://doi.org/10.1016/j.bpj.2016.10.006>.

LINDAHL; ABRAHAM; HESS; SPOEL, V. D. Gromacs 2021.4 manual. *Gromacs Manual*, Zenodo, 2021. Disponível em: <https://zenodo.org/record/5636522>.

LINDAHL, E.; EDHOLM, O. Spatial and energetic-entropic decomposition of surface tension in lipid bilayers from molecular dynamics simulations. *The Journal of Chemical Physics*, AIP Publishing, v. 113, n. 9, p. 3882–3893, 2000. Disponível em: <https://doi.org/10.1063/1.1287423>.

LIU, Y.; CAI, Y.; YING, D.; FU, Y.; XIONG, Y.; LE, X. Ovalbumin as a carrier to significantly enhance the aqueous solubility and photostability of curcumin: Interaction and binding mechanism study. *International Journal of Biological Macromolecules*, Elsevier BV, v. 116, p. 893–900, 2018. Disponível em: <https://doi.org/10.1016/j.ijbiomac.2018.05.089>.

LIU, Y.; WANG, H.; LI, S.; CHEN, C.; XU, L.; HUANG, P.; LIU, F.; SU, Y.; QI, M.; YU, C.; ZHOU, Y. In situ supramolecular polymerization-enhanced self-assembly of polymer vesicles for highly efficient photothermal therapy. *Nature Communications*, Springer Science and Business Media LLC, v. 11, n. 1724, p. 1–12, 2020. Disponível em: <https://doi.org/10.1038/s41467-020-15427-1>.

LLAVE, Y.; FUKUDA, S.; FUKUOKA, M.; SHIBATA-ISHIWATARI, N.; SAKAI, N. Analysis of color changes in chicken egg yolks and whites based on degree of thermal protein denaturation during ohmic heating and water bath treatment. *Journal of Food Engineering*, Elsevier BV, v. 222, p. 151–161, 2018. Disponível em: <https://doi.org/10.1016/j.jfoodeng.2017.11.024>.

LONDON, E. Lipid bilayer structure. In: *Encyclopedia of Biological Chemistry*. Cambridge, UK: Elsevier, 2013. p. 733–735. Disponível em: <https://doi.org/10.1016/b978-0-12-378630-2.00114-6>.

LU, H.; ZHANG, S.; WANG, J.; CHEN, Q. A review on polymer and lipid-based nanocarriers and its application to nano-pharmaceutical and food-based systems. *Frontiers in Nutrition*, Frontiers Media SA, v. 8, 2021. Disponível em: <https://doi.org/10.3389/fnut.2021.783831>.

MACDONALD, A. G. The effects of pressure on the molecular structure and physiological functions of cell membranes. *Philosophical Transactions of the Royal Society of London. B, Biological Sciences*, The Royal Society, v. 304, n. 1118, p. 47–68, 1984. Disponível em: <https://doi.org/10.1098/rstb.1984.0008>.

MACKERELL, A. D.; BANAVALI, N.; FOLOPPE, N. Development and current status of the CHARMM force field for nucleic acids. *Biopolymers*, Wiley, v. 56, n. 4, p. 257–265, 2000. Disponível em: <https://doi.org/10.1002/1097-0282(2000)56:4<257::aid-bip10029>3.0.co;2-w>.

MACKERELL, A. D.; BASHFORD, D.; BELLOTT, M.; DUNBRACK, R. L.; EVANSECK, J. D.; FIELD, M. J.; FISCHER, S.; GAO, J.; GUO, H.; HA, S.; JOSEPH-MCCARTHY, D.; KUCHNIR, L.; KUCZERA, K.; LAU, F. T. K.; MATTOS, C.; MICHNICK, S.; NGO, T.; NGUYEN, D. T.; PRODHOM, B.; REIHER, W. E.; ROUX, B.; SCHLENKRICH, M.; SMITH, J. C.; STOTE, R.; STRAUB, J.; WATANABE, M.; WIÓRKIEWICZ-KUCZERA, J.; YIN, D.; KARPLUS, M. All-atom empirical potential for molecular modeling and dynamics studies of proteins. *The Journal of Physical Chemistry B*, American Chemical Society (ACS), v. 102, n. 18, p. 3586–3616, 1998. Disponível em: <https://doi.org/10.1021/jp973084f>.

MACKERELL, A. D.; FEIG, M.; BROOKS, C. L. Improved treatment of the protein backbone in empirical force fields. *Journal of the American Chemical Society*, American Chemical Society (ACS), v. 126, n. 3, p. 698–699, 2004. Disponível em: <https://doi.org/10.1021/ja036959e>.

MAJD, S.; YUSKO, E. C.; BILLEH, Y. N.; MACRAE, M. X.; YANG, J.; MAYER, M. Applications of biological pores in nanomedicine, sensing, and nanoelectronics. *Curr. Opin. Biotechnol.*, Elsevier BV, v. 21, n. 4, p. 439–476, 2010. Disponível em: <https://doi.org/10.1016/j.copbio.2010.05.002>.

MAN, V. H.; LI, M. S.; DERREUMAUX, P.; WANG, J.; NGUYEN, P. H. Molecular mechanism of ultrasound-induced structural defects in liposomes: A nonequilibrium molecular dynamics simulation study. *Langmuir*, American Chemical Society (ACS), v. 37, n. 26, p. 7945–7954, 2021. Disponível em: <https://doi.org/10.1021/acs.langmuir.1c00555>.

MANZOOR, M. F.; ZENG, X.-A.; RAHAMAN, A.; SIDDEEG, A.; AADIL, R. M.; AHMED, Z.; LI, J.; NIU, D. Combined impact of pulsed electric field and ultrasound on bioactive compounds and FT-IR analysis of almond extract. *Journal of Food Science and Technology*, Springer Science and Business Media LLC, v. 56, n. 5, p. 2355–2364, 2019. Disponível em: <https://doi.org/10.1007%2Fs13197-019-03627-7>.

MARRACINO, P.; HAVELKA, D.; PRŮŠA, J.; LIBERTI, M.; TUSZYNSKI, J.; AYOUB, A. T.; APOLLONIO, F.; CIFRA, M. Tubulin response to intense nanosecond-scale electric field in molecular dynamics simulation. *Scientific Reports*, Springer Science and Business Media LLC, v. 9, n. 1, 2019. Disponível em: <https://doi.org/10.1038/s41598-019-46636-4>.

MARRINK, S. J.; RISSELADA, H. J.; YEFIMOV, S.; TIELEMAN, D. P.; VRIES, A. H. de. The MARTINI force field: coarse grained model for biomolecular simulations. *The Journal of Physical Chemistry B*, American Chemical Society (ACS), v. 111, n. 27, p. 7812–7824, 2007. Disponível em: <https://doi.org/10.1021/jp071097f>.

MARSH, D. Lipid bilayer lateral pressure profile. In: *Encyclopedia of Biophysics*. Springer Berlin Heidelberg, 2013. p. 1253–1256. Disponível em: <https://doi.org/10.1007/978-3-642-16712-6_544>.

MARTIN, J.; LETELLIER, G.; MARIN, A.; TALY, J.-F.; BREVERN, A. G. de; GIBRAT, J.-F. Protein secondary structure assignment revisited: a detailed analysis of different assignment methods. *BMC Structural Biology*, Springer Science and Business Media LLC, v. 5, n. 1, p. 17, 2005. Disponível em: <https://doi.org/10.1186/1472-6807-5-17>.

MARTÍNEZ, J. M.; DELSO, C.; ÁLVAREZ, I.; RASO, J. Pulsed electric field-assisted extraction of valuable compounds from microorganisms. *Comprehensive Reviews in Food Science and Food Safety*, Wiley, v. 19, n. 2, p. 530–552, 2020. Disponível em: <https://doi.org/10.1111/1541-4337.12512>.

MARUŠIČ, N.; OTRIN, L.; RAUCHHAUS, J.; ZHAO, Z.; KYRILIS, F. L.; HAMDI, F.; KASTRITIS, P. L.; DIMOVA, R.; IVANOV, I.; SUNDMACHER, K. Increased efficiency of charge-mediated fusion in polymer/lipid hybrid membranes. *Proceedings of the National Academy of Sciences*, Proceedings of the National Academy of Sciences, v. 119, n. 20, p. 1–12, 2022. Disponível em: <https://doi.org/10.1073/pnas.2122468119>.

MASSOUD, R.; BELGHEISI, S.; MASSOUD, A. Effect of high pressure homogenization on improving the quality of milk and sensory properties of yogurt: A review. *International Journal of Chemical Engineering and Applications*, EJournal Publishing, v. 7, n. 1, p. 66–70, 2016. Disponível em: <https://doi.org/10.7763/ijcea.2016.v7.544>.

MATHAI, J. C.; TRISTRAM-NAGLE, S.; NAGLE, J. F.; ZEIDEL, M. L. Structural determinants of water permeability through the lipid membrane. *Journal of General Physiology*, Rockefeller University Press, v. 131, n. 1, p. 69–76, 2007. Disponível em: <https://doi.org/10.1085/jgp.200709848>.

MAZUR, F.; BALLY, M.; STÄDLER, B.; CHANDRAWATI, R. Liposomes and lipid bilayers in biosensors. *Advances in Colloid and Interface Science*, Elsevier BV, v. 249, p. 88–99, 2017. Disponível em: <https://doi.org/10.1016/j.cis.2017.05.020>.

MEINS, J.-F. L.; SCHATZ, C.; LECOMMANDOUX, S.; SANDRE, O. Hybrid polymer/lipid vesicles: state of the art and future perspectives. *Materials Today*, Elsevier BV, v. 16, n. 10, p. 397–402, 2013. Disponível em: <https://doi.org/10.1016/j.mattod.2013.09.002>.

MINE, Y.; NOUTOMI, T.; HAGA, N. Emulsifying and structural properties of ovalbumin. *Journal of Agricultural and Food Chemistry*, American Chemical Society (ACS), v. 39, n. 3, p. 443–446, 1991. Disponível em: <https://doi.org/10.1021/jf00003a003>.

MIRAFZALI, Z.; THOMPSON, C. S.; TALLUA, K. Application of liposomes in the food industry. In: *Microencapsulation in the Food Industry*. Elsevier, 2014. p. 139–150. Disponível em: <https://doi.org/10.1016/b978-0-12-404568-2.00013-3>.

MOHAMMADALINEJHAD, S.; KUREK, M. A. Microencapsulation of anthocyanins — critical review of techniques and wall materials. *Applied Sciences*, MDPI AG, v. 11, n. 9, p. 3936, 2021. Disponível em: <https://doi.org/10.3390/app11093936>.

MONFORT, S.; MAÑAS, P.; CONDÓN, S.; RASO, J.; ÁLVAREZ, I. Physicochemical and functional properties of liquid whole egg treated by the application of pulsed electric fields followed by heat in the presence of triethyl citrate. *Food Research International*, Elsevier BV, v. 48, n. 2, p. 484–490, 2012. Disponível em: <https://doi.org/10.1016/j.foodres.2012.04.015>.

MONTICELLI, L.; KANDASAMY, S. K.; PERIOLE, X.; LARSON, R. G.; TIELEMAN, D. P.; MARRINK, S.-J. The MARTINI coarse-grained force field: Extension to proteins. *Journal of Chemical Theory and Computation*, American Chemical Society (ACS), v. 4, n. 5, p. 819–834, 2008. Disponível em: <https://doi.org/10.1021/ct700324x>.

MORADI, S.; NOWROOZI, A.; SHAHLAEI, M. Shedding light on the structural properties of lipid bilayers using molecular dynamics simulation: a review study. *RSC Advances*, Royal Society of Chemistry (RSC), v. 9, n. 8, p. 4644–4658, 2019. Disponível em: <https://doi.org/10.1039/c8ra08441f>.

MUHAMMAD, N.; DWORECK, T.; FIORONI, M.; SCHWANEBERG, U. Engineering of the *E. coli* outer membrane protein FhuA to overcome the hydrophobic mismatch in thick polymeric membranes. *Journal of Nanobiotechnology*, Springer Science and Business Media LLC, v. 9, n. 8, p. 1–9, 2011. Disponível em: <https://doi.org/10.1186/1477-3155-9-8>.

MUKHERJEE, A.; WATERS, A. K.; KALYAN, P.; ACHROL, A. S.; KESARI, S.; YENUGONDA, V. M. Lipid-polymer hybrid nanoparticles as a next-generation drug delivery platform: state of the art, emerging technologies, and perspectives. *International Journal of Nanomedicine*, Informa UK Limited, Volume 14, p. 1937–1952, 2019. Disponível em: <https://doi.org/10.2147/ijn.s198353>.

MULLAKAEV, M. S.; VOLKOVA, G. I.; GRADOV, O. M. Effect of ultrasound on the viscosity-temperature properties of crude oils of various compositions. *Theoretical Foundations of Chemical Engineering*, Pleiades Publishing Ltd, v. 49, n. 3, p. 287–296, 2015. Disponível em: <https://doi.org/10.1134/s0040579515030094>.

MULLIN, J. Microwave processing. In: *New Methods of Food Preservation*. Boston,USA: Springer US, 1995. p. 112–134. Disponível em: <https://doi.org/10.1007/978-1-4615-2105-1_6>.

MURALIDHARAN, A.; REMS, L.; KREUTZER, M. T.; BOUKANY, P. E. Actin networks regulate the cell membrane permeability during electroporation. *Biochimica et Biophysica Acta (BBA) - Biomembranes*, Elsevier BV, v. 1863, n. 1, p. 183468, 2021. Disponível em: <https://doi.org/10.1016/j.bbamem.2020.183468>.

MURASHITA, S.; KAWAMURA, S.; KOSEKI, S. Effects of ohmic heating, including electric field intensity and frequency, on thermal inactivation of *Bacillus subtilis* spores. *Journal of Food Protection*, International Association for Food Protection,

v. 80, n. 1, p. 164–168, 2016. Disponível em: <https://doi.org/10.4315/0362-028x.jfp-16-300>.

MUSSA, D.; RAMASWAMY, H. Ultra high pressure pasteurization of milk: Kinetics of microbial destruction and changes in physico-chemical characteristics. *LWT - Food Science and Technology*, Elsevier BV, v. 30, n. 6, p. 551–557, 1997. Disponível em: <https://doi.org/10.1006/fstl.1996.0223>.

MÜLLER, W. A.; PASIN, M. V. A.; SARKIS, J. R.; MARCZAK, L. D. F. Effect of pasteurization on *Aspergillus fumigatus* in apple juice: Analysis of the thermal and electric effects. *International Journal of Food Microbiology*, Elsevier BV, v. 338, p. 108993, 2021. Disponível em: <https://doi.org/10.1016/j.ijfoodmicro.2020.108993>.

NAGLE, J. F.; TRISTRAM-NAGLE, S. Lipid bilayer structure. *Current Opinion in Structural Biology*, Elsevier BV, v. 10, n. 4, p. 474–480, 2000. Disponível em: <https://doi.org/10.1016/s0959-440x(00)00117-2>.

NAM, J.; BEALES, P. A.; VANDERLICK, T. K. Giant phospholipid/block copolymer hybrid vesicles: Mixing behavior and domain formation. *Langmuir*, American Chemical Society (ACS), v. 27, n. 1, p. 1–6, 2010. Disponível em: <https://doi.org/10.1021/la103428g>.

NAM, J.; VANDERLICK, T. K.; BEALES, P. A. Formation and dissolution of phospholipid domains with varying textures in hybrid lipo-polymersomes. *Soft Matter*, Royal Society of Chemistry (RSC), v. 8, n. 30, p. 7982, 2012. Disponível em: <https://doi.org/10.1039/c2sm25646k>.

NGUYEN, C.; DESGRANGES, F.; ROY, G.; GALANIS, N.; MARÉ, T.; BOUCHER, S.; MINTSA, H. A. Temperature and particle-size dependent viscosity data for water-based nanofluids – hysteresis phenomenon. *International Journal of Heat and Fluid Flow*, Elsevier BV, v. 28, n. 6, p. 1492–1506, 2007. Disponível em: <https://doi.org/10.1016/j.ijheatfluidflow.2007.02.004>.

NORTON, S. J. Can ultrasound be used to stimulate nerve tissue? *BioMedical Engineering OnLine*, Springer Science and Business Media LLC, v. 2, n. 1, 2003. Disponível em: <https://doi.org/10.1186%2F1475-925x-2-6>.

NOTMAN, R.; NORO, M. G.; ANWAR, J. Interaction of oleic acid with dipalmitoylphosphatidylcholine (DPPC) bilayers simulated by molecular dynamics. *The Journal of Physical Chemistry B*, American Chemical Society (ACS), v. 111, n. 44, p. 12748–12755, 2007. Disponível em: <https://doi.org/10.1021/jp0723564>.

OHTAKI, H. Effects of temperature and pressure on hydrogen bonds in water and in formamide. *Journal of Molecular Liquids*, Elsevier BV, v. 103-104, p. 3–13, 2003. Disponível em: <https://doi.org/10.1016/s0167-7322(02)00124-1>.

OLIVEIRA, C. H.; BOIAGO, M. M.; GUARAGNI, A. Effects of heat treatments and edible shell coatings on egg quality after storage at room temperature. *Food Science and Technology*, FapUNIFESP (SciELO), v. 40, n. suppl 1, p. 344–348, 2020. Disponível em: <https://doi.org/10.1590/fst.13019>.

OPENSTAX. *Biology: Proteins*. USA: OpenStax CNX, 2015. Disponível em: <http://cnx.org/contents/185cbf87-c72e-48f5-b51e-f14f21b5eabd@9.85>.

OTRIN, L.; MARUŠIČ, N.; BEDNARZ, C.; VIDAKOVIĆ-KOCH, T.; LIEBERWIRTH, I.; LANDFESTER, K.; SUNDMACHER, K. Toward artificial mitochondrion: Mimicking oxidative phosphorylation in polymer and hybrid membranes. *Nano Letters*, American Chemical Society (ACS), v. 17, n. 11, p. 6816–6821, 2017. Disponível em: <https://doi.org/10.1021/acs.nanolett.7b03093>.

PABST, G.; KATSARAS, J.; RAGHUNATHAN, V. A. Enhancement of steric repulsion with temperature in oriented lipid multilayers. *Physical Review Letters*, American Physical Society (APS), v. 88, n. 12, 2002. Disponível em: <https://doi.org/10.1103/physrevlett.88.128101>.

PAN, J.; TRISTRAM-NAGLE, S.; KUČERKA, N.; NAGLE, J. F. Temperature dependence of structure, bending rigidity, and bilayer interactions of dioleoylphosphatidylcholine bilayers. *Biophysical Journal*, Elsevier BV, v. 94, n. 1, p. 117–124, 2008. Disponível em: <https://doi.org/10.1529/biophysj.107.115691>.

PAPAHADJOPOULOS, D.; KIMELBERG, H. K. Phospholipid vesicles (liposomes) as models for biological membranes: Their properties and interactions with cholesterol and proteins. *Progress in Surface Science*, Elsevier BV, v. 4, p. 141–232, 1974. Disponível em: <https://doi.org/10.1016/s0079-6816(74)80006-7>.

PARK, S. H.; SON, J. W.; PARK, J.; CHA, M. S. Elevated pressure increases the effect of electric fields on ionic wind in methane premixed jet flames. *Proceedings of the Combustion Institute*, Elsevier BV, v. 38, n. 4, p. 6679–6686, 2021. Disponível em: <https://doi.org/10.1016/j.proci.2020.11.003>.

PATRA, M. Lateral pressure profiles in cholesterol–DPPC bilayers. *European Biophysics Journal*, Springer Science and Business Media LLC, v. 35, n. 1, p. 79–88, 2005. Disponível em: <https://doi.org/10.1007/s00249-005-0011-0>.

PENG, X.; JONAS, A.; JONAS, J. High pressure 2H-NMR study of the order and dynamics of selectively deuterated dipalmitoyl phosphatidylcholine in multilamellar aqueous dispersions. *Biophysics Journal*, Elsevier BV, v. 68, n. 3, p. 1137–1144, 1995. Disponível em: <https://doi.org/10.1016/S0006-3495(95)80288-2>.

PEREIRA, R.; VICENTE, A. Environmental impact of novel thermal and non-thermal technologies in food processing. *Food Research International*, Elsevier BV, v. 43, n. 7, p. 1936–1943, 2010. Disponível em: <https://doi.org/10.1016/j.foodres.2009.09.013>.

PERERA, R. M.; GUPTA, S.; LI, T.; LEEUWEN, C. J. V.; BLEUEL, M.; HONG, K.; SCHNEIDER, G. J. Nanoscale lipid/polymer hybrid vesicles: Effects of triblock copolymer composition and hydrophilic weight fraction. *ACS Applied Polymer Materials*, American Chemical Society (ACS), v. 4, n. 12, p. 8858–8868, 2022. Disponível em: <https://doi.org/10.1021/acsapm.2c01272>.

PETELSKA, A. D.; FIGASZEWSKI, Z. A. Effect of pH on the interfacial tension of lipid bilayer membrane. *Biophysical Journal*, Elsevier BV, v. 78, n. 2, p. 812–817, 2000. Disponível em: <https://doi.org/10.1016/s0006-3495(00)76638-0>.

PHILLIPS, G. O.; WILLIAMS, P. A. *Handbook of food proteins*. Cambridge, UK: Elsevier Science, 2011.

PITT, W.; ROSS, S. Ultrasound increases the rate of bacterial cell growth. *Biotechnology Progress*, Wiley, v. 19, n. 3, p. 1038–1044, 2003. Disponível em: <https://doi.org/10.1021/bp0340685>.

PIYASENA, P.; MOHAREB, E.; MCKELLAR, R. Inactivation of microbes using ultrasound: a review. *International Journal of Food Microbiology*, Elsevier BV, v. 87, n. 3, p. 207–216, 2003. Disponível em: <https://doi.org/10.1016/s0168-1605(03)00075-8>.

PLIMPTON, S. Fast parallel algorithms for short-range molecular dynamics. *Journal of Computational Physics*, Elsevier BV, v. 117, n. 1, p. 1–19, 1995. Disponível em: <https://doi.org/10.1006/jcph.1995.1039>.

POSTMA, P.; PATARO, G.; CAPITOLI, M.; BARBOSA, M.; WIJFFELS, R.; EPPINK, M.; OLIVIERI, G.; FERRARI, G. Selective extraction of intracellular components from the microalga *Chlorella vulgaris* by combined pulsed electric field–temperature treatment. *Bioresource Technology*, Elsevier BV, v. 203, p. 80–88, 2016. Disponível em: <https://doi.org/10.1016/j.biortech.2015.12.012>.

PRIAMBODO, G.; KARTONO, A.; BATUBARA, I.; WAHYUDI, S. T. Structures prediction of *Plasmodium falciparum* signal peptide peptidase (PfSPP) and identification of binding site. *IOP Conference Series: Earth and Environmental Science*, IOP Publishing, v. 299, p. 012007, 2019. Disponível em: <https://doi.org/10.1088/1755-1315/299/1/012007>.

PRŮŠA, J.; CIFRA, M. Molecular dynamics simulation of the nanosecond pulsed electric field effect on kinesin nanomotor. *Scientific Reports*, Springer Science and Business Media LLC, v. 9, n. 1, 2019. Disponível em: <https://doi.org/10.1038/s41598-019-56052-3>.

PUÉRTOLAS, E.; LUENGO, E.; ÁLVAREZ, I.; RASO, J. Improving mass transfer to soften tissues by pulsed electric fields: Fundamentals and applications. *Annual Review of Food Science and Technology*, Annual Reviews, v. 3, n. 1, p. 263–282, 2012. Disponível em: <https://doi.org/10.1146/annurev-food-022811-101208>.

PYATKOVSKYY, T. I.; SHYNKARYK, M. V.; MOHAMED, H. M.; YOUSEF, A. E.; SASTRY, S. K. Effects of combined high pressure (HPP), pulsed electric field (PEF) and sonication treatments on inactivation of *Listeria innocua*. *Journal of Food Engineering*, Elsevier BV, v. 233, p. 49–56, 2018. Disponível em: <https://doi.org/10.1016/j.jfoodeng.2018.04.002>.

QIAN, J.-Y.; MA, L.-J.; WANG, L.-J.; JIANG, W. Effect of pulsed electric field on structural properties of protein in solid state. *LWT - Food Science and Technology*, Elsevier

BV, v. 74, p. 331–337, 2016. Disponível em: <https://doi.org/10.1016/j.lwt.2016.07.068>.

QIN, X.-S.; LUO, S.-Z.; CAI, J.; ZHONG, X.-Y.; JIANG, S.-T.; ZHENG, Z.; ZHAO, Y.-Y. Effects of microwave pretreatment and transglutaminase crosslinking on the gelation properties of soybean protein isolate and wheat gluten mixtures. *Journal of the Science of Food and Agriculture*, Wiley, v. 96, n. 10, p. 3559–3566, 2016. Disponível em: <https://doi.org/10.1002/jsfa.7541>.

RAMACHANDRAN, G.; RAMAKRISHNAN, C.; SASISEKHARAN, V. Stereochemistry of polypeptide chain configurations. *Journal of Molecular Biology*, Elsevier BV, v. 7, n. 1, p. 95–99, 1963. Disponível em: <https://doi.org/10.1016/s0022-2836(63)80023-6>.

RAMASWAMY, H.; TANG, J. Microwave and radio frequency heating. *Food Science and Technology International*, SAGE Publications, v. 14, n. 5, p. 423–427, 2008. Disponível em: <https://doi.org/10.1177/1082013208100534>.

RAO, D.; CHAWAN, C.; VEERAMACHENI, R. Liposomal encapsulation of β-galactosidase: Comparison of two methods of encapsulation and in vitro lactose digestibility. *Journal of Food Biochemistry*, Hindawi Limited, v. 18, n. 4, p. 239–251, 1994. Disponível em: <https://doi.org/10.1111/j.1745-4514.1994.tb00500.x>.

RAPAPORT, D. C. *The Art of Molecular Dynamics Simulation*. Cambridge University Press, 2004. Disponível em: <https://doi.org/10.1017/cbo9780511816581>.

RAVI, J.; TANTRA, R.; KNIGHT, A. Techniques for the measurement of the structure of proteins in solution, and their complementarity to circular dichroism. *NPL Report*, DQL-AS 023, 2005.

REIHER, W. *Theoretical Studies of Hydrogen Bonding*. Tese (Doutorado) — Harvard University, Cambridge, USA, 1985.

REIMHULT, E.; VIRK, M. M. Hybrid lipopolymer vesicle drug delivery and release systems. *The Journal of Biomedical Research*, Journal of Biomedical Research, v. 35, n. 4, p. 301, 2021. Disponível em: <https://doi.org/10.7555/jbr.35.20200206>.

RIDEAU, E.; DIMOVA, R.; SCHWILLE, P.; WURM, F. R.; LANDFESTER, K. Liposomes and polymersomes: a comparative review towards cell mimicking. *Chemical Society Reviews*, Royal Society of Chemistry (RSC), v. 47, n. 23, p. 8572–8610, 2018. Disponível em: <https://doi.org/10.1039/c8cs00162f>.

RIGAUD, J.-L.; PITARD, B.; LEVY, D. Reconstitution of membrane proteins into liposomes: application to energy-transducing membrane proteins. *Biochimica et Biophysica Acta (BBA) - Bioenergetics*, Elsevier BV, v. 1231, n. 3, p. 223–246, 1995. Disponível em: <https://doi.org/10.1016/0005-2728(95)00091-v>.

ROBINSON, S. W.; AFZAL, A. M.; LEADER, D. P. Bioinformatics: Concepts, methods, and data. In: *Handbook of Pharmacogenomics and Stratified Medicine*. Elsevier, 2014. p. 259–287. Disponível em: <https://doi.org/10.1016/b978-0-12-386882-4.00013-x>.

RODRIGUES, R. M.; AVELAR, Z.; MACHADO, L.; PEREIRA, R. N.; VICENTE, A. A. Electric field effects on proteins – novel perspectives on food and potential health implications. *Food Research International*, Elsevier BV, v. 137, p. 109709, 2020. Disponível em: <https://doi.org/10.1016/j.foodres.2020.109709>.

RODRIGUEZ-GONZALEZ, O.; BUCKOW, R.; KOUTCHMA, T.; BALASUBRAMANIAM, V. M. Energy requirements for alternative food processing technologies-principles, assumptions, and evaluation of efficiency. *Comprehensive Reviews in Food Science and Food Safety*, Wiley, v. 14, n. 5, p. 536–554, 2015. Disponível em: <https://doi.org/10.1111/1541-4337.12142>.

ROSSI, G.; FUCHS, P. F. J.; BARNOUD, J.; MONTICELLI, L. A coarse-grained MARTINI model of polyethylene glycol and of polyoxyethylene alkyl ether surfactants. *The Journal of Physical Chemistry B*, American Chemical Society (ACS), v. 116, n. 49, p. 14353–14362, 2012. Disponível em: <https://doi.org/10.1021%2Fjp3095165>.

ROSSI, G.; MONTICELLI, L.; PUISTO, S. R.; VATTULAINEN, I.; ALA-NISSILA, T. Coarse-graining polymers with the MARTINI force-field: polystyrene as a benchmark case. *Soft Matter*, Royal Society of Chemistry (RSC), v. 7, n. 2, p. 698–708, 2011. Disponível em: <https://doi.org/10.1039%2Fc0sm00481b>.

ROTH, C.; NEAL, B.; LENHOFF, A. Van der Waals interactions involving proteins. *Biophysical Journal*, Elsevier BV, v. 70, n. 2, p. 977–987, 1996. Disponível em: <https://doi.org/10.1016/s0006-3495(96)79641-8>.

RYCKAERT, J.-P.; CICCOTTI, G.; BERENDSEN, H. J. Numerical integration of the cartesian equations of motion of a system with constraints: Molecular dynamics of n-alkanes. *Journal of Computational Physics*, Elsevier BV, v. 23, n. 3, p. 327–341, 1977. Disponível em: <https://doi.org/10.1016/0021-9991(77)90098-5>.

SAFFMAN, P. G.; DELBRüCK, M. Brownian motion in biological membranes. *Proceedings of the National Academy of Sciences*, Proceedings of the National Academy of Sciences, v. 72, n. 8, p. 3111–3113, 1975. Disponível em: <https://doi.org/10.1073/pnas.72.8.3111>.

SALEEM, Q.; LAI, A.; MORALES, H. H.; MACDONALD, P. M. Lateral diffusion of bilayer lipids measured via 31P CODEX NMR. *Chemistry and Physics of Lipids*, Elsevier BV, v. 165, n. 7, p. 721–730, 2012. Disponível em: <https://doi.org/10.1016/j.chemphyslip.2012.08.001>.

SAM, A.; K., V. P.; SATHIAN, S. P. Water flow in carbon nanotubes: The role of tube chirality. *Physical Chemistry Chemical Physics*, Royal Society of Chemistry (RSC), v. 21, n. 12, p. 6566–6573, 2019. Disponível em: <https://doi.org/10.1039/c9cp00429g>.

SAMARANAYAKE, C. P.; SASTRY, S. K. Molecular dynamics evidence for nonthermal effects of electric fields on pectin methylesterase activity. *Physical Chemistry Chemical Physics*, Royal Society of Chemistry (RSC), v. 23, n. 26, p. 14422–14432, 2021. Disponível em: <https://doi.org/10.1039/d0cp05950a>.

SANTO, K. P.; BERKOWITZ, M. L. Shock wave induced collapse of arrays of nanobubbles located next to a lipid membrane: Coarse-grained computer simulations. *The Journal of Physical Chemistry B*, American Chemical Society (ACS), v. 119, n. 29, p. 8879–8889, 2014. Disponível em: <https://doi.org/10.1021/jp505720d>.

SANTO, K. P.; BERKOWITZ, M. L. Shock wave interaction with a phospholipid membrane: Coarse-grained computer simulations. *The Journal of Chemical Physics*, AIP Publishing, v. 140, n. 5, 2014. Disponível em: <https://doi.org/10.1063/1.4862987>.

SASTRE, D. E.; BASSO, L. G.; TRASTOY, B.; CIFUENTE, J. O.; CONTRERAS, X.; GUEIROS-FILHO, F.; MENDOZA, D. de; NAVARRO, M. V.; GUERIN, M. E. Membrane fluidity adjusts the insertion of the transacylase PlsX to regulate phospholipid biosynthesis in Gram-positive bacteria. *Journal of Biological Chemistry*, Elsevier BV, v. 295, n. 7, p. 2136–2147, 2020. Disponível em: <https://doi.org/10.1074/jbc.ra119.011122>.

SASTRY, S. Ohmic heating and moderate electric field processing. *Food Science and Technology International*, SAGE Publications, v. 14, n. 5, p. 419–422, 2008. Disponível em: <https://doi.org/10.1177/1082013208098813>.

SCHERER, D.; KRUST, D.; FREY, W.; MUELLER, G.; NICK, P.; GUSBETH, C. Pulsed electric field (PEF)-assisted protein recovery from *Chlorella vulgaris* is mediated by an enzymatic process after cell death. *Algal Research*, Elsevier BV, v. 41, p. 101536, 2019. Disponível em: <https://doi.org/10.1016/j.algal.2019.101536>.

SEIFERT, U. Configurations of fluid membranes and vesicles. *Advanced Physics*, Informa UK Limited, v. 46, n. 1, p. 13–137, 1997. Disponível em: <https://doi.org/10.1080/00018739700101488>.

SENEVIRATNE, R.; CATANIA, R.; RAPPOLT, M.; JEUKEN, L. J. C.; BEALES, P. A. Membrane mixing and dynamics in hybrid POPC/poly(1, 2-butadiene-block-ethylene oxide) (PBd-b-PEO) lipid/block co-polymer giant vesicles. *Soft Matter*, Royal Society of Chemistry (RSC), v. 18, n. 6, p. 1294–1301, 2022. Disponível em: <https://doi.org/10.1039/d1sm01591e>.

SENEVIRATNE, R.; COATES, G.; XU, Z.; CORNELL, C. E.; THOMPSON, R. F.; SADEGHPOUR, A.; MASKELL, D. P.; JEUKEN, L. J. C.; RAPPOLT, M.; BEALES, P. A. High resolution membrane structures within hybrid lipid-polymer vesicles revealed by combining X-ray scattering and electron microscopy. *Small*, Wiley, v. 19, n. 22, p. 2206267, 2023. Disponível em: <https://doi.org/10.1002/smll.202206267>.

SENEVIRATNE, R.; JEUKEN, L. J. C.; RAPPOLT, M.; BEALES, P. A. Hybrid vesicle stability under sterilisation and preservation processes used in the manufacture of medicinal formulations. *Polymer*, MDPI AG, v. 12, n. 4, p. 914, 2020. Disponível em: <https://doi.org/10.3390/polym12040914>.

SENEVIRATNE, R.; KHAN, S.; MOSCROP, E.; RAPPOLT, M.; MUENCH, S. P.; JEUKEN, L. J.; BEALES, P. A. A reconstitution method for integral membrane proteins in hybrid lipid-polymer vesicles for enhanced functional durability. *Methods*,

Elsevier BV, v. 147, p. 142–149, 2018. Disponível em: <https://doi.org/10.1016/j.ymeth.2018.01.021>.

SERCOMBE, L.; VEERATI, T.; MOHEIMANI, F.; WU, S. Y.; SOOD, A. K.; HUA, S. Advances and challenges of liposome assisted drug delivery. *Frontiers in Pharmacology*, Frontiers Media SA, v. 6, n. 286, p. 1–13, 2015. Disponível em: <https://doi.org/10.3389/fphar.2015.00286>.

SHAFIEE, H.; GARCIA, P. A.; DAVALOS, R. V. A preliminary study to delineate irreversible electroporation from thermal damage using the Arrhenius equation. *Journal of Biomechanical Engineering*, ASME International, v. 131, n. 7, 2009. Disponível em: <https://doi.org/10.1115/1.3143027>.

SHARMA, S.; PODDAR, M. K.; MOHOLKAR, V. S. Enhancement of thermal and mechanical properties of poly(MMA-co-BA)/Cloisite 30B nanocomposites by ultrasound-assisted in-situ emulsion polymerization. *Ultrasonics Sonochemistry*, Elsevier BV, v. 36, p. 212–225, 2017. Disponível em: <https://doi.org/10.1016/j.ultsonch.2016.11.029>.

SHI, J.; MA, Y.; ZHU, J.; CHEN, Y.; SUN, Y.; YAO, Y.; YANG, Z.; XIE, J. A review on electroporation-based intracellular delivery. *Molecules*, MDPI AG, v. 23, n. 11, p. 3044, 2018. Disponível em: <https://doi.org/10.3390/molecules23113044>.

SIEBLER, C.; MARYASIN, B.; KUEMIN, M.; ERDMANN, R. S.; RIGLING, C.; GRÜNENFELDER, C.; OCHSENFELD, C.; WENNEMERS, H. Importance of dipole moments and ambient polarity for the conformation of Xaa–Pro moieties – a combined experimental and theoretical study. *Chemical Science*, Royal Society of Chemistry (RSC), v. 6, n. 12, p. 6725–6730, 2015. Disponível em: <https://doi.org/10.1039/c5sc02211h>.

SINGH, A.; MUNSHI, S.; RAGHAVAN, V. Effect of external electric field stress on gliadin protein conformation. *Proteomes*, MDPI AG, v. 1, n. 2, p. 25–39, 2013. Disponível em: <https://doi.org/10.3390/proteomes1020025>.

SINGH, A.; ORSAT, V.; RAGHAVAN, V. Soybean hydrophobic protein response to external electric field: A molecular modeling approach. *Biomolecules*, MDPI AG, v. 3, n. 4, p. 168–179, 2013. Disponível em: <https://doi.org/10.3390/biom3010168>.

SINGH, P. R.; DENNIS, H. R. *Introduction to Food Engineering*. Amsterdam, Netherlands: Elsevier, 2014. Disponível em: <https://doi.org/10.1016/c2011-0-06101-x>.

SOBOLEV, O. V.; AFONINE, P. V.; MORIARTY, N. W.; HEKKELMAN, M. L.; JOOSTEN, R. P.; PERRAKIS, A.; ADAMS, P. D. A global Ramachandran score identifies protein structures with unlikely stereochemistry. *Structure*, Cold Spring Harbor Laboratory, 2020. Disponível em: <https://doi.org/10.1101/2020.03.26.010587>.

SOKOŁOWSKA, B.; SKĄPSKA, S.; FONBERG-BROCZEK, M.; NIEZGODA, J.; CHOTKIEWICZ, M.; DEKOWSKA, A.; RZOSKA, S. The combined effect of high

pressure and nisin or lysozyme on the inactivation of *Alicyclobacillus acidoterrestris* spores in apple juice. *High Pressure Research*, Informa UK Limited, v. 32, n. 1, p. 119–127, 2012. Disponível em: <https://doi.org/10.1080/08957959.2012.664642>.

SOUZA, P. C. T.; ALESSANDRI, R.; BARNOUD, J.; THALLMAIR, S.; FAUSTINO, I.; GRüNEWALD, F.; PATMANIDIS, I.; ABDIZADEH, H.; BRUININKS, B. M. H.; WASSENAAR, T. A.; KROON, P. C.; MELCR, J.; NIETO, V.; CORRADI, V.; KHAN, H. M.; DOMAŃSKI, J.; JAVANAINEN, M.; MARTINEZ-SEARA, H.; REUTER, N.; BEST, R. B.; VATTULAINEN, I.; MONTICELLI, L.; PERIOLE, X.; TIELEMAN, D. P.; VRIES, A. H. de; MARRINK, S. J. Martini 3: a general purpose force field for coarse-grained molecular dynamics. *Nature Methods*, Springer Science and Business Media LLC, v. 18, n. 4, p. 382–388, 2021. Disponível em: <https://doi.org/10.1038%2Fs41592-021-01098-3>.

SPINTI, J. K.; NUNES, F. N.; MELO, M. N. Room for improvement in the initial Martini 3 parameterization of peptide interactions. *Chemical Physics Letters*, Elsevier BV, v. 819, p. 140436, 2023. Disponível em: <https://doi.org/10.1016/j.cplett.2023.140436>.

SRINIVAS, G.; DISCHER, D. E.; KLEIN, M. L. Self-assembly and properties of diblock copolymers by coarse-grain molecular dynamics. *Nature Materials*, Springer Science and Business Media LLC, v. 3, n. 9, p. 638–644, 2004. Disponível em: <https://doi.org/10.1038/nmat1185>.

STACHURA, S.; KNELLER, G. R. Anomalous lateral diffusion in lipid bilayers observed by molecular dynamics simulations with atomistic and coarse-grained force fields. *Molecular Simulation*, Informa UK Limited, v. 40, n. 1-3, p. 245–250, 2013. Disponível em: <https://doi.org/10.1080/08927022.2013.840902>.

STEIN, P. E.; LESLIE, A. G.; FINCH, J. T.; CARRELL, R. W. Crystal structure of uncleaved ovalbumin at 1.95 A resolution. *Journal of Molecular Biology*, Elsevier BV, v. 221, n. 3, p. 941–959, 1991. Disponível em: <https://doi.org/10.1016/0022-2836(91)80185-w>.

STEINKÜHLER, J.; JACOBS, M. L.; BOYD, M. A.; VILLASEÑOR, C. G.; LOVERDE, S. M.; KAMAT, N. P. Peo-b-pbd diblock copolymers induce packing defects in lipid/hybrid membranes and improve insertion rates of natively folded peptides. *Biomacromolecules*, American Chemical Society (ACS), v. 23, n. 11, p. 4756–4765, 2022. Disponível em: <https://doi.org/10.1021/acs.biomac.2c00936>.

STOENESCU, R.; GRAFF, A.; MEIER, W. Asymmetric ABC-triblock copolymer membranes induce a directed insertion of membrane proteins. *Macromolecular Bioscience*, Wiley, v. 4, n. 10, p. 930–935, 2004. Disponível em: <https://doi.org/10.1002/mabi.200400065>.

SUN, S.; YIN, G.; LEE, Y.-K.; WONG, J. T.; ZHANG, T.-Y. Effects of deformability and thermal motion of lipid membrane on electroporation: By molecular dynamics simulations. *Biochemical and Biophysical Research Communications*, Elsevier BV,

v. 404, n. 2, p. 684–688, 2011. Disponível em: <https://doi.org/10.1016/j.bbrc.2010.12.042>.

SURESH, S. J.; SATISH, A. V.; CHOUDHARY, A. Influence of electric field on the hydrogen bond network of water. *The Journal of Chemical Physics*, AIP Publishing, v. 124, n. 7, p. 074506, 2006. Disponível em: <https://doi.org/10.1063/1.2162888>.

SWAMY, G. J.; MUTHUKUMARAPPAN, K. Microwave and radiofrequency processing of plant-related food products. In: *Innovative Food Processing Technologies*. Elsevier, 2021. p. 731–742. Disponível em: <https://doi.org/10.1016/b978-0-12-815781-7.00010-x>.

TADA, K.; MIYAZAKI, E.; GOTO, M.; TAMAI, N.; MATSUKI, H.; KANESHINA, S. Barotropic and thermotropic bilayer phase behavior of positional isomers of unsaturated mixed-chain phosphatidylcholines. *Biochimica et Biophysica Acta (BBA) - Biomembranes*, Elsevier BV, v. 1788, n. 5, p. 1056–1063, 2009. Disponível em: <https://doi.org/10.1016/j.bbamem.2009.02.008>.

TAECHALERTPAISARN, J.; LYU, R.-L.; ARANCILLO, M.; LIN, C.-M.; PEREZ, L. M.; IOERGER, T. R.; BURGESS, K. Correlations between secondary structure and protein-protein interface-mimicry: The interface mimicry hypothesis. *Organic & Biomolecular Chemistry*, Royal Society of Chemistry (RSC), v. 17, n. 12, p. 3267–3274, 2019. Disponível em: <https://doi.org/10.1039/c9ob00204a>.

TAKAHASHI, N.; MAEDA, M.; YAMASAKI, M.; MIKAMI, B. Protein-engineering study of contribution of conceivable D-Serine residues to the thermostabilization of ovalbumin under alkaline conditions. *Chemistry & Biodiversity*, Wiley, v. 7, n. 6, p. 1634–1643, 2010. Disponível em: <https://doi.org/10.1002/cbdv.200900305>.

TAREK, M. Membrane electroporation: A molecular dynamics simulation. *Biophysical Journal*, Elsevier BV, v. 88, n. 6, p. 4045–4053, 2005. Disponível em: <https://doi.org/10.1529/biophysj.104.050617>.

TEISSIE, J.; GOLZIO, M.; ROLS, M. Mechanisms of cell membrane electropermeabilization: A minireview of our present (lack of ?) knowledge. *Biochimica et Biophysica Acta (BBA) - General Subjects*, Elsevier BV, v. 1724, n. 3, p. 270–280, 2005. Disponível em: <https://doi.org/10.1016/j.bbagen.2005.05.006>.

TEMPLER, R. H.; KHOO, B. J.; SEDDON, J. M. Gaussian curvature modulus of an amphiphilic monolayer. *Langmuir*, American Chemical Society (ACS), v. 14, n. 26, p. 7427–7434, 1998. Disponível em: <https://doi.org/10.1021/la980701y>.

THIRUMDAS, R.; SARANGAPANI, C.; ANNAPURE, U. S. Cold plasma: A novel non-thermal technology for food processing. *Food Biophysics*, Springer Science and Business Media LLC, v. 10, n. 1, p. 1–11, 2014. Disponível em: <https://doi.org/10.1007/s11483-014-9382-z>.

THOMAS, A. S.; ELCOCK, A. H. Molecular simulations suggest protein salt bridges are uniquely suited to life at high temperatures. *Journal of the American Chemical Society*, American Chemical Society (ACS), v. 126, n. 7, p. 2208–2214, 2004. Disponível em: <https://doi.org/10.1021/ja039159c>.

THYSSENKRUPP. *What is HPP? All the relevant information about High Pressure Processing*. 2021. <https://www.thyssenkrupp-industrial-solutions.com/high-pressure-processing/en/what-is-hpp>. Accessed: 2021-20-10.

TIMASHEFF, S. N. Protein-solvent interactions and protein conformation. *Accounts of Chemical Research*, American Chemical Society (ACS), v. 3, n. 2, p. 62–68, 1970. Disponível em: <https://doi.org/10.1021/ar50026a004>.

TING, B. C. P.; POULIOT, Y.; GAUTHIER, S.; MINE, Y. Fractionation of egg proteins and peptides for nutraceutical applications. In: *Separation, extraction and concentration processes in the food, beverage and nutraceutical industries*. Elsevier, 2013. p. 595–618. Disponível em: <https://doi.org/10.1533/9780857090751.2.595>.

TODOROVA, N.; BENTVELZEN, A.; YAROVSKY, I. Electromagnetic field modulates aggregation propensity of amyloid peptides. *The Journal of Chemical Physics*, AIP Publishing, v. 152, n. 3, p. 035104, 2020. Disponível em: <https://doi.org/10.1063/1.5126367>.

TU, Z. cai; HU, Y. ming; WANG, H.; HUANG, X. qin; XIA, S. qi; NIU, P. pei. Microwave heating enhances antioxidant and emulsifying activities of ovalbumin glycated with glucose in solid-state. *Journal of Food Science and Technology*, Springer Science and Business Media LLC, v. 52, n. 3, p. 1453–1461, 2013. Disponível em: <https://doi.org/10.1007/s13197-013-1120-x>.

TUCKERMAN, M. E.; MARTYNA, G. J. Understanding modern molecular dynamics: techniques and applications. *The Journal of Physical Chemistry B*, American Chemical Society (ACS), v. 104, n. 2, p. 159–178, 1999. Disponível em: <https://doi.org/10.1021/jp992433y>.

ULRICH, A. S.; SAMI, M.; WATTS, A. Hydration of DOPC bilayers by differential scanning calorimetry. *Biochimica et Biophysica Acta (BBA) - Biomembranes*, Elsevier BV, v. 1191, n. 1, p. 225–230, 1994. Disponível em: <https://doi.org/10.1016/0005-2736(94)90253-4>.

USAJ, M.; KANDUSER, M. The systematic study of the electroporation and electrofusion of B16-F1 and CHO cells in isotonic and hypotonic buffer. *The Journal of Membrane Biology*, Springer Science and Business Media LLC, v. 245, n. 9, p. 583–590, 2012. Disponível em: <https://doi.org/10.1007/s00232-012-9470-2>.

VAESSEN, E.; BESTEN, H. den; PATRA, T.; MOSSEVELDE, N. van; BOOM, R.; SCHUTYSER, M. Pulsed electric field for increasing intracellular trehalose content in *Lactobacillus plantarum* WCFS1. *Innovative Food Science & Emerging Technologies*, Elsevier BV, v. 47, p. 256–261, 2018. Disponível em: <https://doi.org/10.1016/j.ifset.2018.03.007>.

VAGADIA, B. H.; VANGA, S. K.; SINGH, A.; RAGHAVAN, V. Effects of thermal and electric fields on soybean trypsin inhibitor protein: A molecular modelling study. *Innovative Food Science & Emerging Technologies*, Elsevier BV, v. 35, p. 9–20, 2016. Disponível em: <https://doi.org/10.1016/j.ifset.2016.03.004>.

VANGA, S. K.; SINGH, A.; RAGHAVAN, V. Effect of thermal and electric field treatment on the conformation of Ara h 6 peanut protein allergen. *Innovative Food Science & Emerging Technologies*, Elsevier BV, v. 30, p. 79–88, 2015. Disponível em: <https://doi.org/10.1016/j.ifset.2015.03.003>.

VANGA, S. K.; WANG, J.; JAYARAM, S.; RAGHAVAN, V. Effects of pulsed electric fields and ultrasound processing on proteins and enzymes: A review. *Processes*, MDPI AG, v. 9, n. 4, p. 722, 2021. Disponível em: <https://doi.org/10.3390/pr9040722>.

VEDADI, M.; CHOUBEY, A.; NOMURA, K.; KALIA, R. K.; NAKANO, A.; VASHISHTA, P.; DUIN, A. C. T. van. Structure and dynamics of shock-induced nanobubble collapse in water. *Physical Review Letters*, American Physical Society (APS), v. 105, n. 1, 2010. Disponível em: <https://doi.org/10.1103/physrevlett.105.014503>.

VERMEER, L. S.; GROOT, B. L. de; RÉAT, V.; MILON, A.; CZAPLICKI, J. Acyl chain order parameter profiles in phospholipid bilayers: computation from molecular dynamics simulations and comparison with 2h NMR experiments. *European Biophysics Journal*, Springer Science and Business Media LLC, v. 36, n. 8, p. 919–931, 2007. Disponível em: <https://doi.org/10.1007/s00249-007-0192-9>.

WANG, X.; LI, Y.; HE, X.; CHEN, S.; ZHANG, J. Z. H. Effect of strong electric field on the conformational integrity of insulin. *The Journal of Physical Chemistry A*, American Chemical Society (ACS), v. 118, n. 39, p. 8942–8952, 2014. Disponível em: <https://doi.org/10.1021/jp501051r>.

WANG, Y.; GKEKA, P.; FUCHS, J. E.; LIEDL, K. R.; COURNIA, Z. DPPC-cholesterol phase diagram using coarse-grained molecular dynamics simulations. *Biochimica et Biophysica Acta (BBA) - Biomembranes*, Elsevier BV, v. 1858, n. 11, p. 2846–2857, 2016. Disponível em: <https://doi.org/10.1016/j.bbamem.2016.08.005>.

WANG, Y.; YONG, M.; WEI, S.; ZHANG, Y.; LIU, W.; XU, Z. Performance improvement of hybrid polymer membranes for wastewater treatment by introduction of micro reaction locations. *Progress in Natural Science: Materials International*, Elsevier BV, v. 28, n. 2, p. 148–159, 2018. Disponível em: <https://doi.org/10.1016/j.pnsc.2018.02.011>.

WANG, Z.; LIU, X.; FANG, Y.; WANG, X.; HU, Y.; LI, Y. Microwaves affect the formation of volatile compounds in peper powder by changing the nucleophilic addition reactions in maillard reactions. *Food Chemistry: X*, Elsevier BV, v. 19, p. 100828, 2023. Disponível em: <https://doi.org/10.1016/j.fochx.2023.100828>.

WASSENAAR, T. A.; INGÓLFSSON, H. I.; BÖCKMANN, R. A.; TIELEMAN, D. P.; MARRINK, S. J. Computational lipidomics with insane: A versatile tool for generating custom membranes for molecular simulations. *Journal of Chemical Theory and Computation*, American Chemical Society (ACS), v. 11, n. 5, p. 2144–2155, 2015. Disponível em: <https://doi.org/10.1021/acs.jctc.5b00209>.

WEAVER, J. C.; CHIZMADZHEV, Y. Theory of electroporation: A review. *Bioelectrochemistry and Bioenergetics*, Elsevier BV, v. 41, n. 2, p. 135–160, 1996. Disponível em: <https://doi.org/10.1016/s0302-4598(96)05062-3>.

WEBER, G.; CHARITAT, T.; BAPTISTA, M. S.; UCHOA, A. F.; PAVANI, C.; JUNQUEIRA, H. C.; GUO, Y.; BAULIN, V. A.; ITRI, R.; MARQUES, C. M.; SCHRODER, A. P. Lipid oxidation induces structural changes in biomimetic membranes. *Soft Matter*, Royal Society of Chemistry (RSC), v. 10, n. 24, p. 4241, 2014. Disponível em: <https://doi.org/10.1039/c3sm52740a>.

WEI, Y.; XIAO, Y.; WANG, Z. The interventional therapeutics of irreversible electroporation for pancreatic cancer. In: *Integrative Pancreatic Intervention Therapy*. Elsevier, 2021. p. 355–362. Disponível em: <https://doi.org/10.1016/b978-0-12-819402-7.00014-0>.

WIKTOR, A.; GONDEK, E.; JAKUBCZYK, E.; DADAN, M.; NOWACKA, M.; RYBAK, K.; WITROWA-RAJCHERT, D. Acoustic and mechanical properties of carrot tissue treated by pulsed electric field, ultrasound and combination of both. *Journal of Food Engineering*, Elsevier BV, v. 238, p. 12–21, 2018. Disponível em: <https://doi.org/10.1016%2Fj.jfoodeng.2018.06.001>.

WILLIAMS, C. J.; HEADD, J. J.; MORIARTY, N. W.; PRISANT, M. G.; VIDEAU, L. L.; DEIS, L. N.; VERMA, V.; KEEDY, D. A.; HINTZE, B. J.; CHEN, V. B.; JAIN, S.; LEWIS, S. M.; ARENDALL, W. B.; SNOEYINK, J.; ADAMS, P. D.; LOVELL, S. C.; RICHARDSON, J. S.; RICHARDSON, D. C. MolProbity: More and better reference data for improved all-atom structure validation. *Protein Science*, Wiley, v. 27, n. 1, p. 293–315, 2017. Disponível em: <https://doi.org/10.1002/pro.3330>.

WINGER, M.; TRZESNIAK, D.; BARON, R.; GUNSTEREN, W. F. van. On using a too large integration time step in molecular dynamics simulations of coarse-grained molecular models. *Physical Chemistry Chemical Physics*, Royal Society of Chemistry (RSC), 2009. Disponível em: <https://doi.org/10.1039/b818713d>.

WONG, P. T.; SIMINOVITCH, D. J.; MANTSCH, H. H. Structure and properties of model membranes: new knowledge from high-pressure vibrational spectroscopy. *Biochimica et Biophysica Acta (BBA) - Reviews on Biomembranes*, Elsevier BV, v. 947, n. 1, p. 139–171, 1988. Disponível em: <https://doi.org/10.1016/0304-4157(88)90023-8>.

WU, J. Acoustic streaming and its applications. *Fluids*, MDPI AG, v. 3, n. 4, p. 108, 2018. Disponível em: <https://doi.org/10.3390/fluids3040108>.

WU, L.; ZHAO, W.; YANG, R.; CHEN, X. Effects of pulsed electric fields processing on stability of egg white proteins. *Journal of Food Engineering*, Elsevier BV, v. 139, p. 13–18, 2014. Disponível em: <https://doi.org/10.1016/j.jfoodeng.2014.04.008>.

WU, L.; ZHAO, W.; YANG, R.; YAN, W. Pulsed electric field (PEF)-induced aggregation between lysozyme, ovalbumin and ovotransferrin in multi-protein system. *Food Chemistry*, Elsevier BV, v. 175, p. 115–120, 2015. Disponível em: <https://doi.org/10.1016/j.foodchem.2014.11.136>.

XU, J.; ZHANG, M.; CAO, P.; ADHIKARI, B.; YANG, C. Microorganisms control and quality improvement of stewed pork with carrots using ZnO nanoparticles combined with radio frequency pasteurization. *Food Bioscience*, Elsevier BV, v. 32, p. 100487, 2019. Disponível em: <https://doi.org/10.1016/j.fbio.2019.100487>.

YAMAMOTO, K. Food processing by high hydrostatic pressure. *Bioscience, Biotechnology, and Biochemistry*, Oxford University Press (OUP), v. 81, n. 4, p. 672–679, 2017. Disponível em: <https://doi.org/10.1080/09168451.2017.1281723>.

YANG, W.; TU, Z.; WANG, H.; ZHANG, L.; GAO, Y.; LI, X.; TIAN, M. Immunogenic and structural properties of ovalbumin treated by pulsed electric fields. *International Journal of Food Properties*, Informa UK Limited, v. 20, n. sup3, p. S3164–S3176, 2017. Disponível em: <https://doi.org/10.1080/10942912.2017.1396479>.

YESYLEVSKYY, S. O.; SCHÄFER, L. V.; SENGUPTA, D.; MARRINK, S. J. Polarizable water model for the coarse-grained MARTINI force field. *PLoS Computational Biology*, Public Library of Science (PLoS), v. 6, n. 6, p. e1000810, 2010. Disponível em: <https://doi.org/10.1371/journal.pcbi.1000810>.

YILDIZ, H.; BAYSAL, T. Effects of alternative current heating treatment on *Aspergillus niger*, pectin methylesterase and pectin content in tomato. *Journal of Food Engineering*, Elsevier BV, v. 75, n. 3, p. 327–332, 2006. Disponível em: <https://doi.org/10.1016/j.jfoodeng.2005.04.020>.

YIN, D.; MACKERELL, A. D. Combined ab initio/empirical approach for optimization of lennard-jones parameters. *Journal of Computational Chemistry*, Wiley, v. 19, n. 3, p. 334–348, 1998. Disponível em: <https://doi.org/10.1002/(sici)1096-987x(199802)19:3<334::aid-jcc7>3.0.co;2-u>.

YOGESH, K. Pulsed electric field processing of egg products: A review. *Journal of Food Science and Technology*, Springer Science and Business Media LLC, v. 53, n. 2, p. 934–945, 2015. Disponível em: <https://doi.org/10.1007/s13197-015-2061-3>.

YUE, T.; SUN, M.; ZHANG, S.; REN, H.; GE, B.; HUANG, F. How transmembrane peptides insert and orientate in biomembranes: a combined experimental and simulation study. *Physical Chemistry Chemical Physics*, Royal Society of Chemistry (RSC), v. 18, n. 26, p. 17483–17494, 2016. Disponível em: <https://doi.org/10.1039/c6cp01133k>.

ZÁRATE-RODRÍGUEZ, E.; ORTEGA-RIVAS, E.; BARBOSA-CÁNOVAS, G. Quality changes in apple juice as related to nonthermal processing. *Journal of Food Quality*, Wiley, v. 23, n. 3, p. 337–349, 2000. Disponível em: <https://doi.org/10.1111/j.1745-4557.2000.tb00219.x>.

ZAYAS, J. F. Emulsifying properties of proteins. In: *Functionality of proteins in food*. Springer Berlin Heidelberg, 1997. p. 134–227. Disponível em: <https://doi.org/10.1007/978-3-642-59116-7>.

ZAYAS, J. F. Foaming properties of proteins. In: *Functionality of proteins in food*. Springer Berlin Heidelberg, 1997. p. 260–309. Disponível em: <https://doi.org/10.1007/978-3-642-59116-7>.

ZHANG, R.; CROSS, T. A.; PENG, X.; FU, R. Surprising rigidity of functionally important water molecules buried in the lipid headgroup region. *Journal of the American Chemical Society*, American Chemical Society (ACS), v. 144, n. 17, p. 7881–7888, 2022. Disponível em: <https://doi.org/10.1021/jacs.2c02145>.

ZHANG, Y.; SAGUI, C. Secondary structure assignment for conformationally irregular peptides: Comparison between DSSP, STRIDE and KAKSI. *Journal of Molecular Graphics and Modelling*, Elsevier BV, v. 55, p. 72–84, 2015. Disponível em: <https://doi.org/10.1016/j.jmgm.2014.10.005>.

ZHAO, W.; YANG, R. Pulsed electric field induced aggregation of food proteins: Ovalbumin and bovine serum albumin. *Food and Bioprocess Technology*, Springer Science and Business Media LLC, v. 5, n. 5, p. 1706–1714, 2010. Disponível em: <https://doi.org/10.1007/s11947-010-0464-8>.

ZHAO, Y. Asymmetrical polymer vesicles for drug delivery and other applications. *Frontiers in Pharmacology*, Frontiers Media SA, v. 8, p. 1–9, 2017. Disponível em: <https://doi.org/10.3389/fphar.2017.00374>.

ZHOU, C.; LIU, K. Molecular dynamics simulation of reversible electroporation with Martini force field. *BioMedical Engineering OnLine*, Springer Science and Business Media LLC, v. 18, n. 1, 2019. Disponível em: <https://doi.org/10.1186/s12938-019-0743-1>.

ZHU, K.; WANG, G.; ZHANG, S.; DU, Y.; LU, Y.; NA, R.; MU, Y.; ZHANG, Y. Preparation of organic–inorganic hybrid membranes with superior antifouling property by incorporating polymer-modified multiwall carbon nanotubes. *RSC Advances*, Royal Society of Chemistry (RSC), v. 7, n. 49, p. 30564–30572, 2017. Disponível em: <https://doi.org/10.1039/c7ra04248e>.

ZIDAR, M.; ROZMAN, P.; BELKO-PARKEL, K.; RAVNIK, M. Control of viscosity in biopharmaceutical protein formulations. *Journal of Colloid and Interface Science*, Elsevier BV, v. 580, p. 308–317, 2020. Disponível em: <https://doi.org/10.1016/j.jcis.2020.06.105>.

Appendix A

Chapter 4 complementary information

A.1 Deuterium order parameter profiles

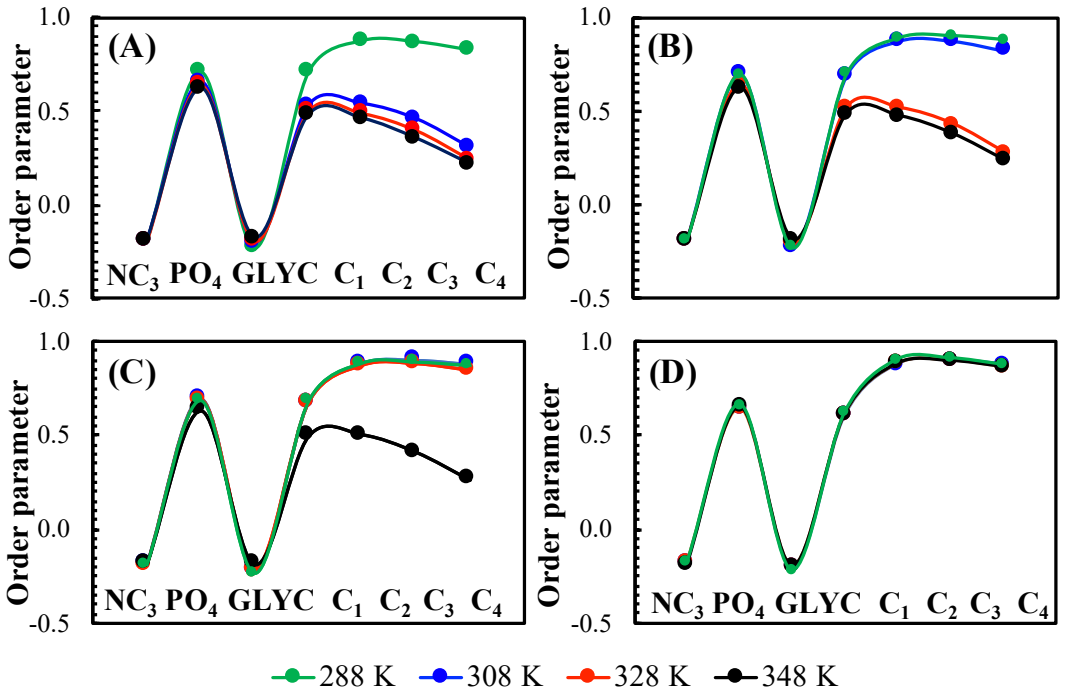

FIGURE A.1. Deuterium order parameter profiles at (A) 1 atm, (B) 500 atm, (C) 1000 atm, (D) 5000 atm.

A.2 Arrhenius model applied to the electroporation kinetics parameters

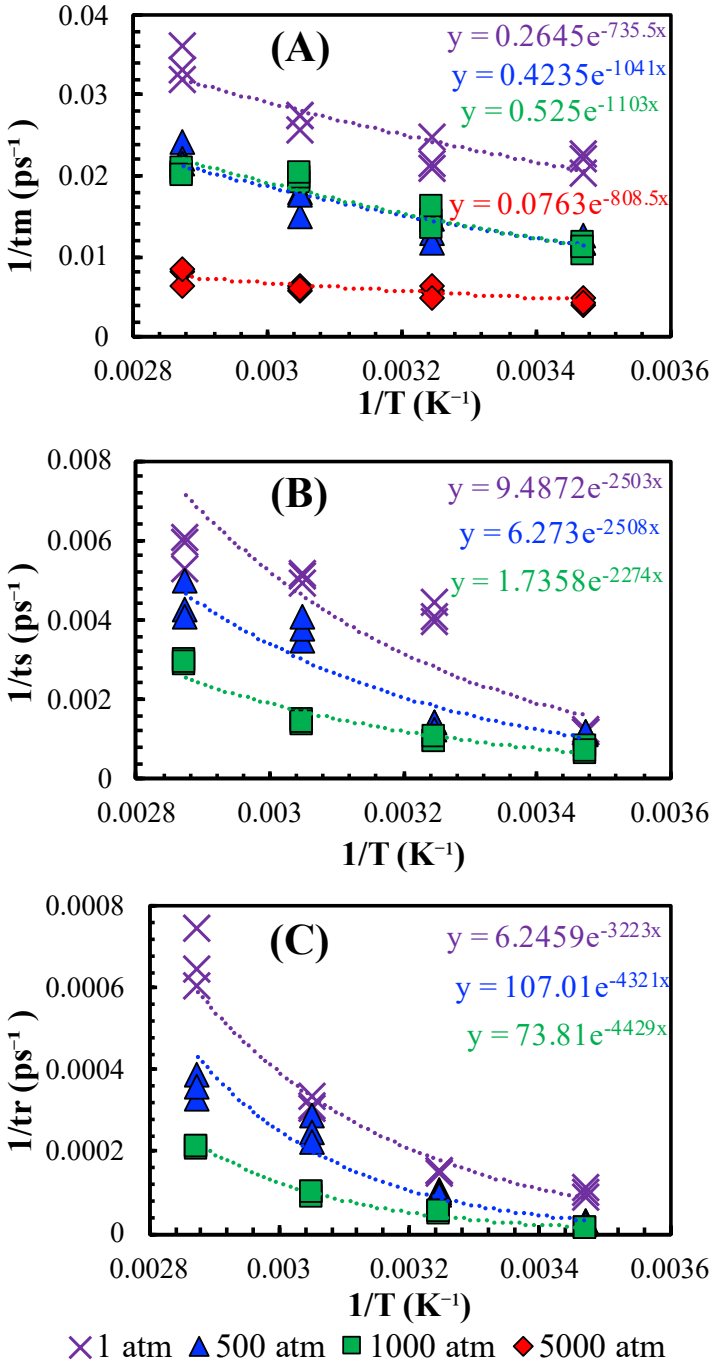

FIGURE A.2. Arrhenius model applied for (A) t_m, (B) t_s, and (C) t_r.

A.3 Evolution of the number of ions in compartment I as function of time

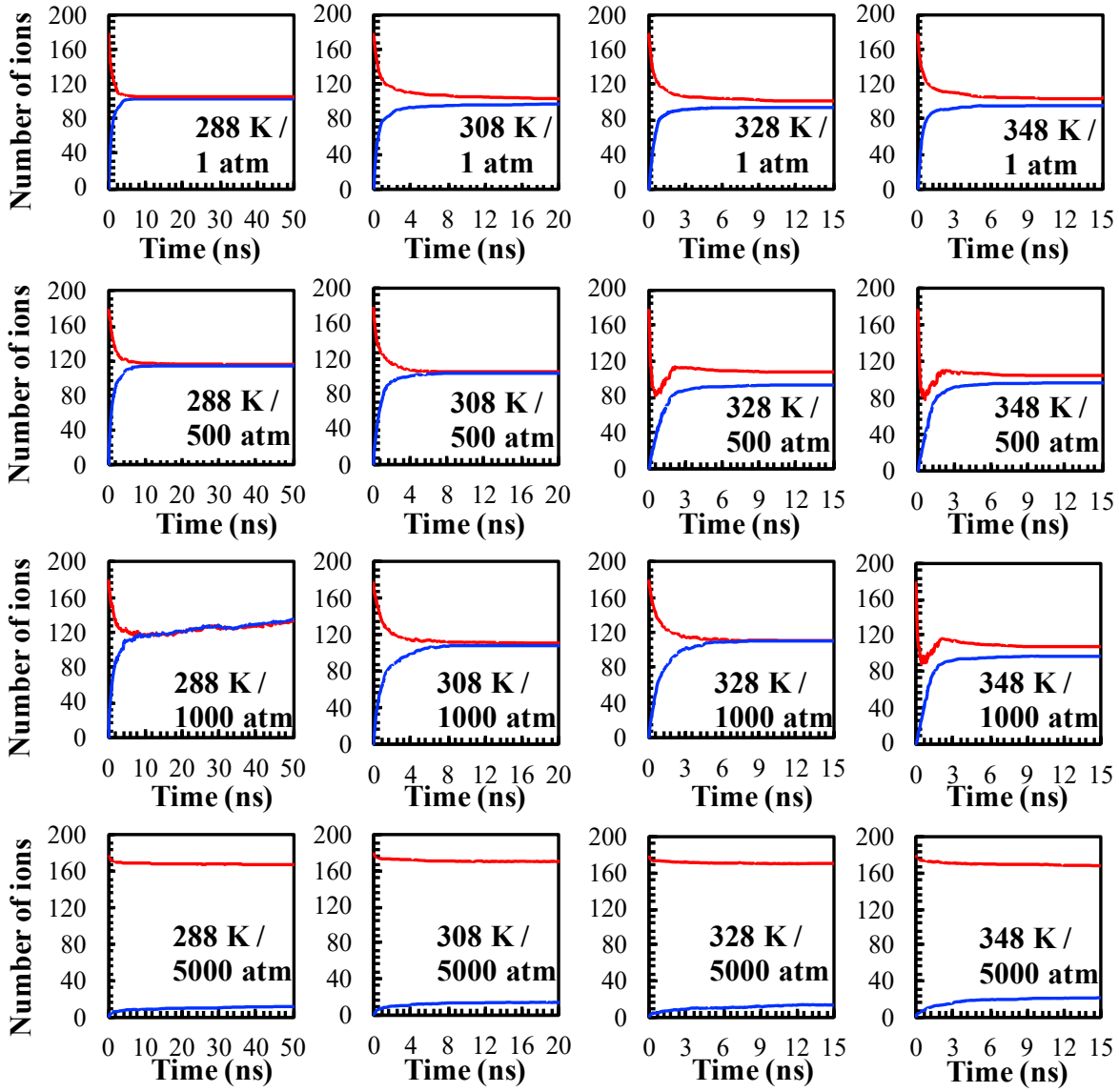

FIGURE A.3. Evolution of the number of ions at compartment I at each combination of temperature and pressure, where the red lines correspond to the Cl^- and the blue lines to Na^+.

Appendix B

Chapter 6 Complementary Information

B.1 Two dimensional profiles of different membranes under WALP incorporation

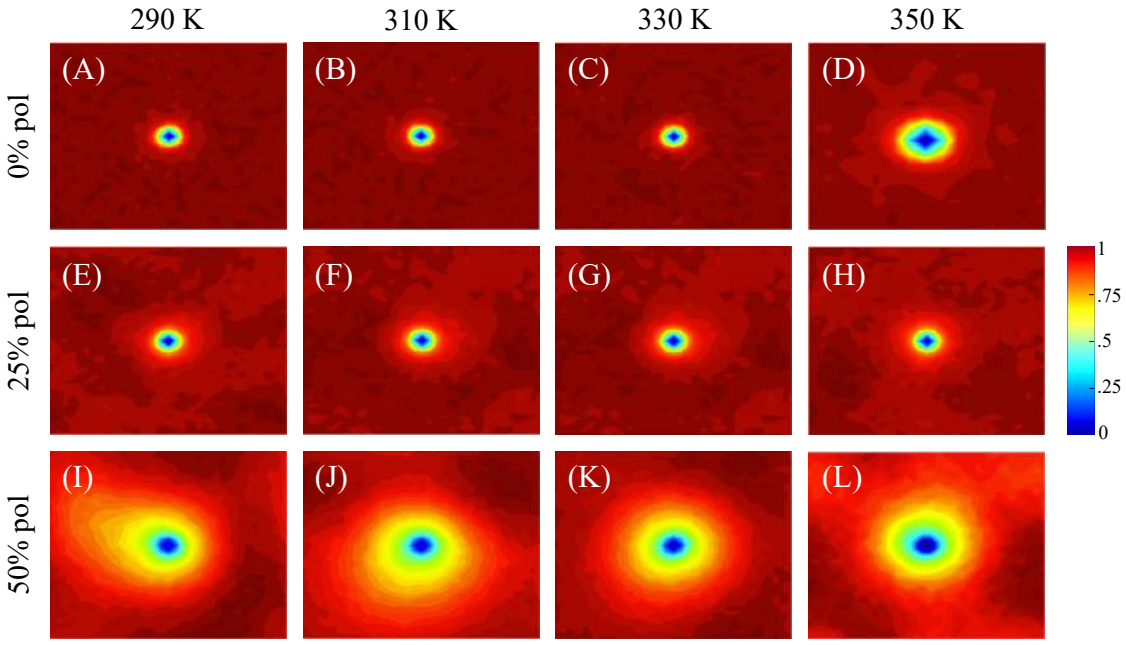

FIGURE B.1. Membrane normalized density profiles as a function of temperature (columns) and polymer concentration (rows): (A) 290 K - 0(polymer):100(lipid), (B) 310 K - 0:100, (C) 330 K - 0:100, (D) 350 K - 0:100, (E) 290 K - 25:75, (F) 310 K - 25:75, (G) 330 K - 25:75, (H) 350 K - 25:75, (I) 290 K - 50:50, (J) 310 K - 50:50, (K) 330 K - 50:50, (L) 350 K - 50:50.

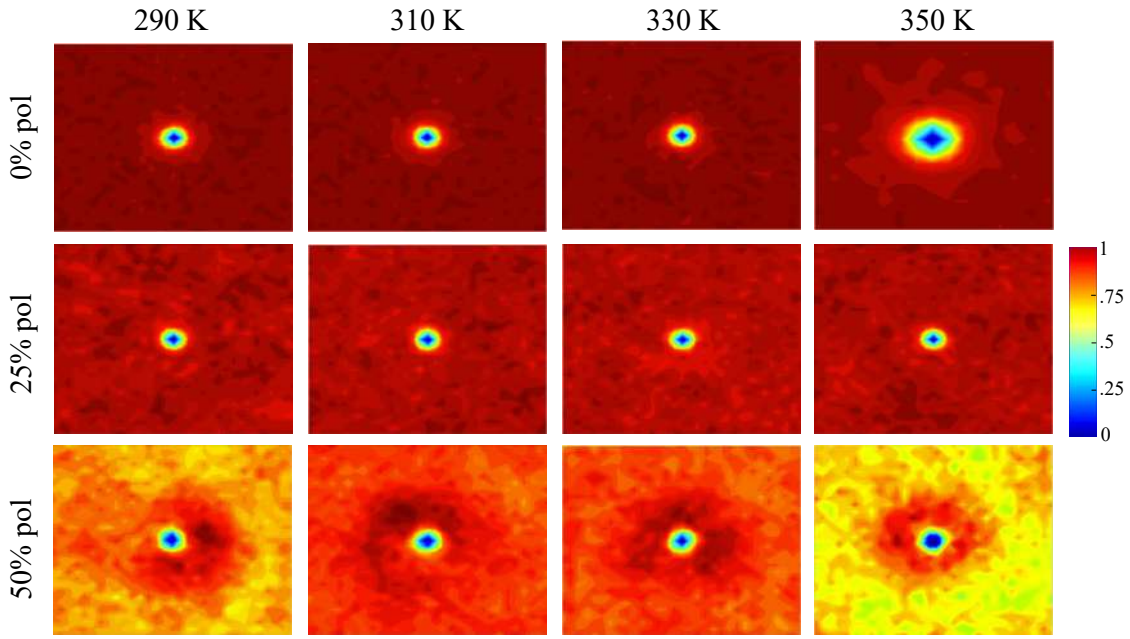

FIGURE B.2. POPC normalized density profiles as function of temperature (columns) and polymer concentration (rows): (A) 290 K - 0(polymer):100(lipid), (B) 310 K - 0:100, (C) 330 K - 0:100, (D) 350 K - 0:100, (E) 290 K - 25:75, (F) 310 K - 25:75, (G) 330 K - 25:75, (H) 350 K - 25:75, (I) 290 K - 50:50, (J) 310 K - 50:50, (K) 330 K - 50:50, (L) 350 K - 50:50.

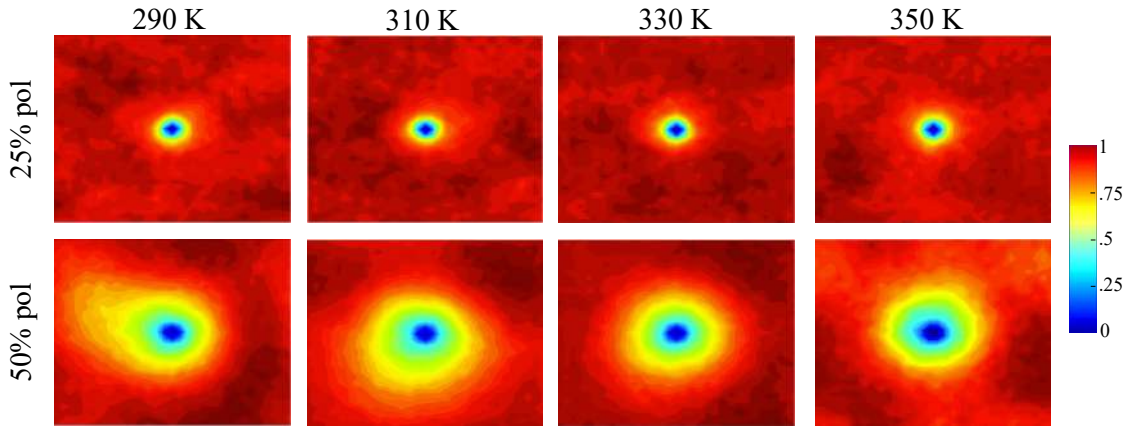

FIGURE B.3. PBD_{22}-*b*-PEO_{14} normalized density profiles as function of temperature (columns) and polymer concentration (rows): (A) 290 K - 0(polymer):100(lipid), (B) 310 K - 0:100, (C) 330 K - 0:100, (D) 350 K - 0:100, (E) 290 K - 25:75, (F) 310 K - 25:75, (G) 330 K - 25:75, (H) 350 K - 25:75, (I) 290 K - 50:50, (J) 310 K - 50:50, (K) 330 K - 50:50, (L) 350 K - 50:50.

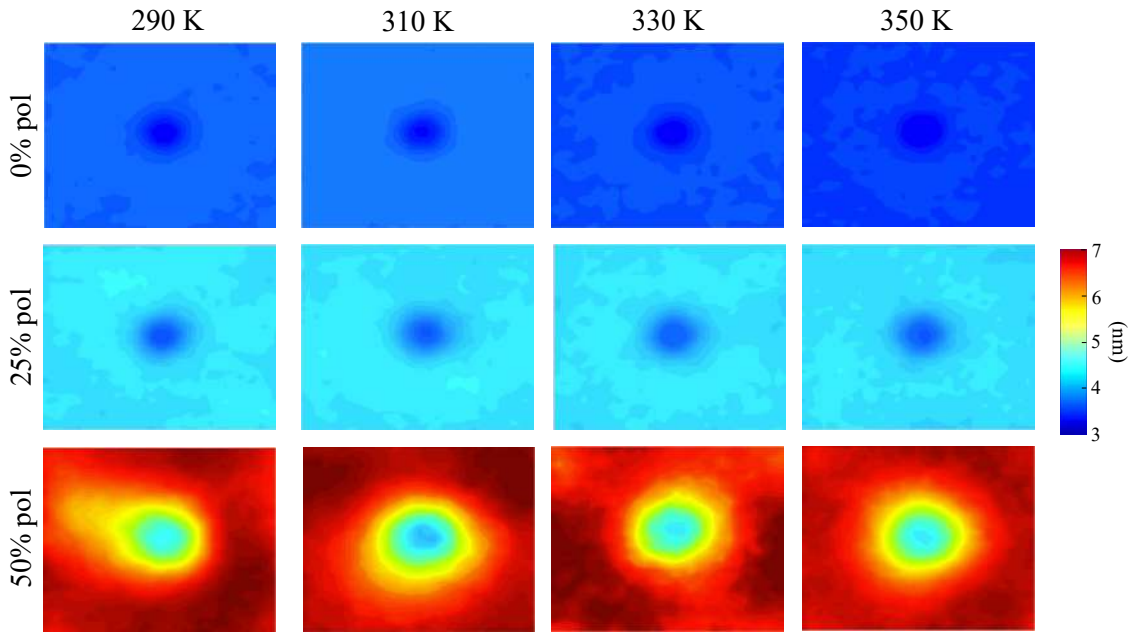

FIGURE B.4. Membrane thickness as a function of temperature (columns) and polymer concentration (rows): (A) 290 K - 0(polymer):100(lipid), (B) 310 K - 0:100, (C) 330 K - 0:100, (D) 350 K - 0:100, (E) 290 K - 25:75, (F) 310 K - 25:75, (G) 330 K - 25:75, (H) 350 K - 25:75, (I) 290 K - 50:50, (J) 310 K - 50:50, (K) 330 K - 50:50, (L) 350 K - 50:50.

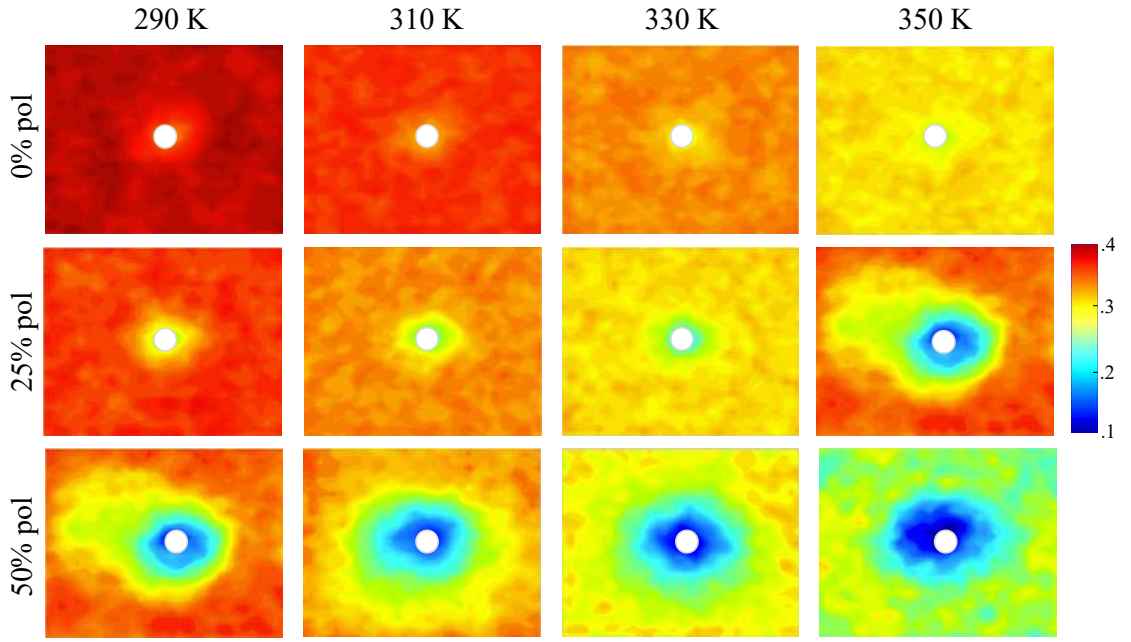

FIGURE B.5. POPC order parameter as a function of temperature (columns) and polymer concentration (rows): (A) 290 K - 0(polymer):100(lipid), (B) 310 K - 0:100, (C) 330 K - 0:100, (D) 350 K - 0:100, (E) 290 K - 25:75, (F) 310 K - 25:75, (G) 330 K - 25:75, (H) 350 K - 25:75, (I) 290 K - 50:50, (J) 310 K - 50:50, (K) 330 K - 50:50, (L) 350 K - 50:50.

B.2 Electron density profiles for all components

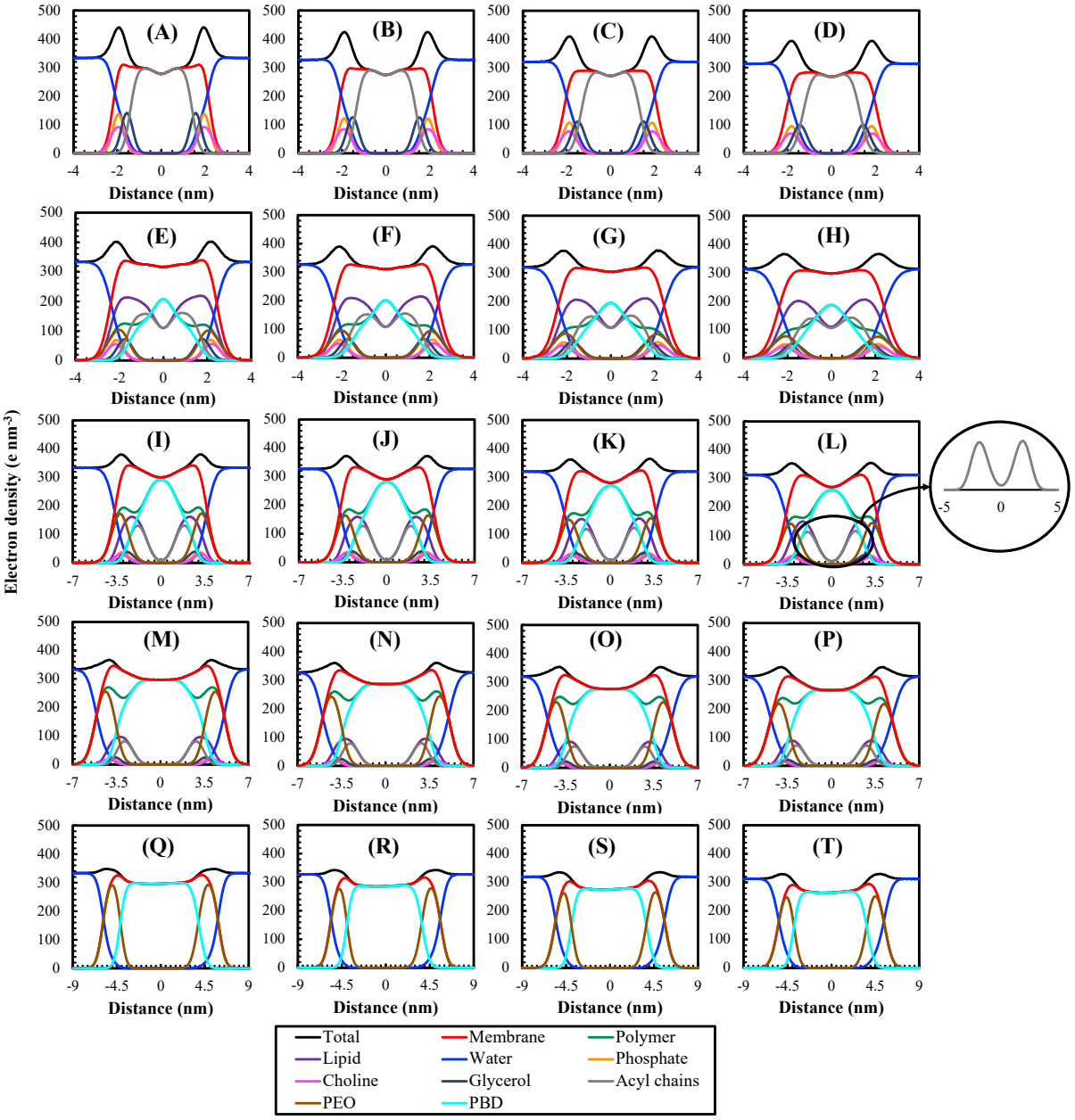

FIGURE B.6. Electron density profiles for membranes at different temperatures (columns) with varying polymer concentrations (rows): (A) 290 K - 0(polymer):100(lipid), (B) 310 K - 0:100, (C) 330 K - 0:100, (D) 350 K - 0:100, (E) 290 K - 25:75, (F) 310 K - 25:75, (G) 330 K - 25:75, (H) 350 K - 25:75, (I) 290 K - 50:50, (J) 310 K - 25:75, (K) 330 K - 50:50, (L) 350 K - 50:50, (M) 290 K - 75:25, (N) 310 K - 75:25, (O) 330 K - 75:25, (P) 350 K - 75:25, (Q) 290 K - 100:0, (R) 310 K - 100:0, (S) 330 K - 100:0, (T) 350 K - 100:0. The detail on the right presents a separate profile for the acyl chains in a 50:50 membrane, revealing the presence of acyl chains both at the center and at the extremities of the bilayer's hydrophobic core.